THE STUDY OF THE INFLUENCE OF THE LIFTER HEIGHT ON THE CHARGE MOTION, VELOCITY PROFILE AND POWER DRAW OF A LABORATORY TUMBLING MILL USING DEM SIMULATIONS.

by

ADRI MARI UYS

A thesis submitted to the Faculty of Engineering and the Built Environment, University of Cape Town in fulfilment of the requirements for the degree of Master of Science in Chemical Engineering

FEBRUARY 2018

CENTRE OF MINERALS RESEARCH

UNIVERSITY OF CAPE TOWN

Abstract

Tumbling mills are considered to be among the most energy intensive devices in comminution circuits and are designed to achieve size reduction and transport. These functions are influenced by the mill speed, filling and the configuration of the lifter bars attached to the mill shell (height, width, face angle, etc.). The lifter height has been shown to influence the charge motion and power draw of the mill. Most of the predictive power models used in industry do not consider lifter heights as a variable.

In comminution, Positron Emission Particle Tracking (PEPT) is used to track the charge motion of particles in tumbling mill systems. The data has been used to derive a velocity profile for particle motion between the mill shell and centre of circulation (COC), a region that highlights the distinct particle motion in tumbling mills. In prior work, a laboratory scale mill and PEPT was used to develop a velocity profile model incorporating the lifter height influence on charge motion. The agreement between PEPT and the model predictions was limited to regions closest to the mill shell and the analysis was restricted for conditions where the lifter height was significantly smaller than the particle diameter. The current study aimed to supplement the PEPT results by using the Discrete Element Method (DEM) to simulate the collective effect of individual particle interactions on the charge motion. The DEM results were used to analyse the influence of the lifter height on the charge motion, velocity profile and power draw for an identical tumbling mill system.

The PEPT and DEM results agreed on charge motion and power draw changes. The assumption of a constant axial pressure drop (dP/dx) along the cross-section of the mill resulted in deviations between DEM and model predictions of the velocity profile. The calculated axial pressure drop varied non-linearly along the mill radius and followed a similar trend at all operating conditions. The relationship between the velocity profile and axial pressure drop was found to vary non-linearly and followed a similar trend to the stress-strain relation of granular media. It is recommended that further research be conducted on the axial pressure drop and its influence on the velocity profile.

Plagiarism Declaration

1. I am aware that plagiarism, the reproduction of the work of another author is wrong.
2. I have used the scientific convention for citation and referencing. Each significant contribution to, and quotation in this thesis from the work(s) of other people has been attributed, and has been cited and referenced.
3. This thesis is my own work.
4. I have not allowed, and will not allow anyone to copy my work with the intention of passing it off as his or her own work.

Signature: Signed by candidate

Date: 30/07/2018

Table of Contents

Acknowledgements

Firstly, I would like to thank God, my Saviour, for making this possible, providing the opportunity and giving me the patience to see it through to the end. To Him be all the glory.

Secondly, I would like to express my gratitude toward a number of people for their valued contributions to this thesis:

Dr Lawrence Bbosa for his endless encouragement, comprehensive feedback and advice while overseeing this work as well as his assistance with the Discrete Element Modelling software and MATLAB coding.

Professor Aubrey Mainza for his support and advice during the course of this study.

Olumide Ogunmodimu for his unrivalled assistance with the Discrete Element Modelling software.

To the CMR team for the consistent encouragement.

Lastly, I would like to thank my family, especially my mother for being patient with me, believing in my abilities, being the support structure and soundboard I so often turned to.

List of Abbreviations

CFS	Charge Free Surface
CoC	Centre of Circulation
COF	Coefficient of Friction
COR	Coefficient of Restitution
DEM	Discrete Element Method
DL	Diametric Line - straight line passing through CoC and origin of mill.
ES	Equilibrium Surface
Granular material	Collection of discrete solid particles (Campbell, 2006)
PEPT	Positron Emission Particle Tracking
RAM	Random Access Memory
SS	Steady State conditions
UCT	University of Cape Town

List of Symbols/Units

D_{GB}; D_m	Diameter of glass beads; Mill diameter
dP/dx	Differential pressure drop along the mill length.
g	Gravitational acceleration, 9.81 m/s^2
e	Void fraction
kWh; MW	Kilo-Watt hours; Mega Watts
L_1	Distance between the CFS and ES along DL.
L_2	Distance between the ES and Mill shell along DL.
L_H / LHt	Lifter Height
m_{DL}/m_{ES}	Gradient of diametric line and equilibrium surfaces at the CoC.
mJ	Milli-joules
v_{mill}	Angular velocity of the mill, m/s
Point A, B	DL intersection with the CFS; DL intersection with mill shell/lifter bar
ω	Angular velocity, m/s
S_{CR}	Critical Speed of mill.
θ	Angle of Inclination of the CoC on the ES from the mill base.
μ	Viscosity, Pa.s

List of Tables

Chapter 2

Chapter 4

Chapter 5

Appendix

List of Figures

Chapter 2

Chapter 4

Chapter 5

Chapter 6

Appendix

1. Project Introduction

1.1. Project Background and Motivation

Tumbling mills are grinding devices that are common to most comminution circuits. Tumbling mills have two functions, transport and breakage. To achieve optimal breakage, tumbling mills are required to achieve charge motion that potentially leads to significant particle collisions resulting in efficient size reduction for the benefit of downstream processes (Schlanz, 1987 and Bbosa, 2013). Tumbling mills have high energy consumption demands and are energy inefficient in that, approximately 70 % of the total energy supplied is used for actions other than mineral recovery processes (Fuerstenau & Han, 2003; Powell & McBride, 2004; Alatalo, 2011; Ghazavi & Ghanad, 2012; Mayank et al., 2015).

Tumbling mills are known for having a complex and aggressive flow environment which has limited the extent of research conducted to understand the charge motion (Rajamani et al., 2000 and Bbosa et al., 2011). Factors like the mill speed, filling, particle size and the configuration of the lifter bars attached to the mill shell i.e. face angle, height, spacing, etc. have been shown to influence the charge motion (Schlanz, 1987; Kulya, 2008; Yang et al., 2008, Brodner, 2013 and Takalimane, 2014). The lifter height has been shown to influence particle motion, particle interactions and the tumbling mill power draw however, most of the predictive power draw models used in industry do not consider lifter heights (Kulya, 2008; Perez-Alonso & Delgadillo, 2012; Brodner, 2013 and Takalimane, 2014).

Brodner (2013) investigated the influence of lifter heights on the charge motion and velocity profile of a tumbling mill. A laboratory scale mill and data from Positron Emission Particle Tracking (PEPT) were used to develop a velocity profile model incorporating the lifter height effects. The results showed that the model predictions only agreed with the PEPT results for regions closest to the mill shell (Brodner, 2013). The extent of the lifter height analysis was limited for conditions where the lifter height was significantly smaller than the diameter of the particles inside the mill (Brodner, 2013). Further research was recommended to address this and supplement the PEPT analysis on the velocity profile.

1.2. Problem Statement and Objectives

The discrete element method (DEM) is a mathematical and computational modelling tool that has been used to simulate the charge motion in comminution devices that typically have thousands of interacting particles like tumbling mills (Vu-Quoc & Zhang, 1999; Di Renzo & Di Maio, 2004; DEM Solutions, 2011; Thornton, Cummins & Cleary, 2011). DEM supplements the results generated from laboratory-scale tumbling mill experiments by aiding the

visualisation of the complex flow environment (Cleary, 1998; Vu-Quoc, Zhang & Walton, 2000 and Kallon, Govender & Mainza, 2011).

DEM makes use of a particle contact force law or contact model, to track all particle interactions taking place to calculate the change in the particle positions, velocity, forces exerted, energy dissipated and the power draw (Vu-Quoc & Zhang, 1999; Morrison, Cleary & Valery, 2001; Di Renzo & Di Maio, 2004; Cleary, 2009b and Perez-Alonso & Delgadillo, 2012). This makes DEM well-suited to examine the velocity profile model developed by Brodner (2013) and thereby supplement the findings generated to add to the current understanding of tumbling mill dynamics on the basis of how the lifter height influences the charge motion, velocity profile and power draw of a tumbling mill.

On the basis of the background information provided, the objectives for this study will be to:

- Investigate the influence of the lifter height on the charge motion, velocity profile and power draw of a tumbling mill using DEM simulations and an identical system to that used in Brodner (2013).
- Compare the DEM results to that of the PEPT system used in Brodner (2013) to supplement the findings on the influence of the lifter height on the velocity profile.
- Examine the predictive capabilities of the velocity profile model developed by Brodner (2013) on the basis of the lifter height influence on charge motion.

1.3. Scope and Limitations

The scope of this project was to investigate the influence of lifter heights on the charge motion, velocity profile and power draw of a tumbling mill using DEM simulations under the same conditions considered by Brodner (2013). The mill speed, filling and lifter height were the only parameters varied in the study. The DEM results were compared to the PEPT results to assess the model developed by Brodner (2013) and the influence of the lifter height on the charge motion. This study did not include a breakage analysis.

All total of 36 DEM simulations were run using the EDEM software package (DEM Solutions, 2011) and the Simplified Hertz-Mindlin Deresiewicz (no slip) contact model. Each simulation required approximately 2 weeks to complete at least 4 mill revolutions which was enough time for the system to reach steady state conditions.

The major limitation of this project consisted of the simulation time constraints associated with running DEM simulations that include thousands of interacting particles. The simulation run-time is dependent on the computer strength (RAM and GHz) and number of particles to be created which is dependent on the mill filling (Cleary & Sawley, 2002; Di Renzo & Di Maio, 2004; DEM Solutions, 2011 and Kallon, 2013). A high particle generation rate (100 000)

ensured that the particle creation was completed and steady state conditions achieved within the first 2 tumbling mill revolutions which reduced the overall simulation run time.

1.4. Thesis Layout

This thesis is divided into 8 major sections according to the list below:

- The introductory chapter provides a brief background and motivation regarding the research area and topic. This section includes the key objectives, scope and limitations of the project.
- The literature review chapter involves a discussion and overview of work done regarding the lifter heights of tumbling mills and how they have been shown to influence the charge motion, velocity profile and power draw. A brief summary of this chapter is included at the end for clarity regarding the research approach of this paper.
- The research approach provides the hypothesis set forward as well as the key questions used to assess it.
- The research methodology chapter summarises the method used to address the hypothesis in terms of the milling system and charge used, key material properties, DEM simulations as well as relevant input parameters required.
- The results analysis and discussion chapters provide an overview of the methods used to extract and analyse the DEM simulation results as well as a summary of key results extracted. Lastly, the results are analysed in conjunction with the key questions to prove or disprove the hypothesis put forward.
- The conclusions are drawn up as well as a few pertinent recommendations from the work reviewed and analysed in the thesis.

2. Literature Review

The literature review consists of an overview of the mechanisms involved in size reduction and the energy intensity of tumbling mills in mineral processing. A review is provided on tumbling mill functions, charge characteristics, flow regimes, lifter configuration characteristics and power draw. The charge characteristics of interest and how they have been incorporated in the velocity profile model derived in Brodner (2013) are discussed.

The Position Emission Particle Tracking method, an invasive method used to understand the flow environment of tumbling mills and its use in the validation of the velocity profile model developed in Brodner (2013) are summarised. The use of the Discrete Element Method is discussed specifically for simulating the flow environment of tumbling mills and the applicability in supplementing the velocity profile model results generated in Brodner (2013).

2.1. Size reduction mechanisms in comminution

Comminution is a process involving the use of mechanical devices to initiate the size reduction of coarse ore particles to produce finer particles for the separation of desired minerals (Kulya, 2008 and Kumar, 2011). Crushing and grinding are typical comminution processes that are used to achieve size reduction by chipping or fracturing particles through various particle impacts as seen in figure 1 below (King, 2000 and Kumar, 2011).

Crushing devices generally produce coarser material through compressive (direct) impacts of particles against rigid surfaces or during the constrained motion of particles (Kumar, 2011 and Kallon, 2013). Grinding devices generally produce a finer charge through both abrasion and attrition interactions (Kallon, 2013) which can take place during the free motion of charge due to high speed impacts or through the compression of small particles between larger particles (Cleary, 2009b and Govender et. al., 2011).

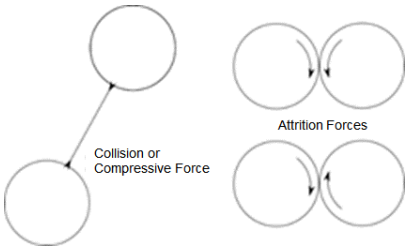

Figure 1: Crushing (compressive) and grinding (attrition) impacts (King, 2000).

When comparing both mechanisms, Djordjevic, Shi & Morrison (2004) found that most particle collisions consist of abrasive collisions (grinding mechanisms) rather than direct impact collisions. Cleary (2009b) reported that effective grinding can be achieved when both direct and shearing impacts occur simultaneously to produce a finer charge. Producing a finer charge ensures larger surface areas which benefits the liberation of valued minerals in down-

stream processes (Kallon, 2013) which forms the basis behind the use of grinding devices in industrial operations (Govender et. al., 2011).

2.2. The Energy Intensity of Grinding Devices

Comminution is known for being one of the most energy intensive operations where size reduction applications are estimated to require only 20 % of the total comminution process energy (Kulya, 2008 and Yahyaei & Banisi, 2010). Fuerstenau & Han (2003) estimated that grinding mills like tumbling mills consume approximately 30 % of the total energy as part of the mineral recovery process (see figure 2, below). The high energy consumption demands make grinding processes an expensive though common practice (Alatalo, 2011 and Ghazavi & Ghanad, 2012).

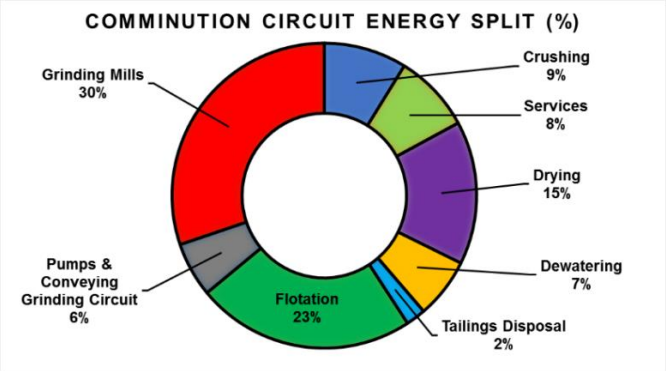

Figure 2: Comminution circuit energy split (Fuerstenau & Han, 2003).

Djordjevic (2003) reported that large mills often require more than 10 MW of power to operate. Kulya (2008) estimated the energy consumption for grinding rock into finer sizes to be between 10 kWh/tonne and 30 kWh/tonne. Significant emphasis has been placed on improving current technologies through performance optimisation rather than developing new technologies to reduce power draw and energy consumption of grinding devices (Perez-Alonso & Delgadillo, 2012; Brodner, 2013).

According to Kulya (2008), an understanding of the mode and mechanisms of energy consumption and power draw enables the identification of saving opportunities for grinding devices like tumbling mills. Zhou et al. (1999), Mishra (2003a) and Campbell (2006) reported that the understanding of tumbling mill grinding mechanisms, which are still not well-understood, can be aided by using computational modelling techniques and power draw models. These techniques enable the development of a thorough understanding of the dynamics of charge motion i.e. the bulk flow behaviour and individual particle interactions and power draw (Zhou et al., 1999).

2.3. Tumbling Mills

2.3.1. General Characteristics

Tumbling mills are common industrial grinding devices used in the South African minerals processing industry (King, 2000; Yang, Zou & Yu, 2003 and Govender, Tupper & Mainza, 2011). Tumbling mills are large rotating cylindrical devices that typically operate at a fraction of the mill speed to centrifuge the particulate material being ground within (Cleary, 2009b). The main function of a tumbling mill is to initiate charge motion that can potentially lead to efficient size reduction and transport (Powell & McBride, 2004). Typical operating conditions include parameters like the mill speed and filling, lifter bar characteristics and charge characteristics like the particle size, shape, etc. (Kallon, 2013).

Tumbling mills typically operate at a rotational speeds of 65 % – 82 % of the mill critical speed but, speeds as high as 90 % of critical have been employed (King, 2000 and Napier-Munn, Morrison & Kojovic, 1999). Burmeister & Kwade (2013) reported that the critical speeds as low as 30 % of critical can ensure grinding between particles and the mill shell while speeds as high as 90 % of critical will result in minimal grinding due centrifuging motion. According to Cleary and Sawley (2002), the chosen critical speed must ensure a high level of shearing between particles due to the charge motion taking place in the mill.

Tumbling mills usually operate at a solids concentration (filling) of 40 % – 60 % solids by volume (Mangesana et al., 2008). Napier-Munn et al. (2005) reported that the average volume should be between 35 % and 45 % of the mill filling.

Since tumbling mills are required to process large ore capacities at higher grinding efficiencies, achieving optimal mill performance (size reduction and transport) is of high importance (Kallon, 2013). An improvement in the grinding efficiency of these devices requires an understanding of the effect of the external environment on the charge and, the internal dynamics of the grinding environment (Kallon, 2013). The key aspect affecting the grinding efficiency and power draw of a tumbling mill is the charge motion according to Yahyaei & Banisi (2010).

2.3.2. Charge Motion and Flow Regimes

The charge motion in a tumbling mill consists of multi-body collisions caused by the transfer of kinetic energy from the mill rotation to the charge (Rajamani, Songfack & Mishra, 2000 and Kulya, 2008). The charge motion and flow regimes have been shown to depend on the mill speed, filling, particle size and the lifters incorporated (Schlanz, 1987; Kulya, 2008; Yang et al., 2008 and Brodner, 2013).

The charge motion affects the particle collisions, charge forces and energy dissipated within the tumbling mill while the flow regime influences the energy dissipated due to friction during

particle impacts (van Nierop et al., 2001; Burmeister & Kwade, 2013). A good understanding of the charge motion and flow regime is necessary i.e. the flow of particles and knowledge of particle movement, to achieve and maintain optimal size reduction (Cleary & Sawley, 2002; Mishra, 2003b; Yang et al., 2008 and Jonsén et al., 2011).

Yang et al. (2008) reported on six typical flow regimes that can be achieved in a tumbling mill which depend on the filling and rotational speed as seen in figure 3 below. To develop an accurate representation of the flow regime, a good understanding of the flow velocity within the mill is required as well (Yang et al., 2008).

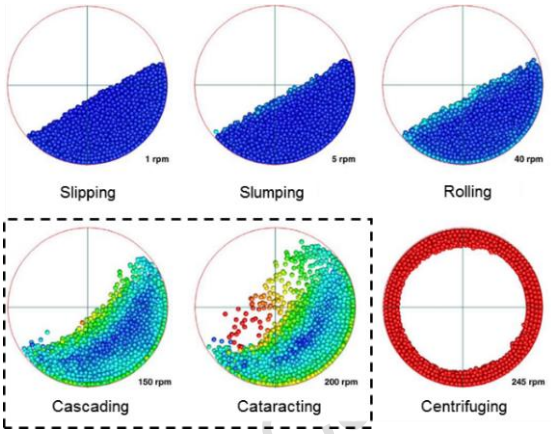

Figure 3: Typical particle flow regimes (Yang et al., 2008).

Yang et al. (2008) gave a detailed description of each regime and reported that tumbling mills usually operate within the cascading and cataracting regimes which are typically described as being complex and difficult to predict (Bbosa, 2013). Operating within these regimes increases the frequency and type of particle interactions to induce more abrasion and attrition interactions (Schlanz, 1987; Bbosa, 2013 and Kallon, 2013).

The charge flow or charge motion in a tumbling mill is described as the behaviour of the mill charge during mill operation which is influenced by the mill rotation and shape of the charge (Kallon, 2013). The charge flow in a tumbling mill undergoes both translational motion along axial distance between the inlet and discharge points of the mill and rotational motion along the radial distance of the mill (Kallon, 2013). Powell & Nurick (1996a) noted that in addition to the radial motion, the particle motion along the length of the mill was influenced by the end walls of the mill as well (Powell & Nurick, 1996a, Zhu & Yu, 2002).

Tumbling mills operating within the cascading and cataracting regimes have charge flows with four typical interaction zones which describe the type of particle interactions taking place as illustrated in figure 4 below (Radziszewsky & Morrell, 1998).

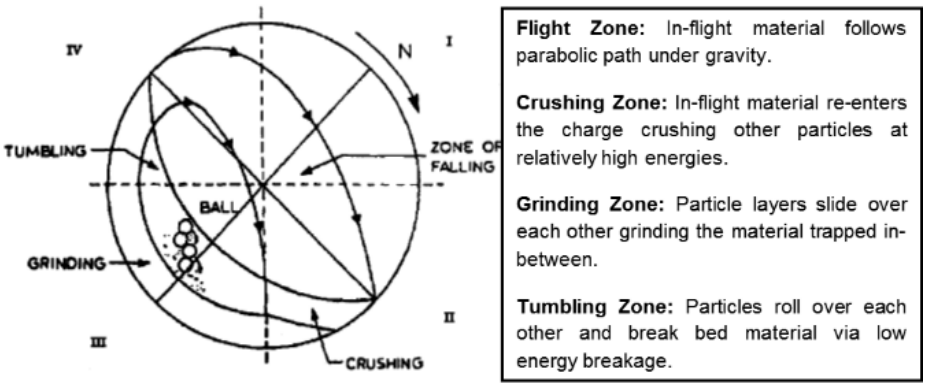

Figure 4: Characteristic flow and interaction zones (Radziszewsky & Morrell, 1998).

The dominance of particle motion occurs in the grinding zone or bulk charge in region 3, followed by the tumbling or rising charge in region 4, free falling charge in region 1 and the high intensity impacts in the crushing zone (region 2) (Djordjevic, Shi & Morrison, 2004).

Within the particle impact regions described above in figure 4, Powell & McBride (2004) described critical charge characteristics that identify basic features of the charge motion as seen in figure 5 below. These characteristics have formed the basis behind tumbling mill charge motion analyses based on changes in the mill speed, particle size, lifter configuration, etc. (Cleary, 2001b).

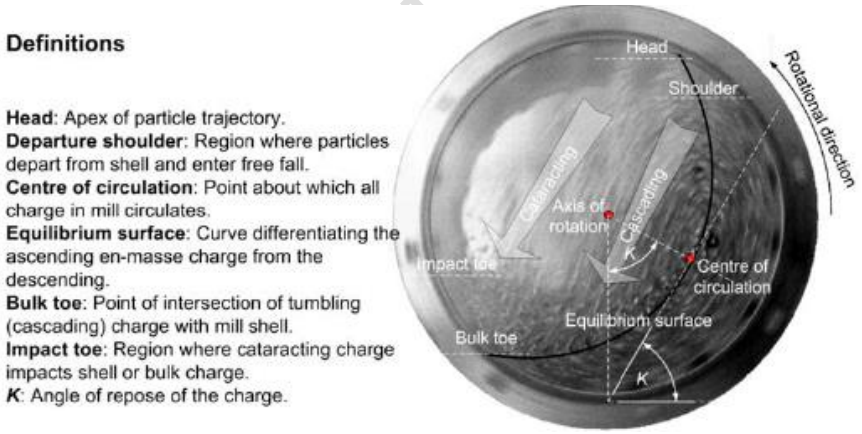

Figure 5: Tumbling mill charge characteristics (Powell & McBride, 2004).

According to figure 5 above, the shoulder and the toe locations, including their respective angles of inclination, are indicative of the shape and boundary conditions of the charge below the equilibrium surface (Nierop et al., 1999, Shi & Napier-Munn, 1999, King, 2000 and Jonson et al., 2011). Cleary (2001b) noted that the shoulder and toe locations are influenced by friction between the charge and the mill shell or lifter bars.

The centre of circulation (CoC) is defined as the vortex centre around which the charge circulates and is key to describing the charge motion in the mill (Cleary, Morrisson & Morrell.,

2003, Kallon, 2013). It has been used to calculate the angle of repose i.e. the inclination of the equilibrium surface above the mill shell or the angular location of the CoC (Powell & McBride, 2004) which represents the slope along which the bulk charge undergoes a consistent oscillation and typically describes the charge flow pattern in a mill (Govender, 2005 and Yang et al., 2008). The CoC has also been used to describe the torque exerted by the charge and power draw of the mill (Govender, 2005; Kallon, Govender & Mainza, 2011).

According to Powell & McBride (2004), a key use of the CoC is in determining the tangent to the equilibrium surface at the CoC which was shown to be perpendicular to a radial line passing through the mill origin and the CoC. Since the shapes of the equilibrium surface and the mill shell do not agree, the only point along the equilibrium surface where the tangent is perpendicular to the radial line described above is at the CoC (Powell & McBride, 2004). This definition has been used by various researchers to understand the complex flow behaviour of tumbling mills.

Figure 4 and 5 above show two distinct charge motion regions separated by the equilibrium surface which indicate distinct flow profiles namely, the active and passive velocity profiles (Cleary, 2001b; Ding et al., 2001 and Brodner, 2013). The active profile or cascading region is situated between the charge free surface and the equilibrium surface while the passive profile or rising en-masse region is located between the equilibrium surface and the mill shell. The profiles differ based on the flow direction and shear (friction) between particles (Cleary, 2001b and Brodner, 2013). Significant abrasion and attrition in these regions could be achieved depending on the magnitude of the shear rates (Yamane et al., 1998 and Cleary, 2001b).

The passive (en-masse) profile consists of particles being carried up along the mill periphery by lifter bars from the (bulk) toe to the (departure) shoulder (Cleary, 2001b; Ding et al., 2001 and Brodner, 2013). The motion in the passive region is caused by the effect of the mill rotation on the charge which decreases as the equilibrium surface is approached due to the friction (shearing) and porosity between particles (Shi & Napier-Munn, 1999). The active profile consists of cascading and cataracting charge, with varying velocity magnitudes, that flows from the lifter bar surface at the (departure) shoulder to the toe of the charge (Shi & Napier-Munn, 1999, Cleary, 2001b and Brodner, 2013).

Kulya (2008), Brodner (2013) and Takalimane (2014) reported that the configuration of the lifter bars attached to the mill shell can influence the charge characteristics discussed above and the transfer of energy from the mill to the charge. This has motivated the importance of the mill shell and the lifter bar configuration when considering the charge motion, size reduction and transport achieved in a mill (Kulya, 2008 and Brodner, 2013).

2.3.3. Lifter Bar Configurations

The main function of the lifter bars in a tumbling mill is to promote high impact motion by lifting and releasing the charge at the highest possible point i.e. departure shoulder (Brodner, 2013). The lifters prevent the charge from slipping down the base of the mill, similar to the sliding of a single body down a smooth, inclined plane (Mellmann, 2001 and Kallon, 2013).

Lifter bars are seen as the mechanical link between the mill and the charge since the transfer of energy from the rotation of the mill and lifters to the charge determines the size reduction achieved (Fuerstenau & Abouzeid, 1985; Makokha & Moys, 2006). Lifters form an important aspect of tumbling mill design as they control the height and angle of departure of the charge and the area, magnitude and impact energy of impact points after trajectories (Cleary, 2001a; Kano et al., 2001 and Brodner, 2013). The design of lifters determines whether the cataracting and cascading charge flows are maintained and whether shear stresses and energy losses due to friction can be prevented (Kallon, 2013).

The lifter bars influence the charge motion by dragging the particles up from the bulk charge to the departure shoulder at which the charge cascades down the free surface (Cleary, Morrisson & Morrell, 2003). The lifter bars act as buckets trapping particles caught between lifter spaces which are gradually poured out in bands as illustrated below (Cleary, 1998; Cleary, 2001a and Mishra 2003b). The cataracting material falls in bands from the spaces between lifters and can generate cyclic variations forming combined impact forces in this region (Cleary, 1998 and Cleary, 2001a).

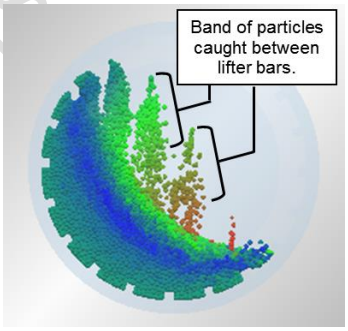

Figure 6: Illustration of bucketed particles caught between lifter bars (EDEM, 2016).

The lifter bar configuration, as per figure 7 below, has been shown to influence the charge flow pattern, grinding performance and tumbling action (Cleary, 1998; Govender et al., 2001; Djordjevic, 2003 and Mokokha and Moys, 2006).

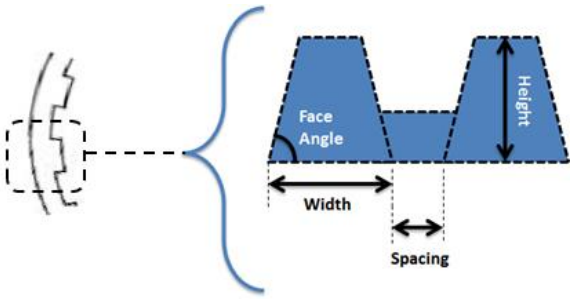

Figure 7: Lifter configuration properties of lifter bars.

Various studies have focussed on understanding the role of the lifter configuration in influencing the charge motion and lifting action of the charge (Mokokha & Moys, 2006; Yahyaei & Banisi, 2010).

The spacing between lifters has been shown to influence the number of particles caught in the particle band and the frequency of charge band collisions with the bulk charge. Djordjevic, Shi & Morrison. (2004) found that the height and number of lifters have been associated with affecting the impact energy of the particle bands. The height and face angle have been linked to how worn the lifter is i.e. small lifter heights and shallow face angles are indicative of worn liners (Yahyaei & Banisi, 2010). The face angle and lifter height were shown to be the most effective parameters influencing the trajectory of charge through the shoulder location (McIvor, 1983; Powell, 1991; Cleary, 1998; Makokha et al., 2007 and Rezaeizadeh et al., 2010). The lifter height and face angle have also be shown to influence the power transferred to the charge (Mokokha & Moys, 2006; Yahyaei & Banisi, 2010).

According to Cleary (1998 & 2001a), Perez-Alonso & Delgadillo (2012), Brodner (2013), Toor et al. (2013) and Takalimane (2014), increasing the lifter height or using steeper face angles resulted in;

- Improved lifting action of the charge with toe locations closer to the mill centre and higher shoulder locations,
- Increased mass of charge trapped between lifter bars during high speed operation,
- Higher impact breakage of coarser material and,
- Increase amount and frequency of cataracting material (particle bands).

Tumbling mills with pronounced lifter wear i.e. shorter lifter heights and shallow face angles, resulted in a lower grinding efficiency due to an increased prevalence of cascading charge and higher levels of packing (Yahyaei & Banisi, 2010; Brodner (2013) and Toor et al., 2013).

The lifter spacing and height form part of the lifter design criterion through the S/H ratio where S is the spacing and H the lifter height. This is similar to the Skega A/B ratio discussed in Powell et al. (2006), an empirical formula shown to change with liner wear (Takalimane, 2014).

Powell et al. (2006) showed how this ratio influenced the mill throughput and power draw. Takalimane (2014) reported that, the spacing was chosen to avoid charge packing between lifters and thereby ensure enough resistance to wear (Powell et al., 2006). The S/H ratio would typically increase from a low valve (newer lifters) to a high valve indicating worn lifters.

Since the extent of tumbling mill research has been restricted to macroscopic-scale studies because of the harsh mill environment, the use of intrusive measuring techniques has been prevented (Rajamani et al., 2000b). The scope of research has shifted from designing new mill shell and lifter designs to exploring ways of improving the performance of pre-existing designs (Mokokha & Moys, 2006).

According to Zhou et al. (1999), Kulya (2008) and Jonsén et al. (2011), investigations into the influence of the lifter design on charge motion and the contact forces, would require modelling basic particle collisions taking place and the bulk charge behaviour inside a mill. These investigations can assist in increasing the understanding of charge motion through the forces acting on and trajectories of individual particles in tumbling mills (Zhu et al., 2007).

2.3.4. Power Draw

The power draw of a tumbling mill is an important measure of the mill behaviour and has been used to evaluate the grinding efficiency and transport of the mill (McBride et al., 2003 and Bbosa et al., 2011). The total power supplied by the electric motor is required to lift the charge being processed and maintain the mill rotation thereafter (King, 2000; Cleary, 2001a; Cleary, Morrisson & Morrell, 2003). According to Mishra (2003b), the grinding efficiency of the mill depends largely on the power used to initiate charge motion resulting in collisions that lead to significant size reduction.

Various definitions have been used to describe the power draw of a tumbling mill. Kulya (2008) and Kallon (2013) defined it as the electricity used per unit of charge mass processed as per the electric motor driving the mill. Cleary (2001a, b and 2009b) defined it as the point at which the energy consumed at steady state conditions for the circulating charge was achieved and maintained. The power drawn by the mill is used according to the energy dissipated during all particle interactions (particle-particle and particle-wall) that are taking place (Cleary, 2001a, b and 2009b). According to Mokokha & Moys (2006), the industrial objective is to draw maximum power to achieve a maximum production rate and high level of size reduction.

These definitions have been used to derive predictive power draw models to assist in their design and optimisation of mills with the aim of ensuring that the method used gives a close representation of the mill system and environment (motion and shape of the charge) as possible (Cleary, Morrisson & Morrell, 2003; Kallon, 2013).

Comprehensive studies have been conducted on the influence of the mill speed and filling on the power draw (Powell & Nurick, 1996c; van Nierop et al., 2001). Cleary (2001a, b) and Van Nierop et al. (2001) reported that the mill filling and speed have a strong influence on the power draw. A higher power draw was recorded at higher filling levels as seen in figure 8 below. Increasing the mill speed resulted in higher power draws up to the point at which the charge starts to centrifuge resulting in a drop in the power draw (Cleary, 2001a, b and Van Nierop et al., 2001). Increasing the speed and filling levels resulted in a higher power draw as seen in figure 8 below.

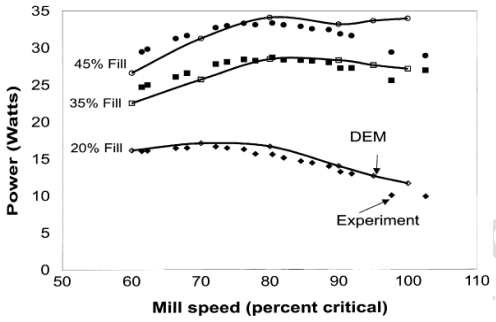

Figure 8: Influence of the mill speed and filling on the power draw (van Nierop et al., 2001).

This is because, for the former condition, less power is required to initiate and maintain motion after achieving steady state conditions. Cleary (1998, 2001a and b) reported that the maximum power draw decreases with mill speed and filling as illustrated in figure 9 below. Van Nierop et al. (2001); Hlungwani et al. (2003); Djordjevic, Shi & Morrison. (2004); Rezaeizadeh et al. (2010); Bbosa et al. (2011) and Perez-Alonsa & Delgadilo, (2012) reported that the maximum power draw increased with mill filling.

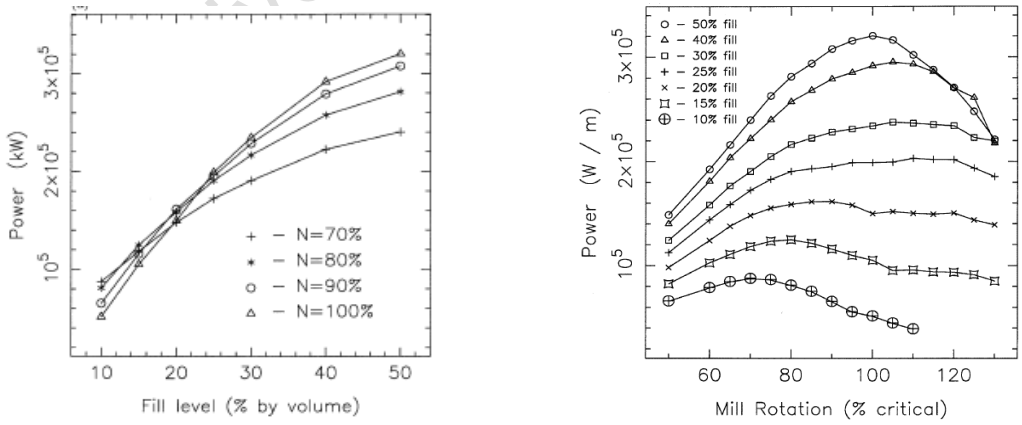

Figure 9: Dependence of mill speed and filling on the power draw Cleary (2001a and b).

According to Cleary (2001a and b) and Rezaeizadeh et al. (2010), since the mill charge also contributes to the power draw, changes in the lifter configuration could potentially influence the power draw of the mill as well. Any change in the mill speed, filling and lifter height results

in an ‘out of balance’ bulk charge which in turn, requires an increased torque (more power) to achieve and maintain steady state conditions (Cleary, 1998).

The lifter face angle was found to influence the power draw in that steeper face angles resulted in less power required to maintain charge motion at high mill speeds and more power was required when using steeper lifters at low mill speeds (Cleary, 2001a and b; Ghazavi & Ghanad, 2012). Cleary (2001a) reported that increasing the mill speed and decreasing the face angle steepness resulted in increasing specific power draw until a maximum (peak) reading was reached as seen in figure 10 below.

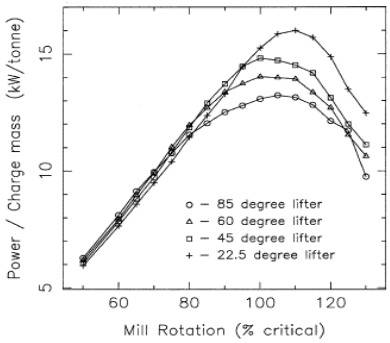

Figure 10: Dependence of specific power draw on mill speed and lifter face angle (Cleary, 2001a).

The lifter height was linked to the face angle in that, steeper face angles typically corresponded to higher lifter bars and thus, higher lifters corresponded to a lower specific power draw with increasing mill speed (Cleary, 2001a). Rezaeizadeh et al. (2010) and Ghazavi & Ghanad (2012) found that the power draw increased with both the mill speed and lifter height. A further increase in the mill speed resulted in a plateau of the power draw (Rezaeizadeh et al., 2010). An increase in the power draw was also reported for shallow lifters due to the effect of slip.

Djordjevic (2003), Hlungwani et al. (2003) and Djordjevic, Shi & Morrison. (2004) reported that an increase in the power draw corresponded to a decrease in the lifter height i.e. mills with lower lifters draw more power than those with higher lifters. This was evident since higher lifters increased the charge impact frequency (Djordjevic, Shi & Morrison, 2004).

The most common method used to calculate the power draw of a mill consists of using the rotational speed of the mill and the total torque exerted due to particle collisions taking place (i.e. particle-particle and particle-wall) (van Nierop et al., 2001; Bbosa et al., 2011 and Kallon, 2013). The total torque has been estimated using a total force balance, an energy dissipation balance, etc. on the basis of the bulk charge body. Bbosa et al. (2011) reported that though frequently used, this method underestimates the power draw due to the assumption that the entire charge moves at the angular velocity of the mill. Researchers have addressed this by incorporating the circulation rate of the charge as discussed in Kallon (2013).

According to Bbosa (2013), modelling the power draw of tumbling mills is one of the major challenges that has been addressed over the years. Some of the methods used to achieve this have consisted of mathematical models that approximate the power draw using charge motion characteristics. These methods however, have proved to be insensitive to material properties like the coefficients of restitution, friction, etc. (Cleary, 1998). In addition to this, the models largely consisted of empirical relationships where the bulk charge was assumed to be a single body (Bbosa et al., 2011). As previously mentioned, these assumptions were made due to the difficulty associated with characterising the charge motion in tumbling mills based on the aggressive internal environment (Bbosa et al., 2011).

2.4. Power Draw Models

Power draw models are used in the design and modelling of industrial grinding mills to predict the product and corresponding power consumed (Doll, 2013). Over the years, the predictive accuracy of these models has been validated through comparisons to lab-scale experiments and industrial data from scale-up procedures (Kulya, 2008).

There are three power models that are widely used in industry namely, the Davis, Bond and Morrell power models which are discussed in Bbosa (2013). These models have been used to predict the power draw in devices like tumbling mills using the mill geometry and characteristics that describe the motion and shape of the charge in the mill (Bbosa, 2013).

The Morrell power model has widely been applied and highly regarded for the design and optimisation of tumbling mills (Morrell, 1996a, b; Napier-Munn, Morrison & Kojovic, 1999; Morrison, Cleary & Valery, 2001 and Bbosa, 2013). The Morrell model applies the influence of the charge velocity on the potential and kinetic energy of the system to the determination of the mill power draw which to date, has been limited to the specific conditions used to develop the model (Morrell, 1993; Bbosa, 2013 and Brodner, 2013).

According to Morrell (1993) and Bbosa (2013), the power draw calculations have been simplified due to the assumptions made regarding the complex charge behaviour and grinding mechanisms in tumbling environments. The findings regarding the influence of the lifter configuration on the charge motion and power draw of a tumbling mill have not been considered (Cleary, Morrisson & Morrell, 2003; Djordjevic, Shi & Morrison, 2004 and Rezaeizadeh et al., 2010; Bbosa, 2013).

Over the years, emphasis has been placed on improving the predictive capabilities of power models by incorporating accurate mathematical descriptions of the charge motion inside a tumbling mill regardless of the complex flow environment (Govender et al., 2001 and Bbosa, 2013). Methods like X-ray imaging and Positron Emission Particle Tracking (PEPT) have been

introduced and used to gain insight into the flow environment of tumbling mills to accurately determine the power draw (Govender et al., 2001; Bbosa, 2013; Bbosa, Govender and Mainza, 2016). The visual representations of the charge motion that these methods can produce, have been used to further understand the complex charge motion in tumbling mills and have aided the design of lifter bars (Mayank et al., 2015).

2.5. Positron Emission Particle Tracking

Over the years, various techniques have been developed to benefit the understanding of the complex tumbling mill environment in order to improve the predictive capabilities of power models used in industry (Kallon, 2013). These techniques have transitioned from high speed filming and photography, to X-ray imaging and Positron Emission Particle Tracking (PEPT) (Govender, Tupper & Mainza, 2011; Bbosa, 2013).

Positron Emission Particle Tracking (PEPT) is a 3D tracking technique used to track changes in the charge motion and trajectory of a single radioactive particle in tumbling mill systems (Parker, 2008 and Bbosa, 2013). A specialised position camera tracks the radioactivity and speed of a single particle inside a mill as illustrated in figure 11 below (Brodner, 2013).

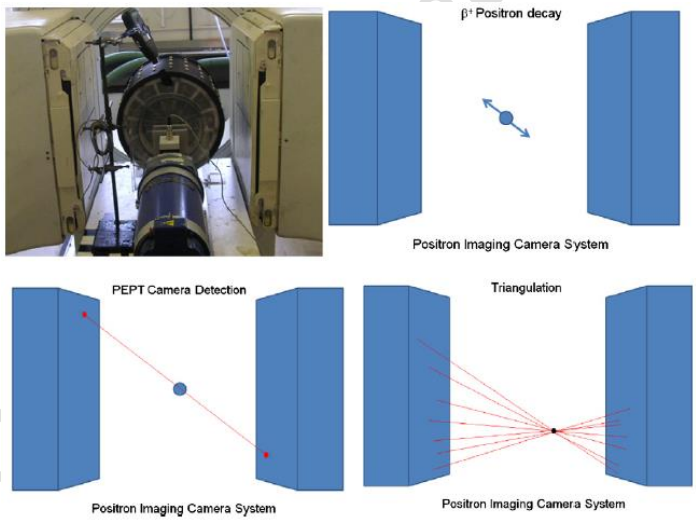

Figure 11: Configuration and schematic of PEPT mill and camera operation (Bbosa et al., 2011).

The specialised camera tracks the particle position based on the decay in radioactivity thereby enabling the position of the particle to be triangulated (Bbosa et al., 2011 and Govender et al., 2011). Once steady state conditions are achieved, the change in the particle position over time is used to assess the particle's flow behaviour (Bertrand, Leclaire & Levecque, 2005; Bbosa et al., 2011, Govender et. al., 2011 and Brodner, 2013). The change in particle position is used to calculate the time-averaged velocity, tangential velocity, acceleration, etc. (Bbosa et al., 2011 and Brodner, 2013). PEPT has also been used to determine the power draw in

tumbling mills using the product of torque and average angular velocities as seen in the equation below (Bbosa et al., 2011; Bbosa, 2013; Bbosa, Govender and Mainza, 2016).

Over the past few years, PEPT has been used to investigate charge flows in comminution devices and has successfully been used to track particles in tumbling mills (Brodner, 2013). Since PEPT allows for a quantitative analysis of the charge motion in a mill, particle velocities, accelerations and contact forces can be determined using the change in particle trajectory within a slurry fluid (Yang et al., 2003 and Brodner, 2013).

PEPT has been used to develop probability distributions of the particle position, velocity, tangential velocities, etc. which in turn, have been used to extract the charge characteristics summarised in Powell & McBride (2004). PEPT has also enabled the determination of charge properties for different particle size distributions and investigations into the shear rate and tangential velocity profiles in tumbling mills (Govender et al., 2011 and Brodner, 2013).

Bbosa et al. (2011) and Bbosa (2013) reported on using PEPT to calculate and develop distributions of the power draw using two methods based on the formulae below namely, the force balance method (P_{COM}) and the cumulated torque per bin method (P_{BIN}). The force balance method seen below, consisted of the total charge mass within a bin (M_i) extracted using the particle position probability plot, the gravitational acceleration (g), the distance of the bin from the centre of the mill (x_i) and the average angular velocity ($\overline{\omega_i}$).

$$P_{COM} = \sum_{i=1}^{2500} M_i \cdot g \cdot x_i \cdot \overline{\omega_i} \quad (1)$$

The cumulated torque per bin method (P_{BIN}) seen below, consisted of the sum of the total force using the force components (F_T – F_x, F_y, F_z) multiplied by the corresponding velocity calculated using the velocity coordinates (v_T – v_x, v_y, v_z) for all the bins in the mill.

$$P_{BIN} = \sum_{i=1}^{2500} |\overrightarrow{F_T} \cdot \overrightarrow{v_T}| \quad (2)$$

Bbosa et al. (2011) reported that the P_{COM} method produced results that under-estimated the power draw determined in lab-scale experiments. This method was based on the assumption of a constant angular velocity similar to that of the mill for the bulk charge. The P_{BIN} method was found to produce values closer to experimental results. The P_{BIN} method became the method of choice for determining the power draw of a tumbling mill using PEPT (Bbosa et al., 2011). The calculated power draw was used to develop power draw distributions where the maximum power draw could be identified and extracted as seen in figure 12 below (Bbosa et al., 2011; Bbosa, Govender and Mainza, 2016).

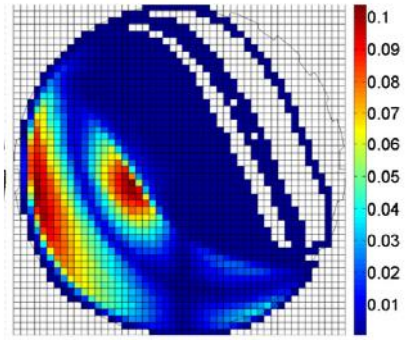

Figure 12: Power draw (Watts) distribution developed using PEPT data (Bbosa et al., 2011).

Since only a single particle is tracked at a time, calculations of inter-particle forces and energy dissipation provide an indirect link between the behaviour of a single particle and that of a particulate system (Zhou et al., 2004, Zhu et al., 2008 and Bbosa, 2013). There is also a size limitation associated with PEPT in that, the system being used must fit within the field of view of the PEPT camera (Bbosa, 2013).

Brodner (2013) reported in a study of the influence of lifter heights on the charge motion and velocity profile of a tumbling mill that the effect of slip encountered in using PEPT limited the extent of the analysis. This was particularly evident for cases where the lifter height was significantly smaller than the diameter of the particle being tracked (Brodner, 2013).

PEPT has been widely validated using mathematical computational techniques developed to meet the challenges of predicting particle motion in tumbling mills (Govender et al., 2001; Bbosa, Govender and Mainza, 2016). Computational techniques like the Discrete Element Method (DEM) have enabled direct comparisons of the charge profiles in tumbling mills and have been used to supplement the findings using a PEPT system (Govender, McBride & Powell, 2004; Bbosa, 2013; Bbosa, Govender and Mainza, 2016)

2.6. A Lifter Height-incorporated Velocity Profile

2.6.1. General Overview

In prior work, Brodner (2013) used a laboratory scale mill and PEPT data to investigate the influence of the lifter height of a tumbling mill on the charge motion and velocity profile. The results were used to develop a velocity profile model incorporating the lifter height effects for the potential inclusion in power models like the Morrell model. Brodner (2013) used an approach similar to work done by Govender et al. (2011) where particle tangential velocities extracted from PEPT data, was used to develop a profile for the shear rates in the mill.

Govender et al. (2011) reported that since the slurry flow behaviour in a typical tumbling mill has a varying viscosity profile and is a function of the shear rate, the viscosity should be

represented according to its varying distribution and not as a constant value. Govender et al. (2011) characterised the shear rate using tangential velocity distributions and displacement data extracted from tumbling mill PEPT experiments.

The tangential velocity was extracted along a diametric line passing through the mill centre and the CoC to capture all the significant changes in the charge flow velocity (Yamane et al., 1998; Govender et al., 2011 and Bbosa, 2013). The diametric line was chosen as such since the CoC is the only point at which the tangents to both the charge free and equilibrium surfaces are perfectly perpendicular to a radial line (Powell & McBride, 2004).

2.6.2. Velocity Profile Shape

Over the years, the velocity profile in a tumbling mill has been widely studied in order to understand the flow behaviour inside the mill. Using the spacial distribution of velocity vector distributions, the shape of the profile was developed and shown to follow the trend illustrated in figure 13 (a and b) below (Yamane et al., 1998; McDonough, 2004; Govender et al., 2011 and Mayank et al., 2015) respectively.

Figure 13a shows that at the mill shell (point A), the tangential velocity along the profile is equal to the angular velocity of the mill at the mill shell and decreases as the profile approaches the CoC where the tangential velocity is zero. The tangential velocity increases in the opposite direction (becomes more negative) as the profile moves away from the CoC and approaches the charge free surface.

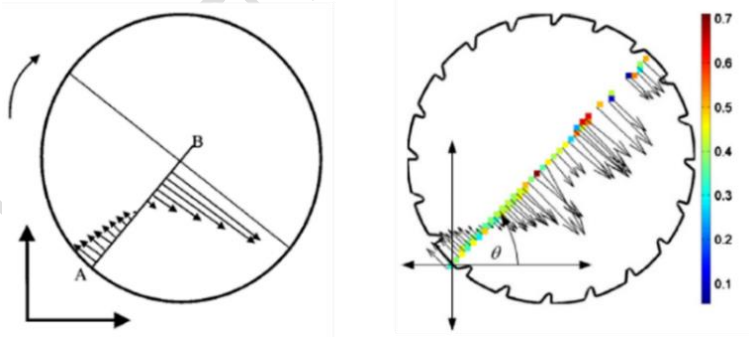

Figure 13: Velocity profile along a diametric perpendicular bisector according to (a) Yamane et al. (1998) and (b) Govender et al. (2011) respectively.

Govender et al. (2011) used the data in the profile in figure 13 (b) to plot the tangential velocity according to the distance along the diametric line as illustrated in figure 14 below.

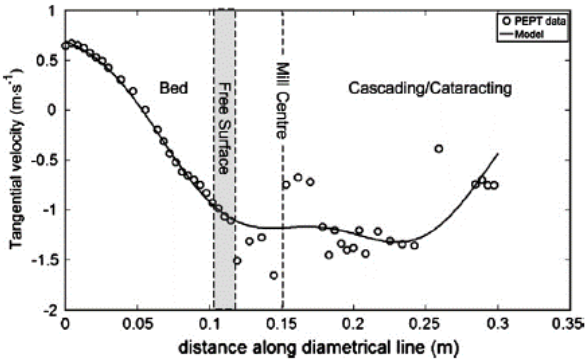

Figure 14: Tangential velocity profile along the diametric line (Govender et al., 2011).

According to the relation illustrated in figures 13 and 14 above,

- The velocity profile decreases from the mill shell to the CoC location. At the mill shell, the profile is similar to the angular velocity at the mill shell.
- At the CoC, the profile passes through zero due to particle contacts, damping effects and high packing levels causing minimal charge motion resulting in increased friction between particles per unit volume (Yamane et al., 1998; Zhou et al., 1999; Mangesana et al., 2008 and Govender et. al., 2011).
- Between the CoC and the charge free surface, where the charge motion is characterised as being cascading, the tangential velocity increases in the opposite direction (Yamane et al., 1998 and Govender et. al., 2011).
- Above the charge free surface, the charge motion is dominated by cataracting motion where the tangential velocity fluctuates making it chaotic and difficult to predict (Govender et al., 2011). Since the porosity is high in this region, there is minimal shear between particles (Yamane et al., 1998).

Various researchers described the change in the tangential velocity profile between the mill shell and the CoC as decreasing following an almost linear relation (Zhu et al., 2008; Govender et al., 2011 and Perez-Alonsa & Delgadilo, 2012). Yamane et al. (1998) reported on a linear trend for low mill speeds due to a constant change in the velocity i.e. laminar flow (Bird, Stewart & Lightfoot, 2002).

For high mill speeds, Parker (1997), Yamane et al. (1998), Shi & Napier-Munn (1999) and Govender et al. (2011) reported a non-linear trend due to the pronounced effects of slip and friction at the mill shell. Above the CoC location, Parker (1997) reported that the profile followed a linear trend due to the change in the tangential velocity being proportional to the distance along the diametric line from the mill centre.

Overall, Nakagawa et al. (1997) reported on a quadratic second-order relation for the velocity profile along the total length of a perpendicular bisector (diametric line). Sanfrantello, Caprihan

& Fukushima. (2006) reported that there was a deviation from this trend near the charge free surface for higher mill speeds due to the chaotic (cataracting) region of the mill.

2.6.3. Results Generated by Brodner (2013)

Brodner (2013) derived a velocity profile model incorporating the effects that the lifter height of a tumbling mill has on the charge motion using the method discussed in Govender et al. (2011). Brodner (2013) identified the charge body (the area between the charge free surface and the mill shell) as the area of interest and not the cataracting material as this was typically difficult to predict due to the chaotic charge behaviour (Govender et al., 2011).

Brodner (2013) postulated that on the basis of what research reported on the influence of the lifter height on the charge motion, the velocity profile of the mill would be affected as well. The model, seen as equation 3 below, aimed to add to the understanding of the flow behaviour and power draw in tumbling mills from the perspective of the lifter height (Brodner, 2013). The model derivation was done using the general Navier-Stokes equation assuming laminar flow, Newtonian fluid characteristics and a constant viscosity and density (incompressible fluid) as highlighted in table 1 below (Brodner, 2013).

$$v_x = \left(\rho g \sin\theta + \frac{dP}{dx} + F_f(y)\right)\frac{(y^2 - L_2 y)}{2\mu} + \frac{v_{mill} y}{L_2} \text{ where } F_f(y) = \mu_e F_N(y) \quad (3)$$

Table 1: Theoretical velocity profile and corresponding variables (Brodner, 2013)

Variables	Units	Constant	PEPT Data	Estimated	Description
ρ	kg/m3	X			Density
g	m/s^2	X			Gravitational acceleration
dP/dx	Pa	X			Applied pressure in x-direction
μ	Pa*s			X	Viscosity
v_{mill}	m/s		X		Tangential velocity at the mill shell
L_2	m		X		Distance from the equilibrium surface to the mill shell
F_N	N		X		Normal force
μ_e	dimensionless			X	Friction coefficient
θ	degrees		X		Angle line perpendicular to the mill shell bottom

According to equation 3, the variables extracted from the PEPT data and incorporating the lifter height effects on the charge motion included the equilibrium surface inclination angle (θ), the distance between the mill shell and equilibrium surface (L_2), normal contact force (F_N) and angular velocity of the mill (v_{mill}) calculated using equations 4 and 5 below.

$$v_{mill}\ (^m/_s) = \omega \cdot \sqrt{(x_1 - x_2)^2 + (y_1 - y_2)^2} \quad (4)$$

$$\omega\left(^{rad}/_s\right) = \left(\frac{42.3}{\sqrt{D_m}}\right) \cdot \left(\frac{\%_{cr}}{100}\right) \cdot \left(\frac{2\pi}{60}\right) \quad (5)$$

Where ω is the angular velocity, D_m is the mill diameter and the distance along the diametric line is ($\sqrt{(x_1 - x_2)^2 + (y_1 - y_2)^2}$).

Figure 15 below, illustrates the variables used in the velocity profile incorporating the influences of the lifter height on the charge motion i.e. the inclination angle and distance L_2.

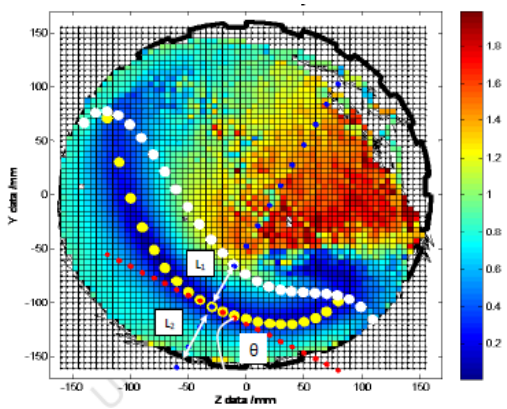

Figure 15: Transverse velocity graph showing extracted variables for the velocity profile model (Brodner, 2013).

Brodner (2013) used a laboratory scale steel mill, spherical glass beads and a PEPT system operated using 3 variables. The mill speed was varied according to 55 %, 70 % and 85 % of critical, the filling was increased from 20 % to 30 % and 40 % and the lifter height was changed using 4 settings i.e. 1.5 mm, 3.0 mm, 6.0 mm and 10.0 mm.

In order to verify the predictive capability of the model, Brodner (2013) extracted the tangential velocity from the PEPT data and found that a consistent trend, similar to figure 13, was maintained at all operating conditions. Figure 16 below shows the influence of the lifter height on the velocity profile between the mill shell and equilibrium surface which was more pronounced at low filling levels.

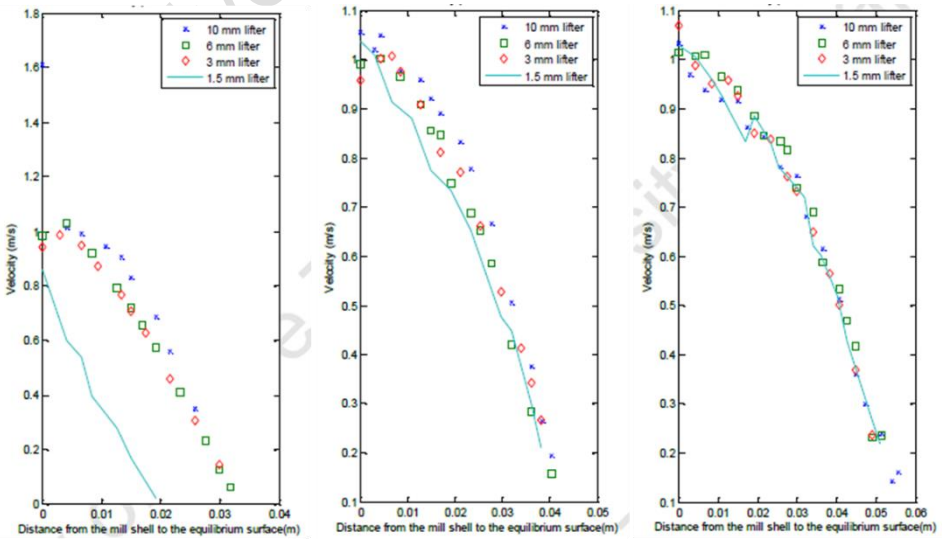

Figure 16: Tangential velocity against the distance along the diametric line for varying lifter heights at 85 % crit. speed for 20, 30 and 40 % filling respectively.

Brodner (2013) found that the PEPT results only agreed with the model predictions in regions closest to the mill shell (L_2) and concluded that the differences could be attributed to the effects of slip encountered in using the PEPT system especially for cases where the lifter height was significantly smaller than the diameter of the particle being tracked. Further research was recommended to interrogate the model's predictive capability (Brodner, 2013).

Simulations are one of the methods employed to investigate the abovementioned particle scale research. One of the aims of simulation platforms is to complement experiments like PEPT to gain a deeper understanding of granular flows in comminution devices (Vu-Quoc, Zhang & Walton, 2000). According to Brodner (2013), an agreement between the results of a simulation and that of an experiment would ensure evidence of a relation between tested conditions and evidence that there is room for improvement on the system being analysed.

2.7. The Discrete Element Method

2.7.1. General Description

It is a well-known fact that the flow environment of tumbling mills is complex due to the particle behaviour which is not fully understood (Vu-Quoc, Zhang & Walton, 2000; Grima & Wypych, 2011). Various investigative techniques have been used to study the flow dynamics of tumbling mills to benefit their design and operation (Di Renzo & Di Maio, 2004). Most of these techniques are based on empirical data which limits the applicability to the specific conditions used to develop them (Di Renzo & Di Maio, 2004).

Techniques like X-ray imaging, MRI, PEPT, etc. have been used to address the limitations associated with the tumbling mill flow behaviour to gain insight to its environment (Govender et al., 2011; Thornton, Cummins & Cleary, 2011). These techniques have restricted the data extraction associated with the charge flow behaviour (Thornton, Cummins & Cleary, 2011).

Di Renzo & Di Maio (2004) discussed simulations and modelling techniques required to increase the current understanding of the flow dynamics of comminution devices like tumbling mills. Thornton, Cummins & Cleary (2011) reported that simulation platforms using predictive models are able to supplement and complement the information obtained from experiments as they aid in the visualisation of the complex charge motion in tumbling mills (Cleary, 1998; Thornton, Cummins & Cleary, 2011; Kallon, Govender & Mainza, 2011).

Several simulation packages and predictive algorithms have been developed to analyse comminution-based devices on both a macroscopic and microscopic scale (Zhu et al., 2008; Grima & Wypych, 2011). In recent years, simulations implementing the Discrete Element Method (DEM) have provided insight into the internal dynamics of common comminution devices like ball and SAG mills (Cleary, Morrisson & Morrell, 2003; Mishra, 2003a).

DEM is a mathematical and computational tool which applies Newton's second law to each particle in a device to calculate changes in the particle position, velocity, acceleration, etc. for all interactions taking place (Vu-Quoc & Zhang, 1999; Di Renzo & Di Maio, 2004). DEM was originally developed to analyse problems associated with rock mechanics but its use has been extended to granular devices like tumbling mills (Cundall & Strack, 1979).

DEM enables an analysis of the flow behaviour of each particle in the charge and the corresponding contributions to the bulk flow behaviour (Zhu & Yu, 2002). It is well-suited to simulating systems that typically contain thousands of interacting particles like tumbling mills as illustrated in figure 17 below (Di Renzo & Di Maio, 2004; Thornton, Cummins & Cleary, 2011; Burmeister & Kwade, 2013).

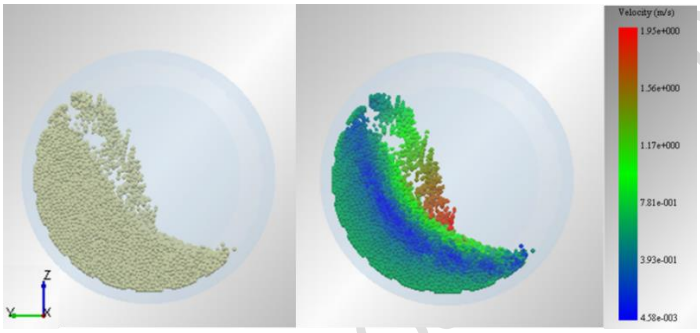

Figure 17: EDEM simulation of the particle position, and velocity distribution in a tumbling mill operating at 55 % of crit., 30 % filling and 3.0 mm lifters heights (DEM Solutions, 2011).

Figure 17, illustrates how the charge flow in the mill is translated into a velocity distribution plot where the colour bar indicates the change in the velocity magnitude. The slowest particles can be identified as that residing in the blue streak i.e. the equilibrium surface which separates the rising en-masse charge above the mill shell from the descending and fast moving cascading charge above the equilibrium surface.

2.7.2. Benefits and Limitations

The use and predictive accuracy of DEM has been well-documented by many researchers (Mishra & Rajamani (1992); Datta, Mishra & Rajamani (1999); Cleary & Hoyer (2000); Govender, McBride & Powell (2004); Kulya (2008), etc.) where DEM has been used to;

- Simulate 3D environments of particle motion in devices using a suitable CAD design of the device (Cleary & Hoyer, 2000).
- Model and characterise particle motion to improve the understanding of granular flow dynamics (Cleary, 1998; Mishra, 2003b; Yang et al., 2008 and Cleary, 2009b).
- Provide particle trajectory and velocity data for all collisions taking place (particle-particle or particle-wall) (Vu-Quoc & Zhang, 1999 and Zhou et al., 2004).

- Extract the charge characteristics described in Powell & McBride (2004) using the results generated (Kulya, 2008).
- Quantify the energy dissipation involved in all particle collisions which can be used to predict the power draw for the simulation duration (Rajamani, Songfack & Mishra, 2000; Morrison, Cleary & Valery, 2001; Cleary, 2009b and Perez-Alonso & Delgadillo, 2012).
- Calculate the torque associated with particle motion and the power consumption of grinding devices like tumbling mills (Cleary & Hoyer, 2000; Cleary, 2001b; Cleary, 2009b; Kulya, 2008; Yahyaei & Banisi, 2010 and Govender, Cleary & Mainza, 2013).

Although DEM has proven to be a useful tool for predicting tumbling mill flow dynamics and thereby make a significant contribution to the mill's design and operation (Grima & Wypych, 2011), there are a few limitations associated with its use.

DEM is only able to simulate particles in dry milling systems and not slurry systems since simulating the behaviour of particles in wet systems can only be achieved through coupling DEM with Computational Fluid Dynamics (CFD) (Morrison, Cleary & Valery, 2001 and Govender, Cleary & Mainza, 2013). Simulating the size distribution of the bulk charge must be approximated because this cannot be completely measured in DEM (Cleary, 2001a).

The simulation run-time associated with DEM has been shown to be strongly influenced by the number of particles in a system, particle shape and the contact mechanics associated with particle interactions i.e. frictional, inelastic spheres and non-spherical particles (Cleary & Sawley, 2002; Di Renzo & Di Maio, 2004; DEM Solutions, 2011 and Kallon, 2013). The more particles in a system, the more irregular and complex the calculations used to evaluate particle collisions, the longer the simulation run-time and the higher the computational intensity of the simulation (Cleary & Sawley, 2002; Di Renzo & Di Maio, 2004; Kallon, 2013).

Most researchers consider the trade-off between the predictive accuracy of DEM and the computational efficiency when selecting the method by which particle interactions are traced (Vu-Quoc & Zhang, 1999). In conducting validation studies, comparisons between DEM and accurate experimental data has enabled realistic conclusions to be drawn regarding the assumptions and predictive accuracy of DEM (Cleary, Morrisson & Morrell, 2003).

2.7.3. Contact Models in DEM

In order to approximate the collision dynamics in various systems, DEM makes use of contact models to describe how particles behave during collisions (Cleary & Sawley, 2002; DEM Solutions, 2011 and Cleary, 2009a, b). Contact models aim to represent particle interactions according to the contribution to the bulk behaviour of the charge which dictates whether the simulated environment resembles the corresponding real-world situation (Grima & Wypych,

2011). Contact models are required to accurately quantify the change in particle displacements, velocities, forces, etc. during all collision events (Thornton, Cummins & Cleary, 2011). Selecting the most appropriate contact model is one of the most important parts of using DEM (Grima & Wypych, 2011).

Contact models enable direct comparisons between DEM and PEPT for similar systems on the basis of the velocity distributions, charge flow patterns, spacial velocity fields, power draw calculations, etc. (Powell & McBride, 2004; Yang et al., 2008; Bbosa, 2013).

In DEM, particle collisions are tracked by enabling interacting particles to overlap to resemble a particle deformation event as seen in figure 18 below. The amount of overlap or deformation represents the compression distance (Campbell, 2006).

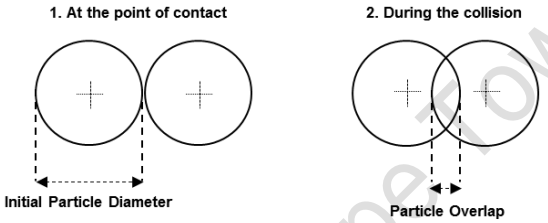

Figure 18: 2D representation of the overlap between particles during a collision.

The contact model uses a contact force-displacement law to measure the amount of overlap to determine how the particle shape is affected during collision events and the corresponding collision or contact forces which can be compressive or shear (frictional) forces (Di Renzo & Di Maio, 2004; Campbell, 2006; Cleary, 2009b; Burmeister & Kwade, 2013).

The overlap and collision forces are used to determine the change in motion (rebound, sliding or rolling), position, velocity, acceleration, etc. using Newton's law of motion which allows for characterisation of the behaviour of interacting particles and the bulk charge (Grima & Wypych, 2011; Burmeister & Kwade, 2013).

Energy is also dissipated according to the contact forces and overlap distances associated with collision events (Morrison, Cleary & Valery, 2001; Campbell, 2006; Burmeister & Kwade, 2013). The collision energies occur through direct and abrasive (shear) particle impacts which take place along the normal and tangential collision plains as seen in figure 19 below.

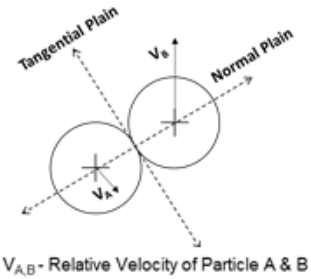

Figure 19: Normal and tangential collision force components.

The energy dissipated during particle collisions can be classified as elastic, plastic, elasto-plastic or as a result of friction experienced between the colliding surfaces (Vu-Quoc & Zhang, 1999; Di Renzo & Di Maio, 2004; Thornton, Cummins & Cleary, 2011). According to Di Renzo & Di Maio (2004) energy can be dissipated as a result of;

- Elastic interactions, where the particle shape is temporarily changed due to the conservation of kinetic energy.
- Plastic interactions, where there is an irreversible change in particle shape as colliding bodies coalesce after a collision and move as a single body thereafter.
- Friction between contacting surfaces.

There are a few contact models, available in literature, which approximate the dynamics of collision events to various extents (Cleary, 2009b). Di Renzo & Di Maio (2004) reported that the physical significance of a contact model depends on whether all the properties calculated by the simulation agree with what is observed in reality. Most contact models differ on the basis of the relationship between the force calculated and the measured particle overlap though all contact models are able to reproduce the general charge motion of colliding particles (Di Renzo & Di Maio, 2004). Zhu et al. (2007) presented a comprehensive study and summary of contact models used in industry (see table 2 below).

Table 2: Contact force and torque models (Zhu et al., 2007)

Force models	Normal force	Tangential force	References
Linear spring–dashpot model	$\mathbf{f}_n = -K_n\delta_n\mathbf{n}_c - C_n(\mathbf{v}_c\cdot\mathbf{n}_c)\mathbf{n}_c$	$\mathbf{f}_t = -K_t\mathbf{v}_c^t + C_t(\mathbf{v}_c\times\mathbf{n}_c)\times\mathbf{n}_c$	Cundall and Strack (1979)
Simplified Hertz–Mindlin and Deresiewicz model	$\mathbf{f}_n = -\frac{4}{3}E^*\sqrt{R^*}(\delta_n)^{3/2}\mathbf{n}_c$ $-C_n(8m^*E^*\sqrt{R^*\delta_n})^{1/2}$ $\cdot(\mathbf{v}_c\cdot\mathbf{n}_c)\mathbf{n}_c$	$\mathbf{f}_t = -\mu\lvert\mathbf{f}_{n,e}\rvert(1-(1-\lvert\mathbf{v}_c^t\rvert/\delta_{\max})^{3/2})\hat{\mathbf{v}}_c^t$ $+2C_t(1.5\,\mu\text{m}*\lvert\mathbf{f}_{n,e}\rvert$ $\cdot\sqrt{1-\lvert\mathbf{v}_c^t\rvert/\delta_{\max}}/\delta_{\max})^{1/2}$ $(\mathbf{v}_c\cdot\mathbf{n}_c)\times\mathbf{n}_c$	Langston et al. (1994, 1995a,b), Zhou et al. (1999) and Zhu and Yu (2002)
Walton and Braun's model	$\mathbf{f}_n = \begin{cases} -k_1\delta_n\mathbf{n}_c, \dot{\delta}_n \geqslant 0 \\ \text{(loading)} \\ -k_2(\delta_n-\delta_{n0})\mathbf{n}_c, \dot{\delta}_n < 0 \\ \text{(unloading)} \end{cases}$	$\mathbf{f}_t = \begin{cases} \mathbf{f}_t' + k_t^0\left(1-\frac{f_t-f_t^*}{\mu f_n-f_t^*}\right)^{1/3}\Delta\mathbf{v}_c^t \\ \text{if } \dot{\mathbf{v}}_c^t \text{ in initial direction} \\ \mathbf{f}_t' + k_t^0\left(1-\frac{f_t^*-f_t}{\mu f_n+f_t^*}\right)^{1/3}\Delta\mathbf{v}_c^t \\ \text{if } \dot{\mathbf{v}}_c^t \text{ in opposite direction} \end{cases}$ where $f_t = \lvert\mathbf{f}_t\rvert,\ f_n = \lvert\mathbf{f}_n\rvert$.	Walton and Braun (1986a), and Walton (1993)
Torque models	Rolling friction torque	Torque from tangential forces	References
Method 1	$\mathbf{m}_r = -k_r\boldsymbol{\theta}_r - C_r\,\mathrm{d}\boldsymbol{\theta}_r/\mathrm{d}t$	$\mathbf{m}_t = \mathbf{R}\times\mathbf{f}_t$	Iwashita and Oda (1998, 2000)
Method 2	$\mathbf{m}_r = -\min\{\mu_r\lvert\mathbf{f}_n\rvert, \mu_r'\lvert\boldsymbol{\omega}_n\rvert\}\hat{\boldsymbol{\omega}}_n$		Zhou et al. (1999), and Zhu and Yu (2002)

The most common contact models make use of a force-displacement relation or contact force law to determine the contact forces involved in a collision. The contact force law which can be linear or non-linear, relates the collision forces to the approximated magnitude and rate of the measured particle overlap and thereby relate particle positions to the force distribution within the bulk material (Grima & Wypych, 2011). After the collision event, Newton's second law of motion is used to determine the new particle positions, velocities and accelerations after which the calculation cycle is repeated (Di Renzo & Di Maio, 2004).

The accuracy and simulation prediction of the contact models listed above depends on the force-displacement relation, the model parameters incorporated and the sensitivity to the charge material properties (Vu-Quoc & Zhang, 1999; Mishra & Murty, 2001). Not all contact models are sensitive to material properties due to a lack of comparable experimental data for the system being considered (Di Renzo & Di Maio, 2004; Kulya, 2008).

Grima & Wypych (2011) reported that selecting inaccurate model parameters affects the calculations completed during collision events and thereby, the representation of the charge flow behaviour. The most common and relevant contact model parameters consist of the contact stiffness (Kn and Kt) and contact damping (Cn and Ct) and the coefficients of restitution and friction (μ).

The stiffness and damping parameters are used to calculate the energy loss during particle impacts which influences the change in contact forces and the duration of the associated simulation (Mishra & Murty, 2001). These parameters cannot be assumed to be constant (Mishra & Murty, 2001; Di Renzo & Di Maio, 2004; Thornton, Cummins & Cleary, 2011).

The contact stiffness influences the particle surface and overlap at the contact point as well as the contact force, time and simulation run-time (Vu-Quoc, Zhang & Walton, 2000; Di Renzo & Di Maio, 2004; Campbell, 2006 and Cleary, 2009b). A low stiffness represents a softer particle which results in a bigger overlap, longer collision contacts and longer calculation times for collision dynamics i.e. longer simulation run-times (Vu-Quoc, Zhang & Walton, 2000; Di Renzo & Di Maio, 2004; Cleary, 2009b). The stiffness varies with the relative particle impact velocity and depends on material properties like Poisson’s ratio, Young’s modulus, etc. (Grima & Wypych, 2011; Thornton, Cummins & Cleary, 2011).

The contact damping, which is proportional to the overlap and the relative particle impact velocities during collisions, influences the coefficient of restitution and the dissipated kinetic energy during collision events (Di Renzo & Di Maio, 2004). The damping is thereby required to maintain the numerical stability of simulations (Cleary, 2009b; Grima & Wypych, 2011).

The coefficient of restitution (COR) is a material interaction property defined as the ratio of the post-collisional to the pre-collisional normal relative velocity (Cleary, 1998). It is dependent on the collision environment and the contact damping which has been shown to influence the energy dissipated during collisions and the power draw of the mill (Cleary, 1998; Di Renzo & Di Maio, 2004; Kulya, 2008). The coefficient of restitution is typically assumed constant due to insufficient experimental data on particle-particle variations of the parameter and difficulty associated with estimating the parameter for particulate systems (Cleary, 2001a; Di Renzo & Di Maio, 2004 and Thornton, Cummins & Cleary, 2011).

Another contact variable parameter is the friction associated with particle-particle interactions due to pre-existing rough areas on the particle surface and particle-wall interactions caused by static or kinetic friction (Kallon, 2013). The friction influences the motion of these bodies through the particle stiffness, resistance to motion and packing in the mill (Campbell, 2006; Gudin, Kaon & Saito, 2007; Aissa, Duchesne & Rodrigue, 2011; Burmeister & Kwade, 2013). The coefficient of friction (COF) on the charge motion has been shown to depend on the mill speed (friction becomes less significant at higher mill speeds) (Kallon, Govender & Mainza, 2011).

The friction coefficient was shown to influence the power draw of the mill in that, the power draw increased with an increase in the friction coefficient (Cleary, 1998; van Nierop et al., 2001; Di Renzo & Di Maio, 2004; Grima & Wypych, 2011). Various researchers showed that since the friction varies with the degree of grinding, it is difficult to measure and cannot be assumed constant due to sensitivity to charge material properties (Di Renzo & Di Maio, 2004; Grima & Wypych, 2011).

In DEM, depending on the contact model, the friction can be split into static and rolling coefficients. The static friction determines the magnitude of the force applied to a motionless object to induce movement and can be estimated from the ratio between the tangential and normal forces (Barrios et al., 2013). The rolling friction is the ratio between the torque required to initiate particle rolling motion and the product of the object's weight and radius (Barrios et al., 2013). It has also been shown to influence the relative velocity and number of collisions occurring (Burmeister & Kwade, 2013).

The contact models commonly used in tumbling mill studies consist of the linear spring dashpot and the simplified Hertz-Mindlin Deresiewicz (no slip) models (Kulya, 2008, Bbosa, 2013). In DEM, both models require similar input variables i.e. coefficients of restitution and friction including material properties like density, Poisson's ratio and shear modulus.

Both models calculate the normal contact force using the particle velocity with reasonable accuracy and both models assume a maximum tangential force since friction between

particles is limited by Coulomb's law of friction as seen in equation 5 below (Vu-Quoc & Zhang, 1999; Vu-Quoc, Zhang & Walton, 2000; Di Renzo & Di Maio, 2004; Kulya, 2008; Bbosa, 2013).

$$F_{t,max} \leq \mu \cdot F_n \quad (6)$$

Where F_t and F_n represent the tangential and normal forces respectively and μ is the friction coefficient. The equation above must be satisfied for each impact event in order to prevent the onset of sliding as a result of shearing at the contact surface (Vu-Quoc, Zhang & Walton, 2000; Cleary, 2001b; Cleary & Sawley, 2002).

The linear spring dashpot model illustrated in figure 20 below, is typically used to represent particle interactions during an impact event (Di Renzo & Di Maio, 2004). It is widely considered to be the most common and well-documented model for tumbling mills for both the normal and shear particle interactions (Morrison, Cleary & Valery, 2001; Grima & Wypych, 2011; Thornton, Cummins & Cleary, 2011). Its preferred use stems from the fact that it has a high level of simplicity with a well understood mathematical approach which reduces the associated computational effort i.e. quicker simulations (Mishra & Murty, 2001; Mishra, 2003a, b; Di Renzo & Di Maio, 2004; Kulya, 2008). Its ease of implementation and flexibility to particles with differing shapes, makes it the conventional model of choice (Thornton, Cummins & Cleary, 2011).

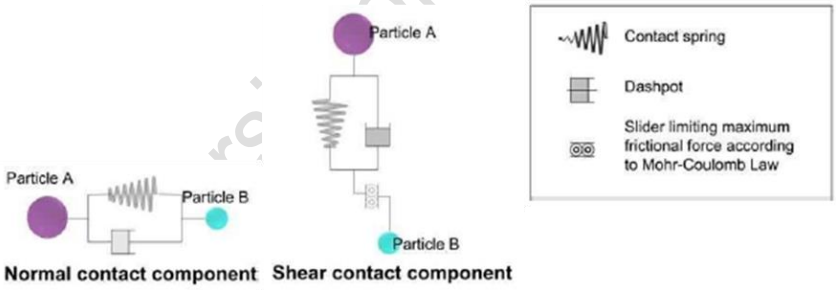

Figure 20: Linear spring dashpot model with normal and shear components (Kulya, 2008)

The spring represents the elastic contribution to the contact response (repulsive force) in the normal direction and stores energy due to the relative tangential particle motion (Cleary, 2001a; Cleary & Sawley, 2002; Kulya, 2008). The dashpot accounts for the damping and relative kinetic energy dissipated due to friction between contacting particles from the tangential motion (Cleary & Sawley, 2002; Di Renzo & Di Maio, 2004; Kulya, 2008).

The linear spring dashpot model is known to deviate from experimentally observed flow behaviours since the (Mishra & Murty, 2001; Di Renzo & Di Maio, 2004 and Kulya, 2008);

- Stiffness and damping are assumed to be constant,
- Model parameters are not accurately and precisely scaled,

- Particle collisions are not accurately approximated as per the charge material properties,
- Impact energy spectra and power draw are inaccurately predicted and over-estimated.

The Hertz-Mindlin Deresiewicz (no slip) contact model provides an alternative to the more common linear spring-and-dashpot model (Kulya, 2008; Bbosa, 2013). This model uses a similar spring and dashpot approach but separately models the normal and tangential force components according to the Hertz theory and the Mindlin-Deresiewicz (no slip) theory respectively (Thornton, Cummins & Cleary, 2011; Barrios et al., 2013).

The Hertz theory determines the elastic contact between particles in the normal direction and the Mindlin-Deresiewicz (no slip) theory determines the elastic-frictional contact in the tangential direction and the energy dissipated due to the collision (Mishra, 2003a, b; Zhu et al., 2007; Thornton, Cummins & Cleary, 2011). Mindlin and Deresiewics assumed a constant coefficient of friction throughout the contact event (Campbell, 2006).

The Hertz-Mindlin Deresiewicz (no slip) contact model is considered more realistic, complex and theoretically sound than the linear model since the (Zhu et al., 2007; Di Renzo & Di Maio, 2004; Kulya, 2008);

- Elastic contacts between spheres are appropriately modelled (Grima & Wypych, 2011).
- Contact stiffness is not assumed constant, but dependent on the overlap and the actual material properties of the charge (Thornton, Cummins & Cleary, 2011; Barrios et al., 2013).
- Complex tangential interactions are calculated more accurately (Mishra & Murty, 2001; Di Renzo & Di Maio, 2004).
- Overall contact response, energy dissipated during collisions and power draw are more accurately predicted (Mishra & Murty (2001).

The Hertz-Mindlin Deresiewicz (no slip) model has a high computational demand resulting in longer simulation run-times even though it is used as the recommended model in EDEM (DEM Solutions, 2011 and Zhu et al., 2007). This is due to a greater accuracy achieved in simulation results and a larger range of calibration options available for the material stiffness and friction parameters (DEM Solutions, 2011).

According to Di Renzo & Di Maio (2004), the examination of the evolution of forces, velocities and displacements during impact events, emphasizes the importance of accounting for non-linearity in contact models. This enables a deeper analysis and understanding of charge motion in tumbling mills, specifically for systems that are dependent on the force and displacement of collisions (Di Renzo & Di Maio, 2004). A more accurate representation of particle velocities and forces over a reduced contact time can be obtained using the Hertz-Mindlin Deresiewicz (no slip) contact model (Di Renzo & Di Maio, 2004).

2.8. Summary of Literature Review

The literature review comprised an investigation into the role lifter heights play in influencing the power draw and charge motion of a tumbling mill. Since the predictive power models typically used in the comminution industry do not incorporate the lifter height, techniques like PEPT and DEM, that are used to track particle motion in tumbling mills, have provided insight into how the lifter height can be incorporated.

In sections 2.1 and 2.2, the importance of size reduction in comminution was reviewed based on the grinding and crushing mechanisms used to achieve this. The grinding and crushing devices, like tumbling mills, typically used in comminution circuits, were shown to have high energy and power requirements. Significant emphasis has been placed on understanding the dynamics of charge motion and how it affects the energy consumption and power draw of tumbling mills. In section 2.3, the general characteristics, functions and typical operating conditions of tumbling mills were reviewed. The characteristic flow regimes of tumbling mills, reviewed by Yang et al. (2008), were discussed. The cascading and cataracting flow behaviour which has been shown to be typical to tumbling mill operation and have been described as complex and difficult to predict (Bbosa, 2013).

It was reported in section 2.3.3 that since tumbling mills are responsible for transport and breakage, the lifter bars along the shell of the mill influence the flow behaviour by lifting and releasing the charge at the highest possible point (Cleary, Morrisson & Morrell, 2003; Brodner, 2013). It was reviewed that the lifter bars aid in achieving high impact motion and are responsible for inducing particle collisions that lead to size reduction (Powell & McBride, 2004; Kulya, 2008 and Kumar, 2011). The influence of the lifter bars on charge motion has been used to characterise the complex flow environment typical to tumbling mills (Kulya, 2008; Bbosa, 2013; Brodner, 2013 and Takalimane, 2014). It was reported that the lifter height influences the trajectory of lifted charge which has affected the impact force with the charge bed and thereby, the power transferred to the charge (Djordjevic, 2003; Mokokha & Moys, 2006; Yahyaei & Banisi, 2010).

In section 2.3.4 it was reported that the power draw is used to evaluate the grinding efficiency and transport of tumbling mills (McBride et al., 2003 and Bbosa et al., 2011). The grinding efficiency depends on the power used to initiate charge motion that ultimately results in collisions that lead to significant size reduction (Mishra, 2003b). The power draw was reported to be influenced by particle collisions induced by the lifter height based on changes in the charge motion, trajectories and bulk charge shape (Cleary, 2001a and b; Djordjevic, Shi & Morrison, 2004; Ghazavi & Ghanad, 2012). It was reported that lifter heights are not included in predictive power draw models regardless of the influence on charge motion and power draw

(Cleary, Morrisson & Morrell, 2003; Djordjevic, Shi & Morrison, 2004 and Rezaeizadeh et al., 2010; Bbosa, 2013).

In section 2.4, it was reported that predictive power models are used to aid the design and optimisation of tumbling mills with the aim of providing a close representation of the mill system and environment (shape and motion of charge) (Cleary, Morrisson & Morrell, 2003; Kallon, 2013). It has been shown that modelling the power draw of tumbling mills is one of the major challenges that has been addressed over the years (Bbosa, 2013). In this work, the mathematical descriptions typically used to calculate the power draw of a tumbling mill have been simplified due to the complex flow environment (Morrell, 1993 and Bbosa, 2013).

In order to incorporate the influence of lifter heights into predictive power models, particle motion and impact collisions have to be tracked and modelled to understand the trajectories of individual particles and quantify the contact forces in tumbling mills (Zhu et al., 2007). Methods like X-ray imaging and Positron Emission Particle Tracking (PEPT) have been used to gain insight into the tumbling mill flow environment to obtain a visual representation and accurately determine the power draw (Govender et al., 2001; Bbosa, 2013; Bbosa, Govender and Mainza, 2016).

Section 2.5 reports on the use of the Positron Emission Particle Tracking (PEPT) technique in comminution to improve the visualisation of charge motion in tumbling mill systems. PEPT allows changes in the charge motion and trajectory of a single radioactive particle to be tracked (Parker, 2008 and Bbosa, 2013). The change in the particle's position over time is used to assess the flow behaviour (Bertrand, Leclaire & Levecque, 2005; Bbosa et al., 2011, Govender et. al., 2011 and Brodner, 2013).

It is reported that PEPT has been used to determine the power draw using methods that make use of the particle's change in torque and angular velocities as well as the balance of forces during impact events (Bbosa et al., 2011; Bbosa, 2013; Bbosa, Govender and Mainza, 2016). The study included a review of work done by Bbosa et al. (2011) and Bbosa (2013) where PEPT was used to develop distributions of the power draw based on calculations using the particle torque which provided results that were similar to that derived from experiments.

Section 2.6 reported on work done by Brodner (2013) where a PEPT analysis was used on a laboratory scale mill to investigate the influence of lifter heights on the charge motion and velocity profile in a tumbling mill in order to develop a velocity profile model incorporating lifter height effects. The research approach was similar to that done by Govender et al. (2011) where particle tangential velocities and displacement data extracted from PEPT data was used to develop a shear rate profile in a mill. Section 2.6 showed that Govender et al. (2011) extracted tangential velocities along a diametric line passing through the mill centre and the

CoC in order to capture the significant changes in charge flow velocity (Yamane et al., 1998; Govender et al., 2011 and Bbosa, 2013).

It was reported that the velocity profile of tumbling mills has been studied by various researchers aiming to mathematically characterise the shape using the charge features discussed in Powell & McBride (2004) (Yamane et al., 1998; McDonough, 2004; Govender et al., 2011 and Mayank et al., 2015). Brodner (2013) aimed to add to the understanding of the flow behaviour and power draw in tumbling mills from the perspective of the lifter height.

The research conducted by Brodner (2013) was reviewed in that the velocity profile model incorporating lifter heights was compared to PEPT experimental data and found to agree in regions closer to the mill shell. The differences between the velocity profile model and PEPT data could be attributed to the effects of slip encountered when using PEPT in cases where the lifter height is significantly smaller than the diameter of the particle being tracked.

In section 2.6 it is reported that PEPT has been widely validated using mathematical computational techniques developed to meet the challenges of predicting particle motion in tumbling mills (Govender et al., 2001; Bbosa, Govender and Mainza, 2016). Computational techniques like the Discrete Element Method (DEM) have enabled direct comparisons of tumbling mill charge profiles and have been used to supplement PEPT findings systems (Govender, McBride & Powell, 2004; Bbosa, 2013; Bbosa, Govender and Mainza, 2016).

In section 2.7 the Discrete Element Method (DEM) is reviewed showing that it has been used to track the motion of particles and thereby, simulate the charge flow behaviour in systems like tumbling mills that typically contain thousands of interacting particles (Zhu & Yu, 2002; Di Renzo & Di Maio, 2004; Thornton, Cummins & Cleary, 2011; Burmeister & Kwade, 2013).

It reported that DEM makes use of contact models that apply Newton's second law to each particle in a system in order to calculate the change in position, velocity and acceleration which are used to determine energy dissipated and contact forces during impact events (Vu-Quoc & Zhang, 1999; Rajamani, Songfack & Mishra, 2000; Morrison, Cleary & Valery, 2001; Di Renzo & Di Maio, 2004; Cleary, 2009b and Perez-Alonso & Delgadillo, 2012). This enables power draw calculations from the torque associated with particle motion and force balances after particle collisions (Cleary & Hoyer, 2000; Cleary, 2001b; Cleary, 2009b; Kulya, 2008; Yahyaei & Banisi, 2010 and Govender, Cleary & Mainza, 2013).

Over the years, the use of DEM has enabled direct comparisons to results generated from PEPT experiments and thereby, can be used to supplement PEPT results by extracting charge characteristics specific to the charge motion (Cleary, Morrisson & Morrell, 2003; Mishra, 2003a; Zhu et al., 2008; Grima & Wypych, 2011).

3. Research Approach

According to Brodner (2013), using a PEPT system to analyse the influence of the lifter height on the charge motion and velocity profile was limited to relating the motion of a single particle to that of the bulk charge. This was especially evident when studying a system with lifter heights smaller than the actual particle being used.

Over the past few years, DEM has been shown to be able to model all particle interactions in a tumbling mill and thereby relate the effects to the behaviour of the charge body. Thus, the influence of the lifter height of a tumbling mill on the charge motion, velocity profile and power draw can be analysed. The results can therefore be used to further examine the predictive capabilities of the velocity profile model developed by Brodner (2013) and thereby, supplement the understanding of the role lifters play in influencing the flow behaviour of a tumbling mill.

3.1. Hypothesis

The kinematic data extracted from the DEM results can be used to show that the lifter height has an effect on the charge motion and velocity profile of a tumbling mill including cases where the lifter height is smaller than the average particle diameter. This is because DEM allows tracking of individual particle contributions to the flow behaviour of the bulk charge in a tumbling mill system with thousands of interacting particles. Since DEM can be directly compared to PEPT-based prior analyses, it can supplement results generated by the velocity profile model developed by Brodner (2013), using PEPT, which incorporates the effects of lifter heights on charge motion.

3.2. Key Questions

Based on the hypothesis posed above, the key questions listed below were put forward.

1. How does the lifter height influence the charge motion and velocity profile on the basis of the charge characteristics analysed in Brodner (2013)?
2. How does the lifter height influence the power draw of the tumbling mill in conjunction with the mill speed and filling?
3. To what extent does the DEM velocity profile agree with the PEPT results generated by Brodner (2013)?
4. To what extent do the predictions of the velocity profile model agree with that generated using the DEM results?

4. Methodology

The research methodology for this study will consist of DEM simulations conducted on a similar tumbling mill system and under the same operating conditions as was used in Brodner (2013) to allow for direct comparison of results. Based on the proposed hypothesis and the key questions, the DEM results were used to gain insight into how lifter heights influence tumbling mill dynamics with the purpose of further examining the predictive capabilities of the velocity profile model developed in Brodner (2013).

4.1. System Specifications and Material Properties

The study conducted by Brodner (2013) involved analysing the flow behaviour of 5 mm diameter spherical glass beads in a laboratory scale steel mill with 20 equally spaced lifter bars. The DEM simulations were based on a replicated system with similar operating conditions. The mill geometry consisted of the mill shell, end plates and equally spaced lifter bars along the periphery of the mill shell as seen in figure 21 below.

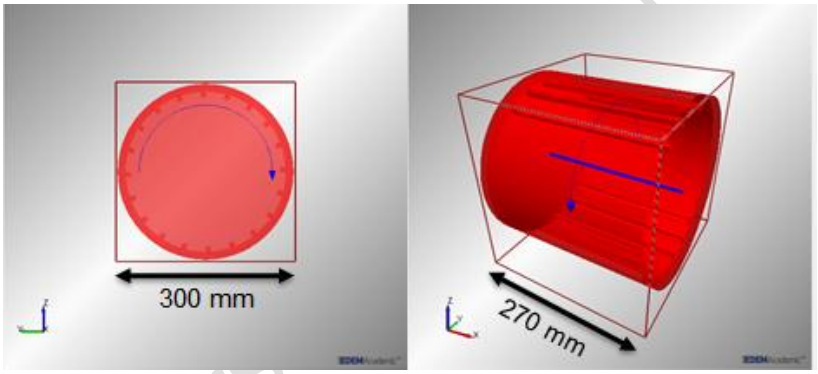

Figure 21: CAD images of tumbling mill rotation and geometry (DEM Solutions, 2011).

Since EDEM is capable of simulating the flow behaviour in tumbling mill environments and creating a particle-scale, parameterized model of the bulk charge, EDEM version 2.7 was the software package used to run all the DEM simulations (DEM Solutions, 2011). The tumbling mill geometry including the endplates, lifter bars, etc. were imported into the software using CAD drawings similar to figure 21 above. The initialisation procedure that was followed is summarised in Appendix A and was similar to that discussed in Bbosa (2013).

In order to initialise an EDEM simulation and ensure the simulation provides a close representation of the experiments, the user is required to provide input parameters i.e. mill material, particle and interaction properties. This includes the material densities, Poisson's ratio, sheer modulus and interaction properties that includes the coefficient of restitution and coefficient of friction. Table 3 below, summarises the material and interaction properties of the steel mill and glass beads (charge) maintained throughout all DEM simulations. The values

quoted in the table below were taken from studies involving similar tumbling mill systems and charge properties (Kulya, 2008; Bbosa, 2013; Brodner, 2013; Von Kallon, 2013).

Table 3: Material properties and interaction parameters

						Coefficient of Friction	
Materials	**Density (kg/m^3)**	**Poisson's Ratio**	**Sheer Modulus (Pa)**	**Particle Interactions**	**Restitution Coefficient**	**Static**	**Rolling**
Steel	7 800	0.29	7.50 E+10	**Glass/Steel**	0.65	0.42	0.01
Glass	2 500	0.23	2.60 E+10	**Glass/Glass**	0.66	0.40	0.01

The coefficient of restitution (COR) and coefficient of friction (COF) are system dependent variables that can significantly influence the system's energy consumption and thereby, vary according to particle impact dynamics (impact velocities, position changes, etc.) (Burmeister & Kwade, 2013). Brodner (2013) found no significant influence between the COF and the measured particle velocity at a constant viscosity since the viscosity of granular material is not well defined at present (Brodner, 2013). In order to simulate an environment resembling the PEPT experiments, gravity was accounted for and maintained at 9.81 m/s^2.

In order to run an EDEM simulation, a contact model must be chosen which EDEM uses to simulate interactions and calculate contact forces, energy losses, etc. As discussed in section 2.7.3 of the literature review, the simplified Hertz Mindlin-Deresiewicz (no slip) model was used in all simulations. It is the recommended EDEM model and was shown to provide an accurate representation of particle interactions in a tumbling mill (DEM Solutions, 2011; Zhu et al., 2007; Kulya, 2008 and Bbosa, 2013). Figure 22 below illustrates the interface.

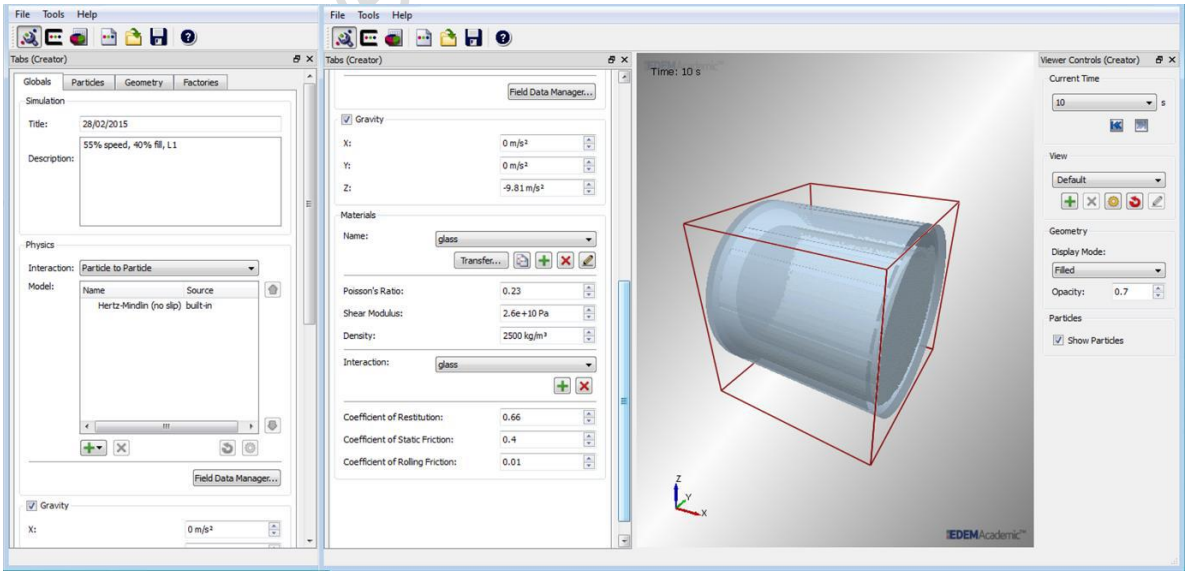

Figure 22: EDEM simulation interface with contact model and material property specifications.

EDEM requires the user to specify particle properties like shape, radius, etc. which is used to determine particle volumes, equivalent mass, etc. All particles were defined as having a 5 mm diameter and a spherical shape as per the default EDEM setting (DEM Solutions, 2011). Figure 23 below illustrated the particle creation and definition interface.

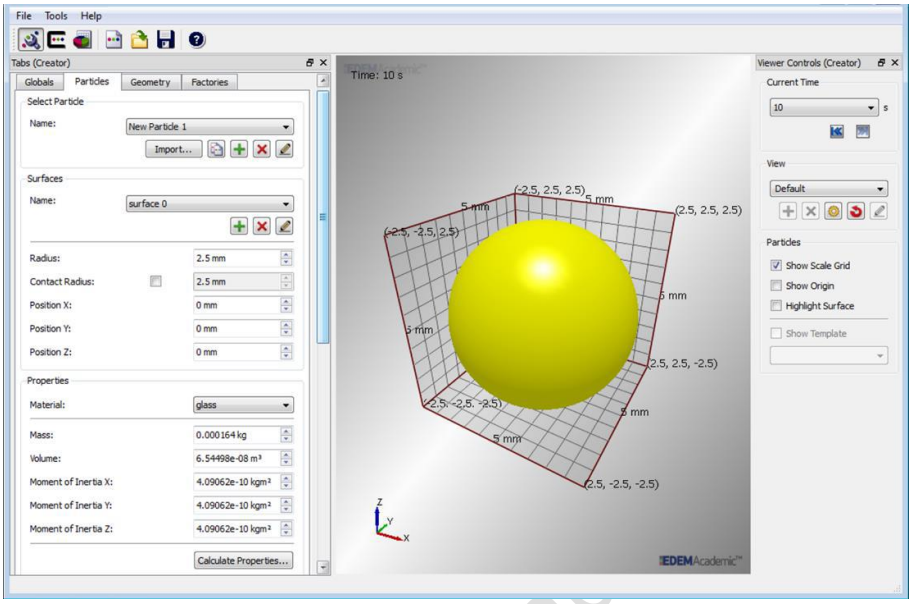

Figure 23: EDEM particle creation interface illustration.

EDEM requires the user to define the environment in which particles interact i.e. mill material, geometry, rotation direction and speed. The mill rotation was set as clockwise and rotated as a single unit by merging the lifter bars and end-plates to the mill.

Figure 24 below illustrates the EDEM interface in which to specify the number of particles to be created and the volume inside the mill in which to create all particles i.e. the particle factory. The particle factory is the virtual volume responsible for defining where, when and how particles are created (DEM Solutions, 2011). The dynamic particle factory option was selected and the particle generation rate was chosen to ensure particle creation within the first mill revolution. This ensures that particles are placed in unoccupied spaces inside the mill which reduces the time taken for steady state to be achieved (Kulya, 2008; DEM Solutions, 2011 and Bbosa, 2013). The calculations used to determine the mill speed and number of particles is summarised in section 4.2 below.

Prior to starting the simulation, the time-step was specified. This is the time taken between calculation iterations as a fraction of the Rayleigh time-step. This is defined as the time required for the effects of contact events to influence the contacting particles (Kulya, 2008 and DEM Solutions, 2011). The time-step is recommended to be between 5 % and 40 % of the Rayleigh time-step which will be used to calculate the contact forces (DEM Solutions, 2011).

If the time step is too short, the simulation will take longer prior to completion and if the time step is too long, particles can behave erratically (Kulya, 2008).

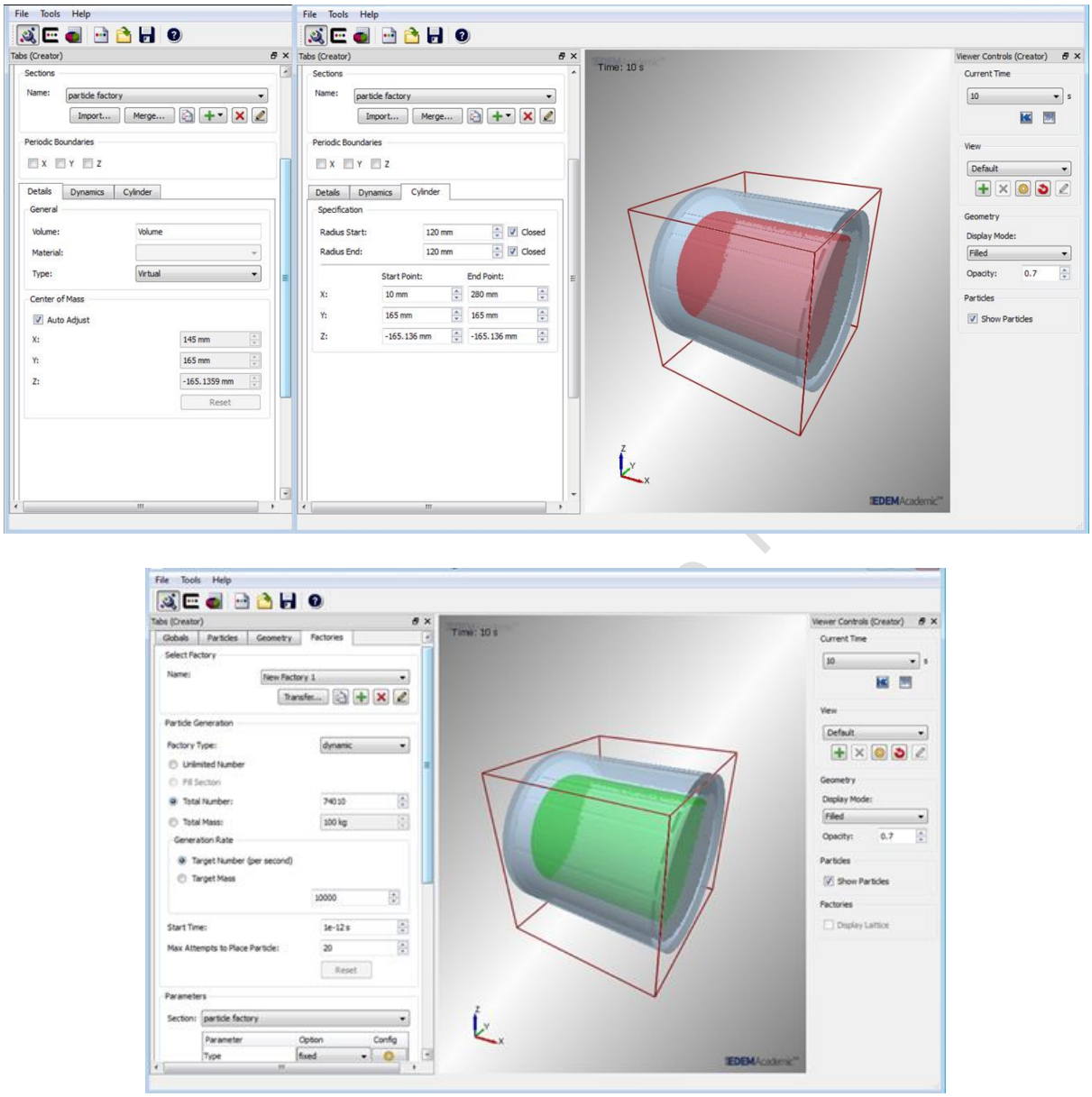

Figure 24: EDEM particle factory specifications.

4.2. Tumbling Mill Operating Conditions

The operating conditions for this study, similar to that used in Brodner (2013), consisted of mill speed, filling and lifter height variations. The mill speed and filling consisted of 3 settings i.e. minimum, intermediate and maximum, as per the general operation settings used in industrial mills (Brodner, 2013). The lifter height was varied according to 4 settings to analyse the charge behaviour in a mill based on newly installed lifters down to extremely worn lifter bars.

4.2.1. Mill Speed Settings

As mentioned in section 2.3 of the literature review, the rotational speed of a tumbling mill influences the flow pattern of the charge and as such, a critical speed exists beyond which the charge centrifuges i.e. no tumbling action occurs. Brodner (2013) assumed that when operating the mill at speeds typical to industrial ranges the velocity profile extracted would hold for all intermediate settings. The mill speed was varied as per the settings listed below;

- 55 % of critical to ensure the cascading motion,
- 70 % of critical which is the general industrial mill speed setting and,
- 85 % of critical to ensure cataracting motion of the charge.

Table 4 below, summarises the mill speed settings in units of RPM and radians/s as required by the EDEM software (DEM Solutions, 2011). Equations 7 and 8 below were used and taken from Kulya (2008); Bbosa (2013) and Brodner (2013). For the purpose of this study, all critical speeds used in EDEM were reported in units of RPM.

$$S_{cr}\ (\mathrm{RPM}) = \left(\frac{42.3}{\sqrt{D_m - D_p}}\right) \cdot \left(\frac{\%_{cr}}{100}\right) \tag{7}$$

$$S_{cr}\ (\mathrm{rad/s}) = S_{cr}(\mathrm{RPM}) \cdot \left(\frac{2\pi}{60}\right) \tag{8}$$

Table 4: Calculated mill speeds in RPM and rad/s

Mill Speed (of Critical)	Rotational Mill Speed (RPM)	Angular Speed (rad/s)
55 %	42.83	4.49
70 %	54.52	5.71
85 %	6.20	6.93

4.2.2. Loading Fractions

The filling fraction was set at 20 %, 30 % and 40 % to replicate general industrial mill operations i.e. low, medium and high settings respectively. Since the mill charge consisted of mono-sized spherical glass beads as was done in Brodner (2013), the average void fraction was assumed to be 0.40 based on experiments using similar media (Kulya, 2008; Bbosa, 2013; Brodner, 2013; Von Kallon, 2013).

As per section 2.7.2 of the literature review, simulating a milling environment using DEM with varying charge sizes adds complexity to the simulation in that the run-time is strongly influenced by the number and shape of particles as well as the contact mechanics associated with the particle interactions i.e. frictional, inelastic spheres and non-spherical particles (Cleary & Sawley, 2002; Di Renzo & Di Maio, 2004; DEM Solutions, 2011 and Kallon, 2013). The more irregular the particle shape, the more complex the calculations used to evaluate collisions, the

longer the simulation run-time and the higher the computational intensity of the simulation (Cleary & Sawley, 2002; Di Renzo & Di Maio, 2004; Kallon, 2013). Even though the charge simulated is not representative of the varied sizes typical found in industry, using mono-sized spherical particles in DEM simplifies the simulations and still provides a view of the charge behaviour in the complex milling environment. The simulations also allowed for direct comparisons to the PEPT experiments conducted by Brodner (2013).

Since EDEM requires either the charge mass or the exact number of particles for each simulation and were calculated using the filling and void fraction. The results are listed in table 5 below. The relevant calculations are summarised in Appendix B.

Table 5: Charge mass and corresponding number of particles

Loading	Charge Mass (kg)	# of Particles
20 %	6.05	37 005
30 %	9.08	55 507
40 %	12.11	74 010

4.2.3. Lifter Height Settings

The lifter height settings for this study were chosen so as to simulate the flow behaviour of charge in a tumbling mill at different stages of lifter wear i.e. newly installed, moderately worn, worn and extremely worn lifters. The lifter height settings chosen for the experimental analysis consisted of 10.0 mm, 6.0 mm, 3.0 mm and 1.5 mm respectively. The lifter bar configuration dimensions that were kept constant throughout all simulations included the spacing, face angle and lifter width as illustrated in figure 25 below.

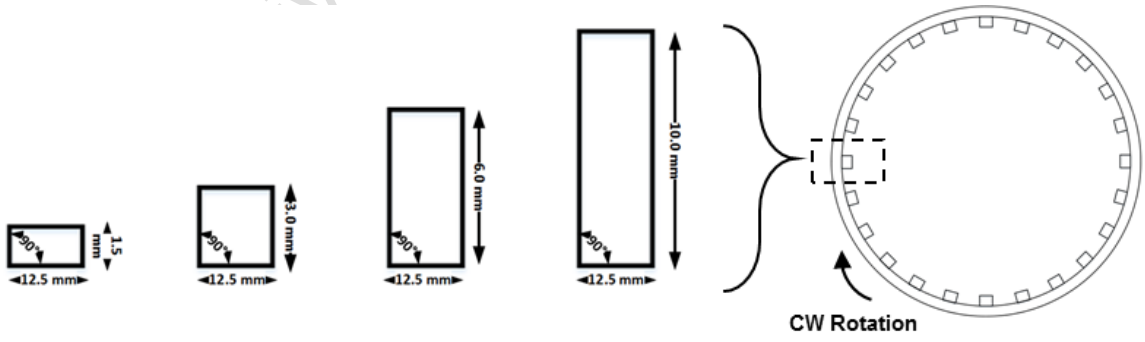

Figure 25: Lifter height variations as adapted from (Brodner, 2013)

The lifter height settings were calculated using the S/H ratio as discussed in section 2.3.3 of the literature review using industrial data generated from a 6 m diameter tumbling mill scaled down to the lab-scale mill dimensions as reported in Brodner (2013). The experimental data showed that the maximum and minimum lifter heights should be double and less than half of the average particle diameter used in the tumbling mill respectively (Brodner, 2013).

The lifter height settings used in this study were calculated by scaling down mill diameter to lifter height ratios using the industrial data quoted in Brodner (2013) to the mill dimensions for this study (Brodner, 2013). The relation between the lifter height and the glass bead diameter is summarised in table 6 below.

Table 6: Lifter height relation to particle diameters

Lifter Height Variations			
Lifter Height	L_H/D_{GB}	Lifter Status	% of New L_H
1.5 mm	0.3	Extremely Worn	15 %
3.0 mm	0.6	Worn	30 %
6.0 mm	1.2	Partially Worn	60 %
10.0 mm	2.0	Newly Installed	100 %

The charge flow behaviour in a mill with no lifter bars is similar to that of the rolling regime. Since the current study focussed on the influence of the lifter height on the charge motion, velocity profile and power draw of a mill, the 'no lifter bar' case was not investigated. A total of 36 simulations were run using the EDEM software based on varying the mill speed (3 settings), filling (3 settings) and lifter height (4 settings).

5. Results Analysis

The EDEM results summarised in Appendix D, were analysed according to the influence of the critical mill speed, mill filling and lifter height on the charge motion, power draw. The extracted data was used to understand the influence of the operating conditions on the velocity profile along the diametric line and the velocity profile model proposed by Brodner (2013).

5.1. Data Extraction and Representation

The EDEM simulation results were used to extract data sets in the form of x, y and z coordinates for particle positions, charge velocity and the total and normal forces exerted during particle impacts. The data sets, in .csv file formats, contained all the coordinates logged at every time-step for the duration of a full revolution of the mill. MATLAB and MS Excel were used to further analyse the data sets based on the charge characteristics, power draw, charge velocity and velocity profile. The EDEM and PEPT results were directly compared using MATLAB to superimpose the x, y and z coordinates onto a 2D reference frame (figure 26 below). The MATLAB code discussed in Bbosa (2013) was used to extract the data sets.

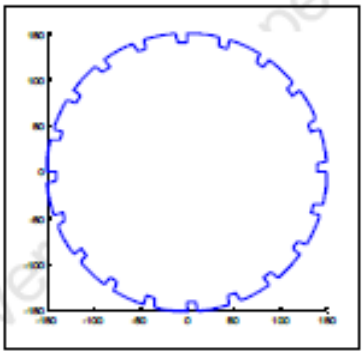

Figure 26: Virtual representation of a tumbling mill, taken from Brodner (2013).

The 2D reference grid used the Cartesian coordinate system and the mill cross-section dimensions when representing the EDEM results. All angles were reported in degrees (°) and converted from MATLAB convention to that used in Brodner (2013) as seen in figure 27 below.

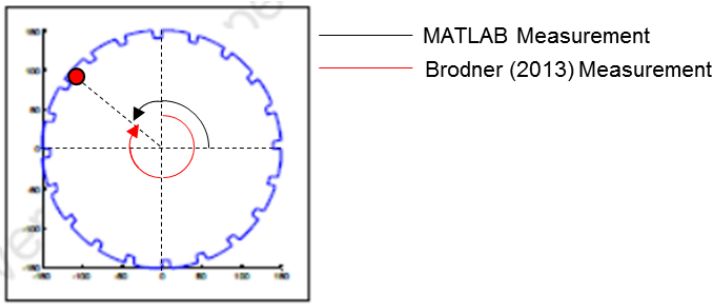

Figure 27: Representation of angle measurements according to MATLAB and Brodner (2013).

5.1.1. EDEM Data Sets

The average kinetic velocity was analysed according to the simulation run-time to determine the point at which steady state motion was achieved by the charge in the mill and the point at which one full revolution was completed by the mill. Figure 28 below illustrates the change in the average kinetic energy for the simulation run-time period and the point at which steady state conditions were achieved.

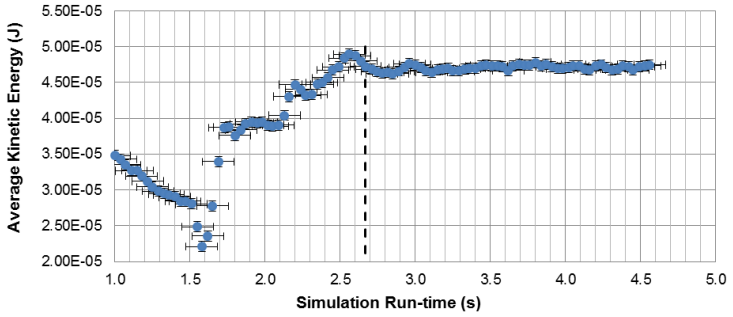

Figure 28: Time taken reach steady state conditions using the average kinetic energy for operation at 85 % critical speed, 40 % filling and 1.5 mm lifter heights.

Figure 28 shows that steady state conditions were achieved at 2.67 s for an average kinetic energy of 4.71×10^{-05} J (0.047 mJ). The results achieved for all operating conditions followed a similar trend. According to Zhou et al. (1999), the small fluctuations showing deviations from the steady state average kinetic energy are due to instabilities in the charge flow behaviour leading to a rearrangement of the particles as the mill rotates.

5.1.2. Particle Position and Charge Velocity

The MATLAB algorithms discussed in the following section are explained in Appendix C. A MATLAB binning algorithm was used to generate probability distribution plots representing changes in the particle position and charge velocity, at all operating conditions, in the reference frame of the mill. The position probability distribution in the mill was generate using the x, y and z coordinates of particle positions over the extraction duration and illustrated in the y-z plane as seen n figure 29 below. The position probability plots generated at all critical speed, filling and lifter height settings are illustrated in Appendix D.1.

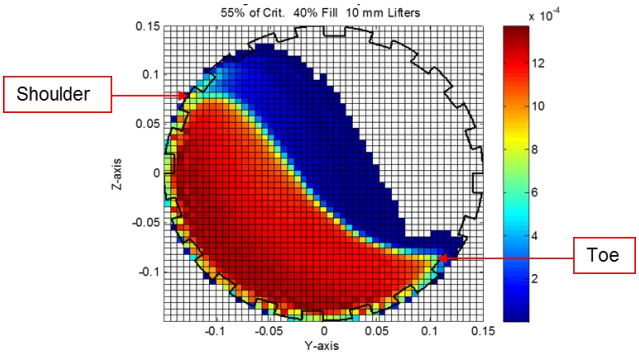

Figure 29: Shoulder and toe locations extracted from the position probability distribution at 55 % critical speed, 40 % filling and 10.0 mm lifter heights.

The 'Ginput' function in MATLAB was used to extract charge characteristics like the shoulder and toe locations as well as the shape of the charge free surface from the particle position distribution plots at all mill critical speed, filling and lifter height settings. The charge free surface across the face of the mill, was required to determine distance L_1, a variable in the velocity profile model derived by Brodner (2013).

The shoulder is the highest particle position at which particles leave the mill shell (Brodner, 2013). The toe is the lowest particle position along the charge free surface, before the lifters drag particles into the charge bed. The change in shoulder and toe locations were analysed using the height above the mill base, radial distance from the mill centre (0, 0) and inclination above the mill centre (0, 0). The inclination angles were calculated using the equations below and were adjusted using the Brodner (2013) convention illustrated in figure 30 below.

$$\theta_{Toe}\ (°) = \tan^{-1}(\text{z coordinate/y coordinate}) \quad (9)$$

$$\theta_{Shoulder}\ (°) = \tan^{-1}(\text{z coordinate/y coordinate}) \quad (10)$$

$$\theta_{Toe\_adjusted}\ (°) = 90° - \theta_{Toe} \quad (11)$$

$$\theta_{Shoulder\_adjusted}\ (°) = 270° - \theta_{Shoulder} \quad (12)$$

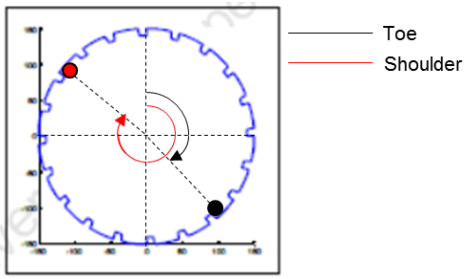

Figure 30: Illustration of toe and shoulder angle calculation convention according to Brodner (2013).

The charge velocity distribution in the mill was generated using the x, y and z coordinates of particle velocities over the extraction duration. The magnitude and direction of the average

charge velocity, within each bin, were used to plot a vector field diagram. Figures 31 and 32 show the charge velocity distribution and velocity vector field illustrated in the y-z plane. The velocity distribution and vector fields generated at all critical speed, filling and lifter height settings are illustrated in Appendix D.2 and D.3 respectively.

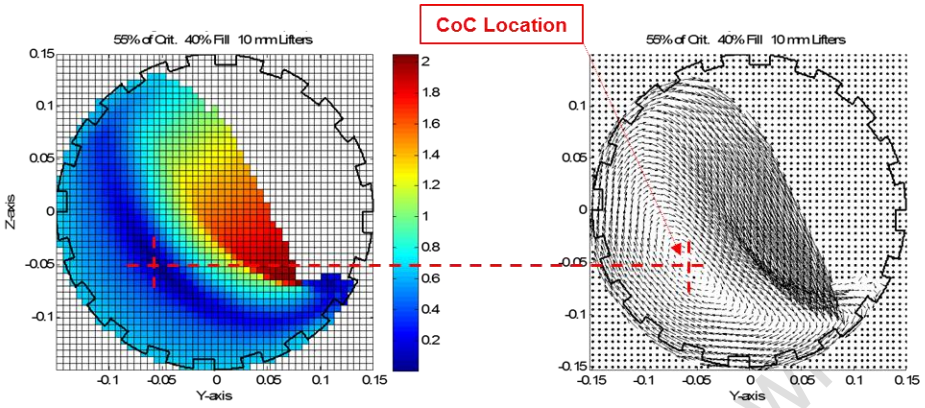

Figure 31: Average velocity probability distribution (m/s)

Figure 32: Average velocity vector field

As illustrated above, the vector field diagrams were used to extract the CoC location and equilibrium surface at all critical speed, filling and lifter height settings. The equilibrium surface, across the face of the mill, was required to determine distance L_2, a variable in the velocity profile model derived by Brodner (2013).

The change in the CoC location for all operating conditions, was analysed according to the height above the mill base, radial distance from the mill centre (0, 0) and the inclination angle of the equilibrium surface, at the CoC, above the mill base. The inclination angle was calculated using the equation 13 below.

$$\theta_{COC} = 90° - \tan^{-1}(\text{CoC z coordinate/CoC y coordinate}) \quad (13)$$

The 'polyval' and 'polyder' functions in MATLAB were used to determine the polynomial equation and derivative equation coefficients for the equilibrium surface (ES) which was used with the CoC coordinates to determine the ES gradient. Since the diametric line (DS) is perpendicular to the ES at the CoC location, equation 14 below was used to determine the gradient of the diametric line.

$$m_{ES} * m_{DL} = -1 \quad (14)$$

Figure 33 below, summarises the charge characteristics of interest extracted from the EDEM simulation results. The results are illustrated in Appendix D.6 at all operating conditions.

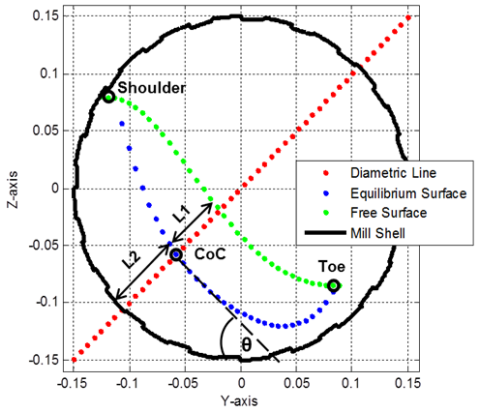

Figure 33: Charge characteristics of interest extracted using position and velocity probability plots.

Distances L_1 and L_2 as illustrated above, were determined using the intersection of the equilibrium and charge free surfaces with the perpendicular bisector (diametric line) passing through the mill centre (0, 0) and the CoC. Distance L_1 was calculated by determining the distance between the charge free surface and the equilibrium surface. Distance L_2 was calculated by determining the distance between the equilibrium surface and the mill shell.

The charge free surface and equilibrium surface was plotted using the 'Ginput' function in MATLAB to extract data points along these surfaces. A 4th order polynomial was fit to the data to determine the equations of these surface in the y-z plane. These equations were used to determine the intersection coordinates for a) the diametric line (DL) and equilibrium surface (ES) and b) charge free surface (CFS) and mill shell, which enabled calculation of the straight line distances L_1 and L_2 along the diametric line using equations 15 and 16 below.

$$L_1 = \sqrt{\left(x_{CFS\_DL} - x_{COC\_DL}\right)^2 + \left(y_{CFS\_DL} - y_{COC\_DL}\right)^2} \quad (15)$$

$$L_2 = \sqrt{\left(x_{COC\_DL} - x_{shell\_DL}\right)^2 + \left(y_{COC\_DL} - y_{shell\_DL}\right)^2} \quad (16)$$

5.1.3. Particle velocity frequency distribution

The charge velocity was analysed according to the frequency of particles achieving specific charge velocities as illustrated in figure 34 below.

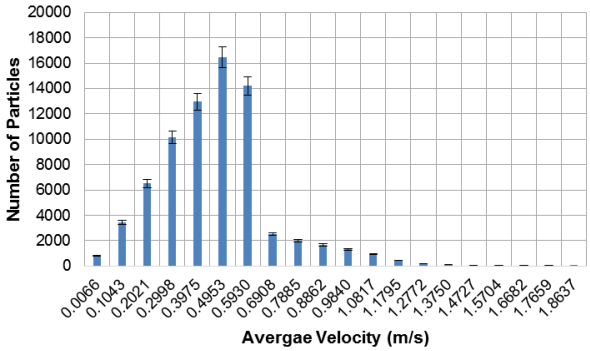

Figure 34: Charge velocity frequency according to the number of particles in the mill.

The frequency plots illustrated the particle distribution according to the charge velocity achieved in the mill at all operating conditions. The distribution plots were used to understand the charge motion using the velocity distribution in the mill. The plots for all critical speed, filling and lifter height settings are illustrated in Appendix D.5.

5.1.4. Power Draw

The calculated power draw was used to develop spacial distribution plots similar to figure 35 below for all critical speed, filling and lifter height changes as illustrated in Appendix D.7.

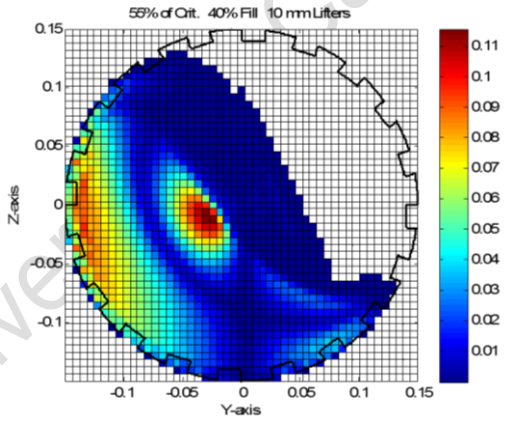

Figure 35: Power draw distribution at 55 % crit. speed, 40 % filling and 10.0 mm lifter heights.

Figure 35 shows how different particle interactions in different flow regions of the mill affected the power draw based on the level of packing and friction during different interactions.

Bbosa et al. (2011) and Bbosa (2013) investigated the use of PEPT to calculate and develop distributions of the power draw using two methods as discussed in section 2.5 of the literature review. The force balance method (P_{COM}) and cumulated torque per bin method (P_{BIN}) were compared based on how closely they represented experimental data. The P_{COM} method assumed constant angular velocity similar to the bulk charge and was shown to under-estimate the power draw (Bbosa et al., 2011). The P_{BIN} results closely represented the experimental data as average angular velocities in each bin that the mill grid was divided into

was used (Bbosa et al., 2011). P_{BIN} was the method of choice for determining the power draw of a tumbling mill using PEPT (Bbosa et al., 2011; Bbosa, Govender and Mainza, 2016).

The power draw was calculated using the BIN method discussed in section 2.5 of the literature review using the total particle contact forces and charge velocities extracted from the EDEM simulation results. The power draw plots were used to identify areas of interest where the maximum power was draw which was attributed to the type of particle interactions taking place i.e. direct impact or abrasive collisions. The change in operating conditions was related to the change in particle collisions and how this affected the maximum power drawn in the mill.

5.1.5. Velocity Profile

In order to compare the PEPT-calculated velocity profile to that of EDEM, the tangential velocity at all operating conditions, was determined. The MATLAB binning algorithm was used to plot the tangential velocity distribution, illustrated in figure 36 below, which was analysed according to all operating conditions in the reference frame of the mill. The special plots for all operating conditions is illustrated in Appendix D.4.

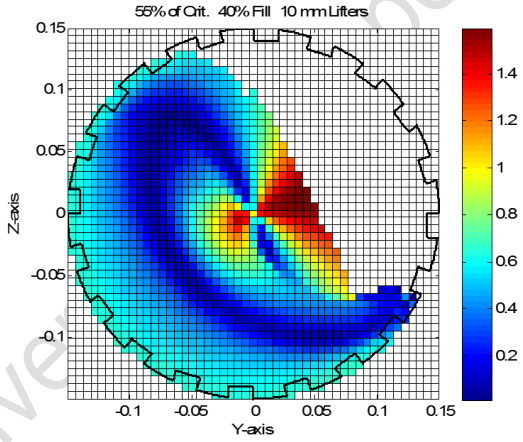

Figure 36: Tangential velocity distribution at 55 % crit. speed, 40 % filling and 10.0 mm lifter heights.

The velocity profile based on the EDEM results, was determined by extracting the tangential velocity along the diametric line as discussed in section 2.6.2 of the literature review. The extracted values were compared to the velocity profile model derived by Brodner (2013) i.e. equation 3, section 2.6.3 seen below.

$$v_x = \left(\rho g \sin\theta + \frac{dP}{dx} + F_f(y)\right)\frac{(y^2 - L_2 y)}{2\mu} + \frac{v_{mill} y}{L_2} \text{ where } F_f(y) = \mu_e F_N(y)$$

The input variables in the velocity profile model consisted of the angular velocity along the diametric line (v_{mill}), distance L_2, normal contact force (F_N) and the inclination angle of the equilibrium surface above the mill shell (θ). These were determined using the extracted data from EDEM simulations and was compared to the PEPT experimental results.

The normal contact force was extracted along the diametric line, similar to the method used to extract the tangential velocity. The angular velocity of the mill was calculated using equations 17 and 18 below.

$$v_{mill}\,(m/s) = \omega \cdot \sqrt{(x_1 - x_2)^2 + \left(y_1 - y_2\right)^2} \tag{17}$$

$$\omega\left(^{rad}/_{s}\right) = \left(\frac{42.3}{\sqrt{D_m}}\right) \cdot \left(\frac{\%_{cr}}{100}\right) \cdot \left(\frac{2\pi}{60}\right) \tag{18}$$

Where ω is the angular velocity, D_m is the mill diameter (m) and the distance along the diametric line (m) is ($\sqrt{(x_1 - x_2)^2 + (y_1 - y_2)^2}$).

The tangential velocity profile along the diametric line was extracted, as seen in figure 37 below, and plotted against the distance from the mill centre as seen in figure 38 below.

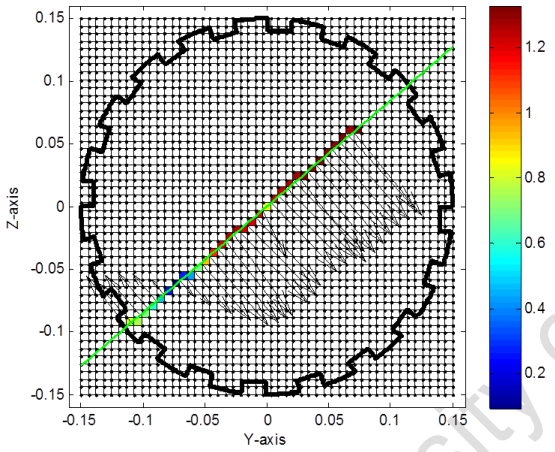

Figure 37: Tangential velocity profile along the diametric line for 70 % crit. speed, 30 % filling and 10.0 mm lifter heights.

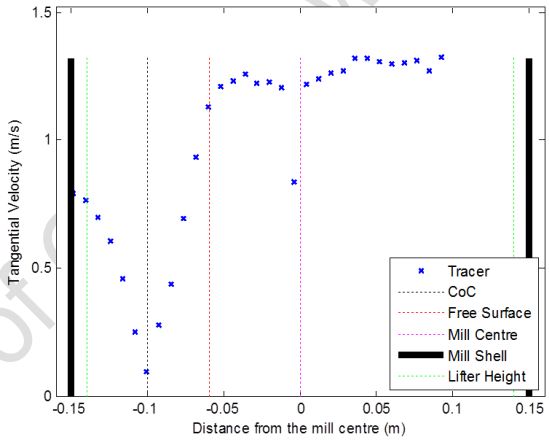

Figure 38: Piece-wise velocity profile along the distance from the mill centre at 70 % crit. speed, 30 % filling and 10.0 mm lifter heights.

The piece-wise illustration was used to analyse the change in the magnitude and direction of the tangential velocity along the diametric line. The change in the velocity profile along L_1, L_2, between the charge free surface and cataracting regions was assessed using the piece-wise distribution. The continuous velocity profile was developed using the piece-wise distribution and was compared to the velocity profile model results as seen in figure 39 below.

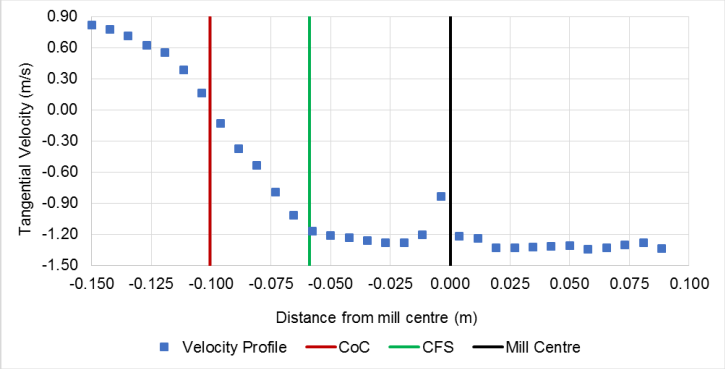

Figure 39: Continuous velocity profile along the diametric line for 70 % crit. speed, 30 % filling and 10.0 mm lifter heights.

The comparison between the calculated velocity profile and that of the model was based on the changes in the model variables corresponding to all critical speed, filling and lifter height settings. The following criteria was also included in the analysis of the velocity profile:

- The maximum velocity extracted along the diametric line.
- The profile gradient for the regions within distances L_1 and L_2.
- The change in CoC location.
- The change in the diametric line intersection with the charge free surface and equilibrium surface.
- The profile trend above the charge free surface, in the cataracting region.

5.1.6. Error Analysis

An error analysis was done on the charge characteristics, tangential velocity and power draw that was calculated using the extracted EDEM results. The standard deviation and standard error were calculated using MS Excel functions as per equations 19 and 20 below.

$$\text{Standard Deviation} = \sqrt{\frac{\sum(x-\bar{x})^2}{n-1}} \tag{19}$$

$$\text{Standard Error} = \frac{\text{Standard Deviation}}{\sqrt{n}} \tag{20}$$

Where x represents the relevant data point, $\bar{x}$ is the average of the data set and n is the total number of data points in the data set. The standard deviation provides an indication of the spread of the data points around the average value and the standard error was used to generate error bars for all bar graphs and/or histograms (Maicke & Majdalani, 2009). The error bars describe the uncertainty in the results and represent the overall data distribution. In addition, regression analyses were conducted on charge motion characteristics relating to the velocity profile in order to determine if the physical properties of the mill could be used to predict the results accurately.

5.2. Charge Motion

The influence of the operating conditions on the charge motion was analysed based on the change in the charge characteristics as discussed in section 2.3.3 i.e. centre of circulation (CoC), shoulder, toe, distances L_1 and L_2. These results were used to understand the influence of the operating conditions on the velocity profile along the diametric line in the mill.

5.2.1. Centre of Circulation (CoC)

The change in the CoC location was assessed by analysing the influence of the filling, critical speed and lifter height on the key CoC location characteristics i.e. vertical height between the CoC and mill base, radial distance between the CoC and the mill centre (0, 0), inclination of the equilibrium surface at the CoC location (θ) as discussed in section 5.1.2. The CoC location was extracted from the average velocity distribution and velocity vector field plots as summarised in Appendix D.2 and Appendix D.3 respectively. Figure 40 below, shows the influence of the mill filling on the CoC location at 55 % crit. speed and 10.0 mm lifter heights.

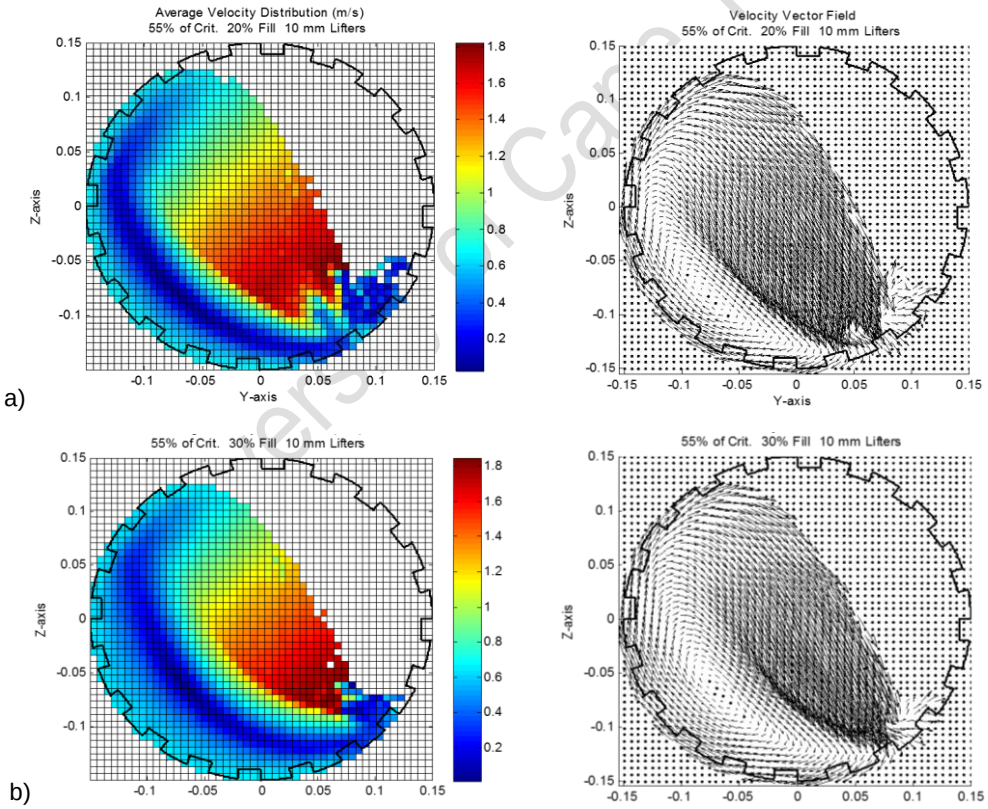

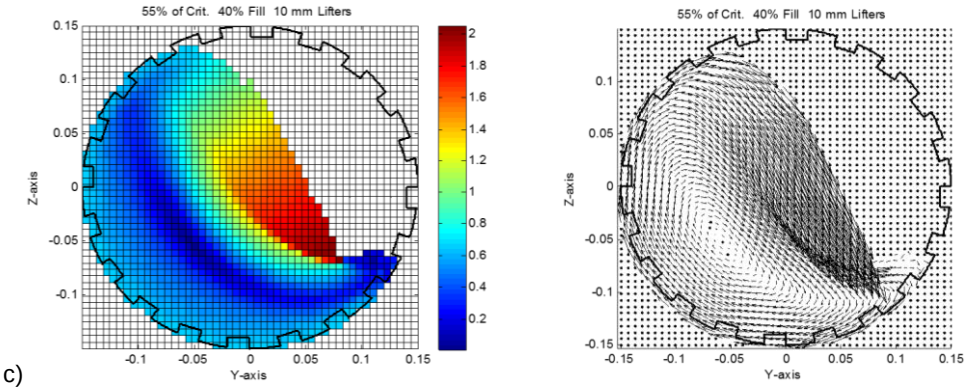

c)

Figure 40: Average velocity distribution (left) and vector field diagrams (right) for 55 % critical speed and 10.0 mm lifter heights operating at a) 20 %, b) 30 % and c) 40 % mill filling.

Figures 40a, b and c show that for an increase in the filling, the span of the equilibrium surface across the charge body decreased resulting in the band being concentrated in a smaller area close to (0.05 m, 0.05 m) based on the cross-sectional view of the mill. The equilibrium surface moved higher up in the mill resulting in a thicker rising en-masse region i.e. more particles in the charge bed below the equilibrium surface. The change in equilibrium surface corresponded to similar changes in the CoC location for changes in the filling i.e. the CoC location moved higher up in the mill, closer to the mill centre.

Figure 41 below, shows the influence of the critical speed on the CoC location at 40 % mill filling and 1.5 mm lifter heights.

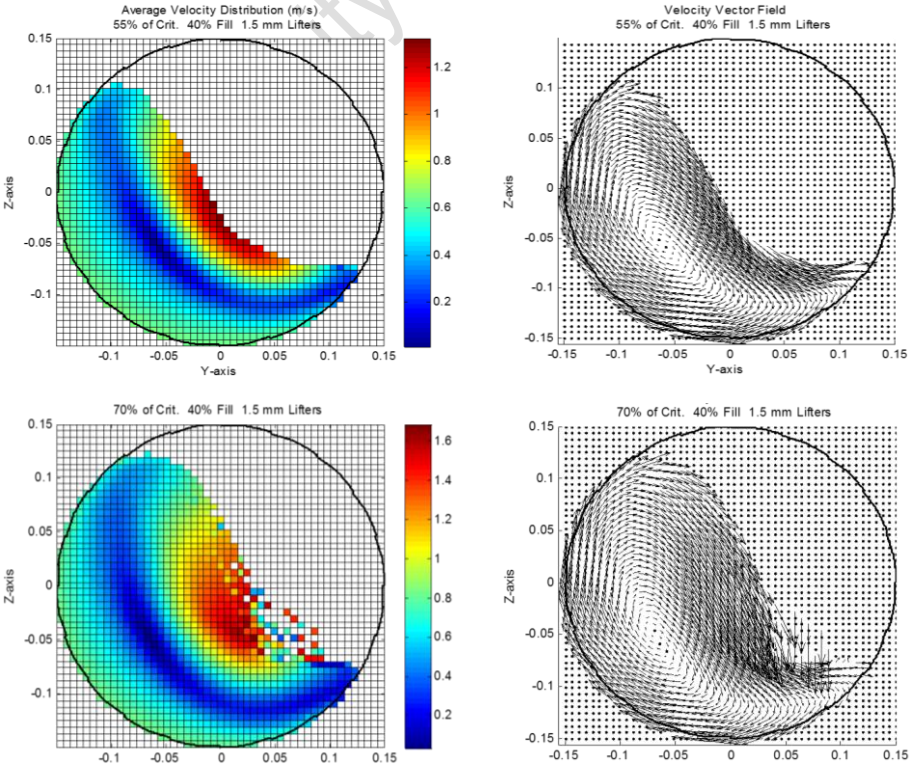

a)

b)

c)

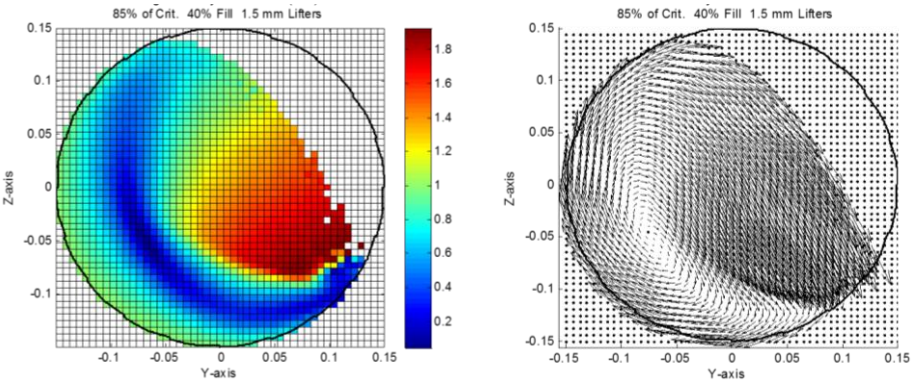

Figure 41: Average velocity distribution (left) and vector field diagrams (right) for 55 % critical speed, 10.0 mm lifter heights and a) 20 %, b) 30 % and c) 40 % mill filling.

Figures 41a, b and c above, show that for an increase in the critical speed, the radial depth of the rising en-masse region decreased. The radial depth of the cascading region (below the charge free surface) decreased with an increase in critical speed. The inclination of the equilibrium surface increased with an increase in critical speed. Figure 42 below, illustrates the influence of the lifter height on the CoC location using the charge velocity and velocity vector fields at 30 % filling and 70 % critical speed.

a)

b)

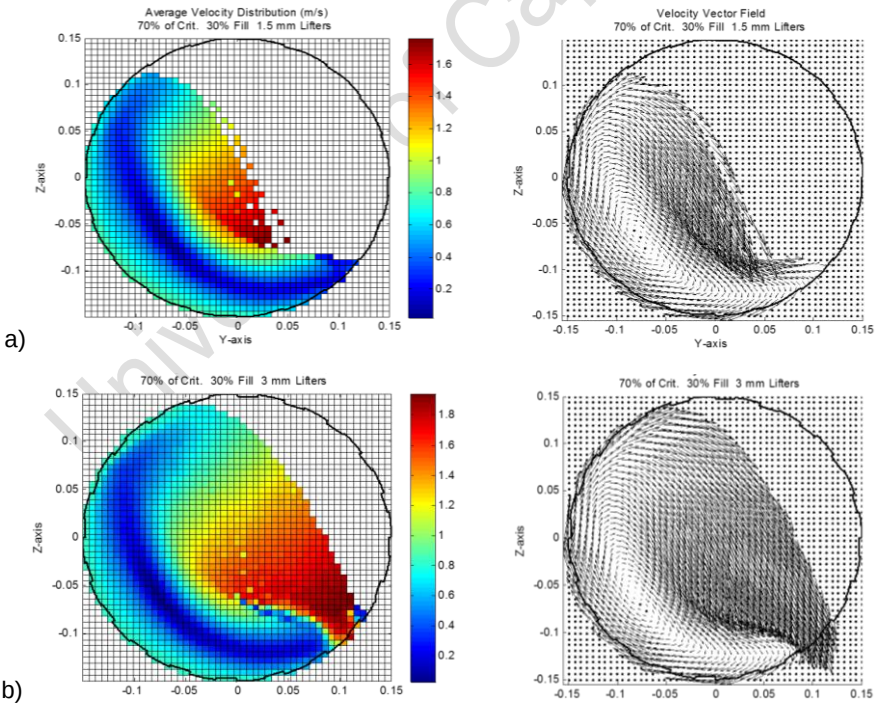

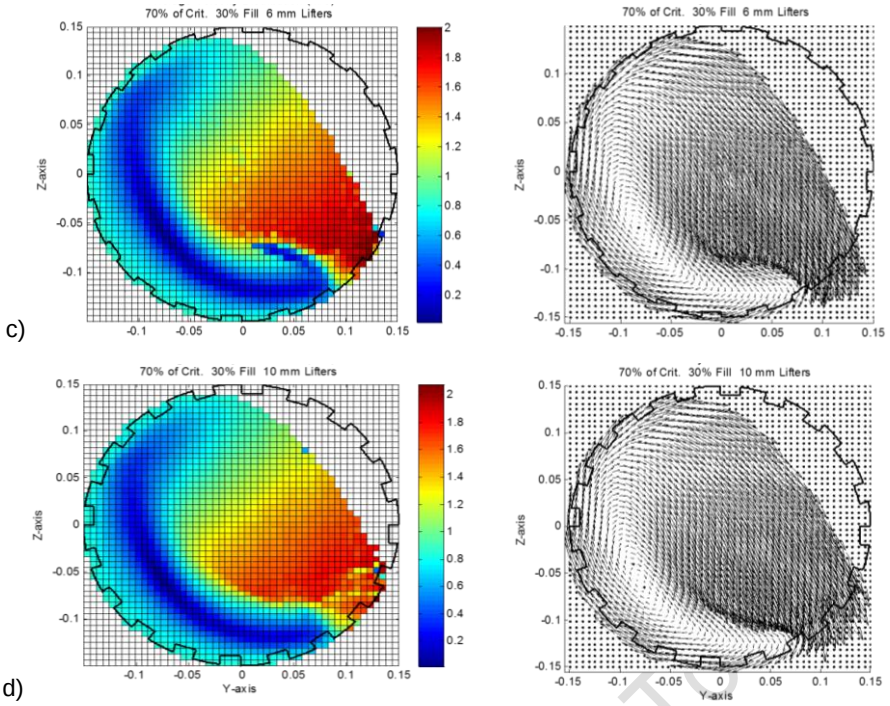

Figure 42: Average velocity distribution (left) and vector field diagrams (right) for 70 % critical speed and 30 % mill filling at a) 1.5 mm, b) 3.0 mm, c) 6.0 mm and d) 10.0 mm lifter heights respectively.

Figures 42a, b and c above show that for an increase in the lifter height, the span of the 'zero velocity' band was not significantly influenced. The lifter height did not significantly influence the movement of the equilibrium surface at the CoC location. The CoC location moved radially higher up along the mill periphery for increases in the lifter height.

Figure 43a, b and c below, illustrate changes in the CoC location extracted from the velocity vector fields at all operating conditions. The coordinates are listed in table 27 in Appendix E.1.

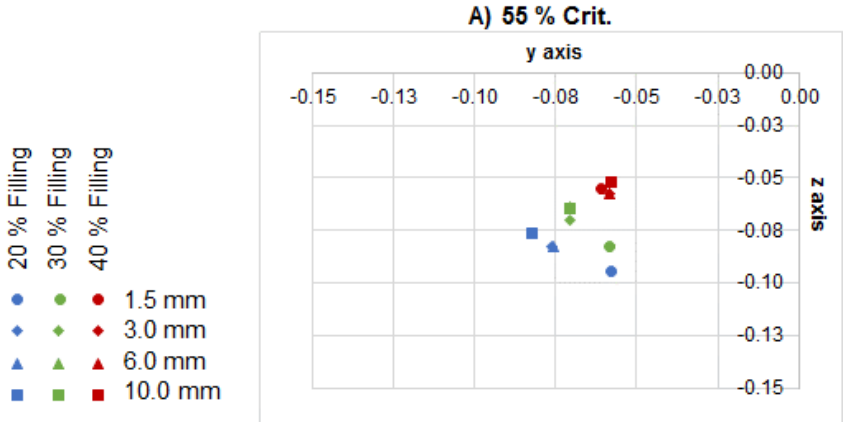

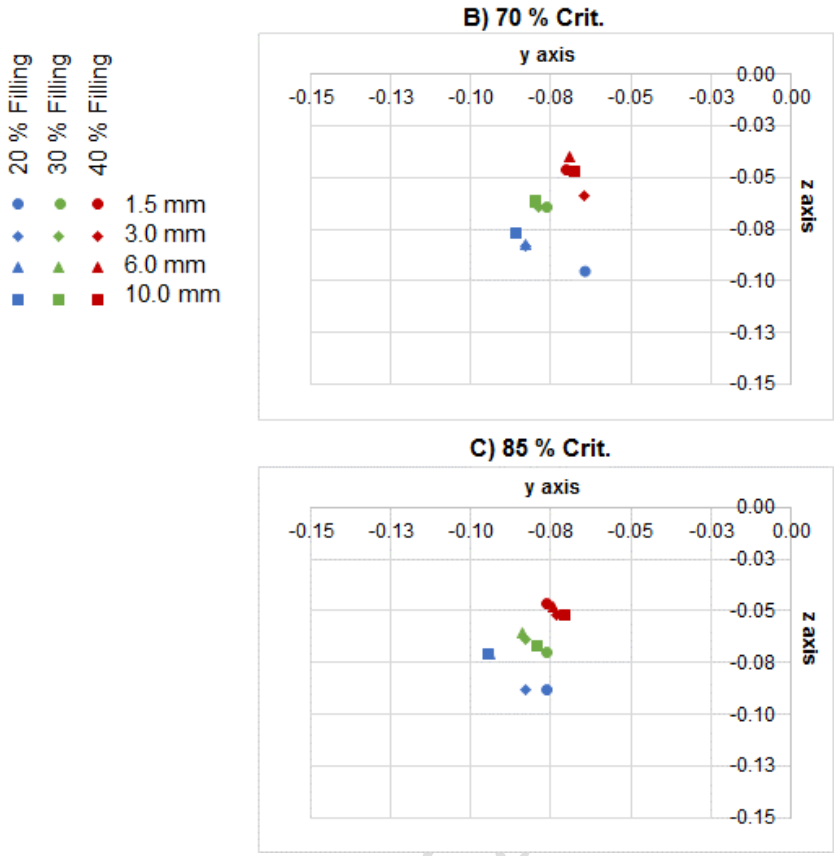

Figure 43: Extracted CoC coordinates at all mill filling, critical speed and lifter height settings.

The CoC coordinates remained within the range of (-0.10, -0.05) on the y-axis and (-0.10, 0.00) on the z-axis at all operating conditions. Increasing the lifter height at 20 % filling and all critical speeds, raised the CoC location diagonally and away from the mill centre. At 30 % filling levels, a similar trend was seen for increases in the lifter height. At 40 % filling, the lifter height did not influence the CoC location. Increasing the filling moved the CoC location closer to the mill centre in a radial direction. Increasing the critical speed increased the radial distance between the CoC and mill centre, moving the CoC closer to the mill shell.

The height of the CoC above the mill base was calculated using the CoC coordinates as summarised in table 7 below. Figures 103a, b and c in Appendix E.1, illustrate the influence of the lifter height at all filling levels for 55 %, 70 % and 85 % critical speeds respectively.

Table 7: CoC height above the mill base at all filling, critical speed and lifter height settings.

		1.5 mm	3.0 mm	6.0 mm	10.0 mm
Mill Speed	**Mill Filling**	**CoC height above the mill base (m)**			
55 % Crit.	20 %	0.0551	0.0672	0.0672	0.0738
	30 %	0.0673	0.0797	0.0861	0.0853
	40 %	0.0950	0.0922	0.0923	0.0979

70 % Crit.	20 %	0.0553	0.0670	0.0677	0.0734
	30 %	0.0855	0.0853	0.0879	0.0891
	40 %	0.1041	0.0915	0.1098	0.1026
85 % Crit.	20 %	0.0615	0.0617	0.0793	0.0795
	30 %	0.0798	0.0861	0.0892	0.0832
	40 %	0.1038	0.0981	0.1017	0.0979

Table 7 above shows that at all critical speeds, the lowest CoC location corresponded to the lowest filling and lifter height settings (20 % filling and 1.5 mm lifter heights). The lowest and highest CoC locations were 0.0551 m and 0.1098 m at 20 % filling, 55 % critical speed, 1.5 mm lifter heights and at 40 % filling, 70 % critical speed, 6.0 mm lifter heights respectively.

At 55 % critical speed, the CoC height increased with increasing lifter height at 20 % and 30 % filling. The change in the CoC height decreased with increasing lifter height. At 40 % filling, the change in the CoC height was not significant and did not follow the same trend to that seen at 20 % and 30 % filling. The biggest change in the CoC height was 0.0124 m at 30 % filling for increasing lifter heights from 1.5 mm to 3.0 mm. The CoC height increased with the filling at each lifter height and critical speed setting. The influence of the filling on the change in the CoC height was not consistent and did not follow a clear trend. The biggest change in the CoC height was 0.0277 m recorded at 1.5 mm lifter heights for an increase from 30 % to 40 % filling.

At 70 % critical speed and 20 % filling, the CoC height increased with increasing lifter height similar to that seen at 55 % critical speed for 20 % and 30 % filling levels. At 40 % filling, the influence of the lifter height on the CoC height was not consistent and did not follow a clear trend. The biggest change in CoC height was 0.0117 m recorded at 20 % filling for an increase from 1.5 mm to 3.0 mm lifter heights. The influence of the filling on the CoC height at 70 % critical speed was similar to that seen at 55 % critical speed i.e. the CoC height increased with increasing filling at all lifter heights. The influence of the filling on the change in the CoC height was not consistent and did not follow a clear trend. The biggest change in the CoC height was 0.0302 m recorded at 1.5 mm lifter heights for a 20 % to 30 % increase in filling.

At 85 % critical speed, the CoC height increased with increasing lifter height at 20 % and 30 % filling. This trend was similar to that seen at 55 % critical speed. At 40 % filling, the change in the CoC height was not significant and did not follow the same trend recorded at 20 % and 30 % filling. The biggest change in the CoC height was 0.0177 m recorded at 20 % filling for an increase from 3.0 mm to 6.0 mm lifter heights. The influence of the filling on the CoC height at 85 % critical speed was similar to that recorded at 55 % and 70 % critical speeds i.e. the CoC height increased with increasing mill filling at all lifter heights. The biggest change in the

CoC height was 0.0244 m recorded at 3.0 mm lifter heights for an increase from 20 % to 30 % filling.

Overall, increasing the critical speed did not consistently influence the CoC height and the change in the CoC height did not follow a trend. At 20 % filling, the biggest change in the CoC height was 0.0116 m at 6.0 mm lifter heights for an increase from 70 % to 85 % critical speed. The decrease in the CoC height was more pronounced for an increase from 70 % to 85 % critical speed at 1.5, 6.0 and 10.0 mm lifter heights.

At 30 % filling, the biggest change was 0.0182 m recorded for an increase from 55 % to 70 % critical speed at 1.5 mm lifter heights. The increase from 55 % to 70 % critical speed increased the CoC height at all lifter heights. The CoC height decreased for an increase in the critical speed form 70 % to 85 %. At 40 % filling, the biggest change was 0.0175 m recorded at 6.0 mm lifter heights for an increase from 55 % to 70 % critical speed.

Overall, the influence of the lifter height was more pronounced between 1.5 mm and 6.0 mm at all filling and critical speed settings. The influence of the lifter height on the CoC height decreased with an increase in filling at all critical speeds. An increase in the filling increased the CoC height at all critical speeds and lifter heights.

The radial distance between the CoC and the mill centre was calculated to indicate the CoC movement for changes in the operating conditions as summarised in table 8 below.

Table 8: Radial distance between the CoC and the mill centre (0, 0) for all mill filling, critical speed and lifter height settings.

		1.5 mm	**3.0 mm**	**6.0 mm**	**10.0 mm**
Speed	**Filling**	**Radial distance between CoC and mill centre (m)**			
55 % Crit.	20 %	0.1112	0.1124	0.1123	0.1123
	30 %	0.1013	0.0997	0.0953	0.0957
	40 %	0.0821	0.0821	0.0820	0.0780
70 % Crit.	20 %	0.1146	0.1172	0.1168	0.1151
	30 %	0.0998	0.1020	0.1011	0.1005
	40 %	0.0840	0.0871	0.0799	0.0827
85 % Crit.	20 %	0.1170	0.1213	0.1178	0.1180
	30 %	0.1035	0.1047	0.1034	0.1038
	40 %	0.0892	0.0896	0.0885	0.0879

According to table 8, at 20 % filling and all critical speeds, increasing the lifter height from 1.5 mm to 3.0 mm increased the CoC radial distance. The opposite trend was seen for an increase from 3.0 mm to 6.0 mm lifter heights at all critical speeds and there was no change in the CoC

height for a further increased from 6.0 mm to 10.0 mm. The CoC radial distance increased with increasing critical speeds at all lifter heights. The change in the radial distance was not consistent for increases in the critical speed. The largest radial distance was 0.1124 m, 0.1172 m and 0.1213 m recorded at 55 %, 70 % and 85 % critical speeds respectively when operating at 3.0 mm lifter heights and 20 % filling.

At 30 % filling, increasing the lifter height between 1.5 mm and 6.0 mm at 55 % critical speed, decreased the CoC radial distance (the CoC moved radially closer to the mill centre). The lifter height did not have an influence on the CoC radial distance at 70 % and 85 % critical speeds. The CoC radial distance increased with increasing critical speeds at 20 % filling levels and all lifter heights. The influence was more pronounced between 6.0 mm and 10.0 mm lifter heights and between 55 % and 70 % critical speeds. The largest radial distance was 0.1013 m at 1.5 mm lifter heights and 55 % critical speed. At 70 % and 85 % critical speeds, the largest radial distance was 0.1020 m and 0.1047 m respectively at 3.0 mm lifter heights.

At 40 % filling and all critical speeds, increasing the lifter height did not have a consistent influence on the CoC radial distance. The largest radial distance was 0.0821 m at 1.5 mm lifter heights and 55 % critical speed. At 70 % and 85 % critical speeds, the largest radial distance was 0.0871 m and 0.0896 m at 3.0 mm lifter heights respectively.

Increasing the filling decreased the radial distance between the CoC and the mill centre at all critical speed and lifter height settings. The change in the radial distance was more pronounced for changes in the filling than for the critical speed and lifter height. At every critical speed setting, the largest radial distance achieved for each filling level decreased with an increase in the filling. The maximum radial distance was 0.1213 m, 0.1047 m and 0.0896 m achieved at 20 %, 30 % and 40 % filling respectively for a 3.0 mm lifter height and 85 % critical speed setting. The change in the radial distance increased with the filling. There was no consistent trend for the influence of the filling on the change in the radial distance between the CoC and the mill centre.

The inclination angle of the equilibrium surface at the CoC, above the mill base is summarised in table 9 below at all operating conditions. Figures 104a, b and c in Appendix E.1 illustrate the influence of the lifter height on the inclination angle.

Table 9: CoC inclination angle of the CoC above the mill base at all filling, critical speed and lifter height settings.

		1.5 mm	3.0 mm	6.0 mm	10.0 mm
Mill Speed	**Mill Filling**	**Inclination angel of the CoC (degrees)**			
55 % Crit.	20 %	31.49	42.58	42.73	47.31
	30 %	35.32	45.19	47.89	47.47
	40 %	47.93	45.22	45.22	48.05
70 % Crit.	20 %	34.24	44.91	45.20	48.30
	30 %	49.73	50.65	52.12	52.69
	40 %	56.85	47.77	59.74	55.06
85 % Crit.	20 %	40.82	43.24	53.12	53.31
	30 %	47.34	52.35	54.02	49.98
	40 %	58.83	54.57	56.94	53.66

According to table 9 above, at 20 % filling, increasing the lifter height increased the CoC inclination at all critical speeds i.e. the inclination of the CoC was steeper at higher lifter heights. The steepest angle was 53.31° at 85 % critical speed and 10.0 mm lifter heights. The lowest inclination was at 31.49° at 55 % critical speed and 1.5 mm lifter heights. The change in the inclination angle decreased with increasing lifter heights at every critical speed level as seen in figure 104a in Appendix E.1. Increasing the critical speed increased the CoC inclination at 20 % filling for all lifter height settings. The change in the CoC inclination with increasing critical speeds did not follow a consistent trend.

At 30 % filling, increasing the lifter height from 1.5 mm to 3.0 mm and 6.0 mm increased the CoC inclination at 55 % and 85 % critical speeds. The trend deviated for an increased from 6.0 mm to 10.0 mm. At 70 % critical speed, increasing the lifter height increased the CoC inclination at every critical speed setting. The steepest angle was 54.02° at 85 % critical speed and 6.0 mm lifter heights. The lowest inclination was at 35.32° at 55 % critical speed and 1.5 mm lifter heights. Increasing the critical speed did not have a consistent influence on the CoC at all lifter heights as seen in figure 104b in Appendix E.1.

At 40 % filling, increasing the lifter height did not have a consistent influence on the CoC inclination at all critical speeds as seen in figure 104c in Appendix E.1. The same was seen for increases in the critical speed. The steepest angle was 59.74° at 70 % critical speed and 6.0 mm lifter heights. The lowest inclination was at 45.22° at 55 % critical speed for 3.0 mm and 6.0 mm lifter heights.

Increasing the filling increased the CoC inclination at 1.5 mm lifter heights and all critical speeds. The same trend was not followed at all other lifter height settings as seen in table 9

above. The most significant change in the inclination angle was recorded for an increase from 20 % to 30 % filling at 1.5 mm lifter heights. The change in the inclination angle decreased with increasing filling i.e. the influence of the filling on the inclination angle was more pronounced at lower filling levels and lower lifter heights.

Overall, the inclination angle of the equilibrium surface at the CoC, increased with increasing lifter heights at 20 % and 30 % filling levels as well as at 55 % and 70 % critical speeds. The change in the inclination at 85 % critical speed and 40 % filling, at all lifter heights, did not follow a consistent trend. The lifter height had a significant influence on the inclination angle between 1.5 mm and 6.0 mm lifter height settings.

The EDEM-extracted CoC inclination angles were similar in magnitude to that of PEPT at 55% critical speeds and 20 % filling levels. The different between the EDEM and PEPT inclinations increased in magnitude with increasing critical speed and filling levels. The figure below illustrates the comparison between the PEPT and EDEM inclination angles for increasing lifter heights as well as the corresponding standard deviation.

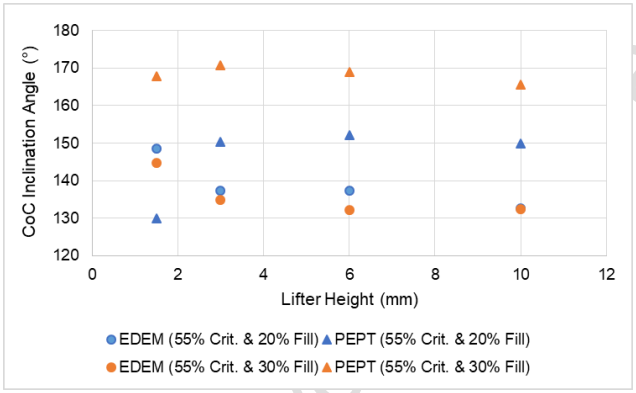

	Standard Deviation (°)		
	20%	30%	40%
55%	14.66	5.38	0.96
70%	11.77	3.62	5.80
85%	8.29	7.55	5.82

Figure 44: Comparison between the EDEM and PEPT CoC inclination angles for increasing lifter heights at 20% and 30% filling for 55% crit. speeds.

The PEPT CoC inclinations were higher in magnitude than that of EDEM results at all operating conditions. However, figure 44 above shows that both the PEPT and EDEM results were similar and followed a similar trend for increasing lifter heights and increasing the filling levels. The standard deviation at the filling and critical speed levels, showing the impact of increasing the lifter height, is less than a maximum of 15°. The biggest difference between EDEM and PEPT results was seen at 55 % and 70 % critical speeds with a 20 % filling level.

A regression analysis was conducted to determine if the operating conditions could be used to predict the CoC inclination angle since this is critical to the charge motion and velocity profile. The regression analysis consisted of 2 focus points i.e. comparing the change in the inclination to varying lifter heights and filling levels vs varying lifter heights and critical speeds.

The CoC inclination at 20 % filling was found to be dependent on the lifter height and critical speed with the R^2 value being above 0.8. The standard deviation was not more than 7% of the average inclination angles at 20 % filling. The remaining data points could not be accurately be predicted using any of the lifter height, critical speeds or filling levels since the R^2 values for all combinations were less than 0.68.

A regression analysis was conducted on all data points including all the effects of the operating conditions which produced the following plot with R^2 values above 0.6, standard deviations below 8% of the average inclination angle and p-values well below 0.05. Figure 45 below illustrates the results.

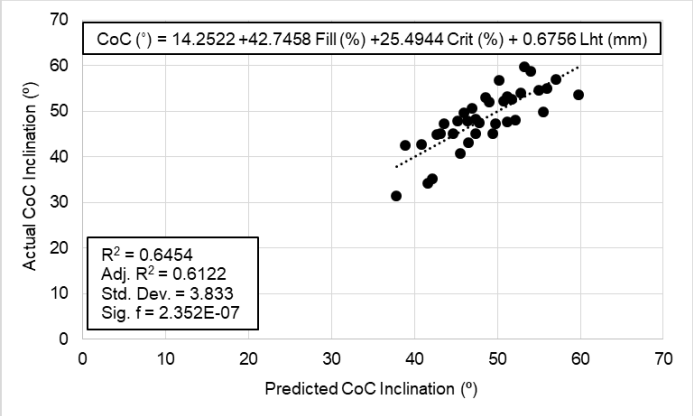

Figure 45: Regression analysis of the CoC inclination angle using the lifter height, filling and critical speeds as predictive variables.

The figure above shows that the operating conditions i.e. physical characteristics of the mill can be used to predict the CoC inclination angle with reasonable accuracy. This simplifies the velocity profile calculation using the equation that will be discussed in section 5.5.2.

5.2.2. Shoulder Location

The position probability distribution plots illustrated in Appendix D.1, were used to extract the shoulder location along the y-z axis as explained in section 5.1.2. The shoulder location was assessed on the basis of the; vertical height of the shoulder location above the mill base, horizontal distance between the shoulder and the mill centre (0, 0), inclination of the shoulder above the mill centre.

Figures 46a, b and c below illustrate the shoulder location movement due to changes in the operating conditions in the upper quadrant of the mill. Table 28 in Appendix E.2 lists the y-z coordinates of the shoulder location at all operating conditions.

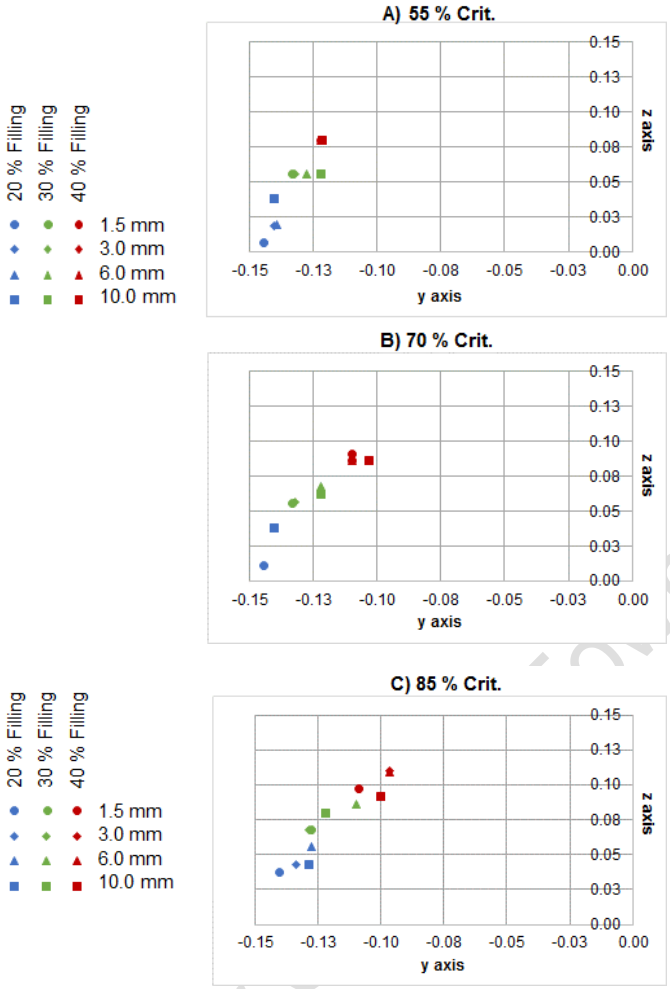

Figure 46: Shoulder movement at a) 55 %, b) 70 % and c) 85% critical speeds for changes in the filling and lifter height.

According to the shoulder coordinates, at 55 % critical speed and 20 % filling, increasing the lifter height moved the shoulder location higher up, radially along the mill periphery. The most significant change was for an increase from 1.5 mm to 3.0 mm lifter heights. Increasing the lifter height at 30 % filling levels, moved the shoulder in a horizontal direction away from the mill shell. At 40 % filling, the shoulder height was not significantly influenced by the lifter height.

Increasing the filling moved the shoulder location higher up, radially along the mill periphery. The influence of the filling on the shoulder height was more pronounced than the lifter height. The most significant change in the shoulder height was seen at 1.5 mm and 3.0 mm lifter heights for an increase from 20 % to 30 % filling.

At 70 % critical speed and 20 % filling, the lifter height had a similar influence on the shoulder height as that at 55 % critical speed. Similarly, the most significant change in shoulder height was for an increase from 1.5 mm to 3.0 mm lifter heights. At 30 % filling, the lifter height influence on the shoulder height followed a similar trend to that at 20 % filling. The most significant change in the shoulder location was for an increase in lifter height from 3.0 mm to

6.0 mm. At 40 % filling, the most pronounced change in the shoulder location was for an increase from 6.0 mm to 10.0 mm.

The influence of the filling on the shoulder location was similar to that at 55 % critical speed. The influence of the filling on the shoulder height was more pronounced than the lifter height. The biggest change in the shoulder was at 1.5 mm and 3.0 mm lifter heights for an increase from 20 % to 30 % filling.

At 85 % critical speed and 20 % filling, the lifter height had the same influence on the shoulder location as that recorded at 55 % and 70 % critical speeds. At 30 % and 40 % filling, no clear trend was followed and the lifter height did not consistently influence the shoulder location. The change in the shoulder location due to increasing the filling followed a similar trend as that at 55 % and 70 % critical speeds i.e. the shoulder moved higher up, radially along the mill periphery with increasing filling.

The critical speed had a similar influence on the shoulder location as with increasing the filling but the change in shoulder location was more pronounced for changes in filling than the critical speed. The change in the shoulder location due to increasing the critical speed was more pronounced at 3.0 mm and 6.0 mm lifter heights and all filling levels.

The height of the shoulder location above the mill base was calculated using the shoulder coordinates as summarised in table 10 below. Figures 105a, b and c in Appendix E.2, illustrate the influence of the lifter height on the shoulder height at all filling levels for 55 %, 70 % and 85 % critical speeds respectively.

Table 10: Shoulder height above the mill base at all critical speed, filling and lifter height settings.

		1.5 mm	3.0 mm	6.0 mm	10.0 mm
Speed	**Filling**	**Shoulder height above the mill base (m)**			
55 % Crit.	20 %	0.1563	0.1688	0.1693	0.1876
	30 %	0.2055	0.2055	0.2055	0.2055
	40 %	0.2297	0.2297	0.2297	0.2297
70 % Crit.	20 %	0.1616	0.1876	0.1876	0.1876
	30 %	0.2055	0.2064	0.2181	0.2118
	40 %	0.2413	0.2360	0.2360	0.2360
85 % Crit.	20 %	0.1876	0.1930	0.2055	0.1930
	30 %	0.2181	0.2181	0.2360	0.2297
	40 %	0.2476	0.2601	0.2593	0.2413

According to table 10 above, at each critical speed setting, the minimum shoulder height was 0.1563 m at 20 % filling, 1.5 mm lifter heights and 55 % critical speed. The maximum shoulder height was 0.2601 m at 3.0 mm lifter heights, 40 % filling and 85 % critical speed.

At 55 % critical speed, as seen in figure 105a in Appendix E.2, an increase in the lifter height increased the shoulder height at 20 % filling. The biggest change in the shoulder height was for a change from 6.0 mm to 10.0 mm lifter heights. At 30 % and 40 % filling, the lifter height did not influence the shoulder height consistently.

Increasing the filling increased the shoulder height at all lifter heights. The biggest change in the shoulder height was at 1.5 mm lifter heights for an increase from 20 % to 30 % filling. The change in the shoulder height decreased with increasing filling from 20 % to 30 % at all lifter heights. The change in the shoulder height, for an increase from 30 % to 40 % filling remained constant at every lifter height setting.

At 70 % critical speed, as seen in figure 105b in Appendix E.2, the influence of the lifter height on the shoulder height followed a similar trend to that at 55 % critical speed. At 20 % filling, the shoulder height increased with the lifter height between 1.5 mm and 3.0 mm. The shoulder height remained constant between 3.0 mm and 10.0 mm lifter heights. At 30 % filling, the shoulder height increased with the lifter height between 1.5 mm and 6.0 mm. The shoulder height decreased with an increase from 6.0 mm to 10.0 mm lifter heights. At 40 % filling, increasing the lifter height from 1.5 mm to 3.0 mm resulted in a decrease in the shoulder height. The shoulder height remained constant between 3.0 mm and 10.0 mm lifter heights. The shoulder height increased with the filling at all lifter height settings. The filling had the strongest influence at 1.5 mm lifter heights for an increase from 20 % to 30 % filling.

At 85 % critical speed, as seen in figure 105c in Appendix E.2, the influence of the lifter height on the shoulder followed the same trend at all filling levels i.e. the shoulder height increased with increasing lifter heights from 1.5 mm to 6.0 mm. The shoulder height decreased for an increase in lifter height from 6.0 mm to 10.0 mm. At 6.0 mm lifter heights, the highest shoulder height was at 20 % and 30 % filling levels while at 40 % filling, the highest shoulder height was at 3.0 mm lifter heights. The filing had the same influence on the shoulder height as that seen at 55 % and 70 % critical speeds i.e. the shoulder height increased with increasing filling levels. The change in the shoulder height did not follow a consistent trend at all lifter heights. Increasing the critical speed increased the shoulder height at every lifter height and filling level. The critical speed had the strongest influence for an increase from 70 % to 85 % critical speed.

Overall, the filling and critical speed settings had a stronger and more consistent influence on the shoulder height than the lifter height. The lifter height influence on the shoulder height was pronounced between 1.5 mm and 3.0 mm at 20 % filling levels and all critical speed settings.

The horizontal distance between the shoulder and the mill centre was calculated at all operating conditions as seen in table 11 below to analyse the movement of the shoulder location away or towards the mill shell at all operating conditions. Figures 106a, b and c in Appendix E.2, illustrate the horizontal change in shoulder location at all operating conditions.

Table 11: Horizontal distance between shoulder location and mill centre (0, 0) at all critical speed, filling and lifter height settings.

		1.5 mm	3.0 mm	6.0 mm	10.0 mm
Speed	**Filling**	**Distance between shoulder and mill centre (m)**			
55 % Crit.	20 %	0.1446	0.1401	0.1393	0.1401
	30 %	0.1330	0.1321	0.1276	0.1222
	40 %	0.1088	0.0963	0.0963	0.0999
70 % Crit.	20 %	0.1446	0.1401	0.1401	0.1401
	30 %	0.1330	0.1321	0.1222	0.1222
	40 %	0.1097	0.1097	0.1097	0.1034
85 % Crit.	20 %	0.1401	0.1339	0.1276	0.1285
	30 %	0.1276	0.1285	0.1097	0.1222
	40 %	0.1088	0.0963	0.0963	0.0999

According to table 11 above, the longest distance between the shoulder and mill centre was at 20 % filling and 1.5 mm lifter heights at both 55 % and 70 % critical speeds. The shortest distance was at 40 % filling for both 3.0 mm and 6.0 mm lifter heights at 55 % and 70 % critical speeds.

At 55 % critical speed and 20 % filling, increasing the lifter height decreased the distance between the shoulder and mill centre between 1.5 mm to 6.0 mm i.e. the shoulder moved away from the mill shell in a horizontal direction. The distance increased for an increase from 6.0 mm to 10.0 mm lifter heights causing the shoulder to move closer to the shell horizontally. At 30 % filling, increasing the lifter height decreased the distance between the shoulder and mill centre. At 40 % filling, the lifter height did not influence the distance between the shoulder and mill centre following a consistent trend.

The distance between the shoulder and mill centre decreased with increasing filling at all lifter heights. The biggest change in the distance between the shoulder and mill centre was at 10.0 mm for an increase from 20 % to 30 % filling. The change in the distance decreased with increasing lifter heights for an increase from 30 % to 40 % filling.

At 70 % critical speed and 20 % filling, increasing the lifter height from 1.5 mm to 3.0 mm decreased the distance between the shoulder and mill centre. The shoulder distance remained unchanged between 3.0 mm to 10.0 mm lifter heights. At 30 % filling, the distance between

the shoulder and mill centre decreased with increasing the lifter height from 1.5 mm to 6.0 mm. The lifter height did not influence the distance between 6.0 mm to 10.0 mm lifter heights. At 40 % filling, the lifter height had no influence on the distance between the shoulder and mill centre between 1.5 mm and 6.0 mm. An increase in the lifter height from 6.0 mm to 10.0 mm, caused the shoulder location to move closer to the mill centre.

The influence of the filling on the distance between the shoulder and mill centre followed the same trend as that seen at 55 % critical speed i.e. the shoulder moved closer to the mill centre due to increased filling at every lifter height setting. The change in the distance between the shoulder and mill centre did not follow a consistent trend.

At 85 % critical speed and at 20 % filling, increasing the lifter height decreased the distance between the shoulder and mill centre. At 30 % and 40 % filling, the influence of the lifter height on the distance did not follow a consistent trend. The influence of the lifter height was more pronounced between 1.5 mm and 6.0 mm. The influence of the filling on the distance between the shoulder and mill centre followed the same trend as that seen at 55 % and 70 % critical speeds i.e. the shoulder moved closer to the mill centre when increasing the filling at every lifter height setting.

The influence of the critical speed on the distance between the shoulder and mill centre, was more pronounced between 70 % and 85 % at 20 % filling and 1.5 mm, 3.0 mm and 10.0 mm lifter heights. The influence was inconsistent at 6.0 mm lifter heights. At 30 % filling, the distance between the shoulder and mill centre decreased for an increase from 70 % and 85 % critical speeds at 1.5 mm and 3.0 mm lifter heights. The distance between the shoulder and mill centre decreased with an increase in the critical speed at 6.0 mm lifter heights and remained constant at 10.0 mm lifter heights. At 40 % filling, the distance between the shoulder and mill centre increased for an increase from 55 % and 70 % critical speed and decreased between 70 % and 85 % critical speed.

The shoulder inclination angle above the mill centre, was calculated using the shoulder coordinates and equation 4 in section 5.2.1. Table 12 below, summarises the inclination angles at all operating conditions. Figures 107a, b and c in Appendix E.2, illustrate the influence of the lifter height on the unadjusted shoulder inclination at all filling levels for 55 %, 70 % and 85 % critical speeds respectively.

Table 12: Shoulder inclination angle above the mill centre at all critical speed, filling and lifter height settings.

		1.5 mm	3.0 mm	6.0 mm	10.0 mm
Speed	**Filling**	**Shoulder Inclination (°)**			

55 % Crit.	20 %	272.48	277.64	277.74	285.02
	30 %	274.60	285.02	285.02	285.02
	40 %	285.02	287.80	293.51	288.49
70 % Crit.	20 %	292.66	292.80	293.51	294.43
	30 %	292.66	293.13	299.11	296.82
	40 %	298.07	297.91	308.08	303.10
85 % Crit.	20 %	303.30	303.10	303.10	303.30
	30 %	309.78	308.08	308.08	309.73
	40 %	311.90	318.85	318.62	312.45

According to table 12 above, at 55 % critical speed, the steepest inclination angle was 293.51° recorded at 40 % filling and 6.0 mm lifter heights. At 70 % critical speed, the steepest angle was 308.08° recorded at 40 % filling and 6.0 mm lifter heights. At 85 % critical speed, the steepest angle was 318.85° at 40 % filling and 3.0 mm lifter heights.

At 55 % critical speed, as seen in table 12 above and figure 107a in Appendix E.2, the shoulder inclination increased in steepness with increasing lifter heights at 20 % filling. The steepest angle was 285.02° recorded at 10.0 mm lifter heights. At 30 % filling, the inclination increased with the lifter height from 1.5 mm to 3.0 mm. There was no change in the inclination angle for a further increase in the lifter height. At 40 % filling, the inclination angle increased with the lifter height from 1.5 mm to 6.0 mm. The steepest angle was 293.51° at 6.0 mm lifter heights.

Increasing the filling increased the shoulder inclination steepness at all lifter height settings. The biggest change in the inclination angle was for an increase from 20 % to 30 % at 1.5 mm lifter heights. The change in the inclination angle decreased at every lifter height setting for an increase from 30 % to 40 % filling.

At 70 % critical speed and 20 % filling as seen in figure 107b in Appendix E.2, the lifter height had the same influence on the shoulder inclination as that seen at 55 % critical speed and 20 % filling. The steepest angle was 294.43° at 10.0 mm lifter heights. The change in the inclination for increasing lifter heights was more pronounced between 6.0 mm and 10.0 mm. At 30 % filling, the inclination increased with the lifter height between 1.5 mm and 6.0 mm. The inclination angle decreased at 10.0 mm. The steepest angle was 299.11° recorded at 6.0 mm. At 40 % filling, the lifter height influence on the shoulder inclination did not follow a clear trend. Increasing the filling increased the shoulder inclination at all lifter height settings, similar to that seen at 55 % critical speed. The influence of the filling was more pronounced for an increase from 30 % to 40 % at 6.0 mm lifter heights. The steepest angle was 308.08° recorded at 40 % filling and 6.0 mm lifter heights.

At 85 % critical speed, increasing the lifter height did not consistently influence on the shoulder inclination at all filling and critical speed settings. At 20 % filling the steepest angle was 303.30° at 1.5 mm and 10.0 mm lifter heights. At 30 % filling the steepest angle was 309.78° at 1.5 mm lifter heights and at 40 % filling, the steepest angle was 318.85° at 3.0 mm lifter heights. An increase in the filling increased the shoulder inclination at all lifter height settings, similar to that seen at 55 % and 70 % critical speeds. The influence of the filling was more pronounced for an increase from 30 % to 40 % at 3.0 mm lifter heights. The steepest angle was 318.85° recorded at 40 % filling and 3.0 mm lifter heights.

Overall, there was no consistent change in the inclination angle for changes in the lifter height. The filling consistently influenced the shoulder inclination at all critical speeds and lifter heights. The change in the inclination was more pronounced for an increase from 30 % to 40 % filling levels.

The EDEM-extracted shoulder inclination angles were similar in magnitude to that of PEPT. Figure 47 below illustrates the comparison between the PEPT and EDEM inclination angles for increasing lifter heights as well as the corresponding standard deviation.

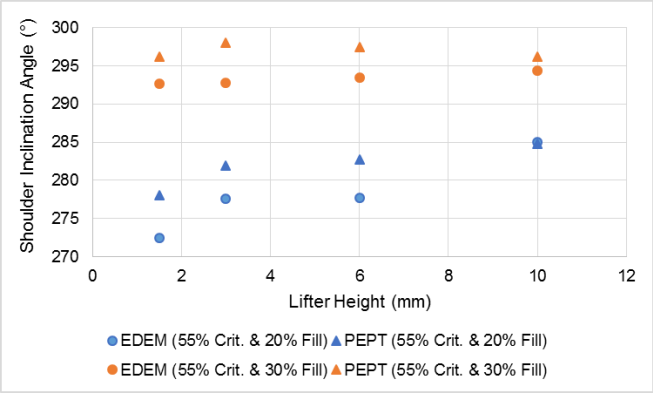

	Standard Deviation (°)		
	20%	30%	40%
55%	2.27	1.24	1.42
70%	3.34	2.11	5.82
85%	3.91	1.99	4.87

Figure 47: Comparison between the EDEM and PEPT shoulder inclination angles for increasing lifter heights at 20% and 30% filling for 55% crit. speeds.

The PEPT shoulder inclinations were higher in magnitude than that of EDEM results at all operating conditions. However, figure 47 above shows that both the PEPT and EDEM results were similar and followed the same trend for increasing lifter heights and increasing the filling levels. The standard deviation at the filling and critical speed levels, showing the impact of increasing the lifter height, is less than a maximum of 6°. A similar result was seen at all operating conditions.

A regression analysis was done to determine if the operating conditions could be used to predict the shoulder inclination angle. The results showed that the shoulder inclination angle

could be accurately predicted using the lifter heights and filling levels at 55 %, 70 % and 85 % critical speeds as seen in table 13 below.

Table 13: Linear fitted equations relating the lifter height (mm) and filling (%) to the shoulder inclination angle (º).

Crit. Speed	Fitted Linear Equation	Std. Deviation	R^2 value
55%	Sh (˚) = 251.5285 + 124.8934 Fill% + 0.5063 LHt	2.3783	0.9497
70%	Sh (˚) = 253.2190 + 132.5195 Fill% + 0.5101 LHt	2.5800	0.9474
85%	Sh (˚) = 260.0073 + 133.7244 Fill% + 0.3628 LHt	3.3483	0.9149

A regression analysis was conducted to see if there exists a formula with combined effects of the operating conditions. Figure 48 below shows the predictive and actual data comparison plot with the combined effects of changing the lifter height, filling and critical speed.

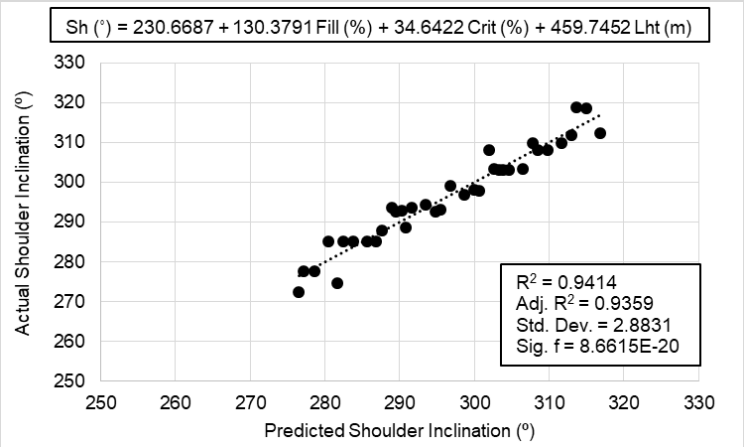

Figure 48: Regression analysis of the shoulder inclination angle using the lifter height, critical speed and filling as variables.

Figure 48 shows that the operating conditions (physical characteristics of the mill) can accurately predict the shoulder inclination based on R^2 values above 0.85, standard deviations below 1% of the average shoulder inclination as well as P-values below 0.01.

5.2.3. Toe Location

The particle probability distributions in Appendix D.1, were used to extract the toe location along the y-z axis as explained in section 5.1.2. The change in the toe location at all operating conditions was assessed using the same analysis as that used for the shoulder location.

Figures 49 a, b and c below, illustrate the movement of the toe location according to changes in all operating conditions. Table 29 in Appendix E.2 summarises the y-z plane coordinates.

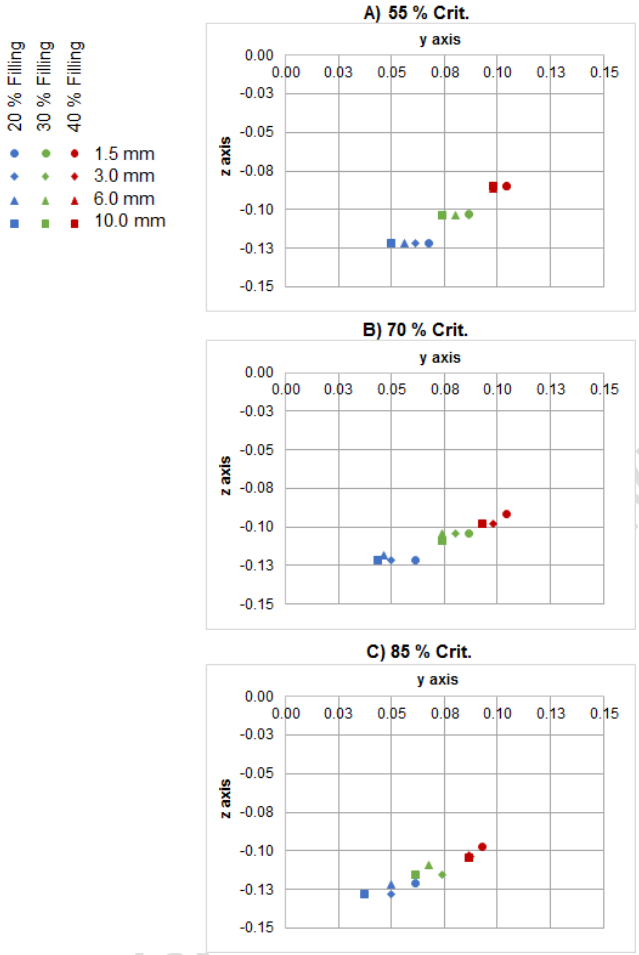

Figure 49: Toe movement at a) 55 %, b) 70 % and c) 85% critical speeds for changes in the filling and lifter height.

Figures 49a, b and c show, at 55 % critical speed and 20 % filling, increasing the lifter height moved the toe location closer to the mill base radially. At 30 % filling, a similar trend was followed for an increase from 3.0 mm to 10.0 mm lifter heights i.e. the toe location moved closer to the mill base radially. At 40 % filling, the only change in the toe location was for an increase from 3.0 mm to 10.0 mm lifter heights i.e. at higher filling levels the influence of the lifter height was less effective. The influence of the lifter height was more pronounced at 20 % filling. Increasing the filling at 55 % critical speed moved the toe higher up, radially along the mill periphery at all lifter heights. The highest and lowest locations were at 40 % and 20 % filling respectively.

At 70 % critical speed and 20 % and 30 % filling, increasing the lifter height moved the toe location closer to the mill base radially. The change in the toe location was more pronounced between 1.5 mm and 3.0 mm lifter heights at 20 % filling and between 1.5 mm and 6.0 mm

lifter heights at 30 % filling. At 40 % filling, the toe location moved lower down radially along the mill periphery, closer to the mill base with increasing lifter height. The change in the toe location was more pronounced between 1.5 mm and 3.0 mm lifter heights. Increasing the filling moved the toe location higher up, radially along the mill periphery at every lifter height setting. The highest toe location was at 40 % filling and for 1.5 mm lifter heights.

At 85 % critical speed and 20 % and 30 % filling, the toe location moved radially down towards the mill base with increasing lifter heights. At 40 % filling, increasing the lifter height from 1.5 mm to 3.0 mm moved the toe location radially down towards the mill base. There was no change in the toe location for further increases from 3.0 mm to 10.0 mm lifter heights. The lowest toe locations were at 10.0 mm lifter heights for all filling levels. Increasing the filling had the same effect on the toe location as that seen at 55 % and 70 % critical speed settings.

Increasing the critical speed caused the toe location to move radially closer to the mill base at all filling and lifter height settings. At 30 % mill filling, the toe movement was less pronounced than that at 20 % and 40 % filling.

Overall, the filling consistently influenced the toe location for all changes in the critical speed and lifter height settings. The filling moved the toe location higher up radially along the mill periphery, the critical speed moved it lower down radially along the mill periphery and the lifter height moved the toe location away from the mill shell, horizontally closer to the mill centre.

The height of the toe above the mill base, summarised in table 14 below, was calculated using the toe coordinates. Figures 108a, b and c in Appendix E.2, illustrate the lifter height influence on the toe height for all filling levels at 55 %, 70 % and 85 % critical speeds respectively.

Table 14: Toe location height above the mill base at all filling, critical speed and lifter height settings.

		1.5 mm	3.0 mm	6.0 mm	10.0 mm
Speed	**Filling**	**Toe height above the mill base (m)**			
55 % Crit.	20 %	0.0282	0.0282	0.0282	0.0282
	30 %	0.0470	0.0461	0.0461	0.0461
	40 %	0.0649	0.0649	0.0640	0.0649
70 % Crit.	20 %	0.0282	0.0282	0.0314	0.0282
	30 %	0.0461	0.0461	0.0461	0.0407
	40 %	0.0587	0.0524	0.0524	0.0524
85 % Crit.	20 %	0.0291	0.0219	0.0282	0.0219
	30 %	0.0461	0.0345	0.0407	0.0345
	40 %	0.0524	0.0461	0.0470	0.0452

According to table 14 above, the maximum toe height was 0.0649 m recorded at 40 % filling and 55 % critical speed. The minimum toe height was 0.219 m recorded at 20 % filling, 85 % critical speed for both the 3.0 mm and 10.0 mm lifter heights.

At 55 %, 70 % and 85 % critical speeds, the lifter height did not influence the toe height at every filling level. The highest toe height was recorded at 1.5 mm lifter heights at all filling levels. Increasing the filling at every critical speed setting, increased the toe height and the change in the toe height remained similar with every increase in filling. The change in the toe height was more pronounced between 20 % and 30 % filling at 1.5 mm lifter height settings.

The influence of the critical speed on the toe height did not follow a consistent trend at 20 % filling and every lifter height setting. At 30 % and 40 % filling, the toe height decreased with increasing critical speeds at all lifter heights and the change in toe height increased with increasing critical speed at higher lifter heights (6.0 mm and 10.0 mm). The influence of the critical speed on the toe height was more pronounced at the 85 % critical speeds.

Overall, the filling consistently influenced the toe height for all the critical speed and lifter height settings. The filling moved the toe location higher up radially, the critical speed caused it to move lower down radially. The influence of the lifter height on the toe location was not consistent.

The horizontal distance between the toe location and the mill centre was at all operating conditions as seen in table 15 below. This allowed an analysis of the movement of the toe location relative to the mill shell at all operating conditions. Figures 109a, b and c in Appendix E.2, illustrate the influence of the lifter height on the distance between the toe and mill centre at 55 %, 70 % and 85 % critical speed respectively.

Table 15: Distance between the toe and mill centre at all filling, critical speed and lifter height settings.

		1.5 mm	**3.0 mm**	**6.0 mm**	**10.0 mm**
Speed	**Filling**	**Distance between toe and mill centre (m)**			
55 % Crit.	20 %	0.0676	0.0613	0.0560	0.0497
	30 %	0.0864	0.0864	0.0801	0.0739
	40 %	0.1043	0.1043	0.0981	0.0981
70 % Crit.	20 %	0.0613	0.0497	0.0466	0.0434
	30 %	0.0864	0.0801	0.0739	0.0739
	40 %	0.1043	0.0981	0.0927	0.0927
85 % Crit.	20 %	0.0613	0.0497	0.0497	0.0372
	30 %	0.0864	0.0739	0.0676	0.0613
	40 %	0.0927	0.0873	0.0864	0.0864

According to table 15 above, at 55 % critical speed, the toe was furthest from the mill centre at 40 % filling for both 1.5 mm and 3.0 mm lifter heights (0.1043 m). At 70 % and 85 % critical speeds, similar to 55 % critical speed results, the furthest distance was 0.1043 m and 0.0972 m respectively at 40 % filling for 1.5 mm lifter heights.

At 55 % and 70 % critical speed, the distance between the toe and mill centre decreased with increasing lifter heights at 20 % and 30 % filling i.e. the toe location moved horizontally closer to the mill centre. At 55 % critical speed and 40 % filling, the influence of the lifter height was not consistent. At 70 % critical speed and 20 % filling, the change in the distance between the toe and mill centre was more pronounced for an increase from 1.5 mm to 3.0 mm lifter heights. At 85 % critical speed, similar to that seen at 55 % and 70 % critical speeds, the distance between the toe and mill centre decreased with increasing lifter height settings at all filling levels. The change in the distance between the toe and mill centre was more pronounced at 20 % filling for an increase from 6.0 mm to 10.0 mm lifter heights.

At 55 %, 70 % and 85 % critical speeds, the distance between the toe and mill centre increased with the filling at all lifter height settings moving the toe horizontally away from the mill centre. For an increase from 20 % to 30 % filling, the change in the distance between the toe and mill centre was more pronounced at 3.0 mm lifter heights and 55 % critical speed while at 70 % critical speed, the change was more pronounced at 10.0 mm lifter heights. At 85 % critical speeds, change in the distance between the toe and mill centre was more pronounced at 1.5 mm and 10.0 mm lifter height settings for an increase in filling from 20 % to 30 % and 30 % to 40 % respectively.

Increasing the critical speed decreased the distance between the toe and mill centre moving the toe horizontally closer to the mill centre at 20 % filling for 1.5 mm, 3.0 mm and 10.0 mm lifter heights. The trend was not consistent at 6.0 mm lifter height settings. The change in the toe location was highest at 20 % filling and 3.0 mm lifter heights for an increase from 55 % to 70 % critical speed.

At 30 % filling, increasing the critical speed from 55 % to 70 % did not consistently influence the distance between the toe and mill centre at all lifter height settings. An increase from 70 % to 85 % critical speed decreased the distance between the toe and mill centre at 3.0 mm, 6.0 mm and 10.0 mm lifter heights. The change in the toe location was highest at 10.0 mm lifter heights for an increase from 70 % to 85 % critical speed. At 40 % filling, the distance between the toe and mill centre decreased with increasing critical mill speeds for 3.0 mm, 6.0 mm and 10.0 mm lifter heights. The change in the toe location was highest at 1.5 mm lifter heights for an increase from 70 % to 85 % critical speed.

Overall, the filling had a consistent influence on the distance between the toe and mill centre. The toe location moved horizontally further away from the mill centre with increasing filling at all lifter heights. The critical speed had the opposite influence on the toe location but this was not a consistent trend.

The inclination angle of the toe location above the mill centre, was calculated using the toe coordinates and the equation 3 in section 5.2.1. Table 16 below, summarises the calculated angles at all operating conditions. Figures 110a, b and c in Appendix E.2, illustrate the influence of the lifter height on the unadjusted toe inclination at all filling levels for 55 %, 70 % and 85 % critical speed settings respectively.

Table 16: Adjusted toe inclination angle for all critical speed, filling and lifter height settings.

		1.5 mm	**3.0 mm**	**6.0 mm**	**10.0 mm**
Speed	**Filling**	**Adjusted toe inclination angle (°)**			
55 % Crit.	20 %	150.96	153.27	155.32	157.80
	30 %	140.00	140.24	142.35	144.58
	40 %	129.20	129.20	131.24	130.94
70 % Crit.	20 %	153.27	157.80	158.60	160.37
	30 %	140.24	143.74	145.93	145.93
	40 %	131.20	134.87	136.48	136.48
85 % Crit.	20 %	153.10	158.79	157.80	163.82
	30 %	141.66	147.40	148.25	152.03
	40 %	136.48	139.95	140.00	140.48

Table 16 above shows the steepest toe inclination was 157.80°, 160.37° and 163.82° at 20 % filling at 55 %, 70 % and 85 % critical speeds for 10.0 mm lifter heights respectively. The minimum inclination angles were seen at 55 % critical speed and 40 % filling for 1.5 mm and 3.0 mm lifter heights.

At 55 % critical speed, the toe inclination increased with increasing lifter heights at 20 % and 30 % filling levels. At 40 % filling, the toe inclination increased with the lifter height from 1.5 mm to 6.0 mm. The trend was not consistent at 10.0 mm lifter heights. The change in the toe inclination was more significant at 20 % filling for an increase from 6.0 mm to 10.0 mm lifter heights. The toe inclination decreased with increasing filling levels at all lifter height settings. The change in the toe inclination was more significant at 10.0 mm lifter heights for an increase from 30 % to 40 % filling.

At 70 % critical speed and 20 % filling, the toe inclination increased with increasing lifter heights. At 30 % and 40 % filling, the toe inclination remained constant for an increase from 6.0 mm to 10.0 mm. The change in the toe location was more significant at 20 % filling for an

increase from 1.5 mm to 3.0 mm lifter heights. The toe inclination decreased with every increase in the filling and at all lifter heights similar to the trend followed at 55 % critical speed. The change in the toe inclination was more significant at 10.0 mm lifter heights for an increase from 20 % to 30 % filling.

At 85 % critical speed and at 20 % filling, the change in the toe inclination was not consistent for increases in the lifter height. At 30 % and 40 % filling, the toe inclination increased with the lifter heights. The change in the toe location was more significant at 20 % filling for an increase from 6.0 mm to 10.0 mm lifter heights. The toe inclination angle decreased with increasing filling at all lifter heights similar to 55 % and 70 % critical speeds. The change in the toe inclination was more significant at 10.0 mm lifter heights for an increase from 20 % to 30 % filling, similar to that seen at 70 % critical speed.

Increasing the critical speed increased the toe inclination at 3.0 mm and 10.0 mm lifter height settings at 20 % filling. There was no clear trend for 1.5 mm and 6.0 mm lifter height settings. At 30 % and 40 % filing, increasing the critical speed increased the toe inclination at every lifter height setting. The biggest change in the toe inclination angle was at 30 % filling, 10.0 mm lifter heights for an increase from 70 % to 85 % critical speed.

Overall, the lifter height caused the toe inclination to decrease, becoming less steep. Increasing the lifter height and critical speed settings increased the toe inclination. The influence of the filling on the toe inclination was more significant than the lifter height and critical speed.

The EDEM-extracted toe inclination angles were not as similar in magnitude to that of PEPT. The figure below illustrates the comparison between the PEPT and EDEM inclination angles for increasing lifter heights as well as the corresponding standard deviation.

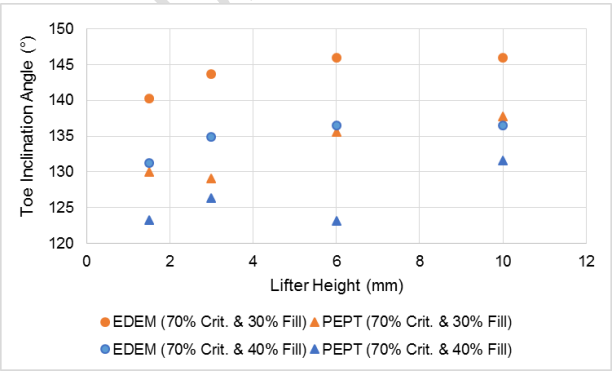

	Standard Deviation (°)		
	20%	30%	40%
55%	8.36	1.64	1.18
70%	6.66	2.38	3.04
85%	3.46	4.19	2.44

Figure 50: Comparison between the EDEM and PEPT toe inclination angles for increasing lifter heights at 30% and 40% filling for 70% crit. speeds.

The PEPT toe inclination was lower in magnitude than that of EDEM results at all operating conditions. However, figure 50 above shows that both the PEPT and EDEM results were similar and followed the same trend for increasing lifter heights and increasing the filling levels. The standard deviation at the filling and critical speed levels, showing effects of increasing the lifter height, is less than a maximum of 9°. A similar result was seen at all operating conditions.

A regression analysis done on the toe inclination gave similar results to that of the shoulder inclination i.e. the lifter height and filling could be used to accurately predict the toe inclination. Table 17 below shows the equations generated using regression relating the lifter height (mm) and filling (%) to the toe inclination angle (º) at 55 %, 70 % and 85 % critical speeds.

Table 17: Linear fitted equations relating the lifter height (mm) and filling (%) to the toe inclination angle (º)

Crit. Speed	Fitted Linear Equation	Std. Deviation	R^2 value
55%	Toe (˚) = -85.6908 + 120.9649 Fill - 0.5249 LHt	0.8412	0.9930
70%	Toe (˚) = -86.3954 + 113.7502 Fill - 0.6126 LHt	1.6536	0.9706
85%	Toe (˚) = -82.8350 + 95.7286 Fill - 0.8189 LHt	1.9200	0.9487

Figure 51 below illustrates the regression result generated by varying the lifter height (m), critical speed (%) and filling (%).

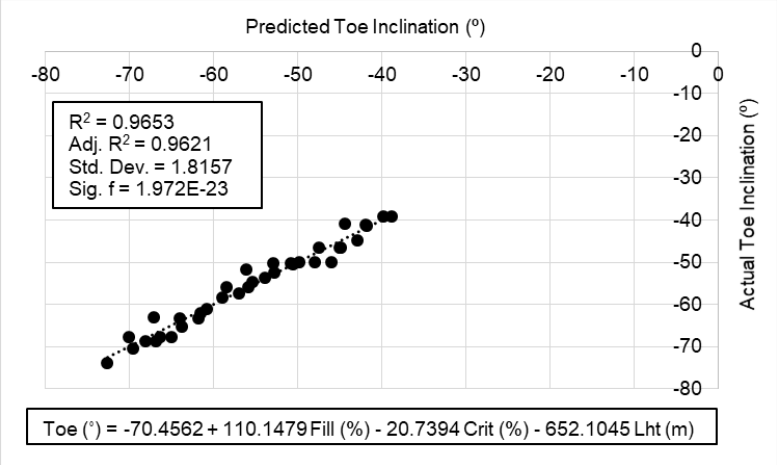

Figure 51: Toe inclination regression analysis using lifter height, critical speed and filling as variables.

Figure 51 shows that the operating conditions (physical characteristics of the mill) can accurately predict the toe inclination based on R^2 values above 0.9, standard deviations below 1 % of the average toe inclination as well as P values below 0.0001.

5.2.4. Distance L_1 and L_2

The position probability as illustrated in Appendix D.1 was used to extract data points along the charge free surface in order to calculate distance L_1 using equations 7 and 8 in Section 5.1.2. Distance L_2 was calculated by determining the distance between the equilibrium surface

at the CoC and the intersection of the diametric line with the mill shell. The change in distance L_1 and L_2 was assessed according to changes in the operating conditions.

The figures illustrated in Appendix D.6 show the charge characteristics of interest extracted from the position and average charge velocity distribution plots including distance L_1 and L_2. According to the figures in Appendix D.6, both distance L_1 and L_2 were influenced by increasing the filling at all critical speeds i.e. the distances increase with increasing filling. Increasing the critical speed decreased distances L_1 and L_2. Increasing the lifter height did not consistently influence distance L_1 and L_2. The lifter height influenced distance L_2 according to whether the diametric line intersection was at the mill shell or at the lifter bar. Distance L_1 decreased with increasing lifter heights at 20 % filling. Table 18 below, summarises the change in distance L_1 for changes at all operating conditions.

Table 18: Change in L_1 according to changes in the mill speed, filling and lifter height settings.

		1.5 mm	**3.0 mm**	**6.0 mm**	**10.0 mm**
Speed	**Filling**	**Distance L_1 (m)**			
55 % Crit.	20 %	0.0363	0.0334	0.0354	0.0348
	30 %	0.0480	0.0456	0.0421	0.0436
	40 %	0.0549	0.0548	0.0554	0.0540
70 % Crit.	20 %	0.0371	0.0318	0.0346	0.0301
	30 %	0.0454	0.0433	0.0429	0.0416
	40 %	0.0542	0.0528	0.0459	0.0520
85 % Crit.	20 %	0.0373	0.0289	0.0266	0.0200
	30 %	0.0454	0.0341	0.0311	0.0296
	40 %	0.0415	0.0307	0.0280	0.0305

According to table 18 above, at 55 % critical speed and 20 % filling, L_1 was not significantly influenced by increasing the lifter height. At 30 % filling, L_1 decreased for an increase from 1.5 mm to 6.0 mm lifter heights but the trend was not followed between 6.0 mm to 10.0 mm lifter heights. At 40 % filling, L_1 was not significantly influenced by the lifter height. The longest L_1 distance was 0.0554 m at 40 % filling and 6.0 mm lifter heights. The biggest change in L_1 was at 30 % filling for an increase from 3.0 mm to 6.0 mm lifter heights. L_1 increased with increasing filling at every lifter height setting. The biggest change in L_1 was at 6.0 mm lifter heights for an increase from 30 % to 40 % filling.

At 70 % critical speed, the change in L_1 did not follow a consistent trend for increases in the lifter height. At 30 % filling, L_1 decreased with increasing lifter heights i.e. the equilibrium surface and charge free surface moved closer together. At 40 % filling, L_1 decreased for an increase from 1.5 mm to 6.0 mm lifter heights but the trend was not followed between 6.0 mm

to 10.0 mm lifter heights. The longest L_1 distance was 0.0542 m at 40 % filling and 1.5 mm lifter heights. The biggest change in L_1 was at 40 % filling for an increase from 3.0 mm to 6.0 mm lifter heights. Similar to that seen at 55 % critical speed, L_1 increased with increasing filling levels at every lifter height. The biggest change in L_1 was at 3.0 mm and 10.0 mm lifter heights for an increase from 20 % to 30 % filling.

At 85 % critical speed for both 20 % and 30 % filling levels, L_1 decreased with increasing lifter heights. At 40 % filling, L_1 decreased for an increase from 1.5 mm to 6.0 mm lifter heights. The trend was not followed for an increase from 6.0 mm to 10.0 mm lifter heights. The longest L_1 distance was 0.0454 m at 30 % filling and 1.5 mm lifter heights. The biggest change in L_1 was at 30 % filling for an increase from 1.5 mm to 3.0 mm lifter heights. At 1.5 mm, 3.0 mm and 6.0 mm lifter heights, the increase in filling did not consistently influence L_1. At 10.0 mm lifter heights the increase in the filling caused L_1 to increase. The biggest change in L_1 was at 10.0 mm lifter heights for an increase from 20 % to 30 % filling.

Increasing the critical speed at 20 % filling and 1.5 mm lifter heights, increased L_1. The opposite was seen at 3.0 mm, 6.0 mm and 10.0 mm lifter heights i.e. L_1 decreased with increasing critical speeds. At 30 % filling, L_1 decreased with the critical speed at 3.0 mm and 10.0 mm lifter heights. The change in L_1 did not follow this trend at 1.5 mm and 6.0 mm lifter heights. At 40 % filling, L_1 decreased with increasing critical speeds at all lifter heights. The biggest change in L_1 was at 3.0 mm lifter heights and 40 % filling for 70 % to 85 % critical speed increase.

Overall, the filling consistently increased L_1 at all critical speeds and had the strongest influence at 55 % and 70 % critical speeds. The influence of the critical speed on L_1 was more pronounced for an increase from 55 % to 70 % of critical at all filling levels. The influence of the lifter height was more pronounced at 85 % critical speed for all filling levels.

Table 19 below summarises the change in L_2 at all operating conditions.

Table 19: Change in L_2 according to changes in the mill speed, filling and lifter height settings.

		1.5 mm	3.0 mm	6.0 mm	10.0 mm
Speed	**Filling**	**Distance L_2 (m)**			
55 % Crit.	20 %	0.0388	0.0346	0.0314	0.0377
	30 %	0.0487	0.0503	0.0547	0.0543
	40 %	0.0679	0.0679	0.0680	0.0720
70 % Crit.	20 %	0.0354	0.0327	0.0332	0.0349
	30 %	0.0502	0.0480	0.0489	0.0495
	40 %	0.0645	0.0629	0.0641	0.0573

85 % Crit.	20 %	0.0330	0.0257	0.0322	0.0320
	30 %	0.0465	0.0453	0.0406	0.0362
	40 %	0.0593	0.0574	0.0555	0.0621

At 55 % critical speed and 20 % filling, L_2 decreased for an increase from 1.5 mm to 6.0 mm lifter heights but the trend was not followed for an increase from 6.0 mm to 10.0 mm lifter heights. The opposite result was seen at 30 % filling, L_2 increased with the lifter height between 1.5 mm to 6.0 mm lifter heights which was not followed for an increase from 6.0 mm to 10.0 mm lifter heights. At 40 % filling, L_2 increased with the lifter height between 3.0 mm and 10.0 mm. The longest distance was 0.0720 m, at 40 % filling and 10.0 mm lifter heights. The biggest change in L_2 was at 30 % filling for an increase from 3.0 mm to 6.0 mm lifter heights. L_2 increased with the filling at every lifter height setting. At 55 % critical speed, the biggest change in L_2 was recorded at 1.5 mm lifter heights for an increase from 30 % to 40 % filling.

At 70 % critical speed, L_2 increased with the lifter height from 3.0 mm to 10.0 mm at 20 % and 30 % filling levels. At 40 % filling, the change in L_2 did not follow a consistent trend for every increase in the lifter height. The longest distance was 0.0645 m at 40 % filling and 1.5 mm lifter heights. The biggest change in L_2 was recorded at 40 % filling for an increase from 6.0 mm to 10.0 mm lifter heights. L_2 increased with increasing filling levels at all lifter heights. The biggest change was recorded at 6.0 mm lifter heights for an increase from 20 % to 30 % filling.

At 85 % critical speed and 20 % filling, the change in L_2 did not follow a consistent trend for every increase in the lifter height. At 30 % filling, L_2 decreased with every increase in the lifter height. At 40 % filling, L_2 decreased for an increase from 1.5 mm to 6.0 mm lifter heights but the trend was not consistent for an increase from 6.0 mm to 10.0 mm. The biggest change in L_2 was at 20 % filling for an increase from 1.5 mm to 3.0 mm lifter heights. L_2 increased with increasing filling at all lifter heights. The biggest change was recorded at 10.0 mm lifter heights for an increase from 30 % to 40 % filling.

At 20 % filling for 1.5 mm, 3.0 mm and 10.0 mm lifter height settings, L_2 decreased with increasing critical speeds. The change in L_2 did not follow a consistent trend at 6.0 mm lifter heights. At 30 % filling for 3.0 mm, 6.0 mm and 10.0 mm lifter height settings, L_2 decreased with increasing critical speeds. At 40 % filling, for 1.5 mm, 3.0 mm and 6.0 mm lifter heights, L_2 decreased with increasing critical speeds. The biggest change in L_2 was recorded at 40 % filling and 10.0 mm lifter heights for an increase from 55 % to 70 % critical speed. Overall, the filling consistently decreased L_2 at all critical speeds. The influence of the critical speed on L_2 was more pronounced at 20 % and 30 % filling levels. The influence of the lifter height on L_2 was not consistent at all filling and critical speed settings.

Since distance L_2 is critical to the predictive velocity profile model equation, a regression analysis was done to determine if the operating variables can be used to predict the distance L_2. The results showed that the lifter height and critical speed could be used to accurately predict distance L_2 at 20 %, 30 % and 40 % filling. Table 20 below lists the linear fitted equations generated as a result showing the lifter height (m) and filing (%) as variables.

Table 20: Linear fitted equations relating the lifter height (m) and the filling (%) to distance L_2 (m).

Crit. Speed	Fitted Linear Equation	Std. Deviation	R^2 value
55%	L2 (m) = 0.0045 + 0.1554 Fill + 0.3570 LHt	0.0016	0.9853
70%	L2 (m) = 0.0053 + 0.1501 Fill - 0.2429 LHt	0.0027	0.9539
85%	L2 (m) = 0.0052 + 0.1393 Fill - 0.3706 LHt	0.0031	0.9334

Based on the results in Table 20 above, another regression analysis was done to determine if a single equation could be determined relating all operating conditions. Figure 52 below shows the results that the lifter height (m), filling (%) and critical speed (%) can be used to predict distance L_2.

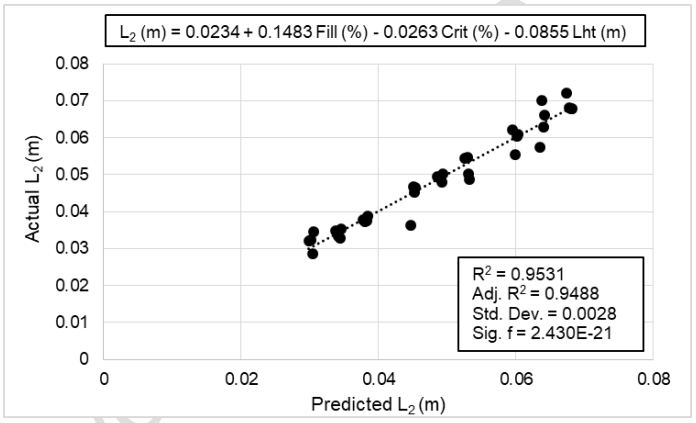

Figure 52: Regression analysis of distance L_2 using the lifter height, critical speed and filling as variables.

Figure 52 shows these variables can be used to accurately predict distance L_2 with R^2 values above 0.9, the standard deviation recorded to be less than 6 % of the average distance L_2 and the significant-f value being less than 0.001.

5.3. Power Draw

The power draw was analysed using the power draw distributions in Appendix D.7 and the maximum power draw extracted at all operating conditions.

5.3.1. Influence of operating conditions on the power draw distribution

Figures 53a to f below, show the influence of the critical speed and filling on the power draw distribution at all lifter heights. This was used to identify the high power draw that corresponds to specific charge motion regions i.e. cascading, cataracting, rising en-masse, etc.

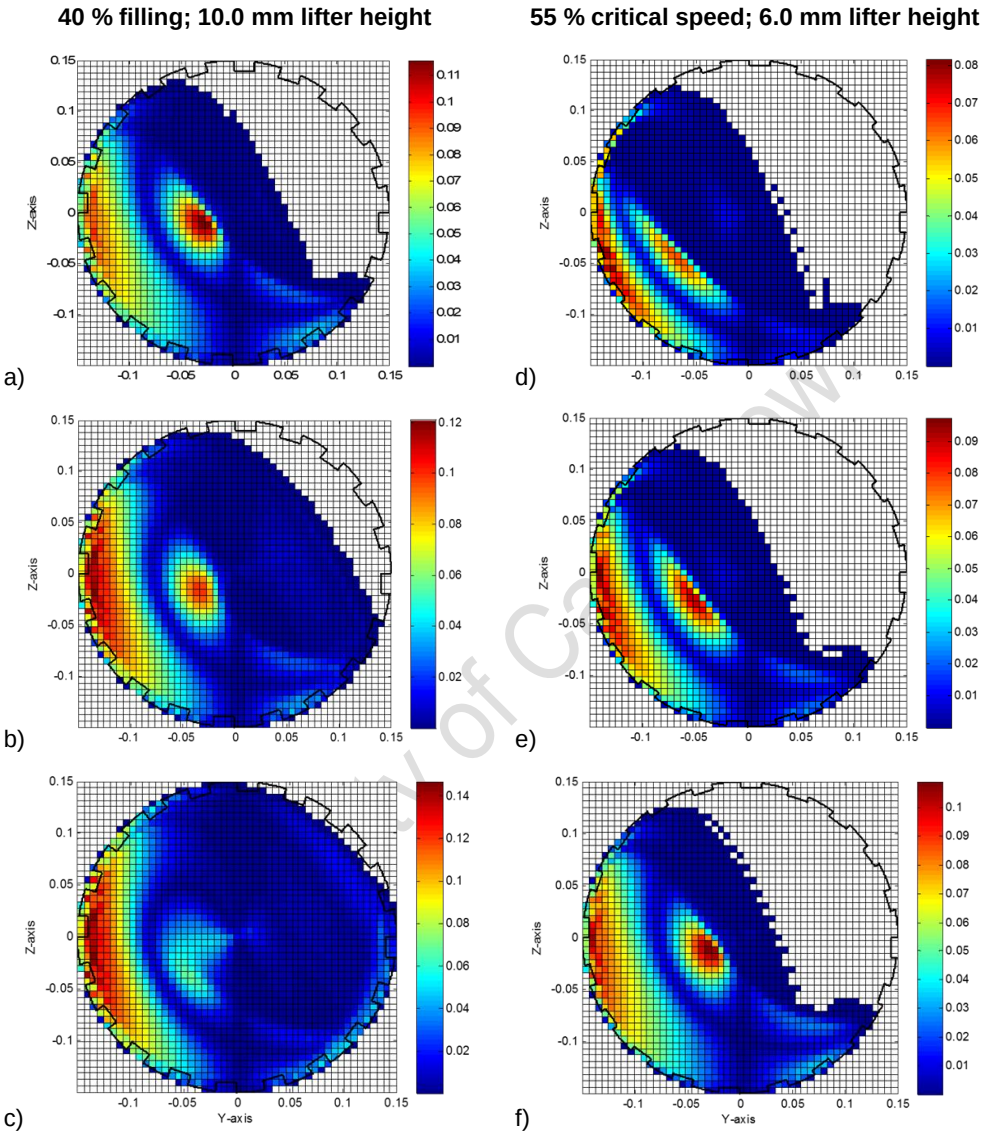

Figure 53: Power draw distribution plots illustrating the influence of a) 55 %, b) 70 % and c) 85 % critical speed settings and d) 20 %, e) 30 % and f) 40 % filling levels.

The distribution plots show that for changes in the critical speed, filling and lifter height, the highest power drawn was concentrated in 2 regions i.e. the cascading region directly above the equilibrium surface, and the rising en-masse region along the mill shell. The operating conditions influenced the magnitude of the power drawn in these regions including the charge concentrated in these regions. The lowest power draw contributors existed in the equilibrium region and in the cataracting region where the particle impacts were a reduced.

At 55 % critical speed and 20 % filling, increasing the lifter height increased the charge contributions in the high power draw regions where the charge concentration was higher at 6.0 mm and 10.0 mm lifter heights in the rising en-masse region. A similar trend was followed in the cascading region.

The influence of the lifter height on the charge interactions contributing to the high power draw regions was similar at 30 % and 40 % filling. The high power draw regions became more distinct at 30 % and 40 % filling levels due to the increase in charge concentration in the rising en-masse and cascading regions. The number of bins indicative of the high power draw, increased with an increase in the lifter height and was higher at 10.0 mm lifter height and 6.0 mm respectively. The increased lifter heights increased the intensity and span of the high power draw zones in both the rising en-masse and cascading regions.

At 40 % filling, the number of high power draw bins in the cascading region remained unchanged for every increase in the lifter height. The influence of increasing the filling on both the rising en-masse and cascading regions, increased the span, intensity and number of bins in the high power draw regions. The highest intensity for the power drawn was recorded at 40 % filling levels for 1.5 mm, 3.0 mm and 6.0 mm lifter heights. The intensity was less pronounced at 10.0 mm lifter heights.

At 70 % critical speed and all filling levels, the colour intensity of the power drawn in the cascading region was reduced compared to the rising en-masse region for all lifter height settings. The intensity of the highest power draw regions were at 6.0 mm and 10.0 mm lifter heights in the rising en-masse region. The area covered by the high power draw region in the rising en-masse region increased with an increase in lifter height.

Increasing the filling caused the high power draw zones, in the rising en-masse region, to be concentrated higher up along the mill shell, further away from the mill base. The number of bins in the high power draw regions increased with an increase in filling. The shape of the high power draw area in the cascading region changed and the intensity increased with the filling.

At 85 % critical speed and 20 % filling, the number of high power draw bins increased with an increase in lifter height in the rising en-masse region. The colour intensity of the rising en-masse region was higher than the cascading region at all lifter height settings. The area covered by the rising en-masse region moved higher up along the mill shell, further away from the mill base with increasing lifter heights.

At 30 % and 40 % filling, the high power draw area (red colour zones) in the rising en-masse region increased in intensity and moved higher up along the mill shell, further away from the mill base with increasing lifter heights. The intensity and number of bins in the high power

draw area in the cascading region decreased with an increase in lifter height. The colour intensity in the high power draw zones increased at 1.5 mm and 10.0 mm lifter heights for the cascading and rising en-masse regions respectively.

Increasing the filling caused the colour intensity of the rising en-masse region to increase and move higher up along the mill shell, further away from the mill base. The high power draw area in the rising en-masse region increased with increasing filling. The span of the high power draw area in the cascading region reduced and was concentrated closer to the mill centre for increasing filling levels.

The influence of increasing the critical speed caused the intensity and span of the high power draw area to decrease at 20 % filling and all lifter height settings. The rising en-masse region had the highest intensity for the colour of the high power draw area. At 30 % filling, the colour intensity of the high power area in the cascading region reduced with increasing critical speeds at all lifter heights.

The span of the high power draw area in the rising en-masse region increased with increasing critical speed. At 40 % filling, the colour intensity and span of the high power draw area in the rising en-masse region increased with the critical speed. The cascading region's colour intensity reduced as the critical speed increased.

5.3.2. Influence of operating conditions on the highest power drawn

The maximum power draw was extracted from the EDEM results to assess the influence of the operating conditions. Table 21 below summarises the extracted data and figure 110 in Appendix F illustrates the influence of the lifter height at all filling levels for 55 %, 70 % and 85 % critical speeds respectively.

Table 21: Maximum power draw extracted at every critical speed, filling and lifter height.

		1.5 mm	3.0 mm	6.0 mm	10.0 mm
Speed	**Filling**	**Maximum Power Drawn (W)**			
55 % Crit.	20 %	10.45	13.60	14.14	15.44
	30 %	21.11	22.93	23.23	24.05
	40 %	30.46	30.93	31.15	31.60
70 % Crit.	20 %	13.25	17.91	18.88	20.21
	30 %	25.45	28.66	29.49	30.29
	40 %	37.50	39.31	39.51	39.89
85 % Crit.	20 %	16.11	23.12	23.66	26.63
	30 %	29.43	35.50	35.92	38.13
	40 %	43.88	47.30	47.42	49.21

According to table 21 above and figure 111 in Appendix F, at 55 %, 70 % and 85 % critical speeds, the highest power draw was recorded at 10.0 mm lifter heights and 40 % filling levels. The lowest power draw was recorded at 1.5 mm lifter heights and 20 % filing levels.

At all the critical speed and filling levels, the maximum power draw increased with increasing lifter heights. The change in the maximum power draw was more pronounced for an increase from 1.5 mm to 3.0 mm lifter heights at all filling levels. Overall, the biggest change in the maximum power draw was at 85 % critical speed and 20 % filling for an increase from 1.5 mm to 3.0 mm lifter heights.

Increasing the filling increased the maximum power draw at every lifter height and critical speed setting. The change in the maximum power draw decreased with increasing filling levels at all lifter heights. The biggest change in the maximum power draw was at 1.5 mm lifter heights and 85 % critical speed for an increase from 30 % to 40 % filling.

Increasing the critical speed had the same influence as that of increasing the lifter height and filling i.e. the maximum power draw increased with increasing critical speeds. The biggest change in the maximum power draw was at 10.0 mm lifter heights and 40 % filling for an increase from 70 % to 85 % critical speed.

In Appendix F, the trend-lines in figure 111 and equations in table 30 show that there is a correlation between the lifter height and maximum power draw at all critical speed and filling levels. The R^2 values at each setting were greater than 0.95 and the magnitude of the equation coefficients increased with increasing critical speeds. Overall, the influence of the filling on the maximum power draw was more pronounced than that of the critical speeds and lifter heights based on the change in the maximum power draw at every increase in the filling.

5.4. Charge Velocity

The charge velocity was analysed using the EDEM-generated average and tangential charge distributions. The average charge velocity was used to generate velocity frequency plots and the tangential charge velocity was used to assess the velocity profile along the diametric line.

5.4.1. Average charge velocity distribution

Figures 54a to f below, show the average velocity distributions at 30 % filling and 70 % critical speed as extracted from Appendix D.2 respectively.

30 % Fill and 10.0 mm lifter height **70 % Crit. and 10.0 mm lifter height**

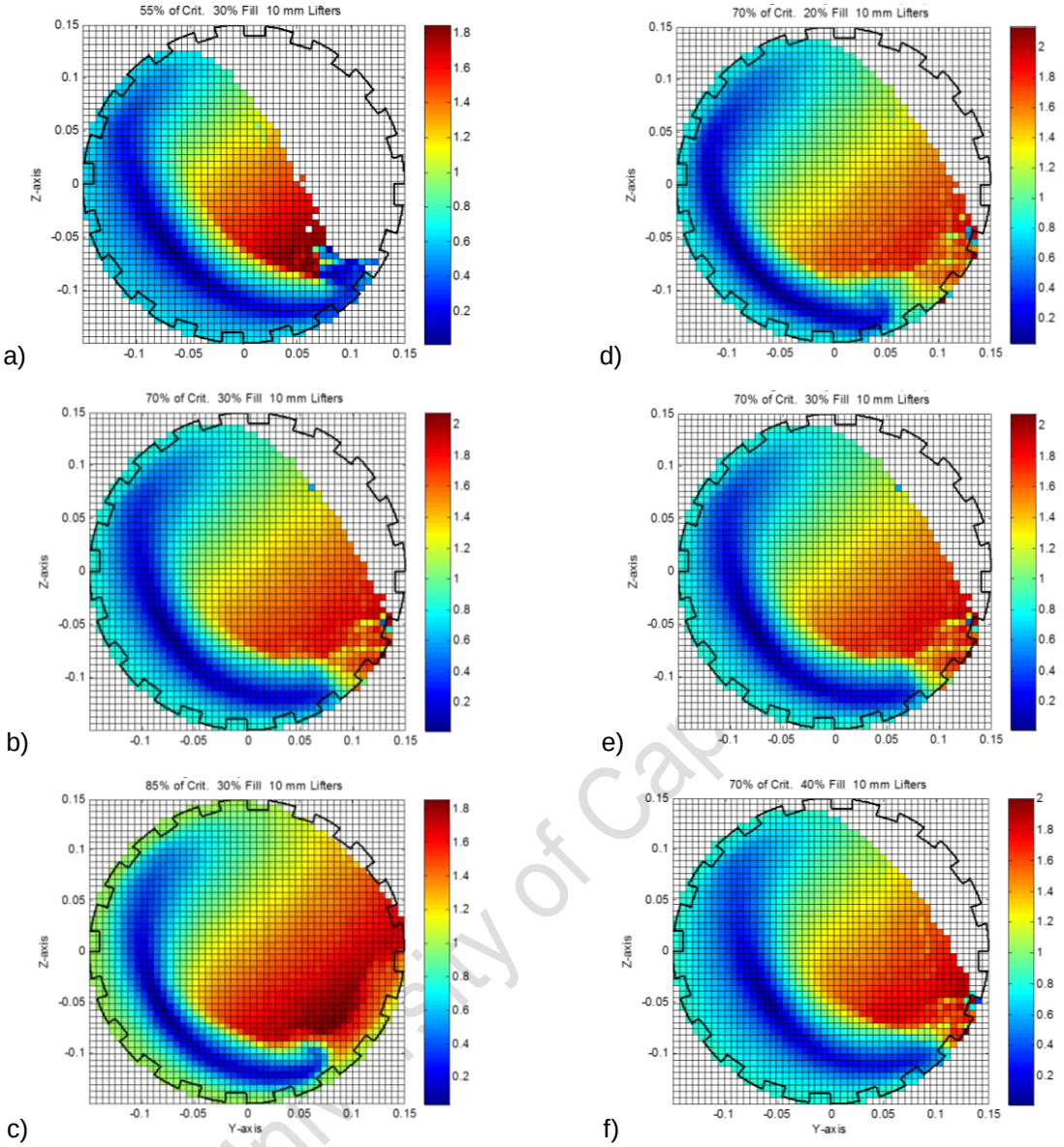

Figure 54: Average velocity distribution at 10.0 mm lifter heights, 30 % filling for a) 55 %, b) 70 % and c) 85 % critical speed and at 70 % critical speed for d) 20 %, e) 30 % and f) 40 % filling.

According to figures 54a to f above, moving in a radial direction from the mill shell to the equilibrium region, the charge velocity decreased in magnitude as the 'zero velocity' band is approached. The charge velocity increased moving radially from the equilibrium surface to the cascading and cataracting regions at all critical speeds. The highest average velocity was achieved in the cataracting region where the particles were in free fall trajectories.

Figures 54a, b and c above, the charge velocity magnitude along the mill shell in the rising en-masse region increased with every increase in the critical speed. The number of bins in the cataracting region increased with increasing critical speed i.e. more particles were recorded in the high charge velocity range (1.4 – 2.0 m/s). The number of bins along the equilibrium

surface band decreased with an increase in the critical speed as fewer particles were recorded in the low velocity range (0 – 0.6 m/s) due to increased critical speeds. The same trend was seen at all filling and lifter height settings as illustrated in Appendix D.2. Figures 54d, e and f illustrate that the number of bins in the cataracting region decreased and the number of bins in the equilibrium surface increased with increasing critical speeds. The same trend was seen for increases at all filling and lifter height settings as illustrated in Appendix D.2.

The influence of increasing the lifter height, as seen in Appendix D.2, showed the charge velocity magnitude for every bin in this region, decreased at the mill shell. At 85 % critical speed, the opposite was seen i.e. charge velocity magnitudes at the mill shell increased with increasing lifter heights. The bins in the cataracting region increased with the lifter heights i.e. fewer particles were caught in the free fall trajectory zone (cataracting region). The opposite trend was seen for the number of bins in the equilibrium surface for increasing lifter heights.

Overall, the highest charge velocity magnitude at the mill shell was recorded at 85 % critical speed and 40 % filling. The highest number of bins in the cataracting region was recorded at 85 % critical speed, 40 % filling and 10.0 mm lifter heights.

5.4.2. Particle velocity frequency

The charge velocity frequency plots in Appendices D.5, discussed in section 5.1.3, were used to determine the particle distribution according to the charge velocity achieved. Figures 55a to f below, illustrate the influence of the critical speed (55 % and 70 %) at 20 %, 30 % and 40 % filling, on the particle velocity frequency at all lifter height settings.

a)

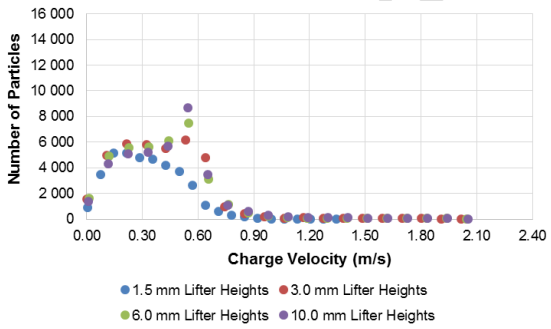

d)

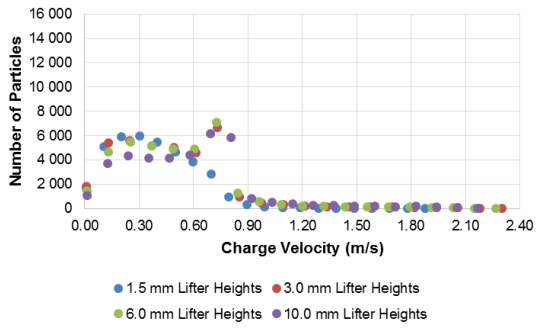

b)

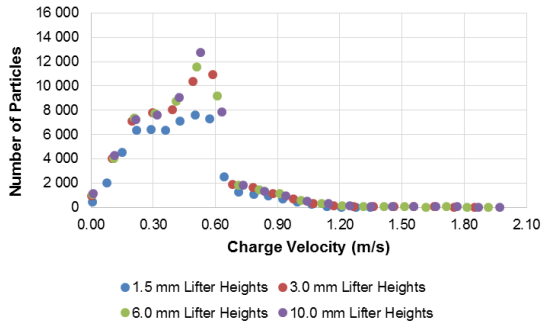

e)

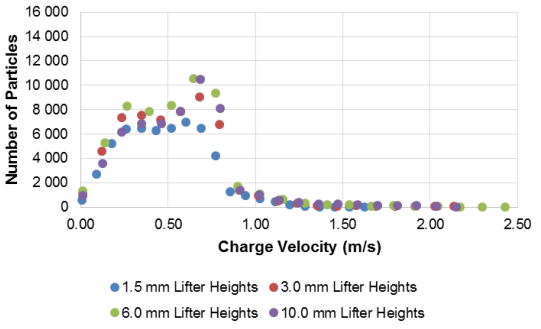

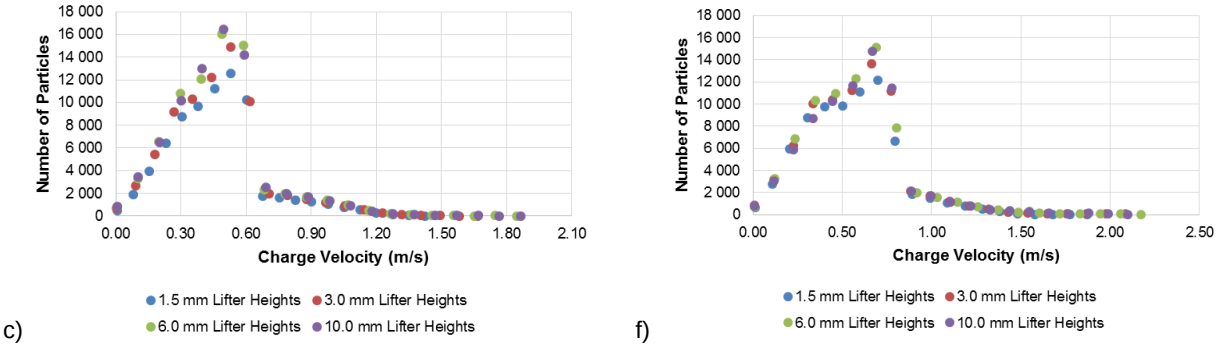

Figure 55: Charge velocity frequency at 55 % critical speed for a) 20 %, b) 30 % and c) 40 % filling and at 70 % critical speed for d) 20 %, e) 30 % and f) 40 % filling at all lifter height levels.

Figures 55a to f above, show that for changes in the critical speed and filling, more particles were recorded to achieve charge velocities higher than 1.0 m/s. The number of particles caught in the low velocity regions (0 – 0.6 m/s) increased with the filling. The increase in critical speed had the opposite effect on the number of particles in the low velocity region (0 – 0.6 m/s) i.e. fewer particles achieving the low velocities typical to the equilibrium surface band.

The concentration of particles in the 0.6 – 1.0 m/s range corresponded to areas close to the mill shell (rising en-masse) and cascading regions. This concentration increased with increasing filling and critical speeds. Increasing the critical speed caused this region to be the highest concentration of particles due the increased charge motion and more particles moving into these regions. Increasing the critical speed also increased the charge velocity achieved by the highest concentration of particles.

The figures in Appendix D.5 show that increasing the lifter height at 55 % critical speeds and all filling levels, increased the concentration of particles in the 0.6 – 1.0 m/s range. Increasing the lifter height did not consistently influence the charge velocity at 30 % and 40 % filling levels for 70 % and 85 % critical speeds. The highest concentration of particles with the same velocity increased with increasing lifter height at all operating conditions. Higher lifter heights were found to reduce the particle concentration in the 'zero velocity' band in the equilibrium surface. The lifter height influence on the concentration of particles became less pronounced at 40 % filling for 70 % and 85 % critical speeds.

Table 22 below, summarises the highest charge velocity recorded at all operating conditions.

Table 22: Highest average charge velocity at all critical speed, filling and lifter height settings.

		1.5 mm	3.0 mm	6.0 mm	10.0 mm
Speed	**Filling**	**Highest average charge velocity (m/s)**			
55 % Crit.	20 %	1.346	2.016	2.044	2.052
	30 %	1.348	1.849	1.915	1.971

	40 %	1.425	1.668	1.845	1.864
70 % Crit.	20 %	1.879	2.300	2.269	2.168
	30 %	1.624	2.137	2.427	2.148
	40 %	1.873	2.087	2.171	2.098
85 % Crit.	20 %	2.017	2.157	2.171	2.079
	30 %	1.956	2.166	2.109	2.192
	40 %	2.004	2.175	2.145	2.330

According to table 22 above, the highest charge velocity was not consistently influenced by the lifter height and filling. The highest average charge velocity increased with increasing lifter heights at 55 % critical speed. This trend was not consistent at 70 % and 85 % critical speeds. Increasing the critical speed did not consistently influence the highest average charge velocity. At 1.5 mm lifter heights, the highest average charge velocity increased with the critical speed. At 3.0 mm, 6.0 mm and 10.0 mm lifter heights, the highest average charge velocity increased for an increase from 70 % to 85 % filling levels.

Overall, the filling and critical speed had the most pronounced influence on the velocity frequency distributions. More particles were concentrated in low velocity regions for an increase in filling and the opposite was seen for an increase in critical speed. The distributions for an increasing critical speed were smoother and the change in the velocity frequency was more gradual as opposed to the change in filling levels.

5.4.3. Tangential charge velocity

The tangential velocity was used to analyse the velocity profile along the diametric line as discussed in sections 5.1.5 and 2.6 of the literature review at all filling, critical speed and lifter height settings. Figures 56a to f below, taken from Appendix D.4, illustrate the influence of the operating conditions on the tangential velocity distributions.

55 % critical speed, 3 mm lifter heights.

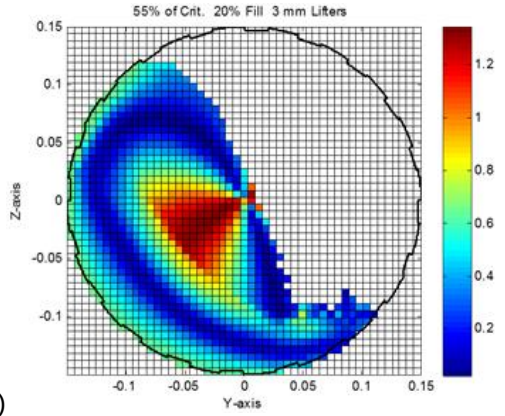

a)

40 % filling, 1.5 mm lifter heights

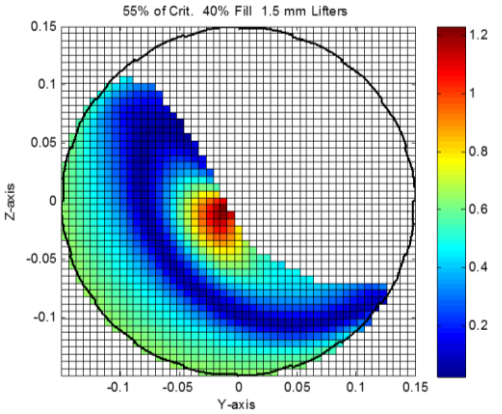

d)

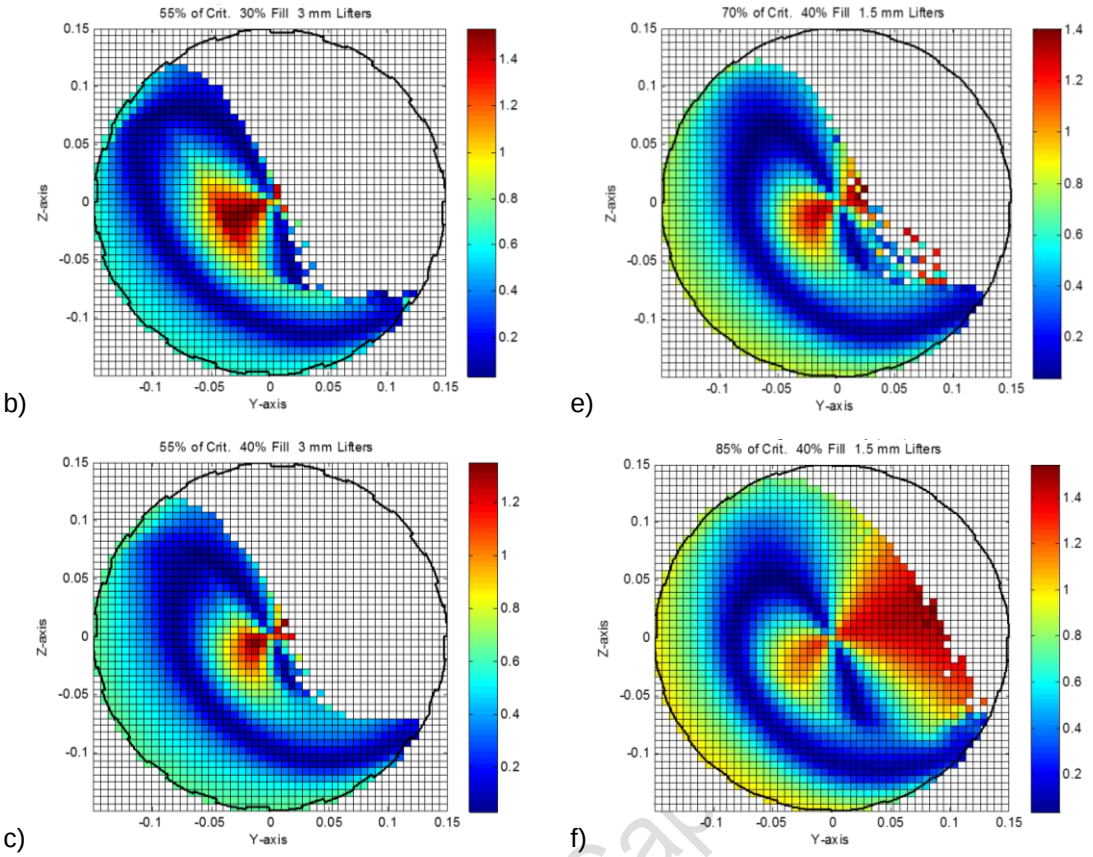

Figure 56: Average tangential velocity distribution at 3 mm and 1.5 mm lifter heights respectively for 55 % critical speed at a) 20 %, b) 30 % and c) 40 % filling and for 40 % filling at d) 55 %, e) 70 % and 85 % critical speed settings respectively.

According to Figure 56 above, the tangential velocity decreased in magnitude from the mill shell to the equilibrium surface in a radial direction. The opposite was seen between the equilibrium surface and the cataracting region at all critical speed, filling and lifter height settings. The highest tangential velocity was seen in the cascading and cataracting regions.

According to figures 56a, b and c, the number of bins in the low velocity range in the equilibrium surface band (less than 0.4 m/s) increased with increasing filling. The tangential velocity along the mill shell in the rising en-masse region, increased in magnitude with increasing filling. The number of bins in the 0.4 – 0.7 m/s range, corresponding to the cascading and rising en-masse regions, increased with increasing filling. The number of bins in the high velocity range (1.0 – 1.5 m/s) in cataracting region decreased in magnitude with increasing filling levels. The increased filling caused fewer particles to be caught in the cataracting region.

Figures 56d, e and f illustrate that the tangential velocity along the mill shell, in the rising en-masse region, increased in magnitude with increasing critical speeds. The number of bins in this region increased with the critical speed due to the increased charge motion. The tangential velocity in the cataracting regions, for speeds above 1.0 m/s, increased with increasing critical

speeds. The number of bins in this region increased as well. The tangential velocity between 0.6 and 1.0 m/s, in the cascading region, decreased with increasing critical speeds based on the colour intensity of the bins.

According to the figures in Appendix D.4, increasing the lifter height increased the number of bins in the cataracting region for velocities above 1.0 m/s as more particles were raised out of the charge bed. Similarly, the number of bins along the mill shell, in the rising en-masse region, increased with increasing lifter heights due to increased charge motion. The increase in the lifter height did not significantly influence the number of bins in the equilibrium surface band.

Overall, the tangential velocity distribution was similar to that of the average charge velocity as it decreased radially between the shell and equilibrium surface as well as increased between the equilibrium surface and cataracting region. The filling increased the charge concentration in the equilibrium surface and rising en-masse regions but had the opposite influence on the cataracting region. The critical speed increased the particle concentration and tangential velocities in the rising en-masse and cataracting regions. The lifter height influence was similar to the critical speed i.e. increased the concentration in the cataracting region.

5.5. Velocity profile along diametric line

The velocity profile consisted of the tangential velocity extracted along a diametric line passing through the CoC and mill centre as discussed in section 2.3.1 and 5.1.5. The velocity profile was extracted from the EDEM results based on changes in the critical speed, filling and lifter heights. The profile was compared to the model derived by Brodner (2013) using PEPT data.

5.5.1. Influence of operating conditions on the velocity profile

The velocity profile along the diametric line, at all operating conditions, was extracted using the tangential velocity distributions in Appendix D.4. The data at all operating conditions are summarised in tables 31, 32 and 33, Appendix G. The change in tangential velocity (magnitude and direction) along the diametric line as illustrated in Appendix D.8, was analysed according to the influence of the operating conditions and that of the charge flow regimes along the cross-section of the tumbling mill.

According to changes in the critical speed, filling and lifter height settings, the velocity profile followed a similar trend whereby, the profile along the diametric line decreased radially from the mill shell to the CoC location and increased in the opposite direction in the cascading region of the mill. A plateau trend was followed in the cataracting region as the change in the tangential velocity remained constant. At the centre of the mill (0, 0), the profile deviated from the plateau trend where the tangential velocity decreased in magnitude and changed direction.

The operating conditions influenced the number of data points extracted along the diametric line according to changes in the distribution of the mill charge. Increasing the lifter height, filling and critical speed increased the number of data points along the diametric line. The operating conditions influenced the change in the magnitude of the tangential velocity along the diametric line, its inclination and its intersections with the CoC and charge free surface.

The velocity profile data points, extracted from Appendix D.8, were plotted against the radial distance from the mill centre and analysed using both continuous and piece-wise distributions. The piece-wise distributions, illustrated in Appendix D.9, were used to analyse the change in the tangential velocity in all regions of the mill. Figures 57a to h below, illustrate the piece-wise distributions based on the influence of the lifter height at 85 % critical speeds for 30 % and 40 % filling levels. The profile was analysed based on the angular velocity at the mill shell, intersection of the diametric line with the CoC and charge free surface as well as the change in tangential velocity in the rising en-masse (distance L_2), cascading (distance L_1) and cataracting regions.

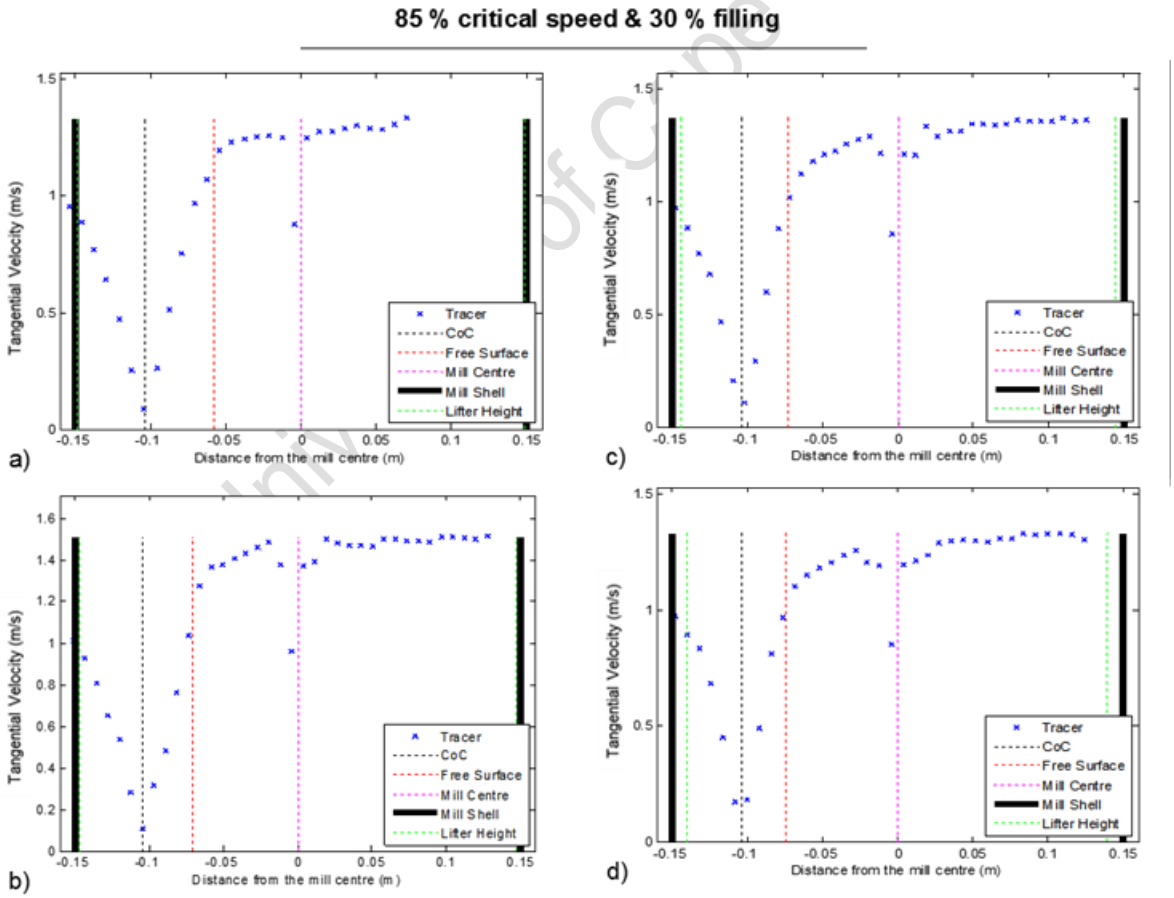

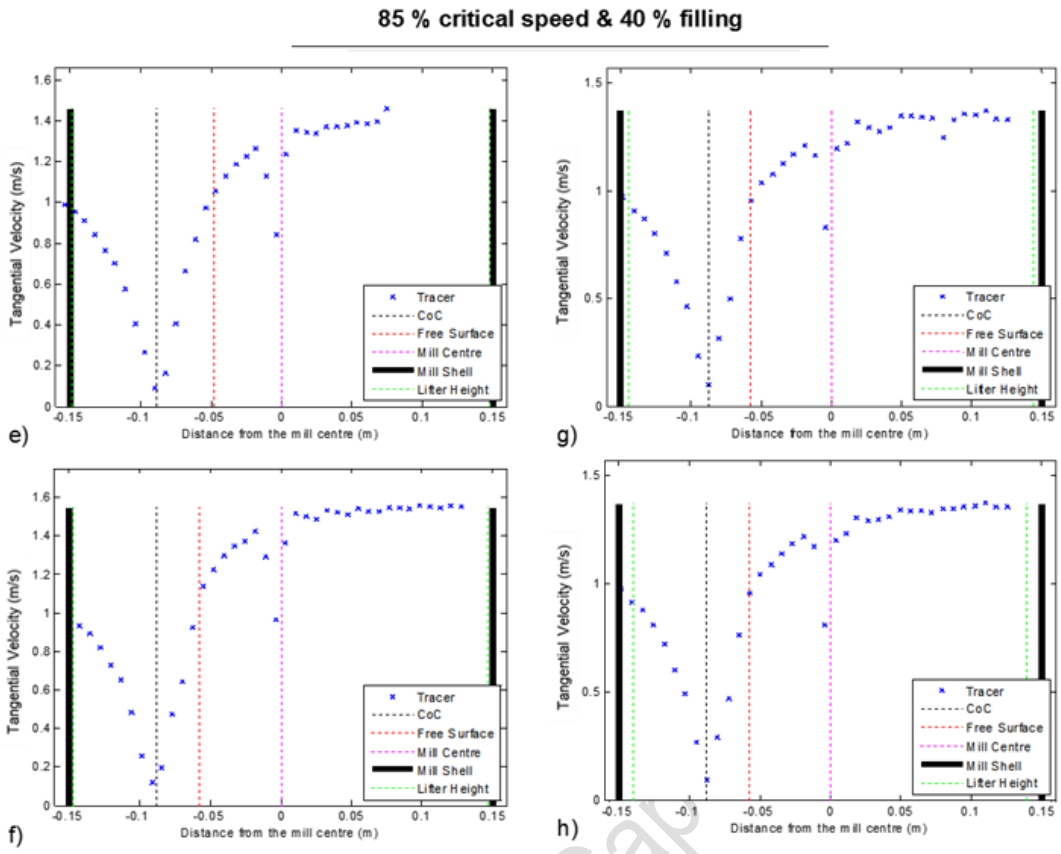

Figure 57: Piece-wise velocity profile at 85 % crit., 30 % fill for a) 1.5 mm, b) 3.0 mm, c) 6.0 mm, d) 10.0 mm lifter heights; 85 % crit., 40 % fill for e) 1.5 mm, f) 3.0 mm, g) 6.0 mm, 10.0 mm respectively.

Figure 57 (a to d) and the figures in Appendix D.9 show that, at 55 % critical speed and 20 % filling, increasing the lifter height increased the tangential velocity at the mill shell which was similar to the angular velocity of the mill. This trend was not consistent at all critical speed and filling levels. The lifter height influence on the tangential velocity at the shell was more pronounced for an increase from 1.5 mm to 3.0 mm lifter heights.

Increasing the critical speed increased the tangential velocity at the mill shell similar to the influence on the average charge velocity. This was seen at all filling levels and lifter heights. The influence of the critical speed was more pronounced for an increase from 55 % to 70 % critical speeds at 20 % filling and 1.5 mm lifter heights.

Increasing the filling at all critical speeds and for 1.5 mm lifter heights, increased the tangential velocity at the mill shell. The influence of the filling was not consistent at all operating conditions. Increasing the filling reduced the effect of increasing critical speeds and lifter heights on the tangential velocity at the mill shell. The critical speed had the strongest influence on the tangential velocity at the mill shell.

The change in the velocity profile between the shell and CoC location was assessed based on the movement of the CoC and the change in the tangential velocity along the diametric line

(distance L_2). As discussed in section 5.2.1, increasing the lifter height moved the CoC closer to the mill shell for lifter heights larger than 3.0 mm. This change increased the gradient of the profile along L_2 i.e. the profile became steeper as the tangential velocity decreased. This was not a consistent trend at all filling and critical speeds. The lifter height had the strongest effect for increases from 1.5 mm to 3.0 mm lifter heights at 20 % filling levels.

Increasing the filling, as discussed in section 5.2.1, moved the CoC closer to the mill centre in a radial direction as the bed thickness increased. This change increased distance L_2 along the diametric line, as discussed in section 5.3.4, which reduced the steepness of the profile as the tangential velocity decreased along the diametric line.

Since increasing the critical speed moved the CoC closer to the mill shell decreasing the bed thickness in a radial direction, as shown in section 5.2.1, the decreasing tangential velocity profile slope became steeper. The influence of the critical speed was less pronounced at higher filling levels as the filling had a stronger influence on the CoC location. The same was seen for the lifter height. The lifter height was also shown to have a stronger effect on the profile at higher critical speeds for increases from 1.5 mm to 3.0 mm.

The change in the profile between the CoC and charge free surface was assessed based on the change in the tangential velocity along the diametric line (distance L_1) including the change in the intersection of the diametric line with charge free surface. The lifter height had a similar effect on the intersection of the diametric line with the charge free surface as with the CoC i.e. the intersection point radially moved closer to the mill shell. The change was more pronounced for increases from 6.0 mm to 10.0 mm at high critical speeds and from 1.5 mm to 3.0 mm at low filling levels. The increased lifter heights increased the profile gradient i.e. the profile slope became steeper as the tangential velocity increased along the diametric line. This was not consistent at all filling and critical speed settings. The lifter height had a more pronounced effect on the profile for an increase from 1.5 mm to 3.0 mm at higher critical speeds. The opposite influence was seen at higher filling levels.

Increasing the filling decreased the profile slope as the diametric line and charge free surface intersection point moved radially further away from the equilibrium surface. This was due to a thicker cascading region corresponding to an increase in distance L_1 (section 5.3.4). Increasing the critical speed increased the profile gradient since the diametric line and charge free surface intersection point radially moved closer to the equilibrium surface. The influence of the critical speed on the tangential velocity profile was less pronounced at higher filling levels.

The influence of the operating conditions on the plateau region of the tangential velocity profile showed that increasing the lifter height did not have a consistent influence at all filling and

critical speed settings. The location of the plateau region moved further away from the mill centre and higher up along the diametric line, in the cataracting charge region, for every increase in the lifter height. The biggest change was seen for an increase from 1.5 mm to 3.0 mm lifter heights.

Increasing the filling did not consistently influence the maximum tangential velocity in the plateau region. At 10.0 mm lifter heights, the maximum tangential velocity increased with increasing filling. At 70 % and 85 % critical speeds, increasing the filling decreased the maximum tangential velocity. Increasing the critical speed increased the maximum tangential velocity in the plateau region similar to the effect on that at the mill shell. The plateau region moved further away from the mill centre for increases in the critical speed. The influence of the critical speed was found to decrease with increasing filling levels.

The continuous tangential velocity trends were used to determine the influence of the operating conditions on the slope of the profile in regions L_1 and L_2. Figures 58a, b and c below, illustrated the change in the tangential velocity profile at all filling levels for 55 %, 70 % and 85 % critical speeds respectively.

a)

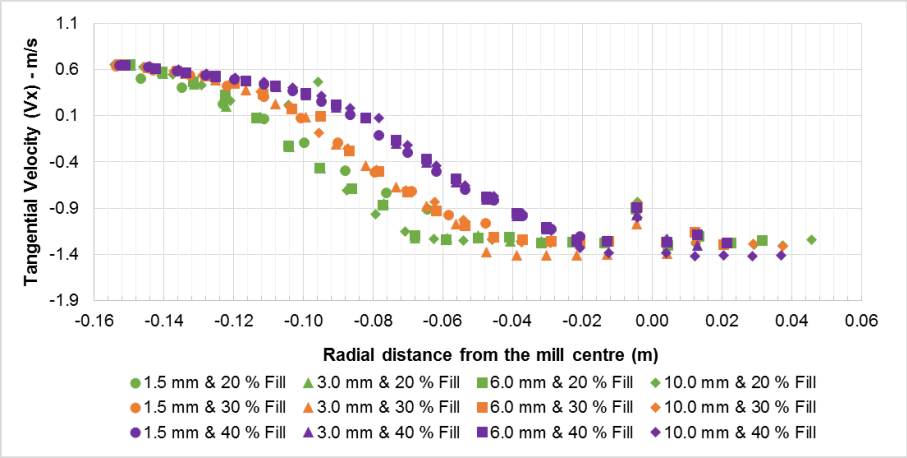

b)

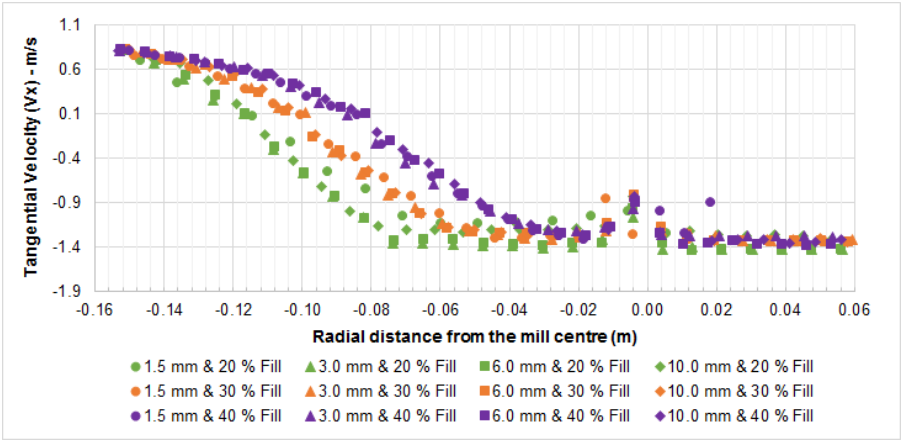

c)

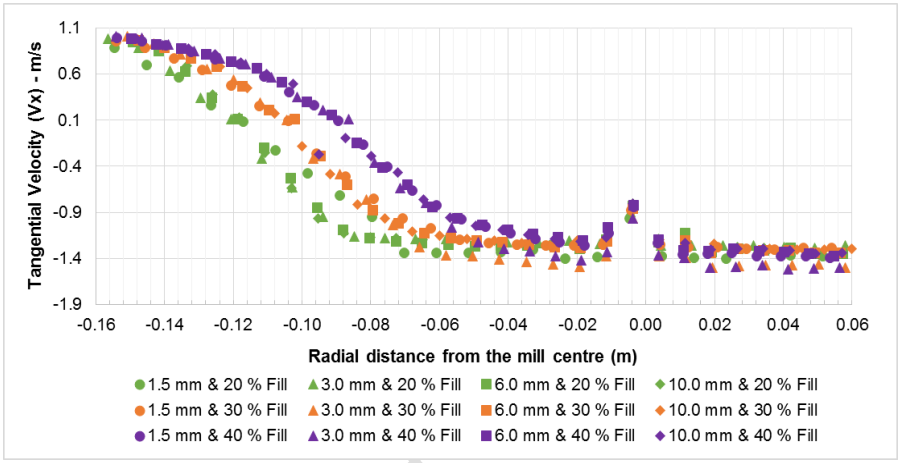

Figure 58: Velocity profile against the radial distance from the mill shell for all filling and lifter height settings at a) 55 %, b) 70 % and c) 85 % critical speeds.

Figures 58a, b and c above, show that at all lifter height settings, increasing the filling stretched the profile along the diametric line resulting in movement of the CoC, charge free surface and plateau region closer to the mill centre.

The change in the tangential velocity between the mill shell and CoC, decreased, becoming less steep with every increase in filling level. The tangential velocity increased in magnitude in the opposite direction between the CoC and charge free surface while the gradients increased in steepness. The cataracting and plateau regions of the profile moved higher up along the diametric line and became more negative with every increase in the mill filing level.

Increasing the critical speed resulted in an increase in the tangential velocity at the mill shell, between 0.6 m/s and 1.1 m/s. The profile between the shell and CoC became steeper, following a non-linear trend with every increase in the critical speed and at all filling levels. The profile followed a linear, decreasing trend between the CoC and charge free surface locations. The gradients increased in steepness with every increase in the critical speed.

5.5.2. Comparison between PEPT and EDEM results

The EDEM results were compared to the PEPT results reported in Brodner (2013) which was analysed based on 3 zones of the mill as seen in figure 59 below. The EDEM - PEPT comparison was based on zone 2 and that reported in literature as this is aligned to the location of the diametric line passing though the mill centre and CoC location.

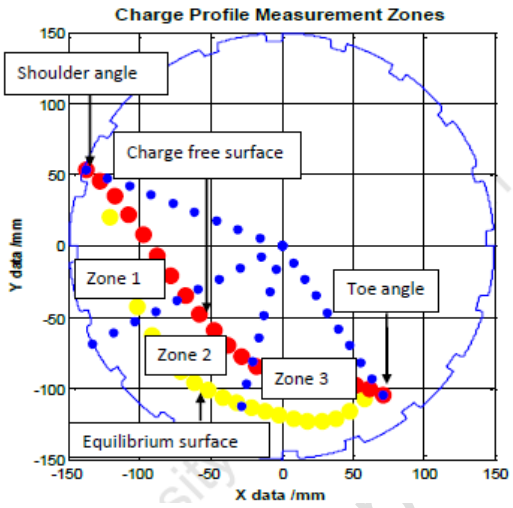

Figure 59: Velocity profile analysis zones used in Brodner (2013).

Figure 60 below shows the comparison between the PEPT results and the EDEM results for the velocity profile along the diametric line between the mill shell and the equilibrium surface.

Figure 60 shows the general shape of the profile is in agreement with that of PEPT as the tangential velocity decreases from the shell to the equilibrium surface (CoC). The velocity profile magnitudes are similar at key points like at the mill shell and at the CoC location along the equilibrium surface.

The influence of the lifter height on the velocity profile was not as distinct as that illustrated by the PEPT results specifically for the increases from 1.5 mm to 3.0 mm lifter heights. However, the figure shows that increasing the lifter height increases the slope steepness. These trends and changes are maintained for increasing the lifter heights at higher filling levels.

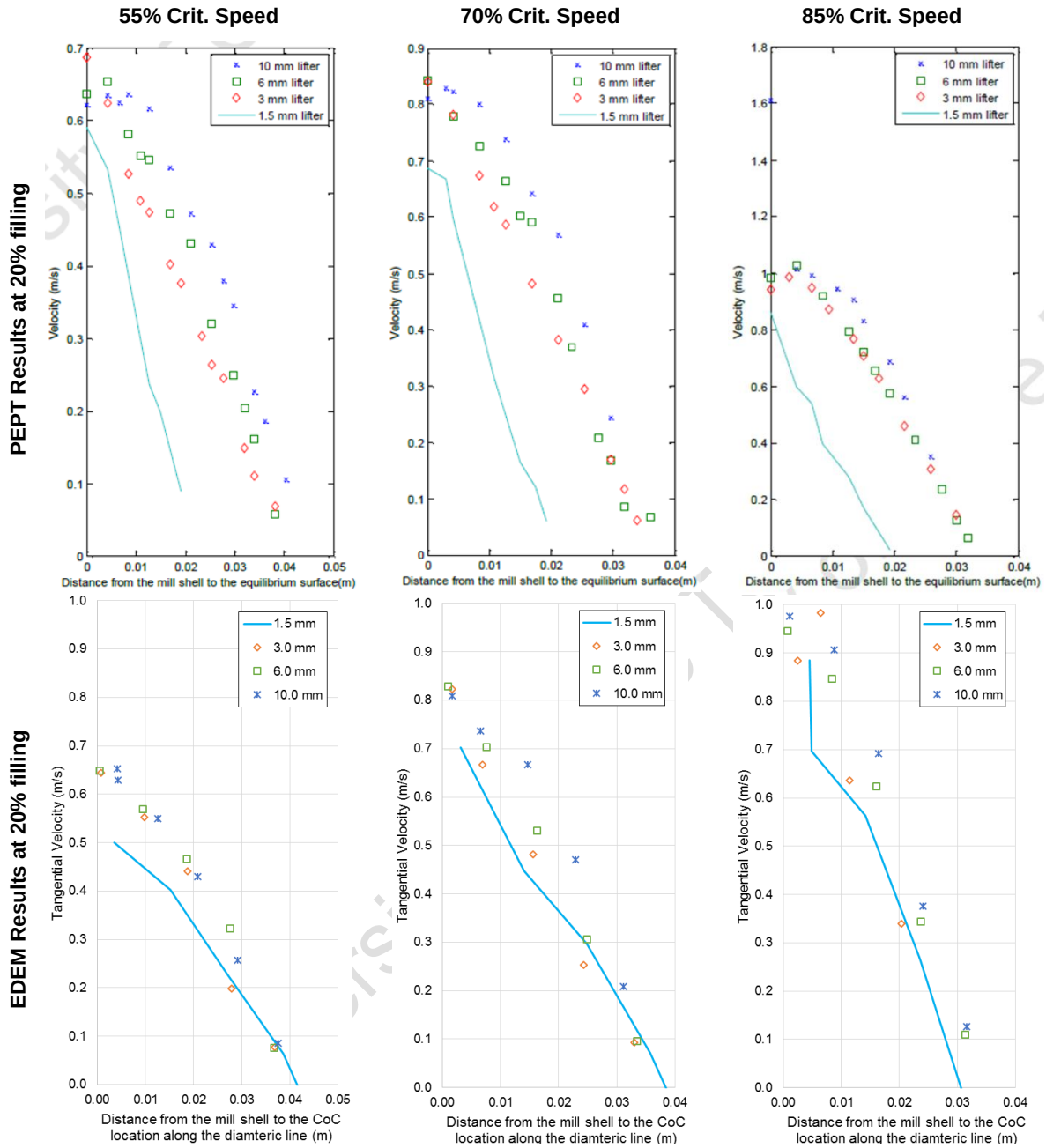

Figure 60: Comparison between PEPT and EDEM velocity profiles from the mill shell to equilibrium surface showing the influence of 55%, 70% and 85% crit. speeds at 20% fill and all lifter heights.

The influence of the critical speed on the profile based on the PEPT results was similar to that of the EDEM results i.e. the tangential velocity at the mill shell increased with the critical speed. Since the CoC location moved away from the mill shell at higher speeds, the slope of the profile increased in steepness with increasing critical speed similar to the PEPT results. The PEPT and EDEM results also showed a more distinct non-linear change in the tangential velocity at lower critical speeds.

The influence of the filling on the profile based on the PEPT results was similar to that of the EDEM results i.e. the tangential velocity at the mill shell remained the same. The CoC location

moved closer to the mill shell at higher filling levels resulting in a decrease in the steepness of the profile slope. The PEPT and EDEM results also showed a more distinct non-linear change in the tangential velocity at higher filling levels.

The velocity profile between the mill shell and charge free surface were analysed by fitting linear and non-linear trend-lines to the data. Table 23 below, lists the non-linear trend-line equations determined using MS Excel for a continuous profile from the shell to charge free surface. The linear equations fitted between the shell and charge free surface in tables 34 and 35 of Appendix G. The linear and non-linear trend-line relationships for the tangential velocity along L_1 and L_2 are summarized in tables 36 and 37 of Appendix G.

Table 23: Trend-line equations and R^2 correlations for the change in the tangential velocity along the diametric line between the mill shell and charge free surface.

	20 % Filling					
Lifter Height	**55 % Crit.**		**70 % Crit.**		**85 % Crit.**	
1.5 mm	y = -131.97 x2 - 47.425 x - 3.6044	R^2 = 0.9978	y = -76.802 x2 - 40.118 x - 3.5453	R^2 = 0.9949	y = -60.876 x2 - 39.383 x - 3.7251	R^2 = 0.9971
3.0 mm	y = -57.094 x2 - 34.965 x - 3.2476	R^2 = 0.9927	y = -118.49 x2 - 55.993 x - 4.9203	R^2 = 0.9953	y = -109.00 x2 - 58.483 x - 5.4223	R^2 = 0.9934
6.0 mm	y = -135.99 x2 - 53.392 x - 4.2481	R^2 = 0.9903	y = -147.73 x2 - 63.464 x - 5.3477	R^2 = 0.9956	y = -173.79 x2 - 76.245 x - 6.5094	R^2 = 0.9970
10.0 mm	y = -189.44 x2 - 66.996 x - 5.1216	R^2 = 0.9924	y = -274.98 x2 - 94.703 x - 7.1827	R^2 = 0.9931	y = -352.98 x2 - 124.24 x - 9.6490	R^2 = 0.9965
	30 % Filling					
Lifter Height	**55 % Crit.**		**70 % Crit.**		**85 % Crit.**	
1.5 mm	y = -154.25 x2 - 50.447 x - 3.4531	R^2 = 0.9942	y = -134.08 x2 - 49.119 x - 3.5488	R^2 = 0.9951	y = -57.065 x2 - 35.863 x - 3.1114	R^2 = 0.9870
3.0 mm	y = -156.44 x2 - 51.618 x - 3.5538	R^2 = 0.9944	y = -109.73 x2 - 46.459 x - 3.6025	R^2 = 0.9909	y = -110.27 x2 - 51.125 x - 4.1133	R^2 = 0.9906
6.0 mm	y = -151.71 x2 - 50.191 x - 3.4411	R^2 = 0.9926	y = -147.19 x2 - 54.113 x - 3.9426	R^2 = 0.9928	y = -95.148 x2 - 48.179 x - 3.9741	R^2 = 0.9865
10.0 mm	y = -140.42 x2 - 47.346 x - 3.2645	R^2 = 0.9899	y = -155.20 x2 - 55.661 x - 3.9809	R^2 = 0.9905	y = -46.119 x2 - 37.831 x - 3.4569	R^2 = 0.9728
	40 % Filling					
Lifter Height	**55 % Crit.**		**70 % Crit.**		**85 % Crit.**	
1.5 mm	y = -105.18 x2 - 34.450 x - 2.1381	R^2 = 0.9909	y = -114.15 x2 - 39.536 x - 2.5255	R^2 = 0.9913	y = -173.29 x2 - 56.686 x - 3.6185	R^2 = 0.9953
3.0 mm	y = -119.94 x2 - 37.236 x - 2.2447	R^2 = 0.9928	y = -116.17 x2 - 40.575 x - 2.6231	R^2 = 0.9883	y = -202.75 x2 - 64.678 x - 4.1306	R^2 = 0.9952
6.0 mm	y = -121.72 x2 - 37.272 x - 2.2147	R^2 = 0.9936	y = -140.99 x2 - 44.867 x - 2.7387	R^2 = 0.9942	y = -226.83 x2 - 69.213 x - 4.3139	R^2 = 0.9963
10.0 mm	y = -126.78 x2 - 38.106 x - 2.2162	R^2 = 0.9917	y = -130.37 x2 - 42.121 x - 2.5629	R^2 = 0.9925	y = -240.91 x2 - 72.363 x - 4.4690	R^2 = 0.9931

According to table 23 above, the R^2 values showed that the non-linear trend-line equations were a good fit to the continuous tangential velocity profile between the mill shell and charge free surface. The change in the profile along the diametric line could be described using a non-linear, second order polynomial. The lifter height and filling did not have a consistent influence on the non-linear trend-line equations at all critical speed settings. At 20 % filling, between 70 % and 85 % critical speeds as well as 40 % filling, between 55 % and 85 % critical speeds, all equation coefficients increased with the lifter height. The c-intercept increased with the lifter height at 20 % filling and all critical speeds.

The increase in filling caused the profile to move higher up (vertically) and stretch along the diametric line resulting in a higher tangential velocity magnitude at the mill shell. The most significant influence of the lifter height was an increase in slope steepness. The influence of the lifter height was clearer between the CoC and the charge free surface.

The influence of the critical speed showed the trend-line coefficients decreased in magnitude with increasing critical speed at 1.5 mm lifter heights for 20 % and 30 % filling levels. The opposite effect was seen for increasing the critical speeds at 6.0 mm and 10.0 mm lifter heights for all filling levels. The increase in the critical speed caused the CoC location to move closer to the shell (opposite to the effect of the lifter height and filling). The magnitude of the profile at the shell increased and the steepness of the change in the profile increased with increasing critical speed. The critical speed influenced the profile more significantly at higher critical speeds and at the charge free surface where the profile was more negative.

The negative trend-line equations showed the profile had a maximum negative velocity at the shell which decreased to a minimum at the CoC. The profile increased, becoming more negative between the CoC and charge free surface. Overall, the lifter height increased the slope steepness. The filling increased the magnitude at the mill shell and stretched the profile along the diametric line. The critical speed increased the magnitude at the mill shell and at the charge free surface which increased the steepness of the profile slope.

The predictive accuracy of the fitted equations were compared using figures 58a and b to assess how closely the models agree to that in literature. In addition, the predicted equations were used to determine if assuming a constant pressure gradient holds true for all conditions. Figures 61a and b below, compare the linear and non-linear trend-line predictions to the EDEM-extracted velocity profile along the diametric line between the shell and charge free surface at; a) 85 % critical speed, 20 % filling and 10.0 mm lifter heights, b) 55 % critical speed, 30 % filling and 10.0 mm lifter heights. The residual plots for linear and non-linear predictions in Figure 62a and b below correspond to the conditions in figures 61a and b below.

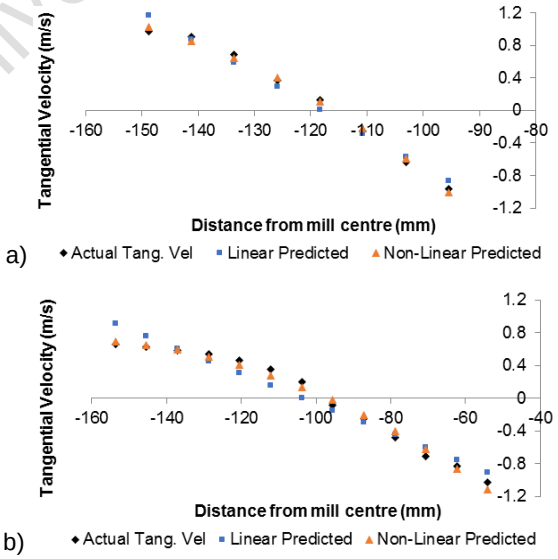

Figure 61: Linear and non-linear trend-line equations for a) 85 % crit. speed, 20 % filling, 10.0 mm lifter heights and b) 55 % crit. speed, 30 % filling, 10.0 mm lifter heights.

a)

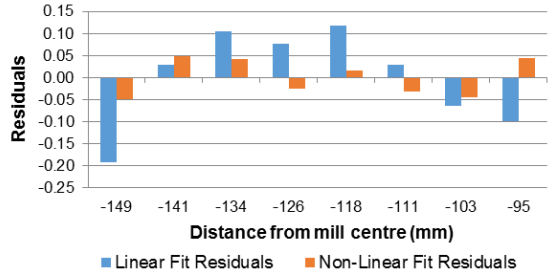

Standard Deviation (m/s)	
Linear	0.102
Non-linear	0.040

b)

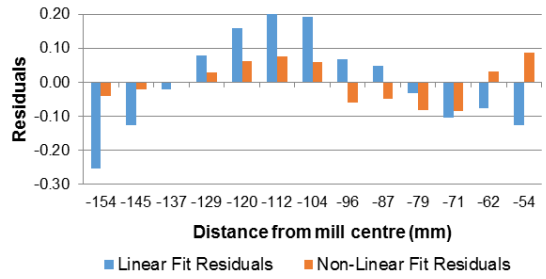

Standard Deviation (m/s)	
Linear	0.134
Non-linear	0.059

Figure 62: Linear and non-linear residual plots for a) 85 % crit. speed, 20 % filling, 10.0 mm lifter heights and b) 55 % crit. speed, 30 % filling, 10.0 mm lifter heights.

Figures 61 and 62 show the non-linear relation closely replicates the EDEM-extracted velocity profile between the mill shell and charge free surface similar to that reported in Brodner (2013), Govender et al. (2011), etc. The same results were seen along L_1 and L_2 separately.

The residual plots in figure 62 show the linear model deviation from the EDEM-generated velocity profile is greater at the mill shell, CoC location and charge free surface. The linear model standard deviation was found to be greater than the non-linear model at all critical speeds, filling levels and lifter heights as seen in figure 62 above. The linear profile over-estimated the velocity profile at the mill shell and charge free surface and underestimated the velocity profile at the CoC. The error between these profiles increased with the filling and critical speed at all operating conditions.

A regression analysis was done on the variables to determine the corresponding influence of the operating conditions. If a relationship can be determined between the change in variables and the operating conditions, these formulae can be used to determine the velocity profile on the basis of physical conditions of the mill i.e. lifter height, critical speed and mill filling.

The regression analysis was used to relate the operating conditions to the variables of the velocity profile equations listed in table 23 above. The results showed that the critical speed and lifter height were found to be driving factors. Table 24 below summarises the equations generated allowing for the velocity profile variables to be determined using the lifter height (mm) and change in critical speed (%). Table 24 includes the standard deviation and adjusted R^2 values at 20 %, 30 % and 40 % filling levels respectively. Figures 63i, ii and iii show residual plots for a, b and c respectively at all operating conditions.

Table 24: Regression results relating the fitted velocity profile equation variables (a, b and c) to the operating conditions.

Polynomial equation variables		Std Dev.	Adjust. R^2
20 % Filling	a = 67.328 - 151.793 Crit Speed - 22.147 LHt	38.49	0.7413
	b = 24.598 - 79.644 Crit Speed - 6.204 LHt	10.02	0.7960
	c = 2.228 - 7.561 Crit Speed - 0.417 LHt	0.67	0.8247
30 % Filling	a = - 294.7649 + 245.1817 Crit Speed + 0.3257 LHt	21.36	0.5896
	b = - 63.1948 + 22.17 Crit Speed - 0.095 LHt	4.95	0.0629
	c = - 3.0092 - 0.786 Crit Speed - 0.0119 LHt	0.28	-0.0768
40 % Filling	a = 84.6065 - 308.4667 Crit Speed - 3.9551 LHt	21.41	0.7267
	b = 23.5545 - 96.5633 Crit Speed - 0.7874 LHt	5.20	0.8092
	c = 1.6833 - 6.4319 Crit Speed - 0.03199 LHt	0.31	0.8406

(i)

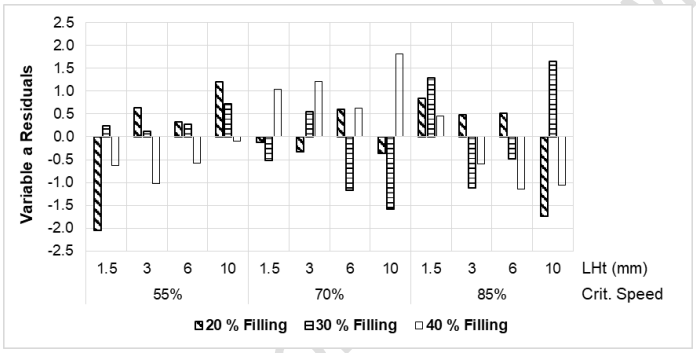

(ii)

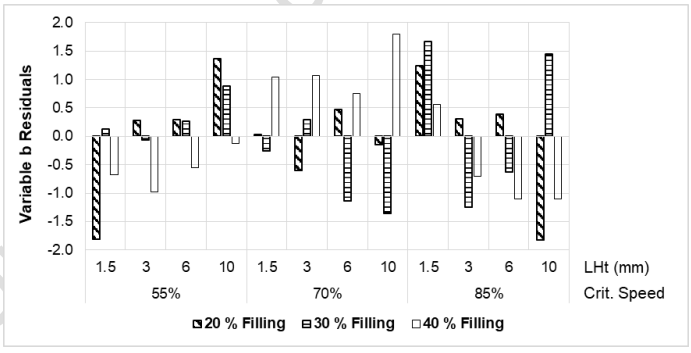

(iii)

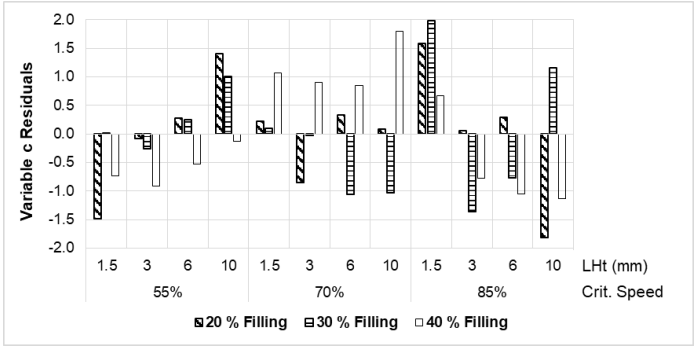

Figure 63: Residual plots relating the lifter height and critical speed to the fitted velocity profile equation variables; i) a, ii) b and iii) c at 20 %, 30 % and 40 % filling.

Table 24 above shows that the standard deviation for variable 'a' at all filling levels remains less than 30 % of the average variable a magnitude at all critical speed and lifter height settings. The standard deviation is highest at 20 % filling. There was no clear trend when investigating the effect of the filling on changes in the variable 'a' equations. The standard deviation determined for variable 'b' was less than 16 % of the average for each set of values at the respective filling levels. Similar to that of variable 'a', the variable 'b' standard deviation was highest at 20 % filing levels. The standard deviation for variable 'c' followed a similar trend and remained less than 16 % of the average.

The adjusted R^2 values listed in Table 24 above show that at 20 % and 40 % filling, the critical speed and lifter height can be used to calculate the velocity profile variables with reasonable accuracy as the R^2 values are greater than 0.72. The equations generated at 30 % filling do not provide an accurate formula to determine the velocity profile variables as all R^2 values are below 0.6. At 30 % filling, the adjusted R^2 values show that there is no relation between the variables and the critical speed and lifter height.

Figure 63i shows the residuals from the regression analysis for variable 'a' at all operating conditions. The greatest deviation between the actual variable 'a' magnitudes and the predicted data does not follow a clear trend for varying lifter height, filling and critical speed settings. The biggest deviation was recorded at 55 % critical speed, 1.5 mm lifter heights and 20 % filling.

Figure 63 (ii) and (iii) shows the residual plots for relating the critical speed and lifter height to variable 'b' and 'c' The residual distribution for variables 'b' and 'c' did not follow the any clear trends similar to that of variable 'a'. The biggest deviation was recorded at 85 % critical speed, 10.0 mm lifter heights and 20 % filling for variable 'b' while that of variable 'c' was recorded at 85 % critical speed, 1.5 mm lifter heights and 30 % filling.

5.5.3. Comparison between EDEM and model calculations

The EDEM-generated profiles were compared to the model developed by Brodner (2013) as seen in table 25 below. The pressure gradient was calculated for boundary conditions where; V_X = 0 m/s at the CoC location and V_X = vmill (angular velocity) at the mill shell. The tangential velocity at the mill shell was also compared to the model to determine the error.

Table 25: Velocity profile model boundary conditions at the mill shell and CoC for 70 % crit. speed, 30 % fill and 3.0 mm lifter heights.

	Pressure gradient	**Velocity model**	**EDEM result**
Mill shell	39.02 kPa	0.8292 m/s	0.7879 m/s
CoC location	32.47 kPa	0 m/s	0 m/s

The error between the EDEM profile and the model was 0.04 m/s. The difference between the pressure gradients at the boundary conditions showed a changing pressure gradient along the diametric line. The pressure gradient was calculated using equation 21 below.

$$\text{Pressure (Pa)} = \frac{\text{Total Force (N)}}{\text{Cross-sectional area (m}^2\text{)}} \therefore \frac{dP}{dx} = \frac{1}{A_x}\frac{dF}{dx} \quad (21)$$

Where F is the total charge force (N) applied over A_X, the cross-sectional area (m^2). F was extracted using EDEM. A_X was assumed to be the voxel area along the diametric line. The calculated pressure gradients were used to plot figure 64 below which shows the non-linear pressure gradient decreased from 40 kPa to 5 kPa between the shell and charge free surface.

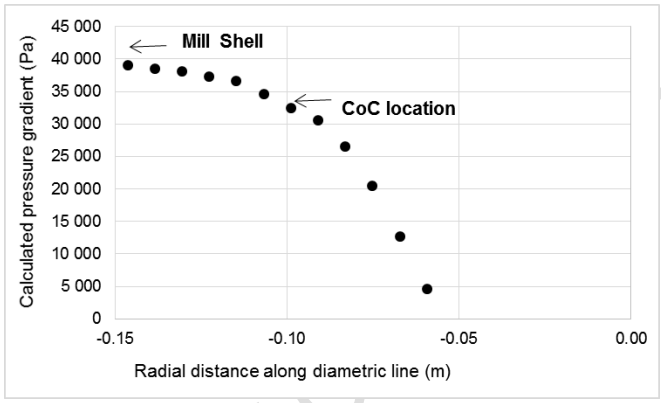

Figure 64: Pressure gradient calculated at 70 % crit. speed, 30 % fill and 3.0 mm lifter heights.

Figures 65a, b and c below, show the pressure gradient profile at all critical speeds.

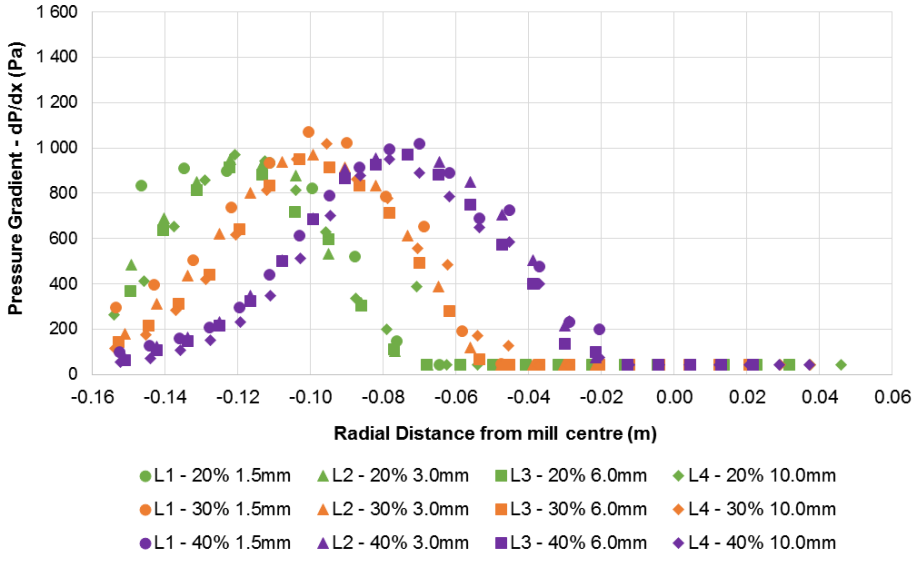

a)

b)

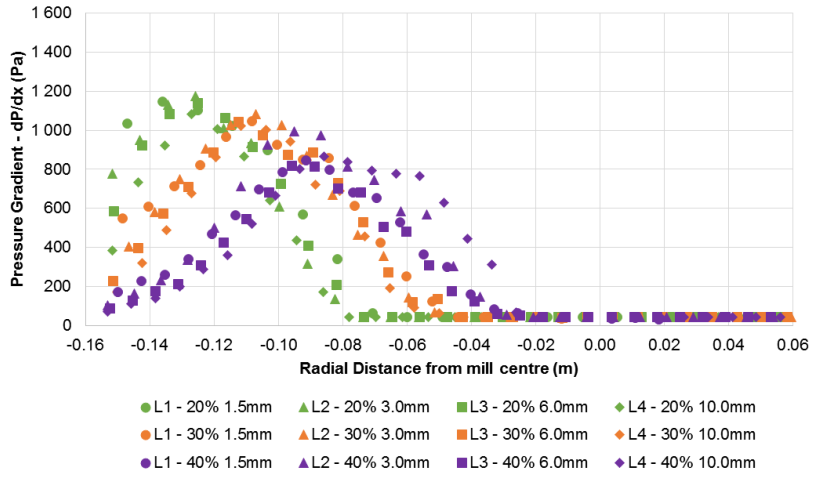

c)

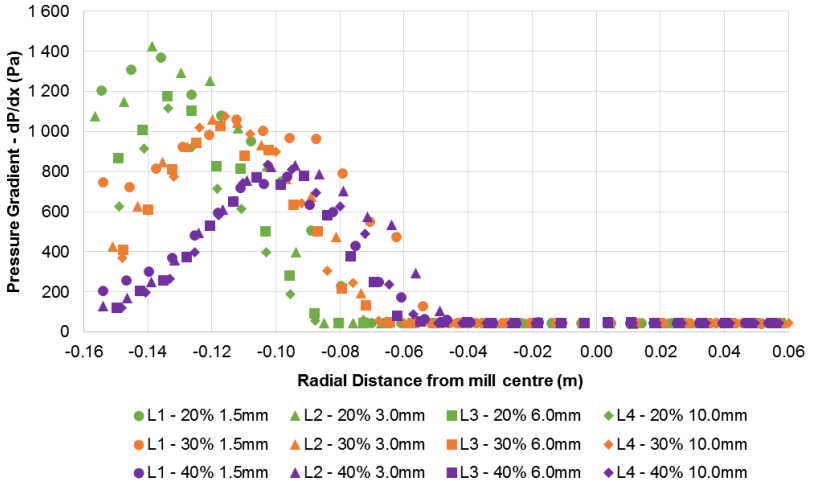

Figure 65: Change in the pressure gradient along the diametric line at all filling and lifter height settings for a) 55 %, b) 70 % and c) 85 % crit. speeds.

Figures 65a, b and c above, show the difference in the magnitude of the maximum pressure gradient at the different critical speeds i.e. 1 070 Pa, 1 200 Pa and 1 424 Pa at 55 %, 70 % and 85 % critical speeds respectively. The pressure gradient followed a non-linear trend along the diametric line i.e. increasing between the mill shell and CoC location, reaching a maximum at the CoC location and decreasing and following a plateau at the charge free surface boundary. The pressure gradient was not consistently influenced by changes in the lifter height at all filling and critical speed settings.

At 55 % critical speed, increasing the filling stretched the pressure gradient along the diametric line and changed L_1 and L_2 which decreased the slope steepness between the shell and CoC location. The maximum pressure and plateau pressure gradient was not influenced by the increase in filling levels. The change in the pressure gradient between the CoC and the charge free surface remained the same for all filling levels. The pressure gradient recorded at the mill shell decreased with every increase in the filing. The increased filling decreased the distance of the diametric line in the cataracting region.

At 70 % and 85 % critical speeds, similar to the trend seen at 55 % critical speed, increasing the filling stretched the pressure gradient along the diametric line i.e. the peak pressure gradient was recorded further along the diametric line, closer to the mill centre. The pressure gradient at the CoC and mill shell decreased with increasing the filling. The change in the pressure gradient between the shell and CoC was less steep at higher filling levels. The opposite was recorded between the CoC and charge free surface i.e. steeper slope at higher filling levels. The pressure gradient at the plateau remained constant at all filling levels and the increased filling decreased the distance of the diametric line in the cataracting region.

The maximum pressure gradient increased with increasing critical speeds at 20 % filling. The opposite was seen at 30 % and 40 % filling where the increased critical speed decreased the maximum pressure gradient at the CoC. The same trend was seen for changes in the pressure gradient at the mill shell. The change in the pressure gradient between the shell and CoC increased in steepness with increasing critical speeds. The change in the pressure gradient was similar between the CoC and charge free surface. The plateau region moved closer to the mill shell and remained constant with increasing critical speeds. Increasing the critical speed increased the diametric line length in the cataracting region.

Increasing the lifter height, at all filling levels, decreased the pressure gradient at the shell and increased the change in the pressure gradient between the shell and CoC. At the shell, the pressure gradient change decreased with increasing lifter heights at higher filling levels.

5.5.4. Influence of pressure gradient on the velocity profile

The pressure gradient was plotted against the tangential velocity for comparison to the model derived by Brodner (2013). Figure 112 in Appendix G illustrates the pressure gradient-velocity profile relationship. Figures 66 (a, b and c), 67 (a, b and c) and 68 (a, b and c) below, illustrate this relationship based on the lifter height influence at all critical speed and filling levels.

a)

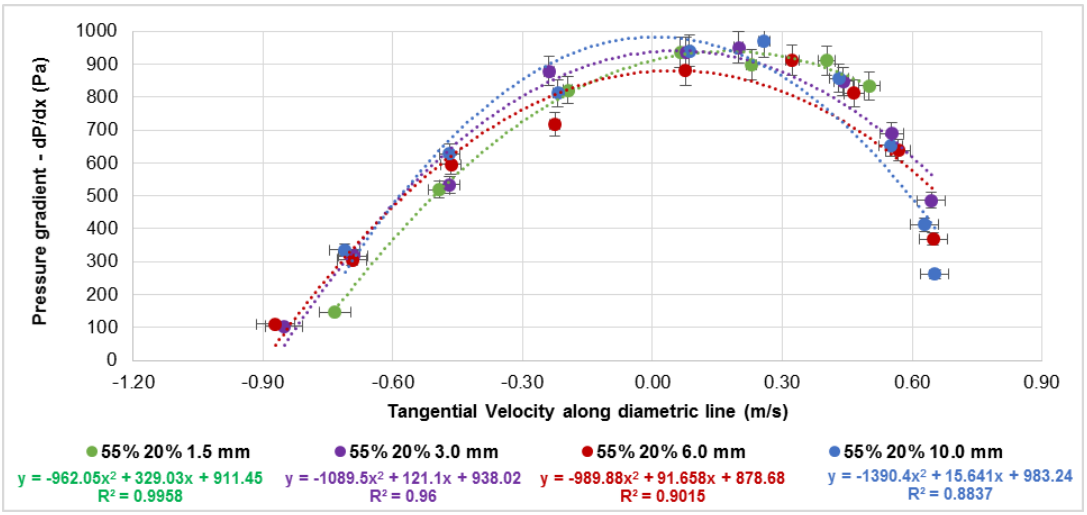

b)

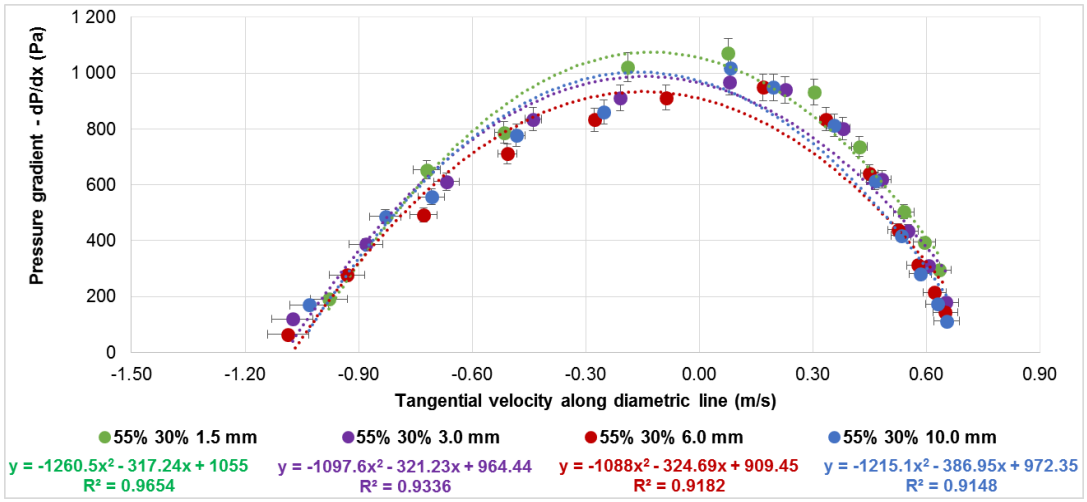

c)

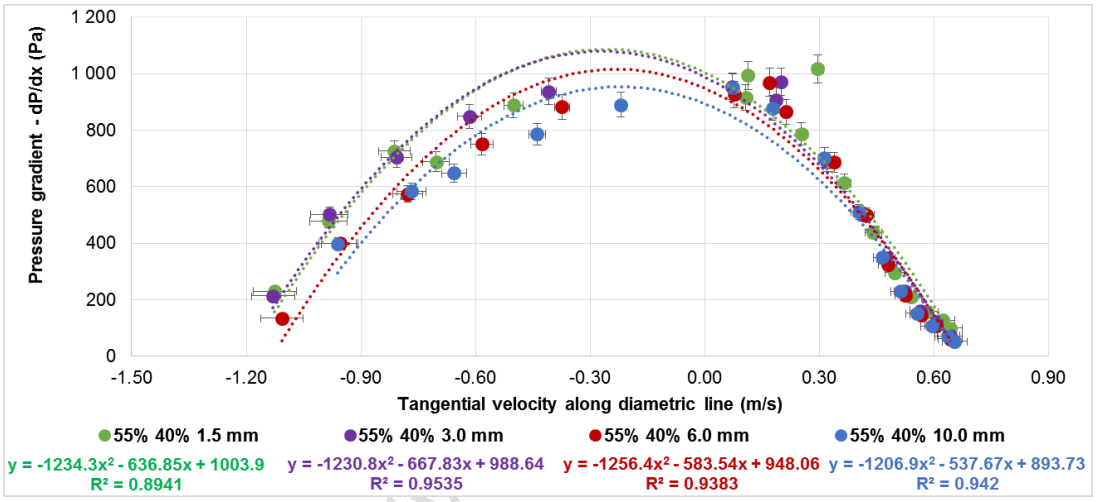

Figure 66: Calculated pressure gradient against the velocity profile for all lifter heights at 55 % crit. speed and a) 20 %, b) 30 % and c) 40 % filling levels.

a)

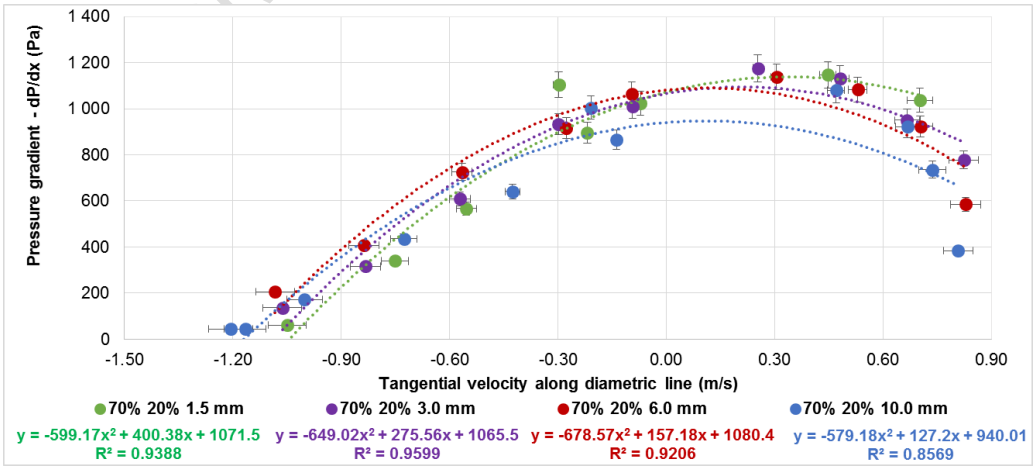

b)

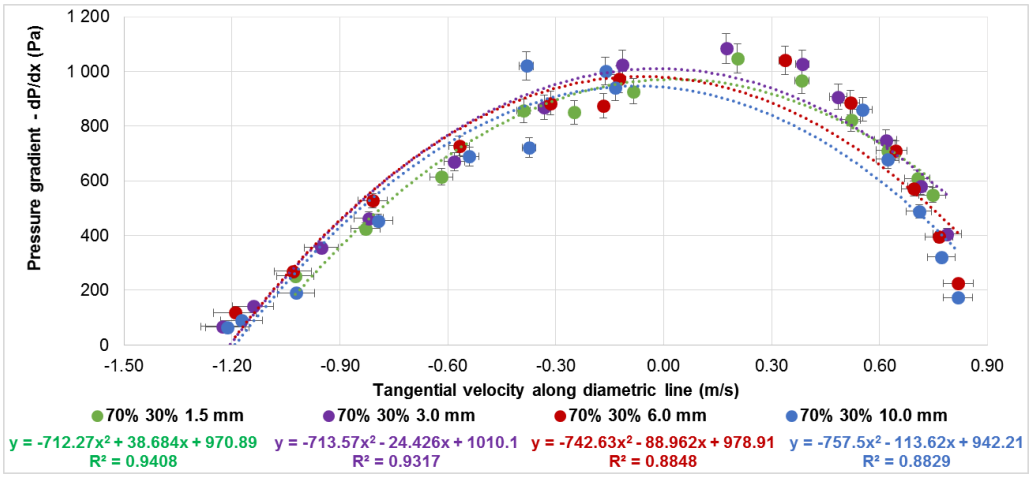

c)

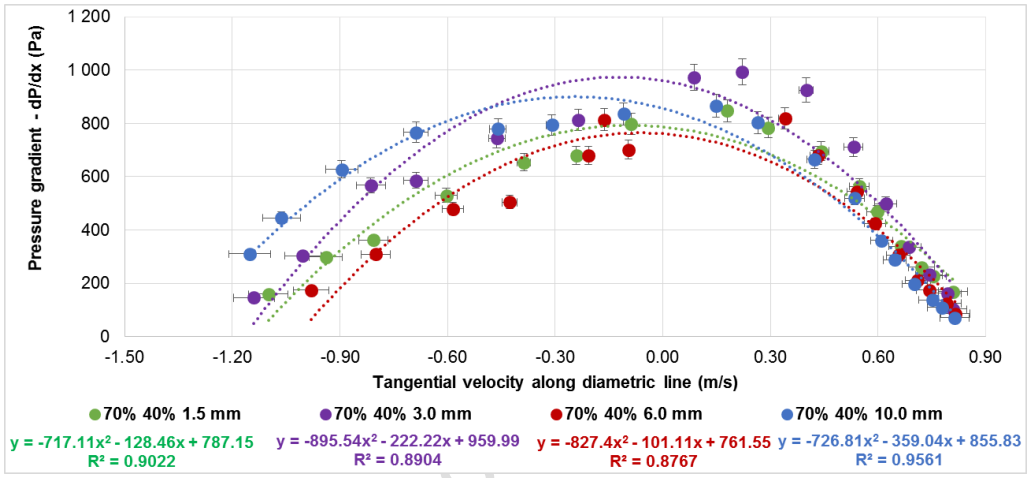

Figure 67: Calculated pressure gradient against the velocity profile for all lifter heights at 70 % crit. speed and a) 20 %, b) 30 % and c) 40 % filling levels.

a)

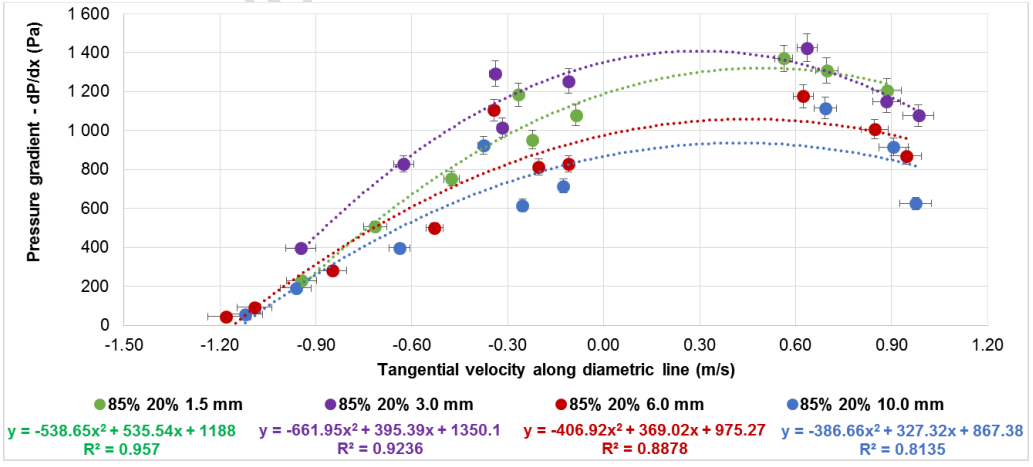

b)

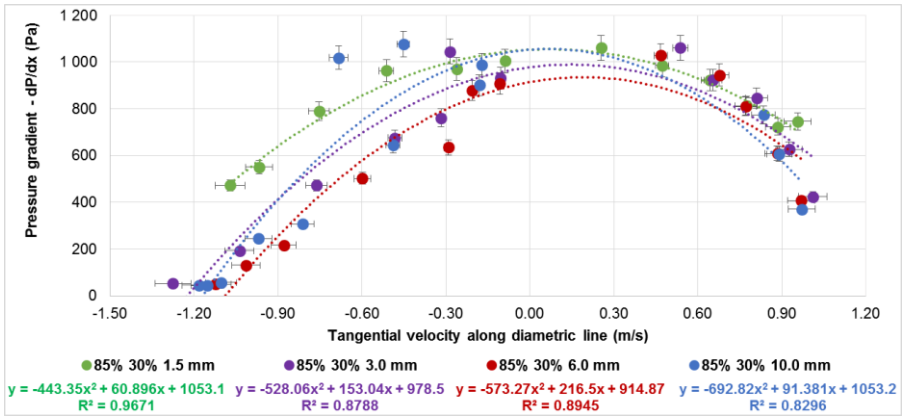

c)

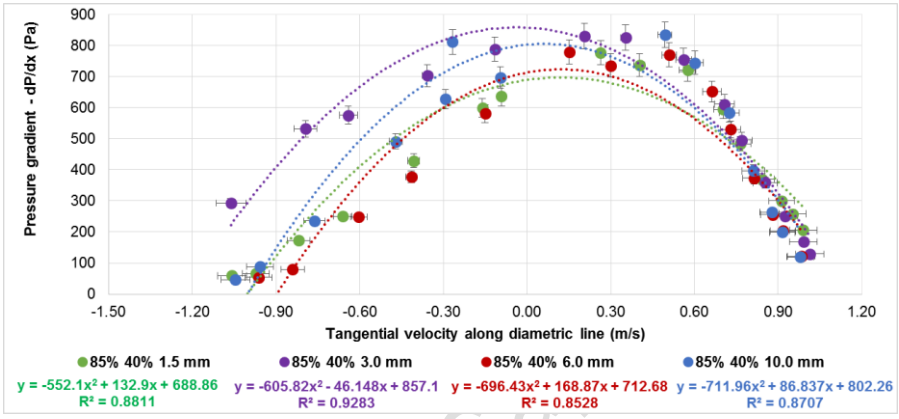

Figure 68: Calculated pressure gradient against the velocity profile for all lifter heights at 85 % crit. speed and a) 20 %, b) 30 % and c) 40 % filling levels.

Figures 66, 67 and 68 above, show that at all critical speed, filling and lifter height settings, the pressure gradient varied non-linearly with the calculated pressure gradient. The pressure gradient increased with a positive, decreasing tangential velocity from the mill shell to the CoC.

At the CoC, the maximum pressure gradient calculated where the velocity profile is zero decreased with every increase in the critical speed and filling. The pressure gradient decreased with a negative, increasing tangential velocity between the CoC and charge free surface. The R^2 values show that the relationship between the pressure gradient and tangential velocity followed a second degree polynomial trend.

At 55 %, 70 % and 85 % critical speeds, increasing the filling level decreased the pressure gradient at the mill shell and the maximum pressure gradient at the CoC. The change in the pressure gradient between the CoC and charge free surface increased with an increase in the filling levels i.e. steeper gradient.

At 55 % critical speed, the change in the filling influenced the coefficients of the trend-line equations i.e. the coefficients increased for 1.5 mm, 3.0 mm and 6.0 mm lifter heights. The opposite was seen for 10.0 mm lifter height. At 70 % and 85 % critical speed settings, the change in filling did not consistently influence the trend-line coefficients.

Increasing the critical speed stretched the graph resulting in a less pronounced influence of the tangential velocity on the pressure gradient. Similar to the influence of the filling on the pressure gradient-tangential velocity relationship, increasing the critical speed increased the pressure gradient at the mill shell and resulted in a less steep change in the pressure gradient between the CoC location and charge free surface. The influence of the critical speed on the trend-line equations was not consistent throughout.

A regression analysis of the relationship between the pressure gradient and the tangential velocity was completed. Figure 69a and b below shows the residuals for the 2nd order polynomial fit and the comparison between the predictive and actual data for 20 % filling and all lifter heights at 55 % and 85 % critical speeds respectively. The residual plots correspond to the non-linear equations shown in figure 66a and 68a respectively.

a)

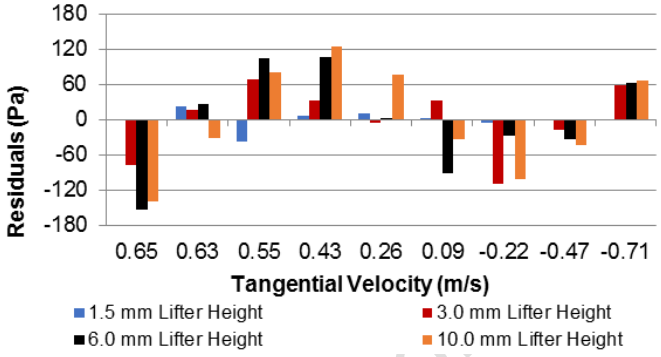

Standard deviation (Pa)	
1.5 mm	17.51
3.0 mm	56.30
6.0 mm	82.15
10.0 mm	85.24

b)

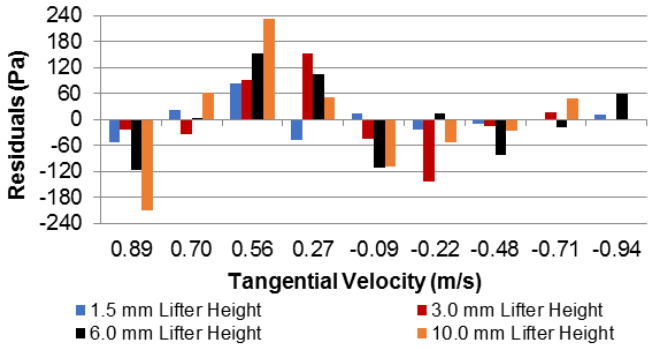

Standard deviation (Pa)	
1.5 mm	38.56
3.0 mm	83.40
6.0 mm	88.52
10.0 mm	123.66

Figure 69: 2nd order polynomial fit residual plot comparison for the differential pressure-tangential velocity graphs at 20% filling and all lifter heights for a) 55% and b) 85% critical speeds respectively.

The residual analysis showed that a linear fit did not satisfy the relationship between the differential pressure and tangential velocity between the mill shell and charge free surface. The residual plots in figure 62 above showed that the 2nd order polynomial plots in 66, 67 and 68 provided a closer fit.

The residuals show a deviation from the actual EDEM-data at the mill shell and in the cascading region, near the charge free surface. The predictive equation overestimated the pressure gradient at the mill shell. The peak dP/dx was underestimated although the position

of the peak pressure gradient coincided with that of the actual data. The standard deviation was found to increase with the lifter height which was also seen at all operating conditions.

Fitting a single or global 2nd order polynomial equation to all data i.e. removing the influence of the lifter height showed promise in that the R^2 was above 0.75. However, the predictive accuracy of the model decreased in that the standard deviation of the global model was higher than those seen for lifter height-specific fits.

The polynomial equations were further scrutinized by assessing the variables specific to that of a second order polynomial where $y = ax^2 + bx + c$. The changes in these variables were also assessed based on corresponding changes to the operating conditions. Based on the understanding of second order polynomial equations, figures 66, 67 and 68, can be used to determine the coordinates of the peak pressured gradient by equating the first derivative to zero and substituting that into the original equation. This can be compared the peak pressure gradient determined by equating x to 0 (y = c) i.e. maximum dP/dx. The intercepts of the equation can also be determined by equating y (pressure gradient) to zero.

The variables of the 2nd order polynomial equations (a, b and c) in figures 66, 67 and 68 were used to do a regression analysis. This was done to determine whether the critical speed, filling and lifter height settings are drivers. The regression results were used to indicate if the physical variables of the mill could be related to the equation used to calculate the differential pressure as a function of the velocity profile. Table 26 below summarises the equations generated which allow for the lifter height (mm) and change in critical speed (%) to be used to determine the variables in the equation calculating the differential pressure as a function of the velocity profile. Table 26 includes the standard deviation and adjusted R^2 values at 20 %, 30 % and 40 % filling levels respectively.

Table 26: Summary of the quadratic equation variables extracted from the 2nd order polynomial equations in figures 66, 67 and 68.

Polynomial equation variables		Std Dev.	Adjust. R^2
20 % Filling	a = - 2157.7163 + 2118.8917 Crit Speed - 9.5731 LHt	152.51	0.6895
	b = - 217.8817 + 898.0842 Crit Speed - 27.9439 LHt	57.42	0.8295
	c = 742.1883 - 498.8833 Crit Speed - 16.3436 LHt	98.98	0.2675
30 % Filling	a = - 2177.1505 + 2019.75 Crit Speed - 10.8092 LHt	85.10	0.8729
	b = - 1137.4379 + 1559.9392 Crit Speed - 7.6561 LHt	52.20	0.9164
	c = 947.0580 + 82.025 Crit Speed - 4.0762 LHt	45.46	-0.0781
40 % Filling	a = - 2153.6333 + 1871.575 Crit Speed - 6.8781 LHt	86.32	0.8494
	b = - 1829.4581 + 2284.5825 Crit Speed - 1.6977 LHt	83.45	0.9002
	c = 1261.8091 - 582.8333 Crit Speed - 0.9787 LHt	62.52	0.4700

Table 26 above shows that the standard deviation for variable ‘a’ at all filling levels remains less than 21 % of the average variable ‘a’ magnitude at all critical speed and lifter height settings. The standard deviation is highest at 20 % filling. There was no clear trend when investigating the effect of the filling on changes in the variable ‘a’ equations. The variable ‘b’ standard deviation was highest at 40 % filing levels. The standard deviation for variable ‘c’ followed a similar trend to that of variable ‘a’ and remained less than 10 % of the average.

The adjusted R^2 values listed in Table 26 above show that for variables ‘a’ and ‘b’, the equations comprising of the critical speed and lifter height provide an accurate representation of the variables. The regression results generated for variable ‘c’ do not provide an accurate representation as the R^2 value is less than 0.75. Figures 70i, ii and iii show the residual plots for variables a, b and c respectively at all operating conditions. These figures were used to determine the accuracy of using the critical speed and lifter height to determine the polynomial variables when calculating the differential pressure as a function of the velocity profile.

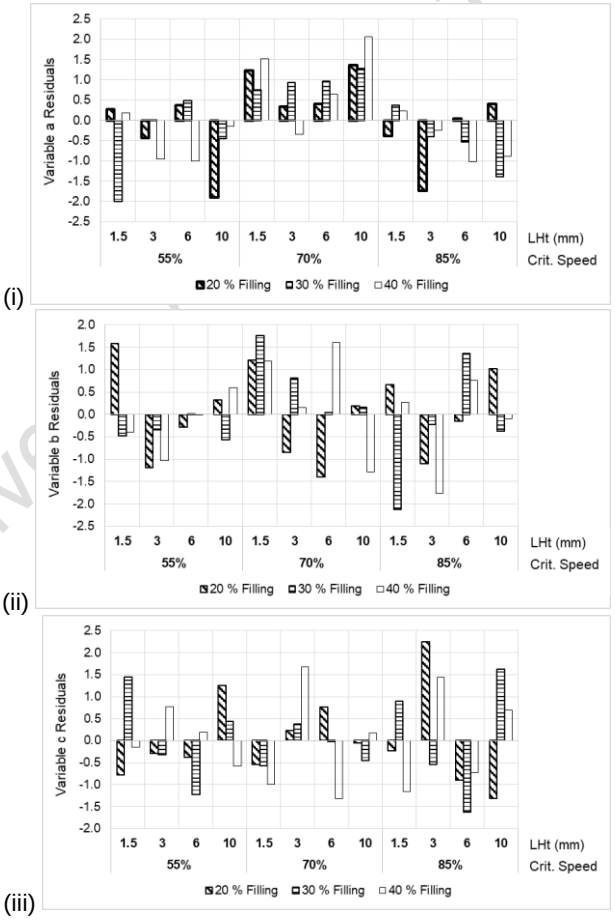

Figure 70: Residual plots relating the lifter height and critical speed to variables i) a, ii) b and iii) c at 20 %, 30 % and 40 % filling for the fitted differential pressure-velocity profile equation.

Figure 70 (i) shows the residuals from the regression analysis for variable ‘a’ at all operating conditions. The greatest deviation between the actual variable ‘a’ magnitudes and the

predicted data does not follow a clear trend for varying lifter height, filling and critical speed settings. The biggest deviation was recorded at 70 % critical speed, 10.0 mm lifter heights and 40 % filling. Figure 70 (ii) and (iii) shows the residual plots for relating the critical speed and lifter height to variable ‘b’ and ‘c’ The residual distribution for variables ‘b’ and ‘c’ did not follow any clear trends similar to that of variable ‘a’. The biggest deviation was recorded at 85 % critical speed, 1.5 mm lifter heights and 30 % filling for variable ‘b’ while that of variable ‘c’ was recorded at 85 % critical speed, 3.0 mm lifter heights and 20 % filling.

An additional regression analysis was done on variable a, b and c data sets to determine if the operating conditions can be used as predictive variables (see figure 71 below).

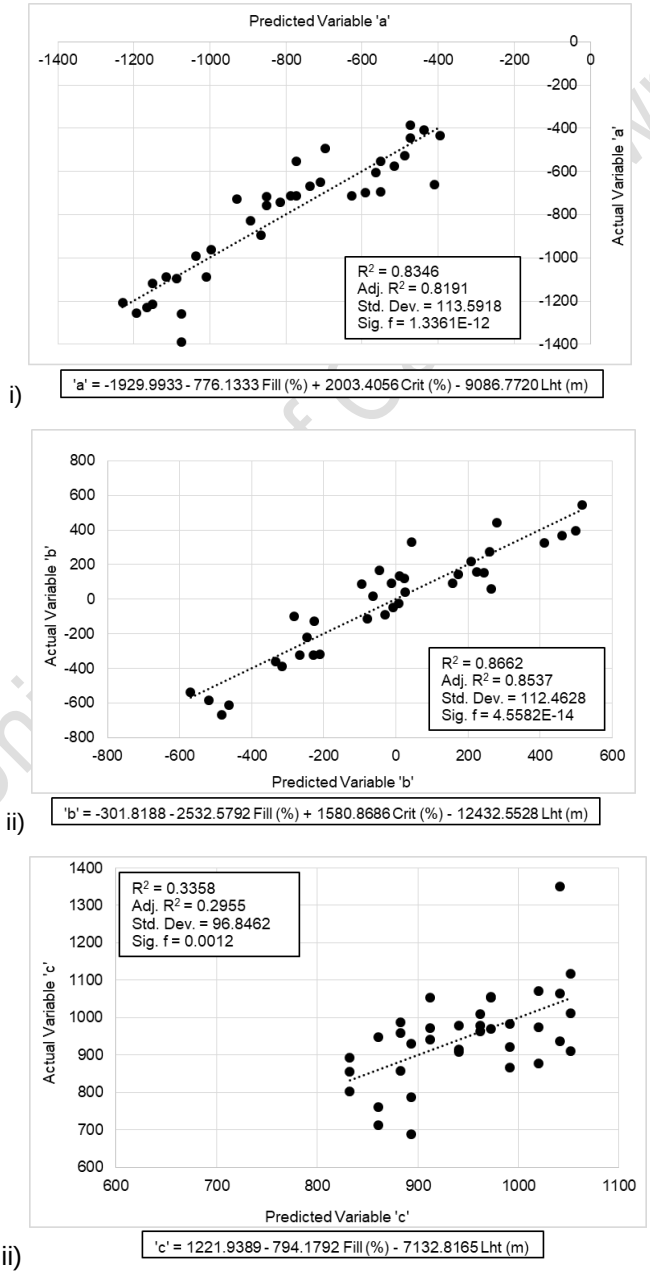

Figure 71: Regression analysis results for variables i) a, ii) b and iii) c at all operating conditions.

Figure 71 (i) and (ii) show that for variable a and b, the lifter height, filling and critical speeds can be used to accurately predict the first two variables of the relationship between the differential pressure and the velocity profile. Since the R^2 values are above 0.8 and significant f values are less than 0.0001 the operating conditions allow for an accurate prediction of the polynomial equation variables.

The regression results for variable c in figure 71 (iii) show that the operating conditions do not provide an accurate prediction of the actual variable c data. The R^2 values are below 0.5 even though the significant f value is well below 0.01. The p-values showed that the critical speed does not impact variable c since it was found to be 0.996. The distribution for this plot shows increased variations in the data spread and a few extreme outliers deviating from any relation that could have been extracted.

These equations allow for the completed equation to be determined using the physical characteristics of the mill at the relevant operating conditions. Furthermore, the varying pressure gradient can be related to the velocity profile at different operating conditions. The figure below illustrates the comparison between the lifter height specific velocity profile and the quadratic equation variable predictive model with that of the EDEM-extracted data. Each of the predictive plots incorporates the varying pressure gradient profile along the diametric line between the mill shell and charge free surface. The plot represents the distribution at 6.0 mm lifter heights, 30 % filling and 55 % critical speeds.

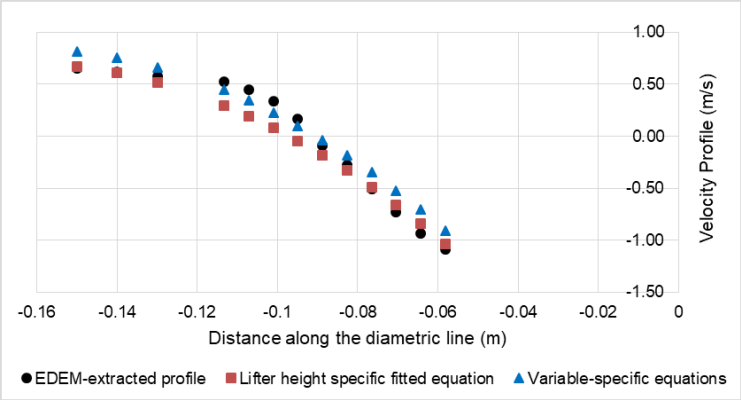

Figure 72: Predicted velocity profiles including varying pressure gradient compared to EDEM profile along the diametric line at 30 % filling, 55 % critical speeds and 6.0 mm lifter heights.

The comparison above shows that predicting the velocity profile using; a) table 23 specific to the lifter height setting and b) table 24 to predict the polynomial variables can provide an accurate model for predicting the velocity profile incorporating the varying pressure gradient in table 26. Using table 24 results in an overestimation at the shell and cascading region while the use of table 23 results in an overestimation in the rising en-masse region near the CoC.

6. Discussion

Chapter 6 has been structured such that the impact of the critical speed, filling and lifter height on the charge characteristics, power draw and charge velocity has been summarised at the start of each section so as to simplify the discussion throughout. Each section will draw on the explanations given in the previous chapter so as to build on the prior discussion points. This will supplement the understanding of the impact of the operating conditions on the charge motion, velocity profile and power draw.

6.1. Charge motion

The charge motion was assessed on the basis of the influence of the lifter height, filling and critical speed settings on the charge characteristics in the mill discussed in section 5.1 i.e. CoC, shoulder, toe as well as distances L_1 and L_2. The impact of the operating conditions on the CoC, shoulder and tow were based on the height above the mil lbase, horizontal distance from the mill centre and inclination angle. Distances L_1 and L_2 were assessed based on the charge motion and packing around the CoC.

6.1.1. CoC location

The effect of increasing the filling, increases the charge mass due to more particles in the mill. The increased number of particles influences the charge distribution in the mill as more particles are caught in the rising en-masse and equilibrium regions resulting in an increased bed thickness. The increased bed thickness restricts charge motion in the mill specifically particles moving out of the rising en-masse region which can be seen in the change in particle positions and average charge velocity distributions illustrated in Appendix D.2. These effects increase the packing in the equilibrium region around the CoC (‘zero velocity’ band). Thus, increasing the filling increases the bed thickness and packing around the CoC due to the reduced charge motion out of the rising en-masse region.

Based on the results generated the effects summarised above were seen in that, increasing the filling resulted in the CoC location moving radially closer to the mill centre which increased the steepness of the equilibrium surface inclination at the CoC. The effect of the filling on the CoC can also be seen in the average charge motion distributions which reveal that increased filling levels reduced the number of particles raised out of the charge bed by the lifter bars and into trajectories in the cataracting region. This results in the CoC location being higher up in the mill due to increased packing.

The effect of increasing the critical speed increased the angular velocity and charge velocity in the mill. Higher critical speeds affected the particle distribution in the various charge regimes as more particles were raised out of the charge bed aided by the motion of the lifter bars, into

the rising en-masse region and into the cascading and cataracting regions. These effects can be seen in the average charge velocity distributions in Appendix D.2. The increased particle motion resulted in a reduced level of packing around the CoC in the equilibrium region and thereby, a radially reduced the bed thickness. This caused the CoC location to move lower down radially and closer towards the mill base i.e. further away from the mill centre. The movement of the CoC resulted in a less steep inclination of the equilibrium surface at the CoC location.

Increasing the lifter height increased the number of particles caught between lifter bars, raised out of the rising en-masse region and into the cascading and cataracting regions. Higher lifter heights influenced the charge distribution around the CoC by moving the CoC radially higher up in the mill along a path almost parallel to the mill periphery. The radially higher CoC location increased the inclination angle of the equilibrium surface calculated at the CoC.

The influence of the lifter height on the movement and inclination of the CoC location was more significant at lower filling levels and higher critical speeds. The higher critical speeds increased the average charge velocity distribution in the mill which reduced the level of packing around the CoC. This allowed increased lifter heights to raise more particles out of the charge bed resulting in a radially higher CoC. Higher filling levels had the opposite effect in that the increased number of particles increased the bed thickness and packing around the CoC which restricted the ability of increased lifter heights to change the CoC location.

The comparison between the PEPT and EDEM data for the CoC inclinations showed that at lower critical speeds and filling, the results closely agreed. This was not seen at higher critical speeds and filling levels where the PEPT results overestimated the inclination angles. The PEPT and EDEM results followed a similar trend for increasing lifter heights and increasing filling levels.

A statistical analysis of the results showed a closer relation between the CoC inclination and the operating conditions. The CoC inclination, which is a key variable in the velocity profile model derived by Brodner (2013), can be predicted using the physical characteristics of the mill i.e. critical speed, filling and lifter heights. The regression analysis revealed that the inclination angle can accurately be predicted using the operating conditions of the mill.

6.1.2. Shoulder Location

Based on the impact that increased filling levels have on the charge motion and packing around the CoC as summarised in section 6.1.1 above, the higher CoC location due to increased packing raised the shoulder location radially higher up in the mill. Similar to the

effect of the filling on the CoC inclination, the higher shoulder locations corresponded to steeper shoulder inclination angles.

Similarly, based on the effect that higher critical speeds have on the charge motion and packing around the CoC, the increase in particles raised out of the charge bed caused the shoulder location to move radially higher up along the mill periphery. This motion was almost parallel to the mill periphery. The higher shoulder location increased its inclination angles above the mill centre. The influence of the lifter height on the charge motion and packing around the CoC showed that as more particles were raised out of the charge bed, the shoulder location moved radially higher up along the mill periphery. The higher shoulder locations increased the inclination angle of the shoulder.

Overall, increasing all operating conditions resulted in shoulder locations higher up in the mill along the mill periphery as well as steeper inclination angles. The filling and critical speed had a stronger influence on the movement of the shoulder than the lifter height. Increasing the filling and critical speed, increased the change in the shoulder such that the effect of the lifter height was less pronounced. The higher the filling and packing around the CoC, the less effective the lifter heights were to lift the charge radially higher along the mill periphery, out of the charge bed and into the cascading and cataracting regions.

The PEPT and EDEM results comparison showed inclination angles that were closely related even though, similar to that seen for the CoC inclination, the PEPT results over-estimated the shoulder inclinations wat all operating conditions. This could be due to the difficulty in extracting the shoulder location during experiments as well as relating the inclination of one particle to that of several thousand in the same region.

The regression analysis on the results showed that the lifter height, filling and critical speeds can be used to predict the shoulder inclination, similar to that of the CoC inclination. These findings can be incorporated into other predictive models as this simplifies having to run simulations to extract the shoulder location and thereby calculate the inclination angle. The operating conditions (physical characteristics of the mill) can accurately predict the shoulder inclination based on R^2 values above 0.85, standard deviations below 1% of the average shoulder inclination as well as P values below 0.01.

6.1.3. Toe Location

The effect of increasing the filling on the charge motion and packing, as discussed in section 6.1.1 above showed that increasing the filling raised the toe location higher up along the mill periphery on a path almost parallel to the mill periphery. The toe location moved away from the mill base and radially away from the mill centre. The higher toe location decreased the

steepness of the toe inclination i.e. decreasing the angle below the mill centre. The filling had the strongest influence on the toe at lower critical speeds and lifter heights due to the reduced charge motion around the CoC and the fewer particles raised out of the charge bed by the lifters into the cascading region.

Increasing the critical speed caused the toe location to move radially closer to the mill centre and further away from the mill shell. The higher toe location increased its inclination angle below the mill centre i.e. steeper inclination angle. The critical speed had the strongest influence on the toe and inclination angle at lower filling levels and higher lifter heights due the reduced packing around the CoC and more particles raised out of the charge bed into the cascading and cataracting regions.

Similar to the effect of higher critical speeds, increasing the lifter height moved the toe location radially closer to the mill centre and away from the mill shell. This increased the toe inclination angle. The influence of the lifter height on the toe was less pronounced at higher filling levels and lower critical speeds due to the increased packing and restricted charge motion around the CoC which limited the number of particles raised out of the charge bed and the number of trajectories. This brought the toe closer to the mill centre.

The PEPT and EDEM comparison on the toe inclination showed that the results were similar and followed similar trends when changing the critical speed, filling and lifter heights. The PEPT extracted data was lower in magnitude compared to that of the EDEM results at all operating conditions. The regression analysis on the toe inclination showed that the operating conditions can be used to accurately predict the inclination angles. The operating conditions (physical characteristics of the mill) can accurately predict the toe inclination based on R^2 values above 0.9, standard deviations below 1 % of average toe inclinations and P values below 0.0001.

6.1.4. Distances L_1 and L_2

Section 5.1.2 introduced distances L_1 and L_2 as part of the charge characteristics of interest for the current study. Distance L_1 was defined as the radial distance between the charge free surface and equilibrium surface along the diametric line. Distance L_2 was defined as the radial distance between the mill shell and equilibrium surface along the diametric line. Since both L_1 and L_2 have the equilibrium surface at the CoC in common, the changes in the CoC location relative to the charge free surface and mill base based on varying the operating conditions were considered.

As discussed in section 6.1.1, since increasing the filling moved the CoC location higher up in the mill and due to the increased packing around the CoC, distances L_1 and L_2 increased in

magnitude along the diametric line. The increased packing around the CoC and reduced charge motion at higher filling levels caused the filling to have a more pronounced effect on L_1 and L_2 at lower critical speeds and lower lifter heights as the reduced charge motion restricted reductions in distances L_1 and L_2.

In section 6.1.1, increasing the critical speed resulted in a reduced bed thickness and packing around the CoC as more particles were raised out of the charge bed. IN addition, the increased charge motion resulted in more particles moving into the cascading and cataracting regimes. This effect decreased distances L_1 and L_2. In contrast to the effect of the filling, the critical speed had a stronger influence on distances L_1 and L_2 at lower filling levels and higher lifter heights. Lower filling levels reduced the packing around the CoC while higher lifter heights increased the number of particles moving out of the charge bed, reducing the bed thickness.

As highlighted above, increasing the lifter heights allowed for more particles to move out of the charge bed via the rising en-masse region. The lifter height did not have similar effects on distances L_1 and L_2. Distance L_1 decreased as more particles were raised by the lifters from the charge bed into the cataracting region. The lifter height had a more pronounced influence on distances L_1 and L_2 at lower filling levels where the packing around the CoC was reduced and more particles were raised into the cataracting region. The influence of the lifter height was restricted at higher filling levels however, it was aided by increasing the critical speeds to the induced charge motion.

Overall, the filling had the strongest influence on L_1 and L_2 than that of the critical speed and lifter height as the change in these distances was more pronounced for increases in the filling than that of the critical speed and lifter heights. At higher filling levels and critical speeds, a higher lifter height is able to influence L_1 and L_2 in order to overcome the packing around the CoC.

The regression analysis showed that an equation could be derived using the filling, lifter height and critical speeds to predict distance L_2 which also forms a key variable in the equation derived by Brodner (2013). Based on R^2 values above 0.9, standard deviation less than 6 % of the average distance L_2 and the significant-f value being less than 0.001, L2 was related to physical conditions of the mill. Thus, in aligning the prediction to the physical properties of the mill, simulations do not have to be conducted in order to extract the charge free surface and CoC locations in order to determine distance L_2.

6.1.5. Summary of charge characteristic changes

The effects of increasing the filling on the bed thickness, packing around the CoC and reduced charge motion influenced the locations and inclinations of the CoC, shoulder and toe. The

error analysis on the position of the charge characteristics included calculating the standard error which was found to be negligible relative the change in the actual positions. The CoC location moved higher up along the mill periphery and radially closer to the mill centre which increased its inclination. The shoulder location moved higher up along the mill periphery resulting in a steeper inclination. The toe location moved radially away from the mill base and further away from the mill centre resulting in a less steep inclination. Based on the change in the CoC due to increased filling, distances L_1 and L_2 increased radially along the diametric line. Through regression analyses, the filling was found to be a key variable in predictive equations used to determine these charge characteristics.

Increasing the critical speed was shown to influence the charge motion in the mill since more particles moved out of the charge bed thereby reducing the bed thickness. Thus, the locations and inclinations of the CoC, shoulder and toe were influenced as well as distances L_1 and L_2. The CoC location moved lower down and radially further away from the mill centre which reduced the inclination. The shoulder was raised radially higher up along the mill periphery which increased the inclination. The toe location moved radially closer to the mill centre and further away from the mill shell which increased the inclination. Based on the change in the CoC due to the critical speed, distances L_1 and L_2 decreased along the diametric line due to the reduced packing and increased motion of charge out of the bed. Through regression, the critical speed was also found to be a key variable in predictive equations that can be used to determine these charge characteristics.

The lifter height was shown to increase the number of particles moving out of the rising en-masse region and into the cascading and cataracting region. These influences were complimented at higher critical speeds as an increase in charge motion was induced however, this was limited when increasing the filling levels. Thus, higher lifter heights moved the CoC radially higher up in the mill which increased the inclination angle. The shoulder was raised radially higher up along the mill periphery which increased the inclination angle. The toe location moved radially closer to the mill centre and away from the mill shell which increased the inclination angle. Distances L_1 and L_2 were not consistently influenced by the lifter height due to a restricted effect at higher filling levels which induced high packing levels around the CoC. The lifter height had a more pronounced influence at lower filling levels due to reduced packing around the CoC and more particles being raised into the cataracting region. Through regression, the lifter height was also found to be a key variable in predictive equations that can be used to determine these charge characteristics.

6.2. Power Draw

The power draw, as discussed in section 5.1.4, was assessed based on the power draw distributions in Appendix D.7 and the maximum power draw extracted at all operating conditions.

6.2.1. Power Draw Distribution

The power draw distribution plots showed that increasing the critical speed, filling and lifter heights resulted in 2 distinct regions in which the maximum power draw was recorded i.e. the rising en-masse and cascading regions due to the interactions caused by the charge motion. The power draw distributions were assessed on how the operating conditions influenced the colour intensity, span and number of bins in these regions.

Increasing the filling increased the colour intensity of the power draw in the cascading and rising en-masse regions due to the increased charge motion resulting from the charge interactions in these regions. As previously mentioned, increasing the filling changed the charge distribution as more particles were caught in the rising en-masse and equilibrium surface regions. This influenced the charge interactions in these regions based on cataracting charge impacts with the charge bed in the cascading region as well as impacts of the lifters raising the charge out of the charge bed in the rising en-masse region. These interactions and change in charge motion increased the power draw. The increased filling had a stronger influence on the power draw in the cascading region than the rising en-masse region due to the more dominant particle interactions and motion in the cascading region.

Increasing the critical speed increased the power draw in both rising en-masse and cascading regions. As previously discussed, increasing the critical speed increased the angular and average charge velocity in the mill. The higher critical speeds affected the distribution of the charge as more particles were raised out of the rising en-masse region and into the cascading and cataracting regions. This increased the cataracting charge impacts with the charge bed in the cascading region as well as impacts of the lifters raising the charge out of the charge bed in the rising en-masse region. These interactions and change in charge motion increased the power draw. At higher critical speeds, the colour intensity in the rising en-masse increased and that in the cascading region decreased due to the more dominant charge interactions in the former region. The increased critical speeds and angular velocity of the mill caused the particle interactions in the rising en-masse region to be more dominant than that in the cascading region resulting in higher power draw magnitudes.

Increasing the lifter height increased the power draw and colour intensity of the high power draw regions in the rising en-masse and cascading regions. Increasing the lifter height increased the number of particles caught between lifter bars, raised out of the rising en-masse

region and into the cascading and cataracting regions. This influenced the charge impacts in these regions as well as the charge motion which increased the power draw. The increased lifter heights influenced the particle motion in the rising en-masse region more than the cascading region resulting in higher power draw magnitudes in the rising en-masse region.

Increasing the critical speed, filling and lifter heights favoured the increased charge motion and impacts in the rising en-masse region which resulted in the maximum power drawn in this region. The increased charge caught between lifters raised influenced the particle impacts, the higher critical speeds increased the angular velocity of the mill which increased particle impacts between cataracting charge and the surface of the charge bed. The influence of the critical speed on the maximum power draw decreased with increasing filling and decreasing lifter heights as the increased charge mass reduced the ability of the critical speed to influence the charge motion and charge interactions leading to reduced power draw.

6.2.2. Summary of power draw changes

Increasing the filling, critical speed and lifter heights increased the power draw recorded in the rising en-masse and cascading regions in the mill. Increasing the filling caused the charge interactions in the cascading region to be more dominant than the rising en-masse resulting in higher power draw magnitudes. Increasing the lifter heights and critical speeds caused the charge interactions in the rising en-masse region to be more dominant than the cascading region resulting in higher power draw magnitudes.

The influence of the filling reduced the change in the power draw at higher lifter heights and critical speeds due to the increased charge interactions in the rising en-masse region caused by the increased angular velocity and charge raised out of the charge bed by the lifters.

The influence of the critical speed on the charge motion contributing to the power draw in the cascading region decreased at higher filling levels and lower lifter heights due to increased packing in the low velocity region around the CoC in the equilibrium surface and fewer particles raised out of the charge bed.

The influence of the lifter height on the interactions contributing to the power draw decreased at higher filling levels and lower critical speeds due to increased packing around the CoC and fewer interactions as a result of lower angular velocities and fewer particles raised out of the charge bed impacting surface charge in the cascading region.

The maximum power drawn was concentrated in the cascading region above the equilibrium surface and the rising en-masse region along the mill shell. The maximum power draw increased by increasing the filling, critical speed and lifter height settings but was higher for increases in the filling. The influence of the filling decreased with increasing lifter heights and

critical speeds and the influence of the lifter height increased with increasing critical speeds and decreasing filling levels.

Overall, the ability of the filling to increase the power draw in the cascading region decreased at higher lifter height and critical speed settings as the dominant charge motion shifted to the rising en-masse region. In contrast, the ability of the lifter height to increase the power draw in the rising en-masse region increased at higher critical speeds and lower filling levels due to the dominant lifting of charge as opposed to the cascading charge interactions. Similarly, the ability of the critical speed to increase the power draw in the rising en-masse region decreased at higher filling levels due to the increased packing restricting charge motion and interactions.

6.3. Charge Velocity

The charge velocity was assessed on the change in average charge velocity, particle velocity frequency and tangential velocity in the mill for changes in the operating conditions.

6.3.1. Average charge velocity

Increasing the filling increased the charge packing around the CoC which increased the charge caught in both the rising en-masse region and cascading region. The increased charge mass in the rising en-masse region increased the charge raised out of the charge bed and into the cascading region. This increased the associated charge velocities due to the angular velocity of the charge leaving the mill shell. The increased filling level decreased the number of particles in the cataracting region due to the increased packing around the CoC as previously discussed.

Increasing the critical speed increased the charge motion in the en-masse region assisted by the lifters raising the charge out of the charge bed which resulted in reduced packing around the CoC. The increase in particles raised out of the charge bed raised into the cataracting and cascading regions increased the associated charge velocity due to the influence of trajectory speeds and gravity. The decreased packing around the CoC due to increased critical speeds, increased the number of particles in the cataracting region resulting in higher charge velocities. This led to a decrease in the charge in the cascading region and the corresponding charge velocities.

Increasing the lifter height resulted in more particles caught between lifter bars which increased the charge motion out of the charge bed assisted by the critical speed of the mill. The more particles raised out of the charge bed, the more interactions in the cascading and cataracting regions which increased the charge velocity in these regions. The decreased packing around the CoC increased the number of particles in the cataracting region resulting in higher charge velocities.

Overall, the critical speed had the strongest influence on the average charge velocity than the filling and lifter height. The average velocity increased with increasing critical speeds and lifter heights but decreased with increasing filling. Increasing the filling resulted in increased packing around the CoC favouring the charge motion in the rising en-masse and cascading regions which reduced the average charge velocity. The charge velocity in the rising en-masse region increased with increasing critical speed and lifter heights due to increased charge motion as more particles were raised out of the charge bed and higher angular velocities.

6.3.2. Particle velocity frequency

Increasing the filling resulted in more charge distributed in all regions. The biggest change was in the low velocity regions where the increased charge increased the packing around the CoC. The increased filling decreased the maximum velocity achieved by particles in the cataracting region as fewer particles were lifted out of the charge bed and released at the angular velocity of the mill. At higher critical speeds, increasing the filling caused movement of particles from the cascading and cataracting regions into the low velocity regions (rising en-masse and equilibrium surface) which influenced the maximum velocity achieved by the highest number of particles in the mill.

Increasing the critical speed caused the movement of charge from low velocity to higher velocity regions resulting in a higher peak velocity achieved by the highest number of particles. This was due to the increased motion of particles, assisted by the raising particles out of the charge bed and into the cascading and cataracting regions by the lifters. The increased critical speed increased the charge motion which decreased the charge concentrated in the rising en-masse region and the level of packing around the CoC. The higher critical speeds increased the maximum velocity achieved by particles in the cataracting region due to particles released at higher angular velocities at the mill shell and lifter bar surfaces. At higher lifter height settings, increasing the critical speed resulted in an increase in charge raised into the cascading and cataracting regions and decreased packing around the CoC.

Increasing the lifter height resulted in an increase in charge caught between lifters raised out of the charge bed. The higher lifter heights increased the charge concentration in lower velocity ranges around the CoC, rising en-masse and cascading regions. The increased lifter height increased the maximum velocity achieved by particles in the cataracting region an increase in charge was lifted out of the charge bed and released at the angular velocity of the mill. The lowest charge velocity, around the CoC, increased with increasing lifter heights due to the increased charge motion caused by the higher lifters raising charge out of the charge bed and the reduced level of packing around the CoC.

Overall, the influence of the lifter height on the particle frequency decreased with increasing filling due to the increased packing around the CoC which resulted in more particles remaining in low velocity regions. Increasing the filling decreased the effect of the critical speed and lifter height on the charge in raising particles out of the rising en-masse region and into the cascading and cataracting regions. The increased lifter height and critical speed settings assisted in raising more charge out of the rising en-masse regions which also decreased the level of packing around the CoC.

6.3.3. Tangential charge velocity

The influence of the operating conditions on the tangential velocity was analysed and found to be similar to that seen for changes in the average charge velocity.

Increasing the filling increased the packing around the CoC which restricted the charge motion and movement of charge out of the charge bed and into the cataracting and cascading regions. The restricted charge motion above the CoC resulted in an increase in the charge in the rising en-masse region which was aided by lifters raising the charge along the mill periphery and increasing the tangential velocity. The reduced number of particles raised into the cascading and cataracting regions as well as the reduced average charge motion decreased the maximum tangential velocity achieved.

Increasing the critical speed caused the charge to move from the low velocity regions to the higher velocity regions resulting in more particles caught in the cascading and cataracting regions. This resulted in a higher maximum tangential velocity. The higher critical speeds increased the charge motion out of the charge bed and into the cascading and cataracting regions aided by the influence of the lifters on the charge. The tangential velocity in the rising en-masse region increased with increasing critical speeds due to the increased angular velocity of the mill and motion of particles raised out of the charge bed.

Increasing the lifter height increased the number of particles caught between lifters raised out of the charge bed which increased the tangential velocity in the rising en-masse region. This also reduced packing around the CoC and charge concentrated in the equilibrium surface. The increased lifter height increased the number of particles raised into the cascading and cataracting regions which increased the corresponding tangential velocity. At higher filling levels, the charge caught in the equilibrium surface increased regardless of the charge raised by the higher lifters i.e. increased filling levels opposed the influence of the lifter height on the charge and the tangential velocity. At higher critical speeds, increasing the lifter height aided the charge motion out of the charge bed and into the cascading and cataracting regions which increased the tangential velocity.

Overall, the increased filling affected the ability of the critical speed to influence the charge motion and that of the lifters to raise charge along the rising en-masse region and into the cascading and cataracting regions. Increasing the lifter height and critical speed had the same influence on the charge motion i.e. increased the charge motion out of the charge bed and into the cascading and cataracting regions. This increased the tangential velocity in the rising en-masse, cascading and cataracting regions.

6.3.4. Summary of charge velocity changes

The average charge velocity increased with increasing critical speeds and lifter heights but decreased with increasing filling levels. The increased filling restricted charge motion in rising en-masse and cascading regions due to increased packing around the CoC. The increased critical speeds and lifter heights increased charge motion due to higher angular velocities and resulted in more charge interactions due to the increased number of particles raised out of the charge bed to impact particles in the cascading region.

The particle velocity frequency was influenced more strongly by the filling as the increased filling resulted in more particles remaining in low velocity regions due to increased packing around the CoC. The increased lifter height and critical speed settings assisted in raising more charge out of the rising en-masse regions which also reduced the level of packing around the CoC and increased the charge in higher velocity regions i.e. cascading and rising en-masse.

The tangential velocity, similar to the average charge velocity, increased with increasing critical speed and lifter heights but decreased with increasing filling. The increased packing around the CoC caused by increased filling levels, reduced particle motion in the rising en-masse and cascading regions. The increased critical speed and lifter heights increased the charge motion and interactions in the rising en-masse due to the increased angular velocity and increased number of particles lifted out of the charge bed. The critical speed and lifter heights also increased the impacts in the cascading region due to the increased charge raised into the cataracting and cascading regions as well as the increased charge velocities.

6.4. Velocity profile along diametric line

The velocity profile, extracted using the EDEM, was assessed based on the influence of the critical speed, filling and lifter height on the tangential velocity extracted along the diametric line passing through the CoC and mill centre. Specific emphasis was placed on the influence of the lifter height. The profile was also compared to the model derived by Brodner (2013) using PEPT as validation.

6.4.1. Influence of the operating conditions on the velocity profile

The velocity profile analysis was based on how the operating conditions influence the tangential velocity extracted along the diametric line from the mill shell to the CoC, charge free surface and cataracting charge region as discussed in section 5.5. The angular velocity at the mill shell, CoC as well as distances L_1 and L_2 were used to describe these changes.

The change in the tangential velocity followed a non-linear relationship at all critical speed, filling and lifter height settings as the tangential velocity decreased from the angular velocity magnitude to zero at the shell and CoC respectively. A similar velocity profile trend was followed at all critical speed, filling and lifter height settings.

The velocity profile decreased from the mill shell, where the magnitude was similar to the angular velocity of the mill, through the rising en-masse region becoming zero at the CoC due to the increased packing and minimal charge movement. Since the charge flow direction in the rising en-masse region is opposite to that in the cascading region, the velocity profile changed direction, becoming negative after which it increased in magnitude from the CoC to the charge free surface boundary.

In the cataracting region, the velocity profile followed a plateau trend due to the increased space between particles falling under the influence of gravity and the chaotic motion of the charge in this region. The tangential velocity increased from the CoC to the charge free surface because of the increased charge motion in the cascading region where the charge packing is reduced. In addition, the impact of the cataracting charge with the cascading charge induces increased charge motion.

As discussed in section 6.1 above, the filling was found to influence the CoC location through increased packing in this region which restricted the charge motion in the rising en-masse and cascading regions. These effects also influenced distances L_1 and L_2 based on the number of particles raised out of the charge bed into the cascading and cataracting regions. The tangential velocity at the shell remained unchanged as it depends on the critical speed. Since the CoC moved higher up thereby increasing L_2 between the mill shell and CoC, the increased filling stretched the velocity profile along the diametric line. This effect decreased the gradient of the tangential velocity along the diametric line (less steep slope).

Between the CoC and charge free surface, the increased filling stretched the profile due to the increase in distance L_1 but the slope of the velocity profile remained unchanged. The decreased trajectory and number of particles raised into the cataracting region decreased the span of the velocity profile in this region. Overall, increasing the filling decreased the slope steepness of the profile and reduced the profile span.

As discussed in section 6.1, increasing the critical speed increased the angular velocity at the mill shell due to the increased charge motion relative to the motion of the mill. In addition, it caused the CoC to move lower down in the mill, further away from the mill centre due to the reduced packing around the CoC and increased charge motion. As a result, distances L_1 and L_2 decreased in magnitude. The velocity profile slope steepness increased due to a decreased distance L_2 i.e. the change in the decreasing tangential velocity increased from the angular velocity at the shell to zero at the CoC. Between the CoC and charge free surface, the decrease in L_1 resulted in a shorter span in the velocity profile and steeper slope.

The tangential velocity increased in the opposite direction due to the increased cascading motion of the charge under the influence of gravity. The increased trajectory and number of particles raised into the cataracting region increased the span of the corresponding velocity profile in the plateau region. Overall, increasing the critical speed increased the slope of the profile and stretched the profile further along the diametric line due to the charge distribution.

In section 6.1 above, it was shown that increasing the lifter height reduced the packing around the CoC due to the increase in charge motion. This moved the CoC higher up in the mill and closer to the mill shell. The lifter height had the strongest influence on the CoC and distance L_2 between 6.0 mm and 10.0 mm lifter heights where the lifter height was higher than the average charge particle diameter. Thus, more particles were lifted out of the charge bed. Between the mill shell and CoC, increasing the lifter height decreased the velocity profile slope as the change in the tangential velocity decreased along the diametric line.

Between the CoC and charge free surface, increasing the lifter height did not consistently influence the slope of the tangential velocity. The change in the tangential velocity along the diametric line remained linear at all lifter heights. The charge motion in the cascading region was influenced by lifter height increases based on the CoC and the decrease in L_1. The increased trajectory and number of particles raised into the cataracting region increased the span of the velocity profile higher up along the diametric line, in the plateau region. Overall, increasing the lifter height decreased the profile slope steepness and decrease the span of the profile along the diametric line.

Overall, increasing the filling decreased the velocity profile slope from the shell and CoC. The slope between the CoC and charge free surface remained unchanged for filling and lifter height increases. Increasing the critical speed increased the steepness of the velocity profile slope along L_1 and L_2. Increasing the lifter height decreased the velocity profile slope between the shell and CoC. The slope between the CoC and charge free surface was steeper than that between the shell and CoC due to the lifter height influencing the change in the tangential velocity in addition to the filling and critical speed.

6.4.2. Velocity profile mathematical relationship

The influence of the operating conditions on the velocity profile discussed above were further investigated using regression analyses of the results. Linear and non-linear trend-line equations were generated for the change in the tangential velocity along the diametric line between the mill shell and the charge free surface ($L_1 + L_2$). Due to the plateau trend of the profile in the cataracting region, this was excluded from the regression analysis. The trend-line coefficients, R^2 values and standard deviation between the linear and non-linear equations were used to analyse the results generated.

The trend-line equations generated for the change in the tangential velocity from the mill shell to charge free surface show that, compared to the extracted velocity profile, the non-linear trend-line equations had a stronger correlation with the EDEM data. The linear trend-lines deviated from the EDEM profile at the mill shell where the tangential velocity was overestimated even though this should be similar to the angular velocity at the mill shell. In addition, the tangential velocity after the CoC in cascading region was overestimated. The standard deviation for the linear trend-line fit was also found to be more than that of the non-linear fit when compared to the EDEM-extracted velocity profile.

The linear trend-line equations did not take into account the change in charge interactions and charge motion in the rising en-masse and cascading regions. At the mill shell, the charge motion was subject to the critical speed and lifter height influences which reduced the packing around the CoC. This decreased the change in the tangential velocity resulting in a non-linear relationship. In the cascading region, the charge motion was subject to cataracting particle impacts and the motion of particles raised by the lifter heights, rolling down the charge bed towards the toe. These influences increased the change in the tangential velocity resulting in a non-linear relationship.

The non-linear trend-line equations showed that, increasing the filling, increased the trend-line coefficients making them less negative which decreased the trend-line slope resulting in a decrease in the change in the tangential velocity along the diametric line. The decrease in the slope can be attributed to the increased packing around the CoC which restricted the charge motion in the rising en-masse and cascading regions.

Increasing the critical speed had the opposite effect on the trend-line equations. The increased critical speed decreased the equation coefficients, making them more negative which increased the trend-line slope and the change in the tangential velocity along the diametric line. The increase in the slope can be attributed to the decreased packing around the CoC due to the increased charge motion in the rising en-masse and cascading regions.

Increasing the lifter height did not consistently influence the velocity profile at the filling and critical speed settings. At lower filling levels, increasing the lifter height increased the slope which increased the change in the tangential velocity due to the increased charge motion and increased number of particles caught between lifters raised out of the charge bed. At higher filling levels, increasing the lifter height had the opposite effect on the trend-line equations i.e. the slope steepness decreased due to the increased packing and reduced charge motion as fewer particles were raised out of the charge bed by the lifters.

At lower critical speeds, increasing the lifter height decreased the trend-line slope due to the reduced charge motion in the rising en-masse and cascading regions even though more particles were caught between lifters and raised out of the charge bed. At higher critical speeds, increasing the lifter height had the opposite effect on the trend-line equations as the higher lifter heights increased the charge motion and change in the tangential velocity.

Since the non-linear trend-line fit was found to be a more accurate fit to that of the EDEM data, a regression analysis was done to determine if the operating conditions could be used to determine the variables of the non-linear equations. This would allow the determination of the velocity profile equations at all operating condition using the physical properties of the mill.

The results showed that the critical speed and lifter height can be used to calculate the velocity profile equation variables according to the y = ax2 + bx +c equation. These equations can be determined at all filling levels. When removing the effect of the lifter height, the R2 value decreased to less than 0.75 while the standard deviation for the model fit was higher than that of a lifter height-specific fit. This shows that the lifter height should be incorporated and plays a role in influencing the velocity profile.

6.4.3. EDEM results compared to predictive velocity profile model

The velocity profiles generated using the EDEM results were compared to the model developed by Brodner (2013) as a means of validation as well as supplementation to the understanding of how lifter heights influence the velocity profile.

The results showed that the trend followed by the EDEM-extracted profile along the diametric line was similar to the trend followed by the PEPT-extracted data. However, when comparing the two data sets it was clear that, when looking at the boundary conditions (at the mill shell and at the CoC), the model did not agree with the EDEM results on the basis of a changing pressure gradient along the diametric line. The pressure gradient which was assumed to be constant throughout by Brodner (2013) was found to vary along the diametric line between L_1 and L_2. In addition, when investigating the change in the calculated pressure gradient, it

followed a non-linear trend along the diametric line at all operating conditions as shown in section 5.5.2.

The pressure gradient at the mill shell was non-zero at all operating conditions due to the friction between the particles and the mill shell/lifters. This was caused by the influence of the rotating mill on the charge motion and the influence of the lifter heights raising particles out of the charge bed in the rising en-masse region. The pressure gradient increased from the mill shell and reached a maximum at the CoC where the charge velocity is zero and increased packing around the CoC. The increased packing was due to restricted charge motion resulting in increased charge forces acting on the charge.

The pressure gradient decreased from the CoC to the charge free surface due to the decreased packing, increased charge motion in the cascading region and increased charge impacts due to cataracting particles impacting the charge bed. In the cataracting region, the pressure gradient followed a plateau trend due to the chaotic behaviour of the charge as well as the reduced interactions and minimal charge packing. The charge forces in the cataracting region were reduced due to the charge motion dominated by the influence of gravity.

In order to assess how the pressure gradient changed along the diametric line, it was analysed based on changes in the critical speed, filling and lifter height. At the mill shell, the pressure gradient was larger than zero due to the influence of the rotating mill shell motion which was due to the influence of the critical speed and angular velocity on the motion of the charge. The influence of the lifter height on the charge motion in the rising en-masse region also influenced the non-zero pressure gradient at the mill shell.

The pressure gradient at the mill shell increased with increasing critical speed due to the increased angular velocity and charge motion which increased the associated charge forces. Increasing the filling decreased the pressure gradient at the mill shell due to increased packing around the CoC which restricted the charge motion and charge interactions in the rising en-masse region. Similarly, increasing the lifter height decreased the pressure gradient at the shell due to increased charge interactions in the rising en-masse region due to the charge lifted out of the charge bed. Since the angular velocity at the mill shell remained the same for increases in the lifter height, the corresponding charge forces decreased.

At the CoC, the maximum pressure gradient was affected by how the amount of packing influenced the charge motion around the CoC. The maximum pressure gradient increased with the filling due to the increased level of packing and corresponding charge forces. The pressure gradient at the CoC was not consistently influenced by the critical speed and lifter heights.

At low filling levels and all lifter height settings, increasing the critical speed increased the peak pressure gradient at the CoC due to reduced packing around the CoC caused by the increased charge motion and associated charge forces in the rising en-masse and cascading regions. At higher filling levels, the peak pressure gradient decreased with increasing critical speed due to increased packing around the CoC which restricted the charge motion in the rising en-masse and cascading regions.

The pressure gradient between the mill shell and CoC, along L_2, increased following a non-linear trend due to the change in the charge motion in the rising en-masse region. The increasing pressure gradient was due to the increase in the packing closer to the CoC where the motion of particles was restricted and the charge velocity was a minimum. The non-linear trend followed was due to; the influence of the lifters raising the charge caught between the lifter bars, the influence of the critical speed on the angular velocity of the mill and thereby the motion of charge closer to the mill shell.

Increasing the filling decreased the slope steepness of the pressure gradient which decreased the change in the pressure gradient. Higher filling levels increased the packing around the CoC which restricted the charge motion in the rising en-masse region resulting in lower tangential velocities and lower contact forces. At the CoC, the restricted charge motion decreased the contact forces and since L_2 increased with increasing filling, the change in the pressure gradient decreased resulting in less steep slopes.

The influence of the lifter height on the change in pressure gradient followed a similar trend to that of the filling. The increased lifter height increased the number of particles raised along the rising en-masse region which reduced the contact forces at the mill shell and the packing around the CoC. This resulted in reduced contact forces at the shell. Since increasing the lifter height increased L_2, the difference between the pressure gradient magnitude at the shell and at the CoC increased resulting in a less steep slope.

Increasing the critical speed had the opposite effect on the change in the pressure gradient to that seen for the filling and lifter height. Higher critical speeds increased the angular velocity of the mill which increased the charge velocities closer to the mill shell and the contact forces. This resulted in an increased pressure gradient. At the CoC, the increased critical speed decreased the packing around the CoC which increased the corresponding contact forces and since L_2 decreased with increasing critical speed, the change in the pressure gradient increased resulting in steeper slopes.

The pressure gradient between the CoC and charge free surface (L_1) decreased following a non-linear trend due to the change in the charge motion in the cascading region. The decreasing slope was due to a decrease in packing closer to the charge free surface as a

result of particles raised out of the charge bed by the lifter bars and increased impacts from the cataracting charge. The non-linear trend was due to the influence of the operating conditions on L_1 which changed the difference between the maximum pressure gradient magnitude at the CoC and that in the plateau region.

Increasing the filling increased the packing around the CoC which decreased the charge in the rising en-masse and cascading regions resulting in a reduced distance L_1. The increased packing around the CoC decreased the charge motion resulting in lower contact forces which decreased the difference between the pressure gradient magnitudes at the CoC and plateau region i.e. less steep slopes.

Increasing the critical speed had the opposite effect on the pressure gradient profile along L_1 than that of the filling. Higher critical speeds increased the charge motion in the cascading region which decreased the packing of charge concentrated around the CoC resulting in both higher contact forces and pressure gradients. The difference between the pressure gradient at the CoC and charge free surface increased and since L_1 increased with the critical speed, the change in the pressure gradient increased (steeper slopes).

The lifter height did not consistently influence L_1 and the maximum pressure gradient at the CoC i.e. a clear trend could not be identified. At low filling levels and critical speeds, increasing the lifter height increased the difference between the pressure gradient at the CoC and the plateau region resulting in a steeper gradient.

The steeper gradient was due to increased charge motion in the cascading region aided by an increase in the charge raised out of the charge bed by the lifter bars which increased the corresponding contact forces. At higher critical speeds, the increased charge motion increased the slope steepness with increasing lifter heights. The opposite was seen for increasing the lifter height at higher filling levels due to the increased packing which decreased the charge motion and contact forces.

Overall, the change in the pressure gradient along the diametric line and specific underlying trend resembled the shear strain-stress distributions reported in Jang & Khonsari (2005) typical to granular media in a rotating mill as seen in figure 73 below. Hudson & Harrison (1997) also reported similar trends for the stress-strain profile which resembled the pressure gradient extracted using the EDEM results along the diametric line. Maicke & Majdalani (2009) reported on a similar trend for the radial (axial) pressure drop.

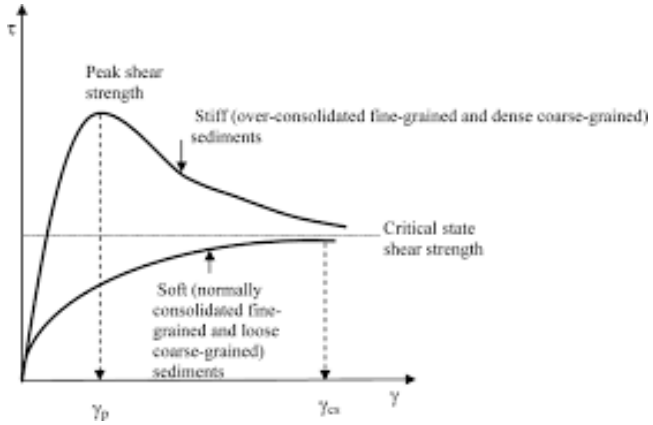

Figure 73: Stress-strain profile for granular media in a mill (Jan & Khonsari, 2005)

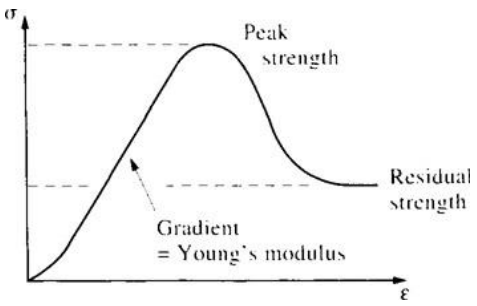

Figure 74: The stress-strain profile in uniaxial compression (Hudson & Harrison, 1997).

Figures 73 and 74 above, show that the shear stress increased reaching a peak corresponding to the maximum volume fraction in the mill (Bird, Stewart & Lightfoot, 2002; Jang & Khonsari, 2005, Hudson & Harrison, 1997). Jang & Khonsari (2005) reported that the peak shear stress corresponded to the location of maximum pressure. The pressure distribution decreased from the peak as the volume fraction decreased and porosity increased before reaching a plateau or residual shear stress (Jang & Khonsari, 2005). Jang & Khonsari (2005) reported that the parabolic-type relation seen above, was similar to the pressure distribution in the mill. According to Campbell (2006), slower granular flows typical to lower mill speeds and higher filling levels, have larger shear strains which restrict the charge motion in the mill.

Jonson et al. (2011) reported that the axial pressure distribution in a mill with lifters recorded a non-zero pressure gradient at the mill shell due to the pressure build-up caused by the collection of charge between and around the lifter bars. The increase in charge mass around the lifters increased the shear stresses leading to higher pressures around the lifter bar and mill shell (Jang & Khonsari, 2005). McDonough (2004) reported that tangential forces arise as a result of shear stresses acting on a particle which is brought about by changes in the tangential velocity and relative motion of layers close to the particle. Pressure arises from collisions of molecules with each other or with the walls of a container (McDonough, 2004).

The pressure drop along the diametric line was also estimated by Shi and Napier-Munn (1999) and Tupper et al. (2013) where; the pressure drop was related to the density, gravitational acceleration and head pressure by the former while the latter related the pressure drop to the porosity, density, gravitational acceleration, head pressure and length of the mill. However, none of the methods could satisfy the model developed by Brodner (2013).

Overall, as a grinding mill rotates, pressure is applied to the bulk charge which must be balanced by the contact forces acting on individual particles (Campbell, 2006). These contact forces and the corresponding energy transferred during particle collisions result in a pressure generation which is necessary to maintain and drive the charge flow in the mill (Jang & Khonsari, 2005). Jang & Khonsari (2005) reported that velocity gradients along the profile depend on the pressure gradient since the pressure gradient is dependent on the total force which in turn, depends on the particle acceleration and mass. Thus, the pressure gradient cannot be assumed to be constant along the diametric line.

The results generated for the pressure gradient show that the pressure gradient remains non-zero along the diametric line similar to the stress-strain relations shown in figures 73 and 74 above. This is also in agreement with that reported in Jonson et al. (2011). The pressure gradient trends were also shown to be influenced by the lifter height, filling and critical speeds.

6.4.4. Relationship between the pressure gradient and velocity profile

The relationship between the velocity profile and pressure gradient was investigated using charge characteristics like the CoC and charge free surface locations as well as the trend-line equations generated at all operating conditions which was discussed in section 6.4.3 above. The aim for this was to determine how to incorporate the varying differential pressure gradient into the velocity profile.

At all operating conditions the relationship between the velocity profile and pressure gradient followed a non-linear trend increasing from a non-zero magnitude at the mill shell and reaching a maximum at the CoC where the tangential velocity is zero. The increased packing closer to the CoC restricted the charge motion in this region. The trend followed decreased from the CoC to the charge free surface boundary due to the increased charge motion in the cascading region induced by the charge raised out of the charge bed and the charge from the cataracting region impacting the charge bed.

The influence of the operating conditions on the relationship between the pressure gradient and the velocity profile was used to determine underlying drivers that can be used as predictive variables which link dP/Dx – velocity profile relationship to physical properties of the mill.

Increasing the filling increased the slope steepness at all lifter heights and critical speeds due to the increased difference between the pressure gradients at the shell and CoC. The tangential velocity at the shell and CoC remained constant. The increased filling increased the packing around the CoC which restricted the charge motion in the rising en-masse region resulting in lower pressure gradients at the shell and an increased difference between the pressure gradient at the shell and CoC. The opposite was seen between the CoC and charge

free surface due to the increased charge motion and decreased packing in the cascading region. The increase in the slope steepness decreased the area under the curve between the shell and CoC while the opposite was seen between the CoC and charge free surface i.e. area under the curve increased.

Increasing the critical speed decreased the slope steepness at all lifter height and filling levels due to the decreased difference between the pressure gradients at the shell and CoC and increase in the tangential velocity at the mill shell. The decreased pressure gradients were caused by the increased charge motion in the rising en-masse region and less packing around the CoC while the higher tangential velocity at the shell was influenced by the increased angular velocity. The same was seen between the CoC and charge free surface due to the increased charge motion and decreased packing in the cascading region. The decrease in the slope steepness increased the area under the curve between the shell and CoC while the opposite was seen between the CoC and charge free surface i.e. area under the curve decreased.

The influence of the lifter height on the relationship between the pressure gradient and velocity profile was not consistent at all critical speed and filling levels. The area under the graph was also not consistently influenced by the lifter height. In order to further investigate the effect of the lifter height at different filling and critical speed levels, a polynomial equation fit was done at each lifter height setting. This resulted in 36 equations each with an R^2 value above 0.8. The residual plots for these polynomial fits showed an overestimated pressure gradient-velocity profile relation at the mill shell and an underestimation at the CoC i.e. peak dP/dx. In addition, the standard deviation increased with the lifter height at all operating conditions.

The use of these equations dictates that EDEM simulations have to be conducted every time in order to extract the data points along the diametric line and thereby fit an equation which is not practical. Furthermore, the use of these equations is specific to the lifter heights at which the equations are generated. Removing the effects of lifter heights by finding a global predictive equation proved promising in that R^2 values remained above 0.75 however, the standard deviation of the residuals increased, higher than those at the individual lifter heights meaning the predictive accuracy decreases.

As such, in order to simplify the prediction of the differential pressure-velocity profile relationship, an additional regression analysis was done on the variables of the fitted polynomial equation (a, b and c) to link the change in these magnitudes to the varying operating conditions. The results show that for variables a and b, the lifter height, filling and critical speeds can be used to accurately predict the first two variables of the relationship between the differential pressure and the velocity profile. Since the R^2 values are above 0.8

and significant-f values are less than 0.0001 the operating conditions allow for an accurate prediction of the polynomial equation variables. The same result was not achieved for variable c due to R^2 values lower than 0.5 even though the significant f value is well below 0.01. The p-values showed that the critical speed does not impact variable c since it was found to be well above 0.5 at 0.996. The residual distribution for predicting variable c however, shows increased variations in the data spread and a few extreme outliers deviating from any relation that could have been extracted.

Overall, these equations allow for the completed differential pressure-velocity profile equation to be determined using the physical characteristics of the mill at the relevant operating conditions. Furthermore, the varying pressure gradient can be related to the velocity profile at different operating conditions as shown in figure 73.

6.4.5. Summary of velocity profile changes

The velocity profile followed a non-linear trend along the diametric line at all operating conditions. The influence of the operating conditions on the profile was based on changes in charge characteristics like L_1, L_2, tangential velocity at the mill shell as well as the slope along L_1 and L_2. The trend-line fit to the profile data revealed a second order polynomial relationship for the change in the profile along the diametric line at all operating conditions. This result was in agreement with that reported in previous literature as shown in chapter 5.

The filling influenced the velocity profile by increasing the packing around the CoC which restricted the charge motion in the rising en-masse and cascading regions resulting in less steep slopes due to increased distances L_1 and L_2. Increasing the critical speed increased the angular velocity and thereby the charge motion in the rising en-masse and cascading regions resulting in steeper slopes and decreased distances L_1 and L_2. Increasing the lifter height increased the number of particles caught between the lifter bars and raised out of the charge bed which decreased the packing around the CoC. Increased lifter heights influenced the charge motion and interactions in the rising en-masse region which increased L_2, decreased L_1 and decreased profile slope steepness.

The extracted EDEM data did not agree with the model developed by Brodner (2013) due to the change in the pressure gradient along the diametric line which was found to follow a non-linear trend as opposed to it remaining constant along the diametric line. The change in the pressure gradient increased from the mill shell, reached a maximum at the CoC and decreased along L_1 before reaching a plateau in the cataracting region. This trend was consistent at all operating conditions and was shown to resemble the stress-strain profile reported in section 6.4.3 above.

The pressure gradient magnitude at the mill shell increased with the critical speed but decreased with the filling and lifter height as it was influenced by the charge contact forces and charge motion. The peak pressure gradient was consistently influenced by the filling and not the critical speed and lifter height as it was subject to the level of packing around the CoC and contact forces. The slope between the mill shell and CoC followed a non-linear trend due to the influence of the lifters raising the charge caught between the lifter bars out of the charge bed, the influence of the critical speed on the angular velocity of the mill and the charge motion closer to the mill shell. The slope decreased with increasing filling and lifter heights but increased with the critical speed.

The change in the profile between the CoC and charge free surface was shown to follow both a linear and non-linear trend. The change in the pressure gradient decreased with a decrease in packing closer to the charge free surface as a result of particles raised out of the charge bed by the lifter bars and increased impacts from cataracting charge. The profile slope decreased with increasing filling and increased with the critical speed but was inconsistently influenced by the lifter height.

The relationship between the pressure gradient and velocity profile followed a non-linear second-order polynomial trend at all operating conditions. The slope between the mill shell and CoC increased with the filling and decreased with the critical speed due to the change in charge motion near the mill shell and packing around the CoC. The opposite effect was seen for the slope between the CoC and the charge free surface. The filling and critical speed levels were also found to influence the area under the curve. The lifter height did not consistently influence the slope and area under the curve.

Through a regression analysis of the pressure gradient-velocity profile relationship revealed that the velocity profile can be used to predict the pressure gradient. Furthermore, this can be incorporated into the velocity profile and linked to the operating conditions such that the physical properties of the mill can be used to predict the velocity profile and pressure gradient. This allows the derivation of these equations without having to run simulations to extract data and thereby fit equations using MS Excel or MATLAB.

The methods available to predict the velocity profile includes using lifter height-specific equations as well as equations predicting the polynomial variables (a, b and c) that make up the velocity profile non-linear trend.

7. Conclusion

The influence of the operating conditions on the charge motion, velocity profile and power draw was investigated using EDEM simulations. The results extracted from EDEM were used to determine the influence of the lifter height on the charge motion in the mill which was compared to the accuracy of the velocity profile model developed by Brodner (2013).

Charge Characteristics

The charge motion was analysed based on charge characteristics like the shoulder, toe, CoC location and inclination angle (θ) with the mill base as well as L_1 and L_2. The power draw was analysed according to the power draw distribution in the mill and the maximum power draw calculated using the BIN method. The velocity profile was analysed using changes in the tangential velocity along the diametric line. The changes in the velocity profile were assessed based on the overall contribution of the charge motion and charge characteristics and corresponding influences due to changes in the operating conditions.

The influence of the operating conditions on the charge characteristics (CoC, inclination angle (θ), shoulder, toe, CFS, L_1 and L_2) were based on changes in the packing and charge motion in the rising en-masse, cascading and cataracting regions. The particle packing around the CoC increased with the filling which reduced the number and trajectory of particles raised out of the charge bed and into the cataracting region. The charge motion was strongly influenced by increasing the critical speeds which in turn, increased the angular velocities in the mill as well as the number of particles raised out of the charge bed. The lifter heights were shown to increase the number of particles raised out of the charge bed thereby reducing the packing around the CoC.

Higher filling levels resulted in higher CoC, shoulder and toe locations which increased L_1 and L_2. Higher critical speeds increased the angular velocities and resulted in higher shoulder locations with lower CoC and toe locations. This effect decreased L_1 and L_2. Higher critical speeds increased the number and trajectory of particles in the cataracting region. Increasing the lifter heights resulted in higher CoC and shoulder locations with lower toe locations. The increased lifter heights ensure an increase in the number and trajectory of particles in the cataracting region. The lifter height did not consistently influence L_1 and L_2. The charge characteristics determined using EDEM was shown to closely agree with that reported in literature and more specifically, by Brodner (2013).

Overall, the filling had the strongest influence on the charge characteristics than the lifter height and critical speed. Changes in the filling and critical speed reduced the influence of the lifter height on the charge characteristics. The influence of the operating conditions on the

charge characteristics, which directly influenced the charge motion and velocity profile along the diametric line, provided an indication of the corresponding influence on the model developed by Brodner (2013). Through regression analyses, the filling, lifter height and critical speeds were used in predictive equations to calculate these charge characteristics which allows the data extraction without having to run simulations. More specifically, the lifter height was shown to be a key predictive variable for the charge characteristics.

Power Draw

The influence of the operating conditions on the power draw distribution was based on how the charge motion in the mill contributed to higher power draw regions. At all critical speed, filling and lifter height settings, the power draw distribution had three distinct regions, the low power draw region along the equilibrium surface and two higher power draw regions along the rising en-masse and cascading regions.

Increasing the filling increased the number of particles contributing to the high power draw in the rising en-masse region and decreased the number of particles contributing to the high power draw in the cascading region. The biggest contributor to the power draw was the cascading region. Increasing the critical speed ensured the rising en-masse region as the dominant contributor to the power draw due to the increased charge motion and particle interactions influenced by the increased angular velocity. The number of particles contributing to power drawn in the cascading region decreased with increasing critical speed. Increasing the lifter height resulted in a similar trend as that of the filling on the power draw distribution.

The maximum power drawn in the mill was concentrated in the cascading region directly above the equilibrium surface as well as the rising en-masse region along the mill shell. The maximum power draw increased with the filling, critical speed and lifter height settings. The filling had the strongest influence on the power draw which decreased with increasing lifter height and critical speed settings. The influence of the lifter height increased with increasing critical speed and decreasing filling levels.

Charge Velocity

The influence of the operating conditions on the charge velocity was based on changes in the average and tangential charge velocity distributions as well as changes in the charge velocity frequency in the mill. The average charge velocity in the mill decreased with increasing filling and increased with increasing critical speed and lifter height. The critical speed had a strongest influence on the average charge velocity which improved with increasing the lifter height. Increasing the filling restricted the influence of the critical speed and lifter height on the charge motion.

The charge velocity frequency was assed based on the concentration of particles in specific velocity regions in the mill. In the cascading and cataracting (high velocity) regions, the velocity frequency decreased with increasing filling which restricted charge motion and increased packing in low velocity regions (equilibrium region).

Increasing the critical speed increased the angular velocity and particle motion in both the low and high velocity regions which increased the corresponding charge velocity frequency i.e. the concentration of particles in high velocity regions increased. The lifter height did not consistently influence the charge velocity frequency in all charge motion regions. Increased lifter heights opposed the influence of the filling on the velocity frequency in both low and high velocity regions due to the increased motion of particles lifted out of the charge bed.

The influence of the operating conditions on the tangential velocity was similar to that on the average charge velocity. Increasing the filling opposed the influence of the critical speed on the charge motion and the ability of the lifters to raise particles out of the charge bed into the cascading and cataracting regions. The lifter height and critical speed increased the charge motion out of the charge bed and into the cascading and cataracting regions which increased the tangential velocity in the rising en-masse region (along the mill periphery) and in the cascading and cataracting regions. The tangential velocity in the rising en-masse region increased with increasing filling, critical speed and lifter height settings.

Velocity Profile and EDEM Results

The influence of the operating conditions on the velocity profile was assessed based on changes in the angular velocity at the mill shell, CoC location, L_1 and L_2 as well as the change in the tangential velocity slope along L_1 and L_2. The velocity profile was also assessed based on the mathematical relationship between the tangential velocity and distance along the diametric line as well as comparisons between the EDEM-generated results and the model developed by Brodner (2013).

The velocity profile extracted along the diametric line using EDEM was shown to vary non-linearly similar to that reported in literature. At the mill shell the velocity profile was similar to the angular velocity of the mill. The profile decreased from the shell to the CoC where it was equal to zero. This point corresponds to where the packing around the CoC is highest. Due to the flow of particles being in the opposite direction in the cascading region, the profile increased, becoming more negative between the CoC and charge free surface.

The velocity profile was found to be influenced by the filling, critical speed and lifter height. Increasing the filling decreased the velocity profile slope between the shell and CoC but did not consistently influence the slope between the CoC and charge free surface. Overall, an

increase in the filling stretched the velocity profile decreasing the slope. Increasing the critical speed increased the profile slope steepness along both L_1 and L_2 on the diametric line as a result of a corresponding increase in the angular velocity at the mill shell. Increasing the lifter height decreased the velocity profile slope between the shell and CoC. The lifter height did not consistently influence the profile between the CoC and charge free surface.

The comparison between the EDEM-extracted profile and that of the PEPT experiments showed produced similar results i.e. the tangential velocity at the mill shell increased with the critical speed. Since the CoC location moved away from the mill shell at higher speeds, the slope of the profile increased in steepness with increasing critical speed similar to the PEPT results. The PEPT and EDEM results also showed a more distinct non-linear change in the tangential velocity specifically at lower critical speeds.

The trend-line equations fitted to the EDEM data to determine whether the relation was non-linear showed a non-linear trend for the change in the tangential velocity between the mill shell and charge free surface. A further analysis of the mathematical relationship along L_2 showed that the non-linear equations were a closer fit to changes in the tangential velocity along the diametric line. The standard deviation for the linear fit was more than double that of the non-linear fit. As a result 36 second order polynomial equations were fit to the tangential velocity data providing an accurate determination of the velocity profile at all operating conditions.

Through an additional regression analysis, this was reduced to 9 equations allowing for the velocity profile variables as per the quadratic equation (a, b and c) to be determined using the lifter height (mm) and critical speed (%). Thus the velocity profile can be predicted using the physical properties of the mill at each filling level.

The EDEM-extracted velocity profile was compared to the model derived by Brodner (2013) and found that there was no agreement under the assumption of a constant pressure gradient along the diametric line. The calculated pressure gradient was found to vary along the diametric line and followed a non-linear relationship between the mill shell and charge free surface. The change in the pressure gradient along the diametric line showed an increase from the mill shell to the CoC, reaching a peak pressure gradient at the CoC where the level of packing is a maximum. The pressure gradient decreased from the CoC to the charge free surface followed by a plateau trend in the cataracting region.

The critical speed had the strongest influence on the pressure gradient as it increased the pressure gradient and slope steepness due to the increased charge motion and associated contact forces. The filling decreased the pressure gradient magnitude and slope due to increased packing which restricted charge motion in the mill and the associated forces. The lifter height consistently decreased the pressure gradient magnitude at the shell and did not

consistently influence the pressure gradient slope. The shape of the pressure gradient plots at all operating conditions were shown to resemble that reported in the shear strain-stress distributions reported in Jang & Khonsari (2005) typical to granular media in a rotating mill. Hudson & Harrison (1997) and Maicke & Majdalani (2009) also reported similar trends for the stress-strain profile of granular media and for the radial (axial) pressure drop respectively. Overall, the pressure gradient remains non-zero along the diametric line similar to the stress-strain relations.

In order to relate the varying pressure gradient to the velocity profile and thereby determine whether it can be used to predict the velocity profile, the change in the pressure gradient was plotted against the extracted velocity profile. The relationship followed a non-linear second-order polynomial trend at all operating conditions. The slope between the mill shell and CoC increased with the filling and decreased with the critical speed. The opposite was seen for the slope between the CoC and the charge free surface. The filling and critical speed were also found to influence the area under the curve. The lifter height did not consistently influence the slope and area under the curve.

The non-linear relationship provided an indication of how the calculated pressure drop would influence the velocity profile model developed by Brodner (2013) incorporating the influence of the operating conditions. Furthermore, the influence of the operating conditions on the area under the curve resembled the relationship between the calculated power draw using the force and velocity.

Through a regression analysis, 36 equations were derived relating the velocity profile to the pressure gradient at each lifter height, critical speed and filling level. However, an additional regression analysis was done relating the operating conditions to the polynomial equation variables (a, b and c) to allow the derivation of the relation between the velocity profile and the pressure gradient using the physical properties of the mill.

In conclusion, DEM was used to analyse the lifter height influence on the charge motion, velocity profile and power draw. The EDEM results showed that the critical speed, filling and specifically the lifter height could be related to the key charge characteristics as seen in section 5.2. The study has thereby, supplemented the understanding of the role lifters play in influencing the flow behaviour of a tumbling mill. This was achieved through direct comparisons to the PEPT results.

The results have also shed more light on how these operating conditions specifically the lifter height affects the velocity profile and varying pressure gradient in the mill. The results were used to further examine the predictive capabilities of the velocity profile model developed by Brodner (2013) in section 5.5.2. The disagreements in the EDEM and PEPT results on the

basis of the velocity profile model were based on the assumption that the pressure gradient remained constant throughout. Section 5.5.3 showed that the pressure gradient varied along the diametric line.

8. Recommendations for future work

Based on the results of this thesis, the following recommendations were put forward;

- In order to extract more information on the influence of the filling and critical speed, the operating condition ranges should be expanded to include the following;
    - 40 % of critical and Filling levels of 25 % to allow for improved visualisation of the effects on the charge motion and velocity profile;
    - Lifter heights of 12.0 mm in order to expand on the influence of the lifter height on the velocity profile and pressure gradient in the mill.
- An investigation into the change in the pressure gradient along the diametric line and along the length of the mill as investigated in Bbosa, Govender & Mainza. (2016) can be used to determine how they can be incorporated into the velocity profile model developed by Brodner (2013).
- Align the change in the velocity profile to charge layering and ultimately the influence on the power draw as referred to by Morrell (1993).
- Investigate the change in the viscosity of granular charge material in order to accurately define its behaviour during particle collision events. This can significantly influence the; predictive ability of the velocity profile model developed by Brodner (2013), the contact models used in EDEM simulations and the associated influence on the charge motion. The viscosity should be investigated using the relation between the velocity profile and the pressure gradient.
- Investigate the influence of charge size distributions on the velocity profile as well as varied particle shapes on the charge motion and velocity profile. This will allow a closer replication of the results in this study and Brodner (2013) to real world applications.
- The EDEM data generated in this study can be used to for the development of predictive models for the charge shape, stress intensity distribution, etc.
- Expand on the scalability of the current study to a pilot scale study based on the methodology of Donkor (2014) whereby vibration sensing technology is used to analyse the charge motion in a large scale mill in real-time with similar charge media and operating conditions.

References

Aissa, A. A., Duchesne, C., & Rodrigue, D. 2011. Effect of friction coefficient and density on mixing particles in the rolling regime. *Powder Technology*. 212, 340-347.

Alatalo, J. 2011. Charge Dynamics in Tumbling Mills. Simulation and Measurements with an In-Mill Sensor. *Department of Civil, Environmental and Natural Resources Engineering, Luleå University of Technology. Postgraduate thesis.*

Barrios, G. K. P., de Carvalho, R. M., Kwade, A., & Tavares, L. M. 2013. Contact parameter estimation for DEM simulation of iron ore pellet handling. *Powder Technology*. 248, 84-93.

Bbosa, L. S. 2013. Probability Based Models for the Power Draw and Energy Spectra of a Tumbling Mill. *Centre for Minerals Research, Department of Chemical Engineering, University of Cape Town. Postgraduate thesis.*

Bbosa, L. S., Govender, I., Mainza, A. N., & Powell, M. S. 2011. Power draw estimates in experimental tumbling mills using PEPT. *Minerals engineering.* 24(3-4), 319-324.

Bbosa, L. S., Govender, I., & Mainza, A. N. 2016. Development of a novel methodology to determine mill power draw. *Minerals engineering.* 149, 94 - 103.

Bertrand, F., Leclaire, L.-A., & Levecque, G. 2005. DEM-based models for the mixing of granular materials. *Chemical Engineering Science*. 60, 2517-2531.

Bird, R. B., Stewart, W. E., & Lightfoot, E. N. 2002. *Transport Phenomena, 2nd ed*. John Wiley & Sons, Inc., New York, USA.

Brodner, H. 2013. Assessing the influence of lifter profiles on the velocity profile and the charge toe and shoulder using data from the PEPT system. *Centre for Minerals Research, Department of Chemical Engineering, University of Cape Town. Postgraduate thesis*.

Burmeister, C., & Kwade, A. 2013. Process engineering with planetary ball mills. *Chem. Soc. Rev.* 21 September, 42(18), 7660-7667.

Campbell, C. S. 2006. Granular material flows – An overview. *Powder Technology*. 162, 208-229.

Cleary, P. W. 1998. Predicting charge motion, power draw, Segregation and wear in ball mills using Discrete Element Methods. *Minerals engineering.* 11(11), 1061-1080.

Cleary, P. W. 2001a. Charge behaviour and power consumption in ball mills: sensitivity to mill operating conditions, liner geometry and charge composition. *International Journal of Mineral Processing.* 63, 79-114.

Cleary, P. W. 2001b. Recent advances in DEM modelling of tumbling mills. *Minerals Engineering.* 14(10), 1295-1319.

Cleary, P.W. 2001c. Modelling comminution devices using DEM. *International Journal of Numerical and Analytical Methods in Geomechanics*. 25, 83–105.

Cleary, P. W. 2009a. Industrial particle flow modelling using discrete element method, *Engineering Computations*. 26(6), 698-743.

Cleary, P. W. 2009b. Ball motion, axial segregation and power consumption in a full scale two chamber cement mill. *Minerals Engineering.* 22, 809-820.

Cleary, P. W., & Hoyer, D. 2000. Centrifugal mill charge motion and power draw: comparison of DEM predictions with experiment. *International Journal of Mineral Processing.* 59, 131-148.

Cleary, P. W., & Sawley, M. L. 2002. DEM modelling of industrial granular flows: 3D case studies and the effect of particle shape on hopper discharge. *Applied Mathematical Modelling.* 26, 89–111.

Cleary, P. W., Morrisson, R., & Morrell, S. 2003. Comparison of DEM and experiment for a scale model SAG mill. *International Journal of Mineral Processing.* 68, 129-165.

Cundall, P. A., & Strack, O. D. L. 1979. A Discrete Numerical Model for Granular Assemblies. *Geotechnique*. *29*, 47-65.

Datta, A., Mishra, B. K., & Rajamani, R. K. 1999. Analysis of Power Draw in ball mills by the Discrete Element Method. *Canadian Metallurgical Quarterly,* 38(2), 133-140.

DEM Solutions. 2011. EDEM 2.5 User Guide. *DEM Solutions Ltd*. Edinburgh, UK.

DEM Solutions. 2013. EDEM 2.5 User Guide. *DEM Solutions Ltd*. Edinburgh, UK.

DEM Solutions. 2016. EDEM 2.7 [Computer Software]. *DEM Solutions Ltd*. Edinburgh, UK.

Di Renzo, A., & Di Maio, F. P. 2004. Comparison of contact-force models for the simulation of collisions in DEM-based granular flow codes. *Chemical Engineering Science.* 59(13), 525-541.

Ding, Y. L., Seville, J. P. K., Forster, R., & Parker, D. J. 2001. Solids motion in rolling mode rotating drums operated at low to medium rotational speeds. *Chemical Engineering Science.* 59, 1769-1780.

Djordjevic, N. 2003. Discrete Element Modelling of the influence of lifters on power draw of tumbling mills. *Minerals Engineering.* 16(4), 331-336.

Djordjevic, N., Shi, F., & Morrison, R. 2004. Determination of lifter design, speed and filling effects in AG mills by 3D DEM. *Minerals Engineering.* 1135-1142.

Doll, A. G. 2013. *A comparison of SAG mill power models. 10th International Mineral Processing Conference, Procemin 2013.* Santiago, Chile, Gecamin, Chile.

Donkor, S. 2014. On-line sensors for measuring the total ball and charge level in tumbling mills. *Centre for Minerals Research, Department of Chemical Engineering, University of Cape Town.* P*ostgraduate thesis.*

Fuerstenau, D. W., & Abouzeid, A. Z. M. 1985. Scale up of lifters in ball mills. *International Journal of Mineral Processing*. 15, 183–192.

Fuerstenau, M., & Han, K. 2003. *Principles of Mineral Processing.* Littelton: SME.

Ghazavi M.R., & Ghanad, M. 2012. Tumbling mill lifter's angle and height influence on net-power based on DEM modelling. *Canadian Journal on Mechanical Sciences & Engineering*. *3*(3), 83-89.

Govender. I. 2005. X-ray motion analysis of charge particles in a laboratory mill. PhD thesis, *Department of Mechanical Engineering, University of Cape Town, Postgraduate Thesis.*

Govender, I., Balden, V., Powell, M., & Nurick. G. 2001. Validated DEM - Potential major improvements to SAG mill modeling. In: Barratt, et al. (eds.), *Proc. Int. Autogenous and Semiautogenous Grinding Technology*. IV. CIM, 101-114.

Govender, I., Cleary, P. W., & Mainza, A. N. 2013. Comparisons of PEPT derived charge features in wet milling environments with a friction-adjusted DEM model. *Chemical Engineering Science*. 97, 162-175.

Govender, I., Mangesana, N., Mainza, A. N., & Franzidis, J.-P. 2011. Measurement of shear rates in a laboratory tumbling mill. *Minerals Engineering.* 24(3-4), 225-229.

Govender, I., Powell, M., & Nurick, G. 2001. 3D particle tracking: a rigorous technique for verifying DEM. *Minerals Engineering.* 14(10), 1329–1340.

Govender, I., Tupper, G. B., & Mainza, A. N. 2011. Towards a mechanistic model for slurry transport in tumbling mills. *Minerals Engineering.* 24, 230-235.

Govender, I., McBride, A. T., & Powell, M. 2004. Improved Experimental Tracking Techniques for Validating Discrete Element Method Simulations of Tumbling Mills. *Journal of Experimental Mechanics,* 44(5), 593-607.

Grima, A., & Wypych, P. 2011. Investigation into calibration of discrete element model parameters for scale-up and validation of particle–structure interactions under impact conditions. *Powder Technology*. 212, 198–209.

Gudin, D., Kano, J., & Saito, F. 2007. Effect of the friction coefficient in the discrete element method simulation on media motion in a wet bead mill. *Advanced Powder Technology.* 18(5), 555-565.

Hlungwani, O., Rikhotso, J., Dong, H., & Moys, M. 2003. Further validation of DEM modelling of milling-effects of liner profile and mill speed. *Minerals Engineering.* 16(10), 993-998.

Hudson, J. A., & Harrison, J. P. 1997. Engineering Rock Mechanics: An Introduction to the Principles. *The complete stress-strain curve in uniaxial compression*. London: Imperial College of Science, Technology and Medicine, University of London: Pergamon. 86 – 88.

Jang, J. Y., & Khonsari, M. M. 2005. On the granular lubrication theory. *Proceedings of the Royal Society.* 461, 3255–3278.

Jonsén, P., Pålsson, P. I., Tano, K., & Berggren, A. 2011. Prediction of mill structure behaviour in a tumbling mill. *Minerals Engineering.* 24, 236-244.

Kallon, D. V. V. 2013. Circulation Rate Modelling Of Tumbling Mill Charge Using Positron Emission Particle Tracking (PEPT). *Centre for Minerals Research, Department of Chemical Engineering, University of Cape Town. Postgraduate thesis.*

Kallon, D. V. V., Govender, I., & Mainza, I. A. 2011. Circulation rate modelling of mill charge using position emission particle tracking. *Minerals Engineering.* 24, 282-289.

Kano, J., Mio, H., Saito, F., & Miyazaki, M. 2001. Correlation of grinding rate of gibbsite with impact energy in tumbling mill with mono-size balls. *Minerals Engineering*. 14(10), 1213–1223.

King, R. P. 2000. Technical Notes 8: Grinding. Available: http://www.mineraltech.com/MODSIM/ModsimTraining/Module6/Grinding.pdf. [2015, January 29]

Kulya, C. 2008. Using Discrete Element Modelling (DEM) and Breakage Experiments to Model the Comminution Action in a Tumbling Mill. *Centre for Minerals Research, Department of Chemical Engineering, University of Cape Town. Postgraduate thesis.*

Kumar, A. 2011. *TechnoMine Mining Technology.* Available: http://technology.infomine.com/reviews/comminution/welcome.asp?view=full. [2015, January 20].

Langston, P. A., Ttiztin, U., & Heyes, D. M. 1995. Discrete element simulation of internal stress and flow fields in funnel flow hoppers. *Powder Technology*. 85, 153-169.

Lynch, A. J., & Rowland, C. A. 2005. *The History of Grinding.* 188-189, SME.

Maicke, B. A., & Majdalani, J. 2009. A constant shear stress core flow model of the bidirectional vortex. *Proceedings of the Royal Society.* 465, 915–935.

Makokha, A. B., & Moys, H. M. 2006. Towards optimising ball-milling capacity: Effect of lifter design. *Minerals Engineering*. 19, 1439-1445.

Mangesana, N., Chikuku, R. S., Mainza, A. N., Govender, I., van der Westhuizen, A. P., & Narashima, M. 2008. The effect of particle sizes and solids concentration on the rheology of silica sand based suspensions. *Southern African Institute of Mining and Metallurgy.* 108, 237-243.

Mayank, K., Malahe, M., Govender, I., & Mangadoddy, N. 2015. Coupled DEM-CFD model to predict the tumbling mill dynamics. *Procedia IUTAM.* 15, 139-149.

McBride, A., & Powell, M. 2006. A structured approach to modelling SAG mill liner wear-Numerical modelling of liner evolution. In *International autogenous and semi autogenous grinding technology 2006*. 3, 120-132, CIM.

McBride, A., Govender, I., Powell, M., & Cloete, T. 2003. Contributions to the experimental validation of the discrete element method applied to tumbling mills. *Engineering Computations*. 21(2/3/4), 119-136.

McDonough, J. M. 2009. *Lectures in elementary fluid dynamics: physics, mathematics and applications.* [Lecture notes]. Departments of Mechanical Engineering and Mathematics. University of Kentucky, Lexington.
Available: https://www.researchgate.net/publication/266217669. [2017, July 04].

McIvor, R. E. 1983. Effects of Speed and Liner Configuration on Ball Mill Performance. *Mineral Engineering.* 618-621.

Mellmann. J. 2001. The transverse motion of solids in rotating cylinders – forms of motion and transition behaviour. *Powder* technology. 118, 251-270.

Mishra, B. K. 2003a. A review of computer simulation of tumbling mills by the discrete element method: Part I-Contact Mechanics. *International Journal of Mineral Processing.* 71(1-4), 73-93.

Mishra, B. K. 2003b. A review of computer simulation of tumbling mills by the discrete element method: Part II- Practical applications. *International Journal of Mineral Processing.* 71(1-4), 95-112.

Mishra, B. K., & Murty, C. V. R. 2001. On the determination of contact parameters for realistic DEM simulations of ball mills. *Powder Technology*. 115, 290-297.

Morrell, S. 1993. The prediction of Power Draw in wet tumbling mills. *Julius Kruttschnitt Mineral Research Centre, Department of Mining, Metallurgical and Materials Engineering, University of Queensland, Postgraduate thesis*.

Morrell, S. 1996a. Power draw of wet tumbling mills and its relationship to charge dynamics. Part 1: a continuum approach to mathematical modelling of mill power draw. *Transactions of the Institution of Mining and Metallurgy.* Section C105, C43-53.

Morrell, S. 1996b. Power draw of wet tumbling mills and its relationship to charge dynamics. Part 2: an empirical approach to modelling of mill power draw. *Transactions of the Institution of Mining and Metallurgy*. Section C105, C54-62.

Morrison, R., Cleary, P. W., & Valery, W. 2001. Comparing power and performance trends from DEM and JK modelling. *SAG 2001*. IV. CIM, 284-300.

Nakagawa, M., Altobelli, S. A., Caprihan, A., & Fukushima, E., 1997. NMR measurement and approximate derivation of velocity depth – Profile of granular flow in rotating, partially filled, horizontal cylinder. In: Behringer, R. P. & Jenkins, T. J. (eds.), *Powder and grains*. 447-450.

Napier-Munn, T. J., Morrison, R. D., & Kojovic, T. 1999. Minerals Comminution Circuits: Their operation and optimization. *Julius Kruttschnitt Mineral Research Centre, Department of Mining, Metallurgical and Materials Engineering, University of Queensland*.

Napier-Munn, T. J., Morrell, S., Morrison, R. D., & Kojovic, T. 2005. Mineral Comminution Circuits: Their operation and optimisation. 3rd ed. Queensland: *Julius Kruttschnitt Mineral Research Centre, Department of Mining, Metallurgical and Materials Engineering, University of Queensland*.

Parker, D. J., Dijkstra, A. E., Martin, T. W., & Seville, J. P. K. 1997. Positron emission particle tracking studies of spherical particle motion in rotating drums. *Chemical Engineering Science.* 52(13), 2011-2022.

Perez-Alonso, C., & Delgadillo, J. A. 2012. Experimental validation of 2D DEM code by digital image analysis in tumbling mills. *Minerals Engineering.* 25, 20-27.

Powell, M. 1991. The effect of liner design on the motion of the outer grinding elements in a rotary mill. *International Journal of Mineral Processing,* 163-193.

Powell, M., Govender, I., & McBride, A. T. 2008. Applying DEM outputs to the unified comminution model. *Minerals Engineering*. 21, 744-750.

Powell, M. S., & McBride, A. T. 2004. A three-dimensional analysis of media motion and grinding regions in mills. *Minerals Engineering.* 17, 1099-1109.

Powell, M. S., & Morrison, R. D. 2007. The future of comminution modelling. *International Journal of Mineral Processing.* 84, 228-239.

Powell, M. S., & Nurick, G. N. 1996a. A study of charge motion in rotary mills: parts 1-3. *Minerals Engineering.* 9(2), 259-268; 9(3), 343-350; 9(4), 399-418.

Powell, M. S., & Nurick, G. N. 1996b. A study of charge motion in Rotary Mills. Part 3 - Analysis of Results. *Minerals Engineering.* 9(4), 399-418.

Powell, M.S., Smit, I., Radziszewski, P., Cleary, P., Rattray, B., Eriksson, K. & Schaeffer, L. 2006. The Selection and Design of Mill Liners. In: Kawatra, S. K. *Advances in Comminution.* Colorado, USA: Society for Mining, Metallurgy, and Exploration, Inc. (SME).

Radziszewsky, P., & Morrell, S. 1998. Fundamental Discrete Element Charge Motion Model Validation. *Minerals Engineering.* 11(12), 1161-1178.

Rajamani, R. K., Songfack, P., & Mishra, B. K. 2000. Impact energy spectra of tumbling mills. *Powder Technology*. 108, 116-121.

Rajamani, R. K., Mishra, B. K., Venugopal, R., & Datta, A. 2000. Discrete element analysis of tumbling mills. *Powder Technology*. 109, 105-112.

Rezaeizadeh, M., Fooladi, M., Powell, M., & Mansouri, S. 2010. Experimental observations of lifter parameters and mill operation on power. *Minerals Engineering,* 23, 1182-1191.

Sanfrantello, L., Caprihan, A., & Fukushima, E. 2006. Velocity depth profile of granular matter in a horizontal rotating drum. *Granular Matter*. 9, 1-6.

Schilling, R. E. 2010. Choose the Right Grinding Mill. *Chemical Processing, October 2010*. Available: http://www.unionprocess.com/tech_papers/ChooseTheRightGrindingMill.pdf. [2015, May 24].

Schlanz, J. W. 1987. Grinding: An Overview of Operation and Design. *Minerals Research Laboratory, North Carolina State University.*

Shi, F. N., & Napier-Munn, T. J. 1999. Estimation of shear rates inside a ball mill. *International Journal of Mineral Processing.* 57, 167-183.

Takalimane, M. 2014. Evaluating the influence of lifter face angle on the trajectory of particles in a tumbling mill using PEPT. *Centre for Minerals Research, Department of Chemical Engineering, University of Cape Town. Postgraduate thesis.*

Thornton, C., Cummins, S. J., & Cleary, P. W. 2011. An investigation of the comparative behaviour of alternative contact force models during elastic collisions. *Powder Technology*. 210, 189-197.

Toor, P., Franke, J., Powell, M., Bird, M., & Waters, T. 2013. Designing liners for performance not life. *Minerals Engineering.* 43-44: 22-28.

van Nierop, M. A., Glover, G., van Tonder, J. C., & Moys, M. H. 1999. 2D DEM verification: Load behaviour and forces on a lifter bar. *The Journal of The South African Institute of Mining and Metallurgy.* 99(2), 93 – 96.

van Nierop, M. A., Gover, G., Hinde, A. L., & Moys, M. H. 2001. A discrete element method investigation of the charge motion and power draw of an experimental two-dimensional mill. *International Journal of Mineral Processing.* 61, 77–92.

Vermeulen, L. A., & Howat, D. D. 1986. Fluctuations in the slip of grinding charge in rotary mills with smooth liners. *International Journal of Mineral Processing.* 16, 153–168.

Vu-Quoc, L., & Zhang, X. 1999. An accurate and efficient tangential force-displacement model for elastic frictional contact in particle-flow simulations. *Mechanics of Materials*. 31, 235-269.

Vu-Quoc, L., Zhang, X., & Walton, O. R. 2000. 3-D discrete-element method for dry granular flows of ellipsoidal particles. *Computer Methods in Applied Mechanical Engineering*. 187, 483-528.

Yahyaei, M., & Banisi, S. 2010. Spreadsheet-based modelling of liner wear impact on charge motion in tumbling mills. *Minerals Engineering*. 23, 1213-1219.

Yamane, K., Nakagawa, M., Altobelli, S. A., Tanaka, T., & Tsuji, Y. 1998. Steady particulate flows in a horizontal rotating cylinder. *Physics of Fluids,* 10(6), 1419-1427.

Yang, R. Y., Zou, R. P., & Yu, A. B. 2003. Microdynamic analysis of particle flow in a horizontal rotating drum. *Powder Technology.* 130, 138-146.

Yang, R. Y., Yu, A. B., McElroy, L., & Bao, J. 2008. Numerical simulation of particle dynamics in different flow regimes in a rotating drum. *Powder Technology.* 188, 170-177.

Zhou, Y.C., Wright, B.D., Yang, R.Y., Xu, B.H., & Yu, A.B. 1999. Rolling friction in the dynamic simulation of sandpile formation. *Physica A.* 269, 536–553.

Zhou, Y. C., Yu, A. B., Stewart, R. L., & Bridgwater, J. 2004. Microdynamic analysis of the particle flow in a cylindrical bladed mixer. *Chemical Engineering Science.* 59, 1343-1364.

Zhu, H. P. & Yu, A. B. 2002. Averaging method of granular materials. *Physical Review.* E66 (021302).

Zhu, H. P., Zhou, Z. Y., Yang, R. Y., & Yu, A. B. 2007. Discrete particle simulation of particulate systems: theoretical developments. *Chemical Engineering Science.* 62, 3378-3392.

Zhu, H. P., Zhou, Z. Y., Yang, R. Y., & Yu, A. B. 2008. Discrete particle simulation of particulate systems: A review of major applications and findings. *Chemical Engineering Science*. 63, 5278-5770.

Appendix

A. EDEM Simulation Algorithm

Once EDEM has been initiated, the steps below were followed.

The 'Global' tab:

The global simulation properties were completed as per figure 22 in section 4.1 of the Methodology.

1. The relevant units were set as required e.g. mill speed: rad/s or rpm, length: mm, etc.
2. The simulation was labelled with an appropriate title and description.
3. The relevant contact model was selected i.e. Simplified (no slip) Hertz-Mindlin Deresiewicz for both particle-particle and particle-geometry interactions.
4. The z axis was chosen as the direction in which gravity acted i.e. z: - 9.81 m/s^2.
5. The relevant materials were defined in the material database i.e. steel and glass.
   If materials and their properties were already created in database, the relevant properties (Poisson's ratio, Shear modulus, Density, etc.) were imported into the relevant fields. The properties were extracted from table 3 in section 4.1 of the Methodology.
6. The material interaction was defined and created i.e. glass-glass and glass-steel. The relevant properties were provided as per table 3 in the Methodology i.e. coefficient of restitution as well as the coefficients of static and rolling friction.

The 'Particles' tab:

The particle creation procedure was completed as per figure 23 in section 4.1 of the Methodology.

1. A new spherical particle was created by clicking on the **+** button.
2. Create a new surface by clicking on the relevant **+** button.
3. Specify the particle radius or diameter i.e. 2.5 mm radius or 5 mm diameter.
4. Select the particle material based on the materials created in the 'Global' tab i.e. glass.
5. Click 'Calculate Properties' to automatically calculate the mass, volume and moment of inertia of each particle.

The 'Geometry' tab:

The information required in the 'Geometry' tab consisted of a specification of the environment in which the particles were allowed to interact i.e. the tumbling mill. The mill geometry was designed using AUTOCAD and as such, uploaded into EDEM in the form of .igs files.

1. The mill geometry was imported by clicking the 'Import' button under 'Sections'.

2. In the pop-up window;
   2.1. The relevant units were selected depending on the user's preference (e.g. mm).
   2.2. The 'Merge Sections' option was selected to enable the mill (shell and lifter bars) to rotate as a single unit.
3. The 'Domain' pop-up window remained unchanged.
4. Under the 'Details' tab:
   4.1. The mill geometry material was specified (i.e. steel).
   4.2. The geometry type was set as 'Physical'.
5. Under the 'Dynamics' tab:
   5.1. The linear rotation option was selected for the mill motion by clicking the **+** button.
   5.2. The start and end time for the mill motion was specified e.g. 0 to 10 seconds.
   5.3. The unit-specific rotational speed was set according to table 4 in the Methodology.
   5.4. Since the mill speed was maintained throughout the simulation, the acceleration remained 0 m/s^2.
   5.5. The rotation direction was specified using the coordinates provided by EDEM i.e. for this study, a clockwise rotation was maintained.
   5.6. The 'Point of Action' section was left unchanged.
6. The 'Reposition' tab was left unchanged as this was not required for the current study.
7. A new geometry was created for the volume in which to create the particles (particle factory) by clicking the **+** button under 'Sections'. A cylinder was chosen since this shape was similar to that of the mill.
8. Under the 'Details' tab:
   8.1. The cylinder's geometry type was set as 'Virtual' i.e. the volume did not actually exist and did not interact with anything in the simulation; it was only required to complete the particle creation.
9. The 'Dynamics' tab was left empty as this was not required for the particle factory.
10. Under the 'Cylinder' tab, the cylinder dimensions were set as per figure 24 in section 4.1 of the Methodology.

The 'Factories' tab:

1. A new factory was created by clicking the **+** button.
2. Under the 'Particles Generation' section:
   2.1. The 'Dynamic' option was selected in the drop-down list.
   2.2. The total number of particles or the equivalent charge mass was specified as per table 5 in section 4.2 of the Methodology.
   2.3. The type of 'Generation Rate' was specified i.e.100 000.
   2.4. The 'Start time' and 'Max Attempts to Place Particle' were the default EDEM values.

3. Under the ‘Parameters’ section, the correct particle factory geometry was selected.

The Simulator Pane:

1. The ‘Fixed Time Step’ was set as 10 % of the Rayleigh time step.
2. The total simulation time (amount of real time that the simulation represents) was specified e.g. 10 seconds.

   The **simulation time** is the amount of real time in which the simulation takes place. This value is usually related to the number of revolutions required to ensure the mill charge reaches a ‘steady state’ flow.
3. Under the ‘Data Save’ section, the data save interval was specified i.e. 0.01 seconds.
4. Under the ‘Simulator Grid’ section, ‘Rmin’ was set as 2Rmin.
5. The ‘Track Collisions’ option was not selected in order to prevent a significant increase in the memory required by the simulation.
6. The number of cores, as per the computing system used, was specified.

B. Charge Mass Calculations

The overall charge mass and the corresponding number of particles were determined according to the equations listed below. The total mill volume ($V_{T,m}$) was required in conjunction with the void fraction (e) to calculate the volume occupied by the mill charge material ($V_{T,gb}$). Since the void fraction is defined as the fraction occupied by the gas phase; the volume fraction occupied by the mill charge is (1 – e) as seen below.

Total Mill Volume (m^3): $V_{T,m} = \pi * (D_m{}^2 / 4) * L$ (1)

Total Charge Volume (m^3): $V_{T,gb} = (1 - e) * V_{T,m}$ (2)

Where, D_m is the mill diameter and L is the mill length.

The overall charge mass was determined using the density of a glass bead (δ_{gb}) and the relevant filling factor of the mill while the corresponding total number of particles required the mass and volume of a single glass bead where, R_{gb} is the radius of a single glass bead.

Total Charge Mass (kg): $M_{T,gb} = V_{T,gb} * (Loading/100) * \delta_{gb}$ (3)

Glass Bead Volume (m^3): $V_{gb} = (4/3) * \pi * (R_{gb}{}^3)$ (4)

Glass Bead Mass (kg): $M_{gb} = \delta_{gb} * V_{gb}$ (5)

Total Number of Particles: $\#_{gb} = M_{T,gb} / M_{gb}$ (6)

C. MATLAB Code Routines

The MATLAB codes used for the EDEM results analysis were extracted taken from Bbosa (2013) and were adapted to analyse the relevant data. The following routines were used:

- **'Ginput' function** – A function used to prompt the user to select a specific point on any figure in order to extract the exact location.
- **Reference Frame Bin Split** – A function that splits the area within the 2D reference frame of the mill into discrete and equal-sized bins. This routine was required to complete the binning routine explained below.
- **Binning routine** – Data population routine used to assign a unique index/location specific number to each data point within the mill reference frame. This was used to plot contour plots where each data point/location was assigned a specific colour depending on the magnitude of the corresponding index.
- **Spline routine** – The binning routine made use of a spline function which assigned all data points with a specific location in the reference frame of the mill. The data points and mill frame were used to determine whether a specific index value converged with the grid partitions (range) in order to place the data point appropriately.

D. Graphs generated from EDEM results

D.1. Position distribution graphs

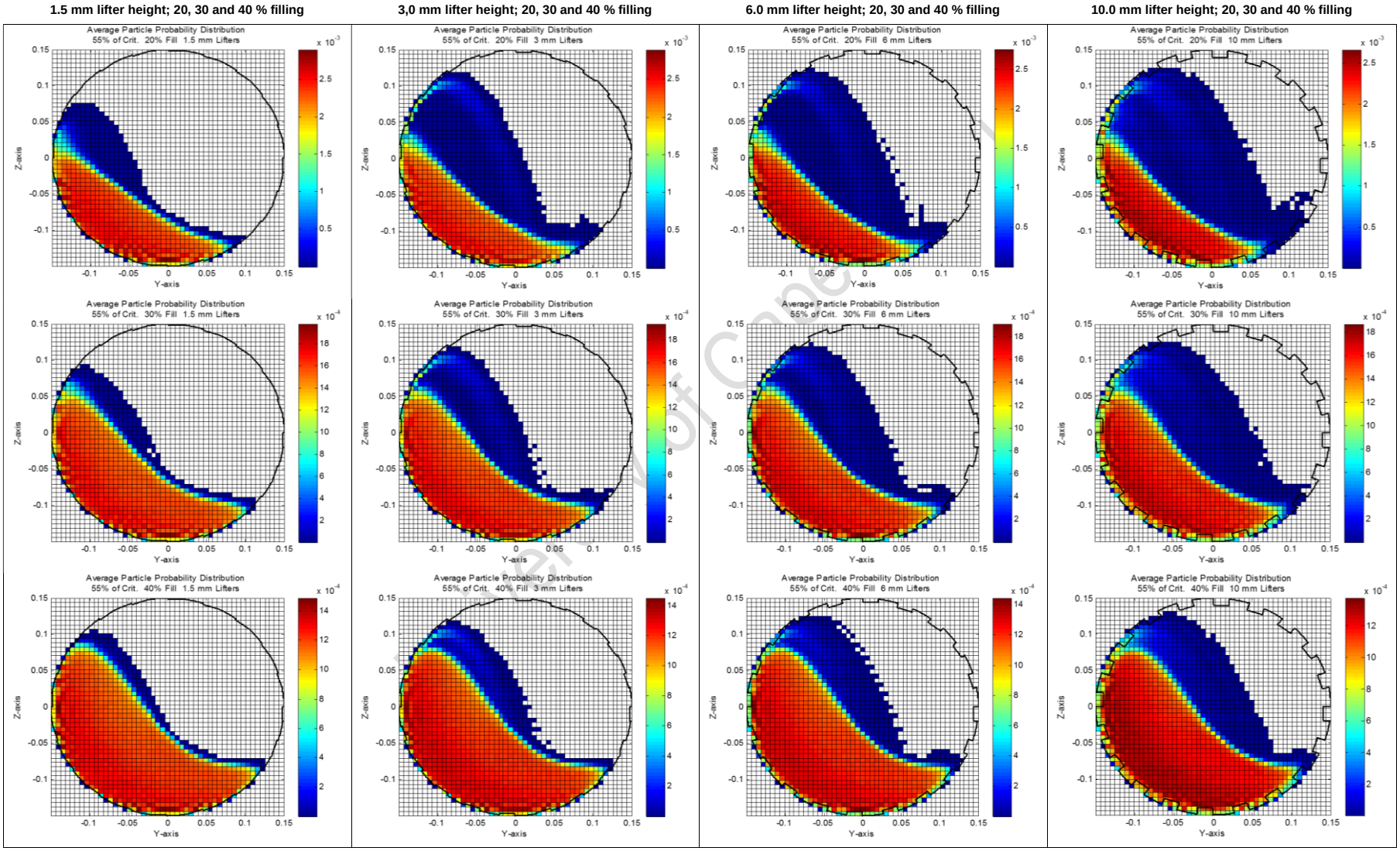

Figure 75: Particle position probability distribution at 55 % mill critical speed for 20, 30 and 40 % mill filling and 1.5, 3.0, 6.0 and 10.0 mm lifter heights.

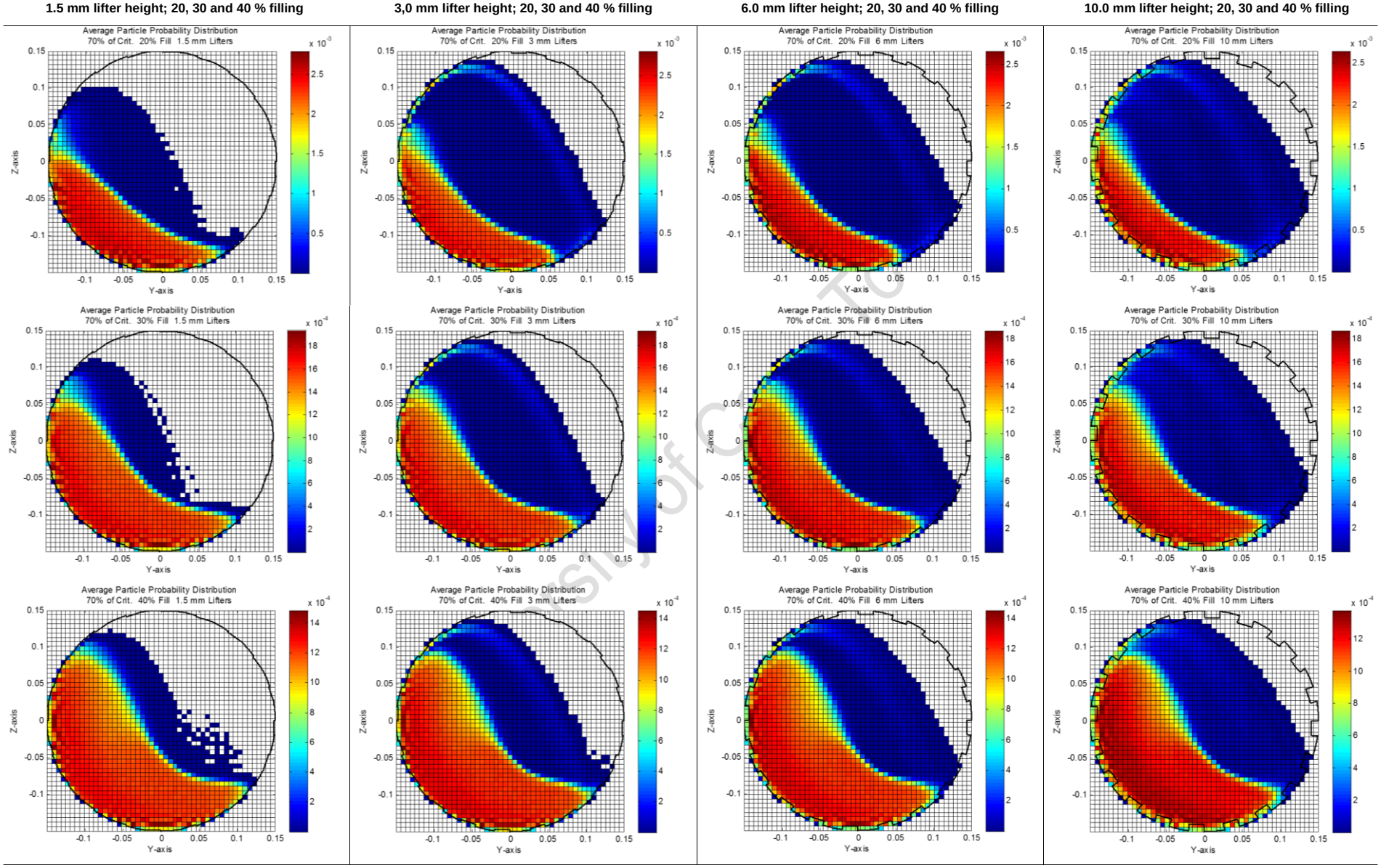

Figure 76: Particle position probability distribution at 70 % mill critical speed for 20, 30 and 40 % mill filling and 1.5, 3.0, 6.0 and 10.0 mm lifter heights.

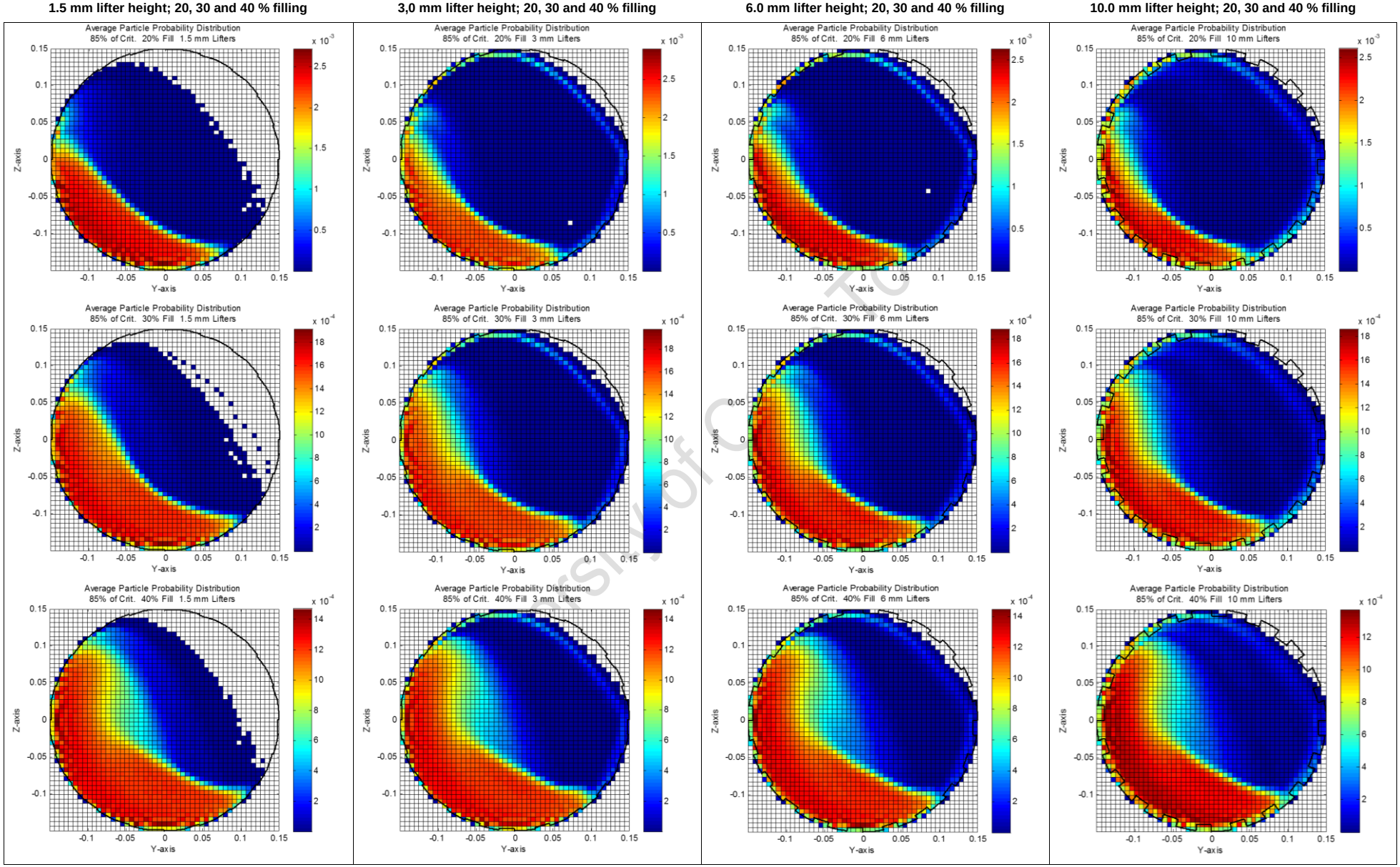

Figure 77: Particle position probability distribution at 85 % mill critical speed for 20, 30 and 40 % mill filling and 1.5, 3.0, 6.0 and 10.0 mm lifter heights.

D.2. Average velocity distribution graphs

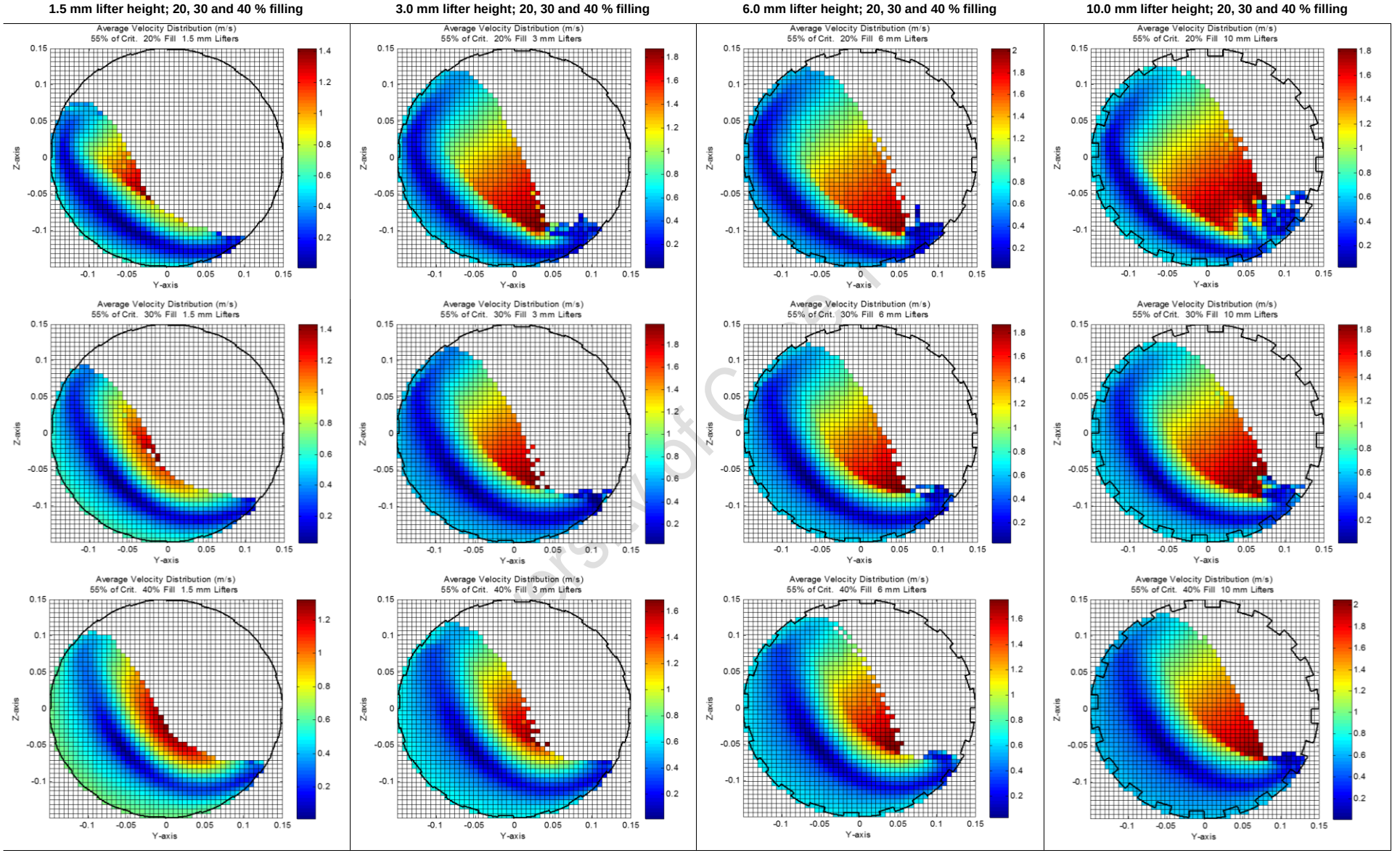

Figure 78: Average particle velocity distribution at 55 % mill critical speed for 20, 30 and 40 % mill filling and 1.5, 3.0, 6.0 and 10.0 mm lifter heights.

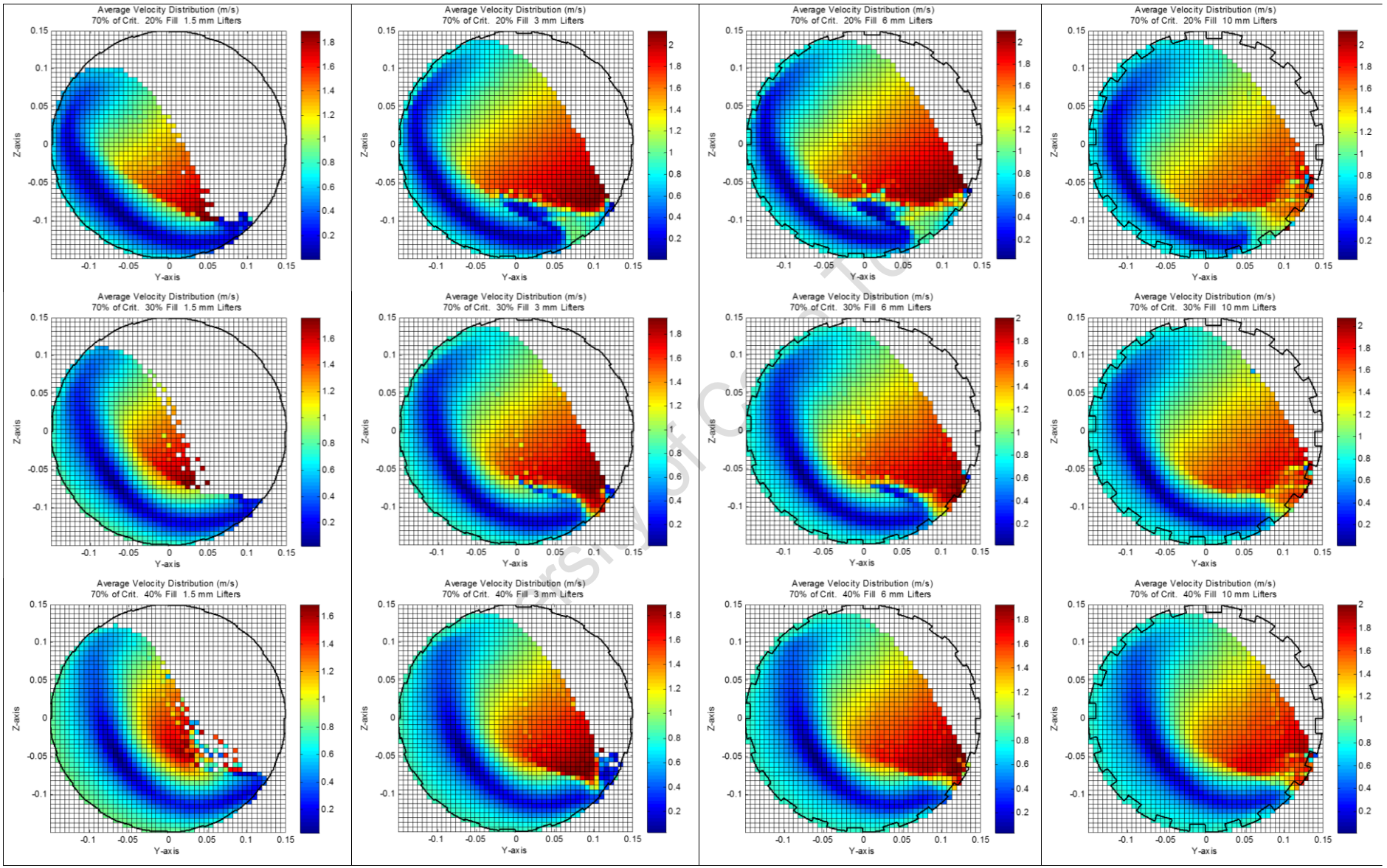

Figure 79: Average particle velocity distribution at 70 % mill critical speed for 20, 30 and 40 % mill filling and 1.5, 3.0, 6.0 and 10.0 mm lifter heights.

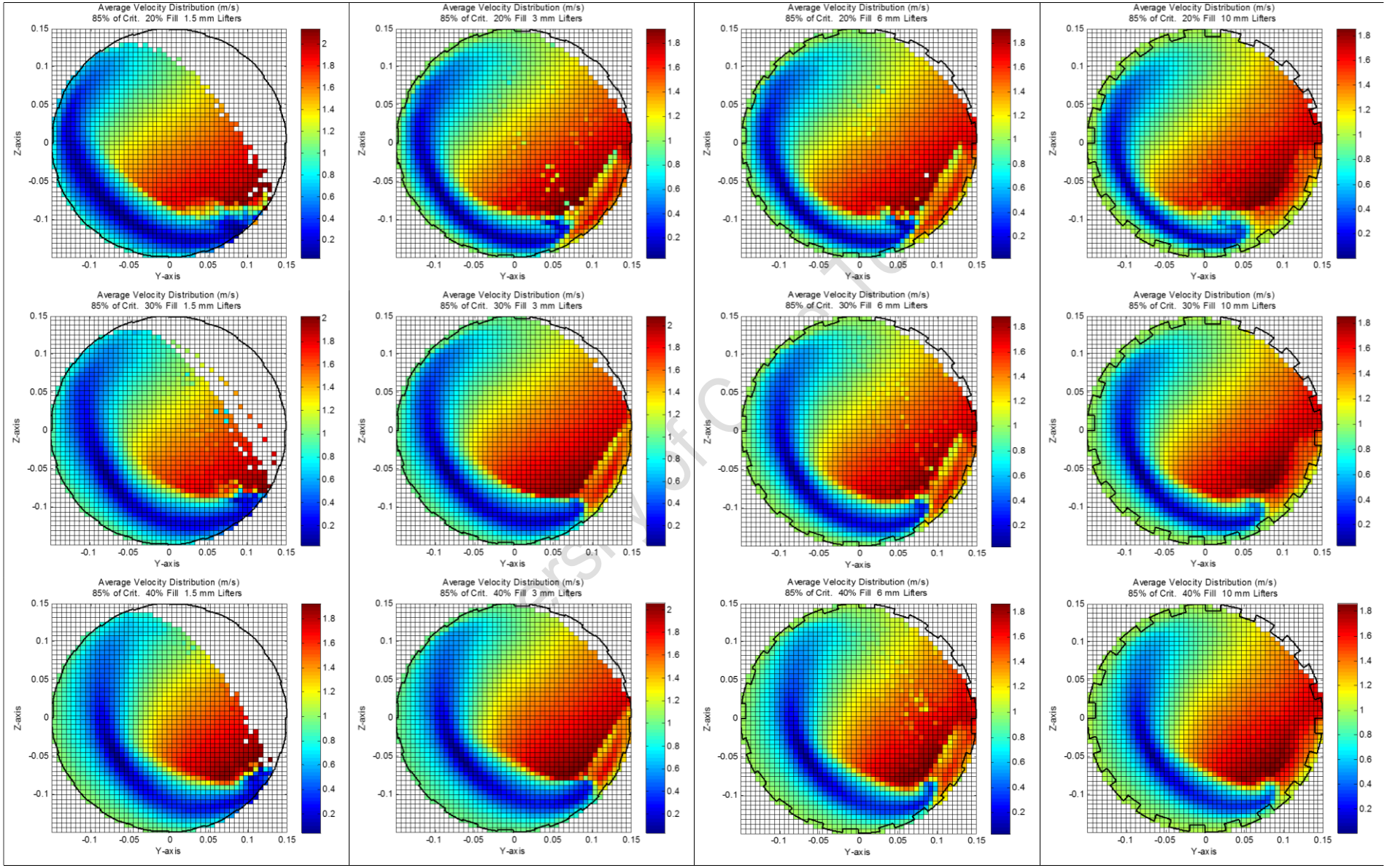

Figure 80: Average particle velocity distribution at 85 % mill critical speed for 20, 30 and 40 % mill filling and 1.5, 3.0, 6.0 and 10.0 mm lifter heights.

D.3. Average velocity vector field distribution

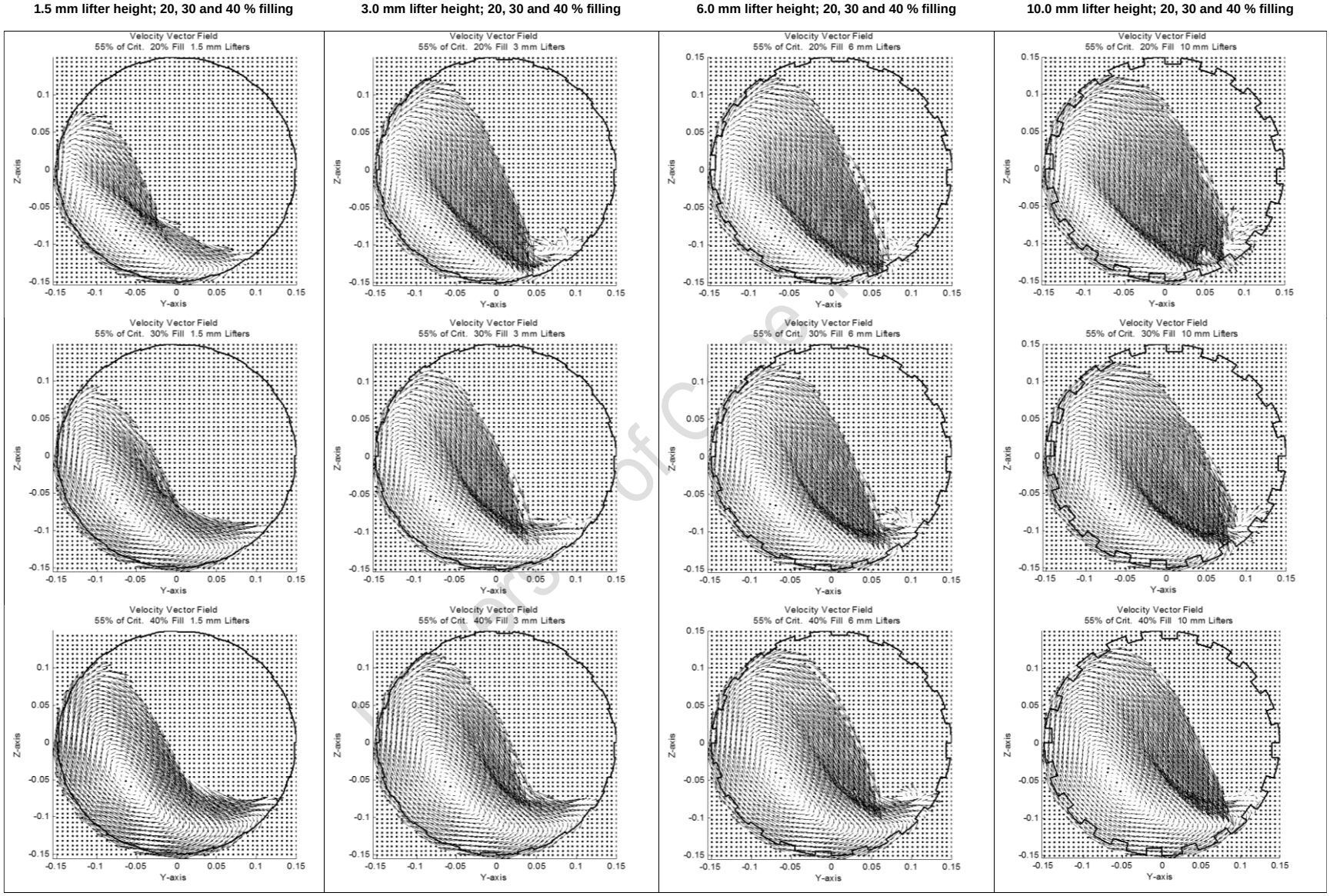

Figure 81: Average particle velocity vector field at 55 % mill critical speed for 20, 30 and 40 % mill filling and 1.5, 3.0, 6.0 and 10.0 mm lifter heights.

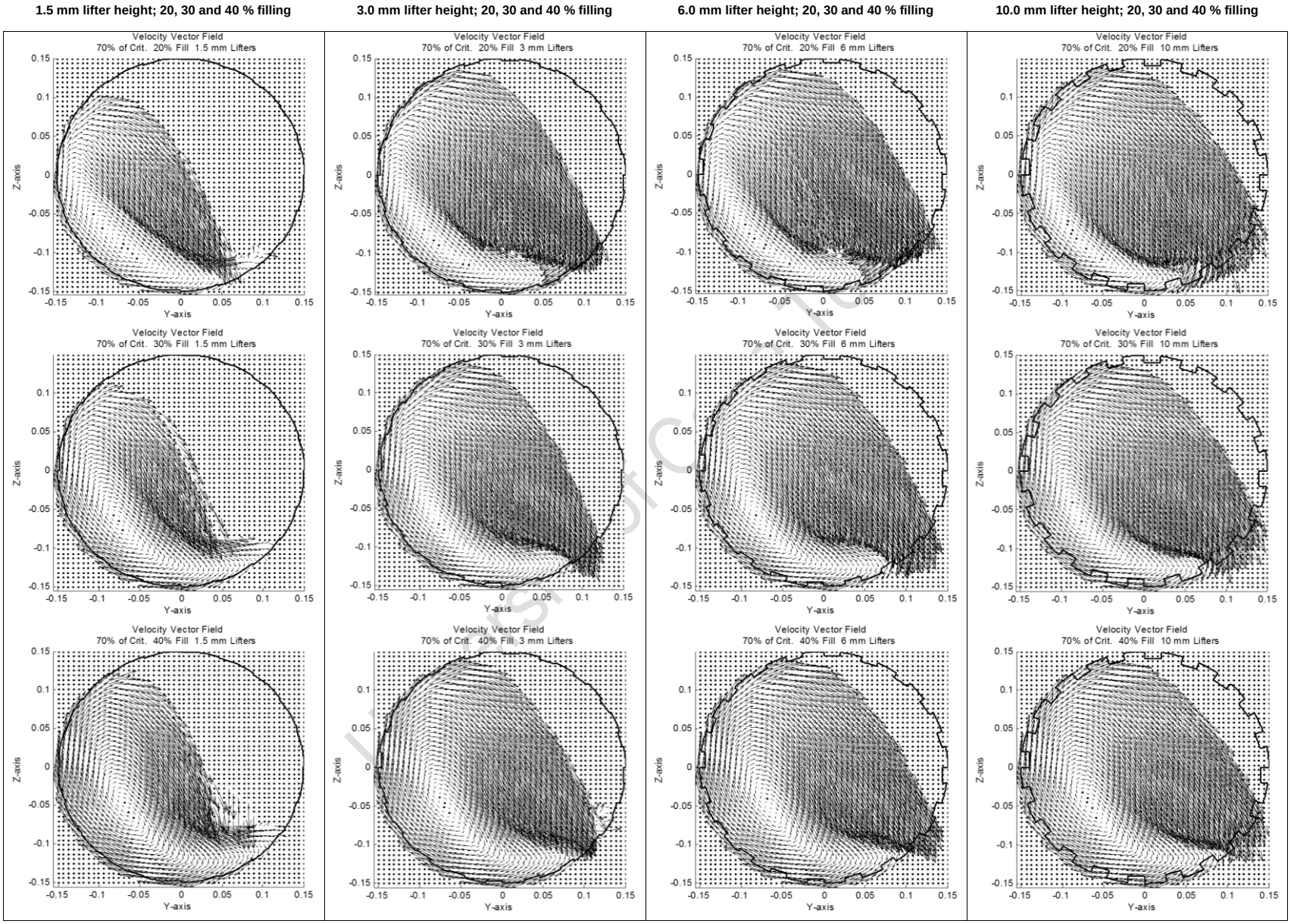

Figure 82: Average particle velocity vector field at 70 % mill critical speed for 20, 30 and 40 % mill filling and 1.5, 3.0, 6.0 and 10.0 mm lifter heights.

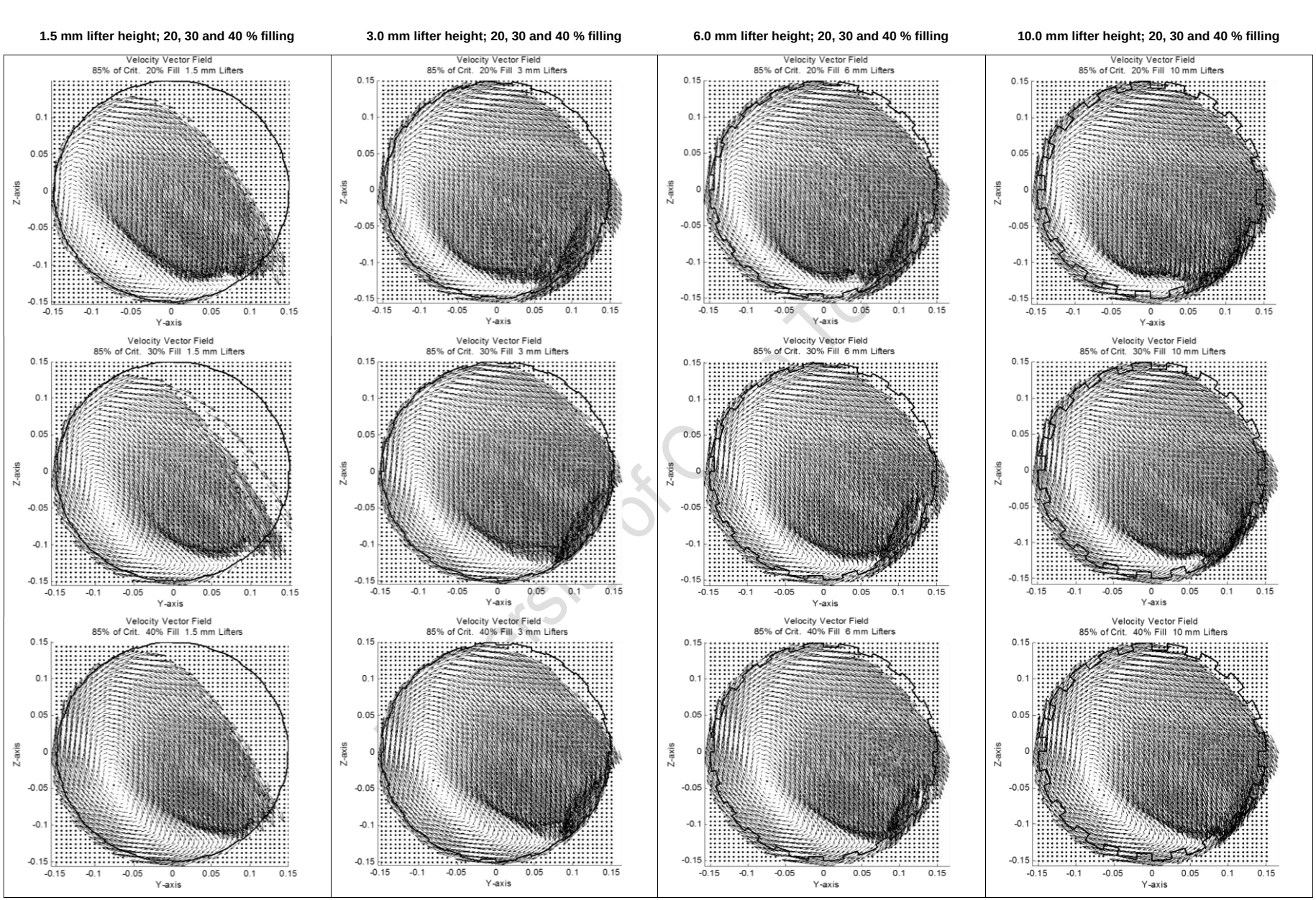

Figure 83: Average particle velocity vector field at 85 % mill critical speed for 20, 30 and 40 % mill filling and 1.5, 3.0, 6.0 and 10.0 mm lifter heights.

D.4. Tangential velocity distribution graphs

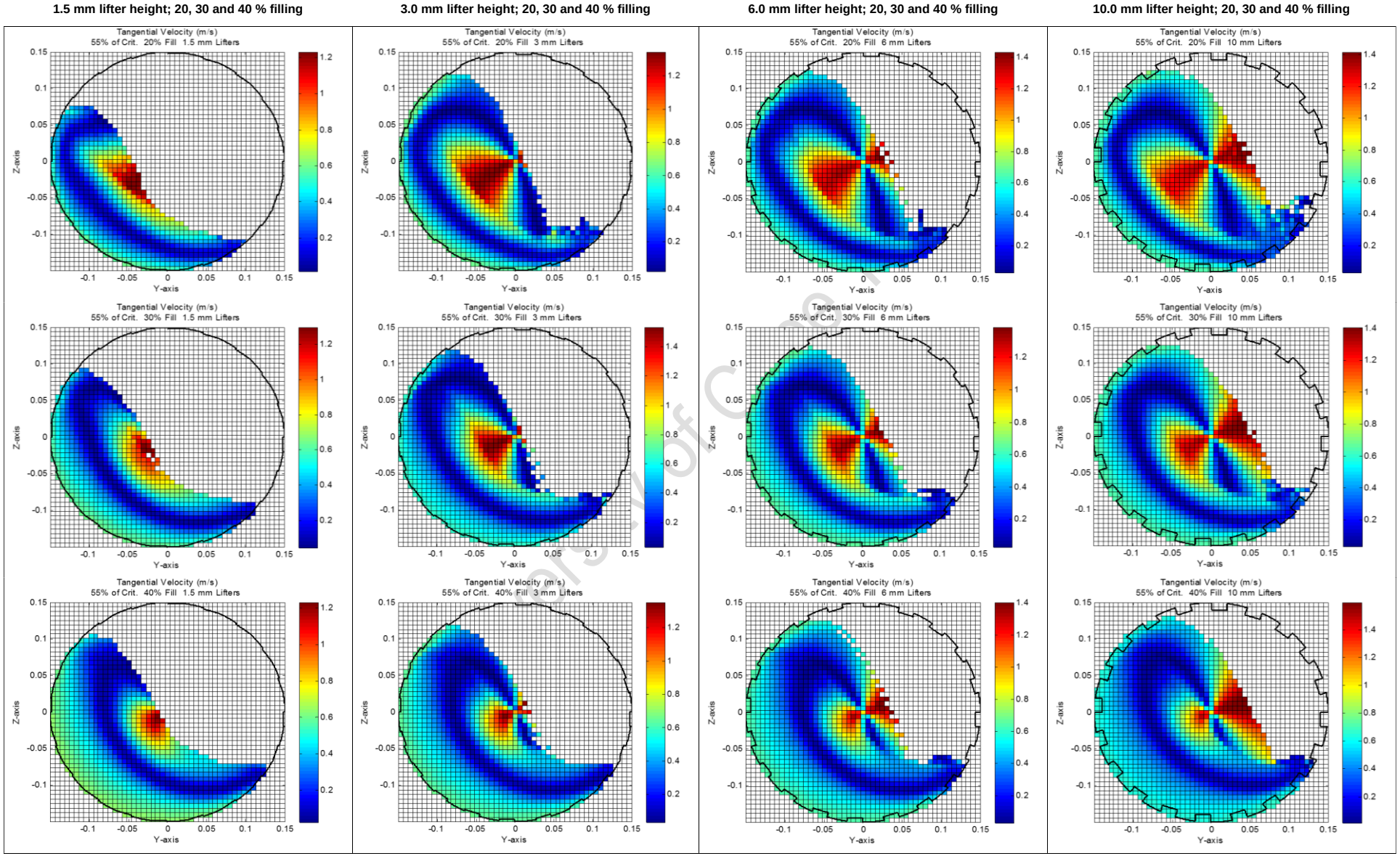

Figure 84: Tangential velocity distribution at 55 % mill critical speed for 20, 30 and 40 % mill filling and 1.5, 3.0, 6.0 and 10.0 mm lifter heights.

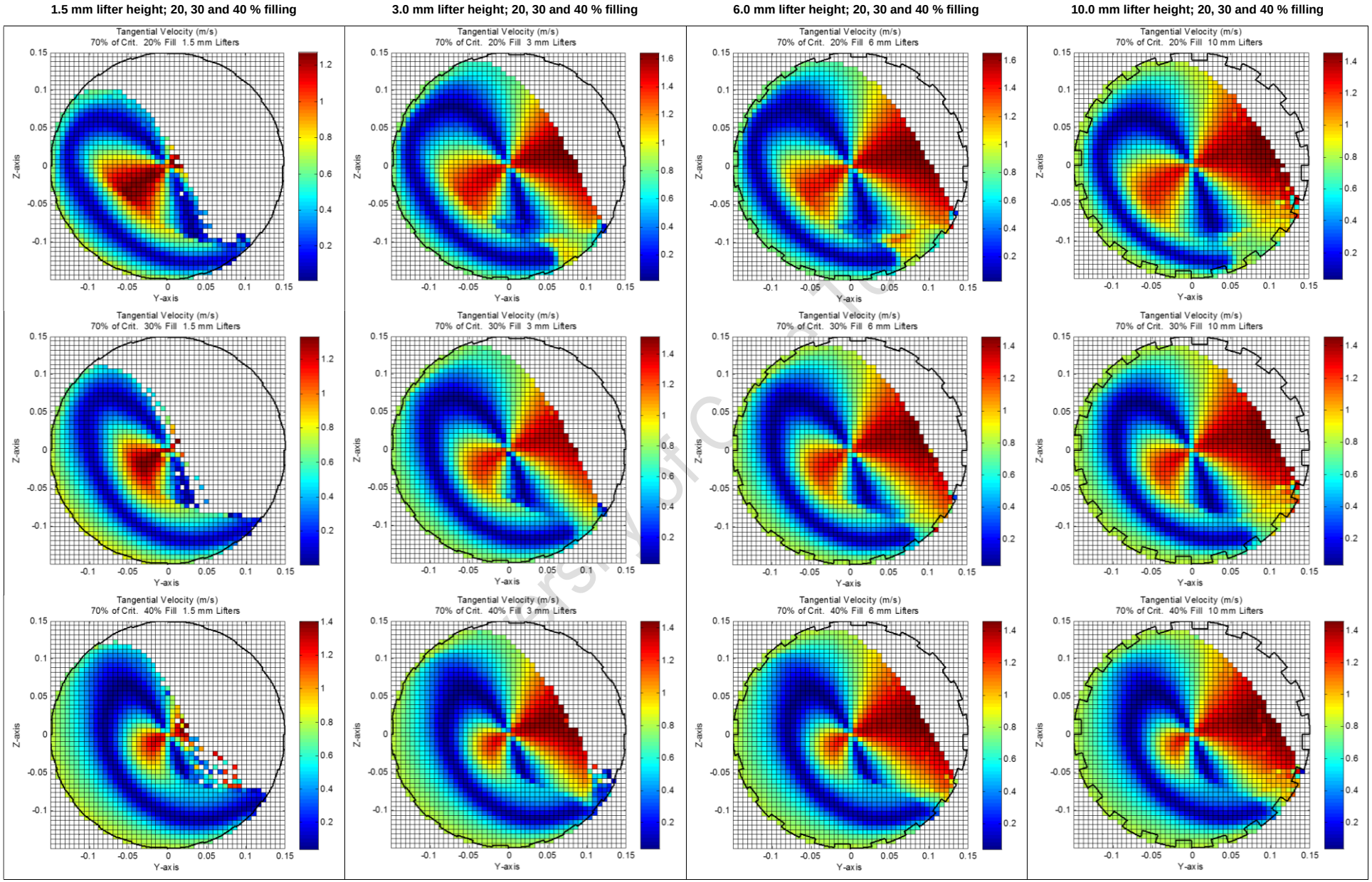

Figure 85: Tangential velocity distribution at 70 % mill critical speed for 20, 30 and 40 % mill filling and 1.5, 3.0, 6.0 and 10.0 mm lifter heights.

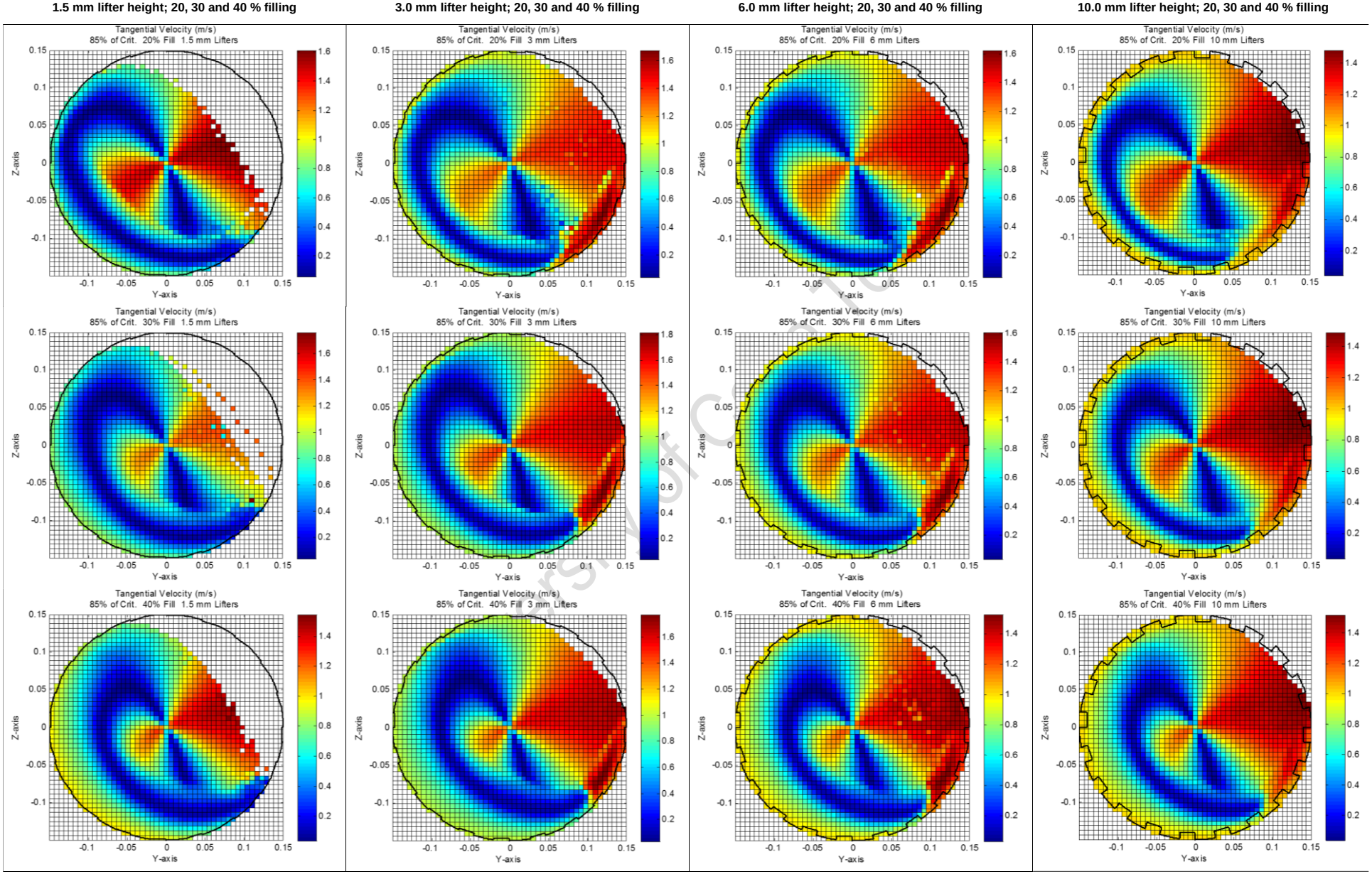

Figure 86: Tangential velocity distribution at 85 % mill critical speed for 20, 30 and 40 % mill filling and 1.5, 3.0, 6.0 and 10.0 mm lifter heights.

D.5. Charge velocity frequency plots

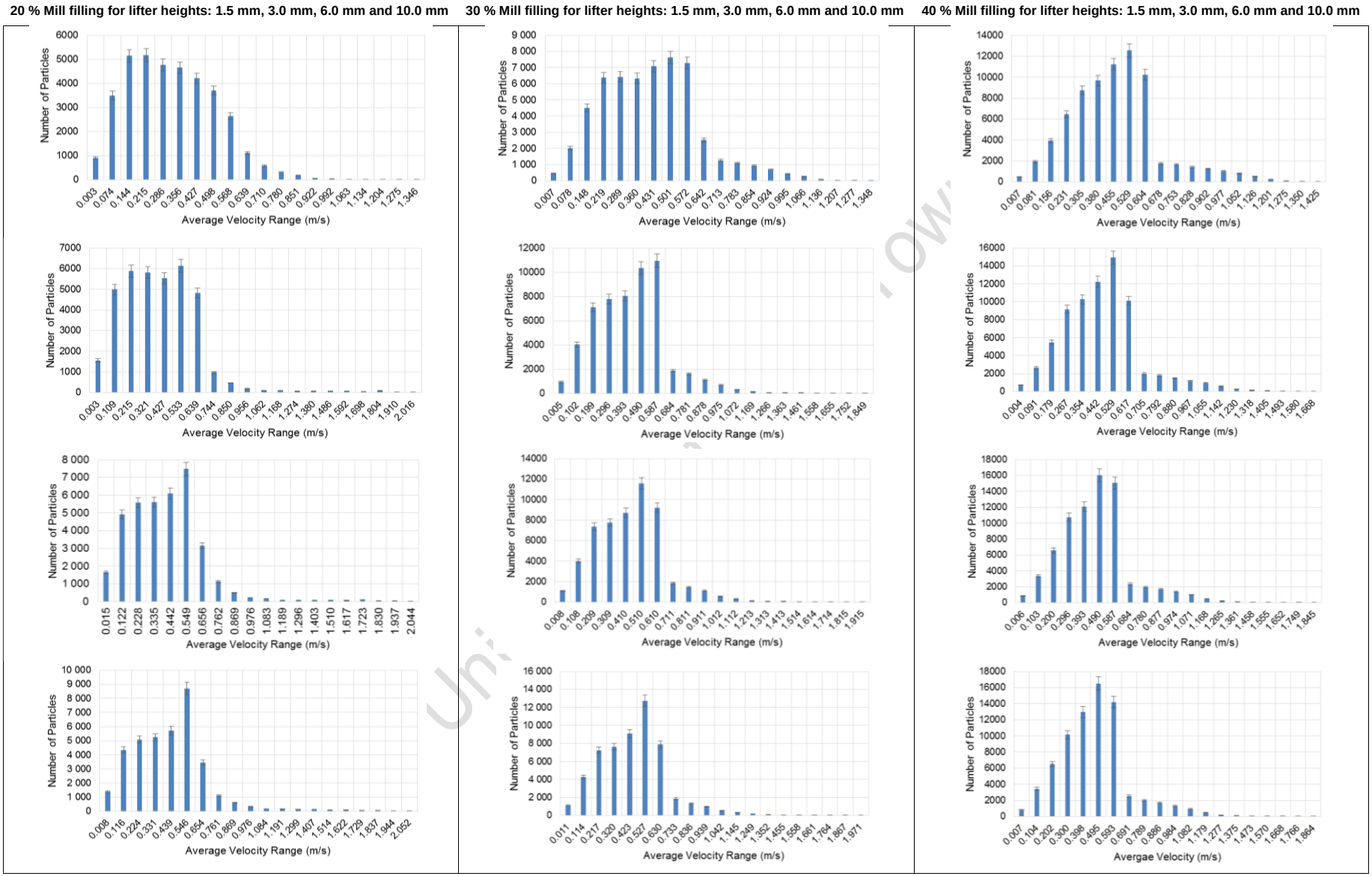

Figure 87: Velocity frequency plots at 55 % mill critical speed for 20 %, 30 % and 40 % mill filling and 1.5 mm, 3.0 mm, 6.0 mm and 10.0 mm lifter heights.

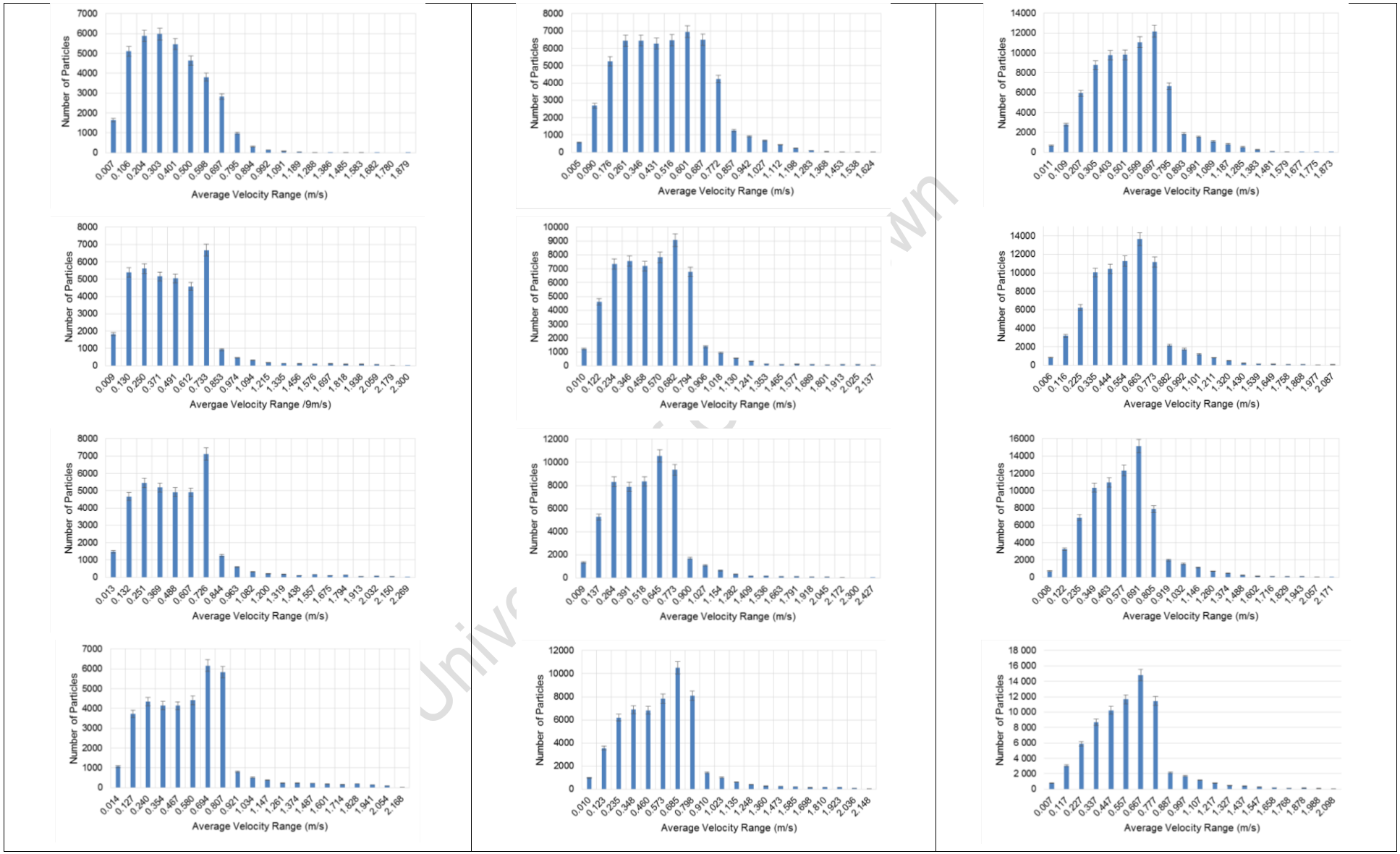

Figure 88: Velocity frequency plots at 70 % mill critical speed for 20 %, 30 % and 40 % mill filling and 1.5 mm, 3.0 mm, 6.0 mm and 10.0 mm lifter heights.

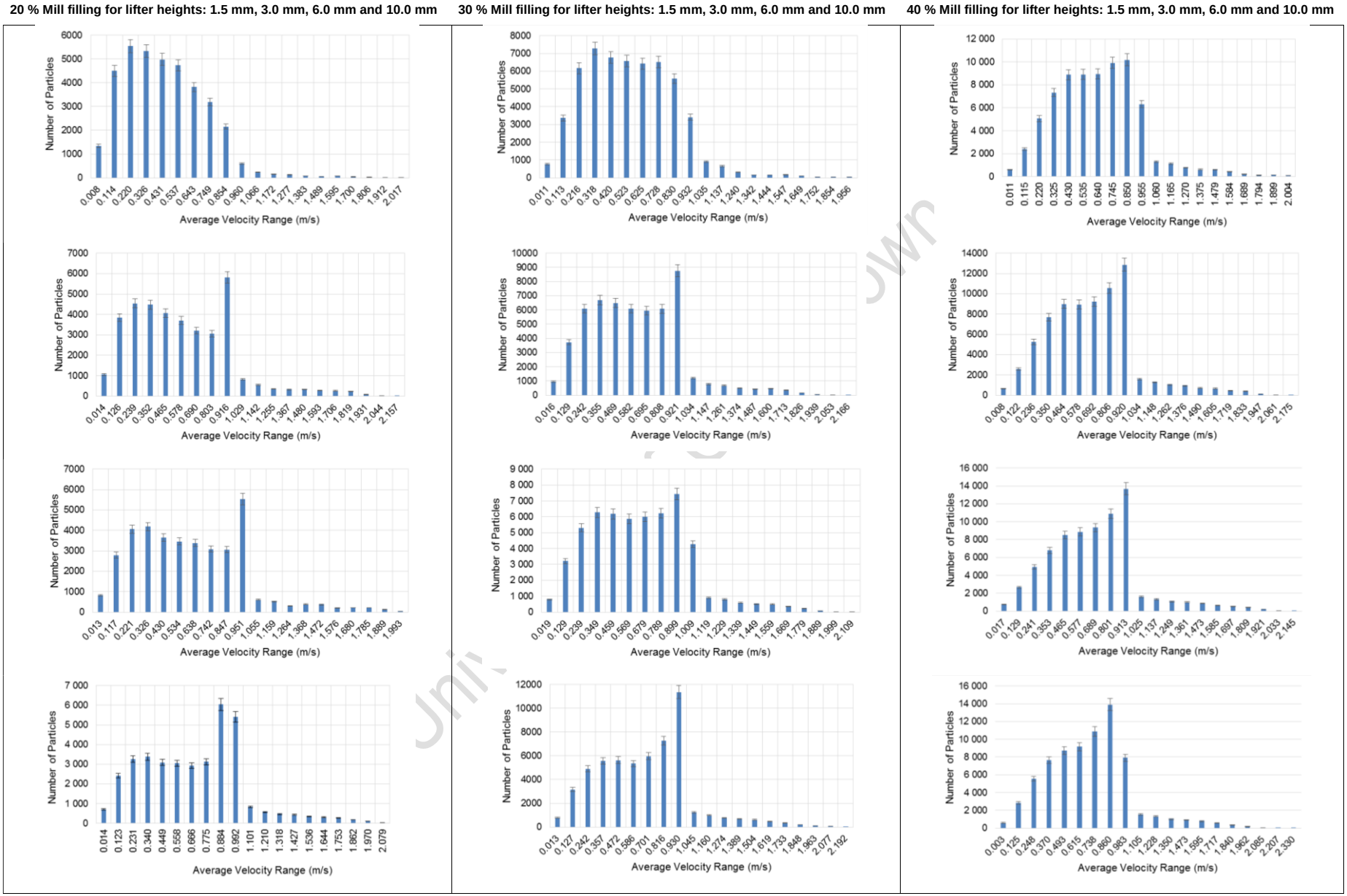

Figure 89: Velocity frequency plots at 85 % mill critical speed for 20 %, 30 % and 40 % mill filling and 1.5 mm, 3.0 mm, 6.0 mm and 10.0 mm lifter heights.

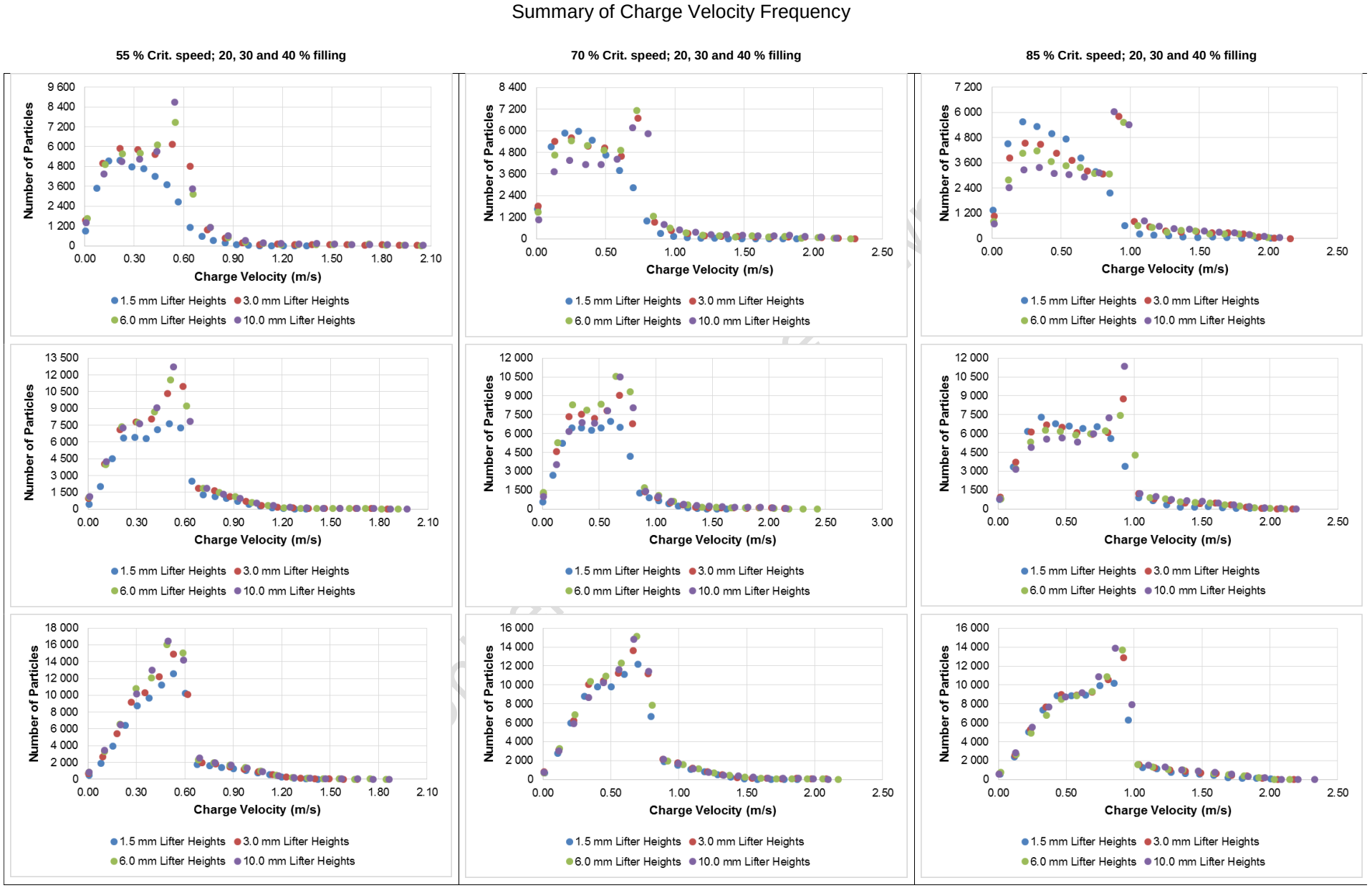

Figure 90: Velocity frequency plots showing lifter height influence at 55%, 70 % and 85 % critical speed respectively for 20 %, 30 % and 40 % mill filling.

D.6. Charge characteristics of interest

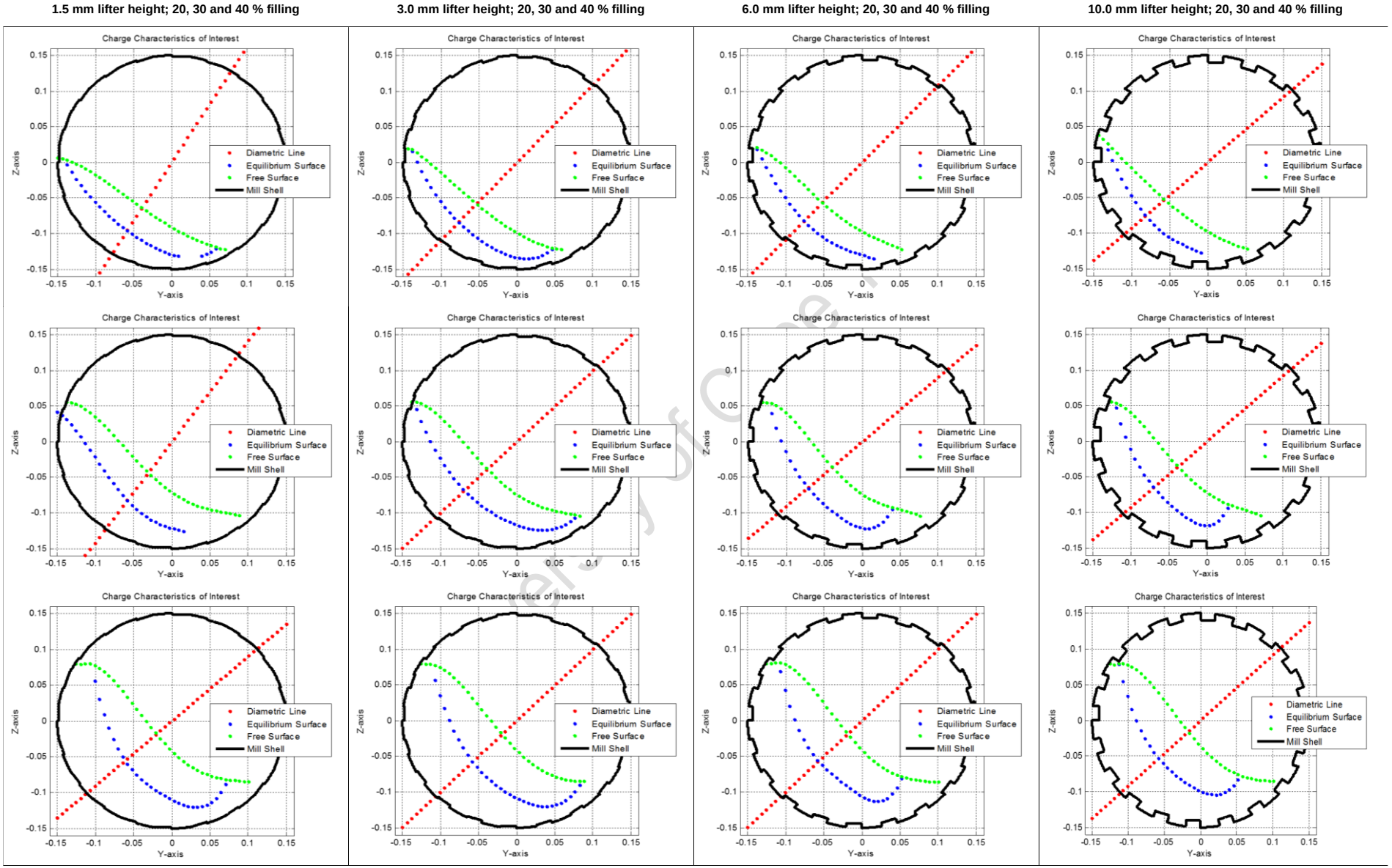

Figure 91: Charge characteristics of interest at 55 % mill critical speed for 20, 30 and 40 % mill filling and 1.5, 3.0, 6.0 and 10.0 mm lifter heights.

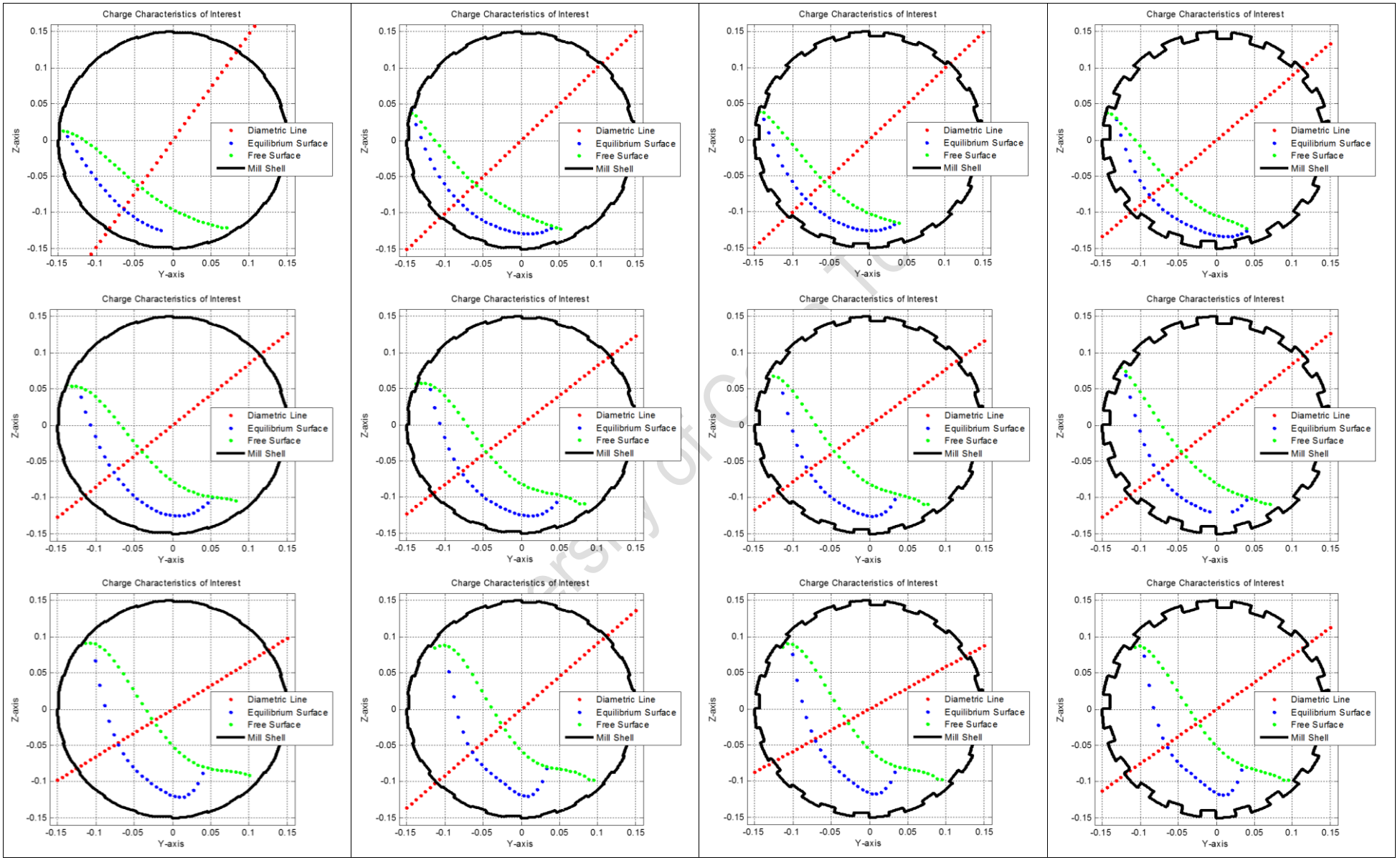

Figure 92: Charge characteristics of interest at 70 % mill critical speed for 20, 30 and 40 % mill filling and 1.5, 3.0, 6.0 and 10.0 mm lifter heights.

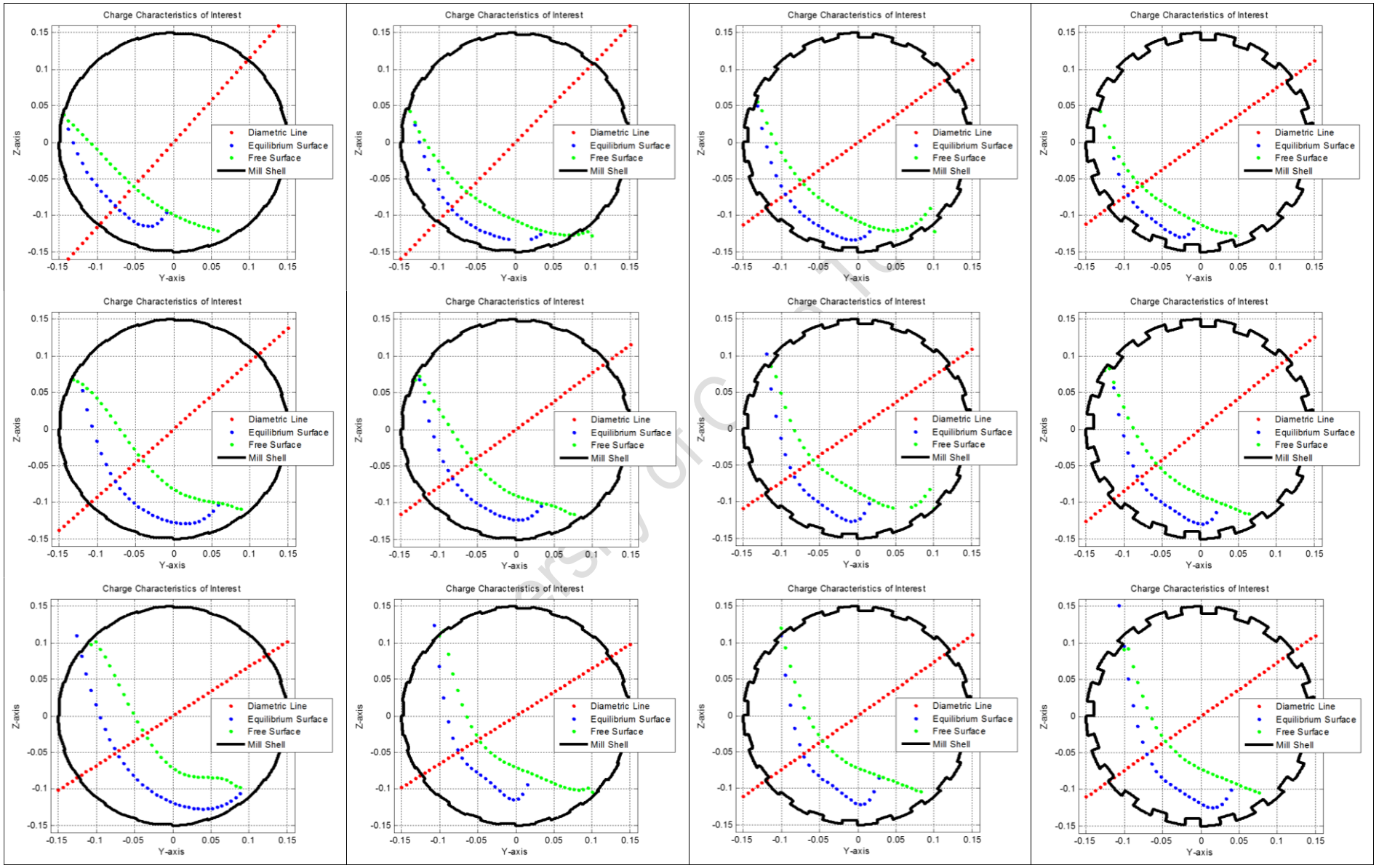

Figure 93: Charge characteristics of interest at 85 % mill critical speed for 20, 30 and 40 % mill filling and 1.5, 3.0, 6.0 and 10.0 mm lifter heights.

D.7. Power draw distribution graphs

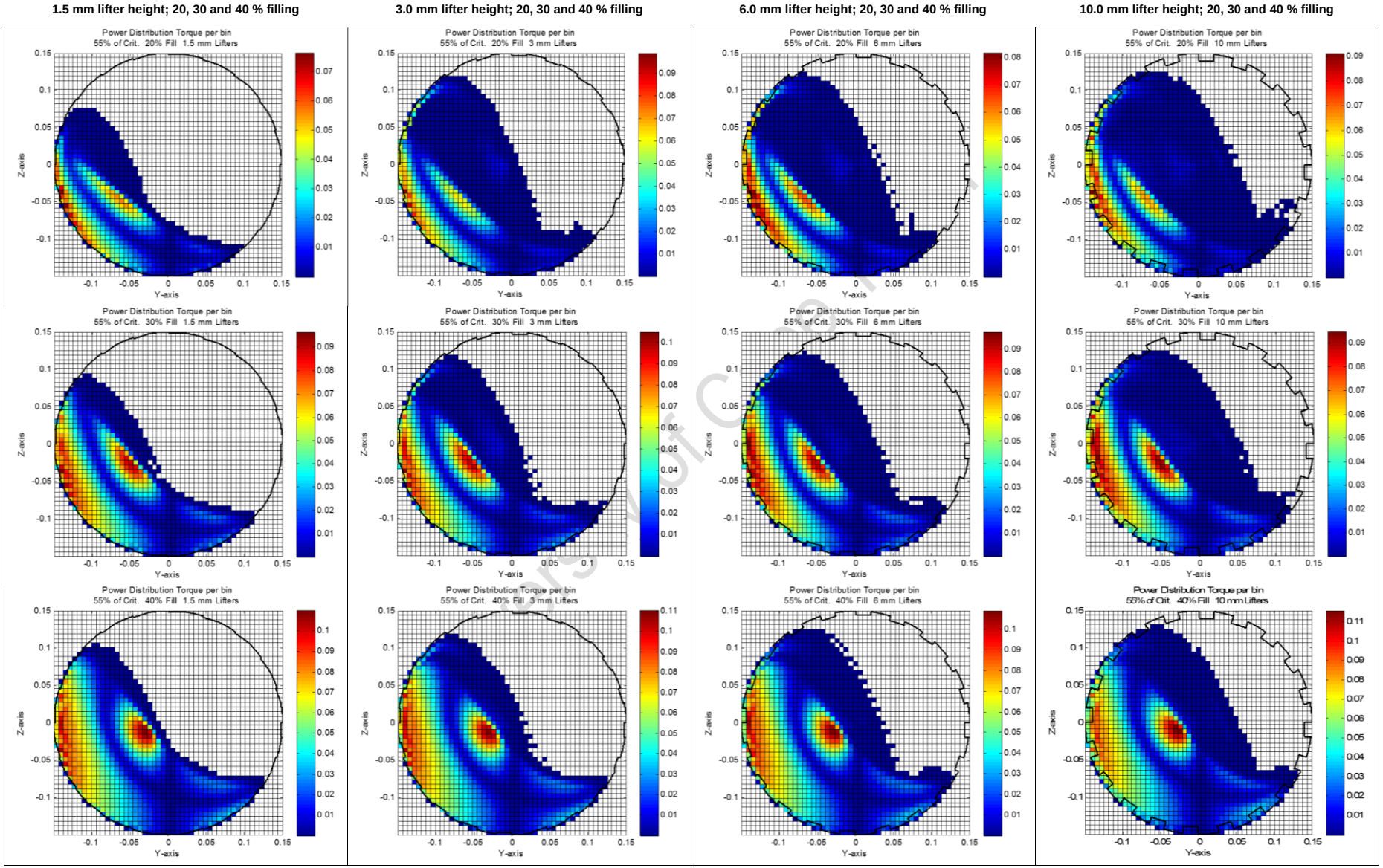

Figure 94: Power draw distribution at 55 % critical mill speed for 20, 30 and 40 % mill filling and 1.5, 3.0, 6.0 and 10.0 mm lifter heights.

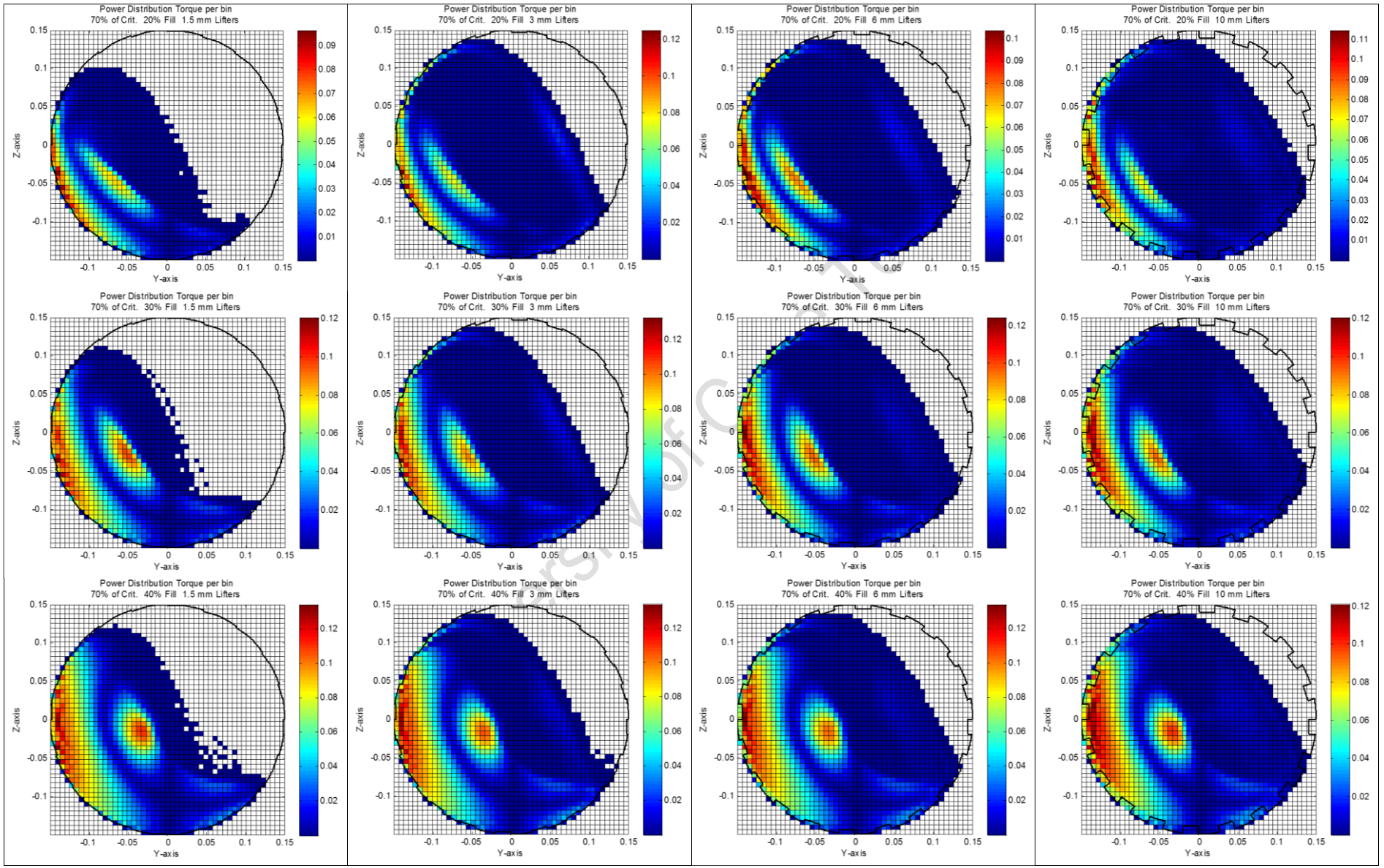

Figure 95: Power draw distribution at 70 % critical mill speed for 20, 30 and 40 % mill filling and 1.5, 3.0, 6.0 and 10.0 mm lifter heights.

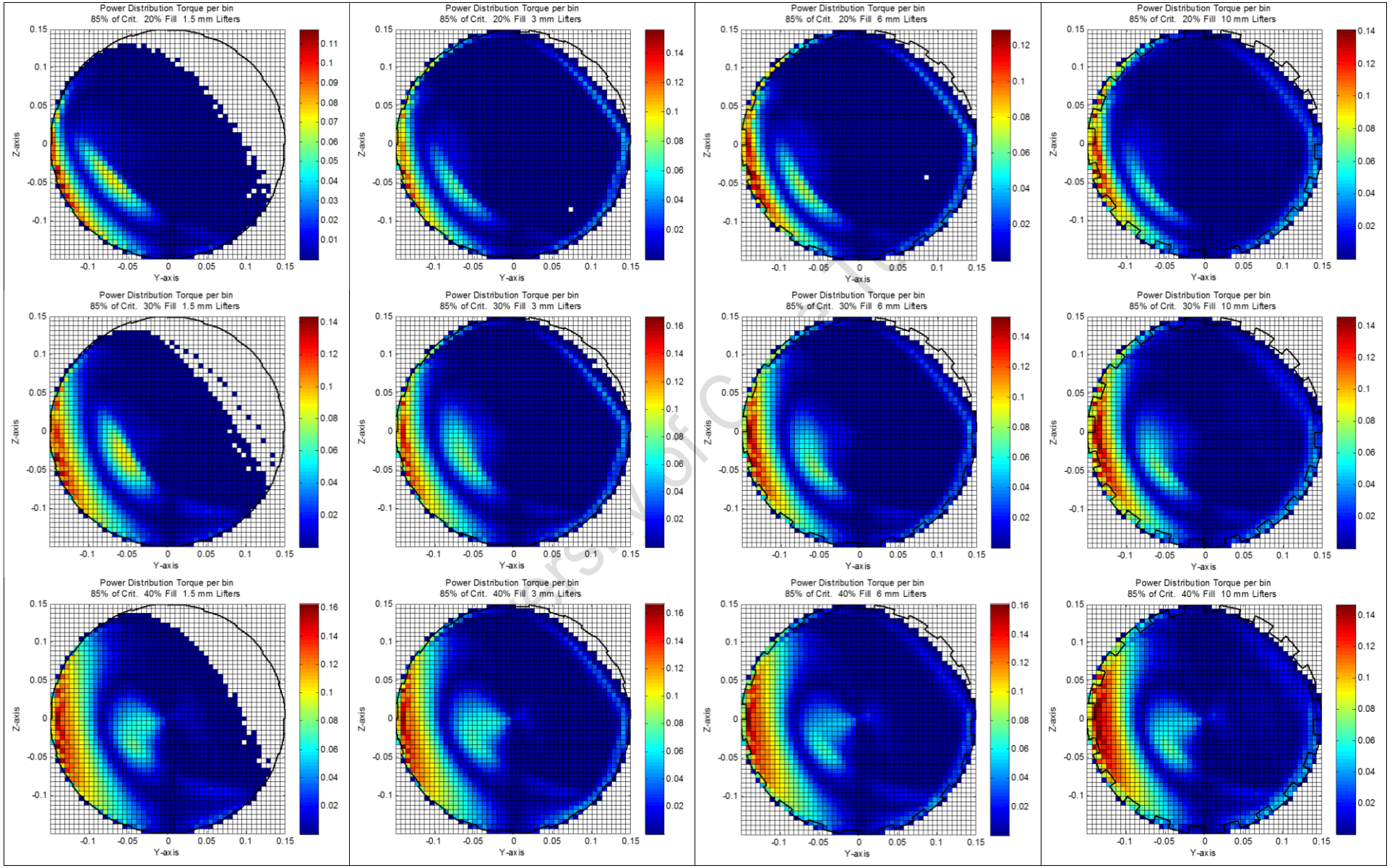

Figure 96: Power draw distribution at 85 % critical mill speed for 20, 30 and 40 % mill filling and 1.5, 3.0, 6.0 and 10.0 mm lifter heights.

D.8. Velocity Profile along the Diametric Line

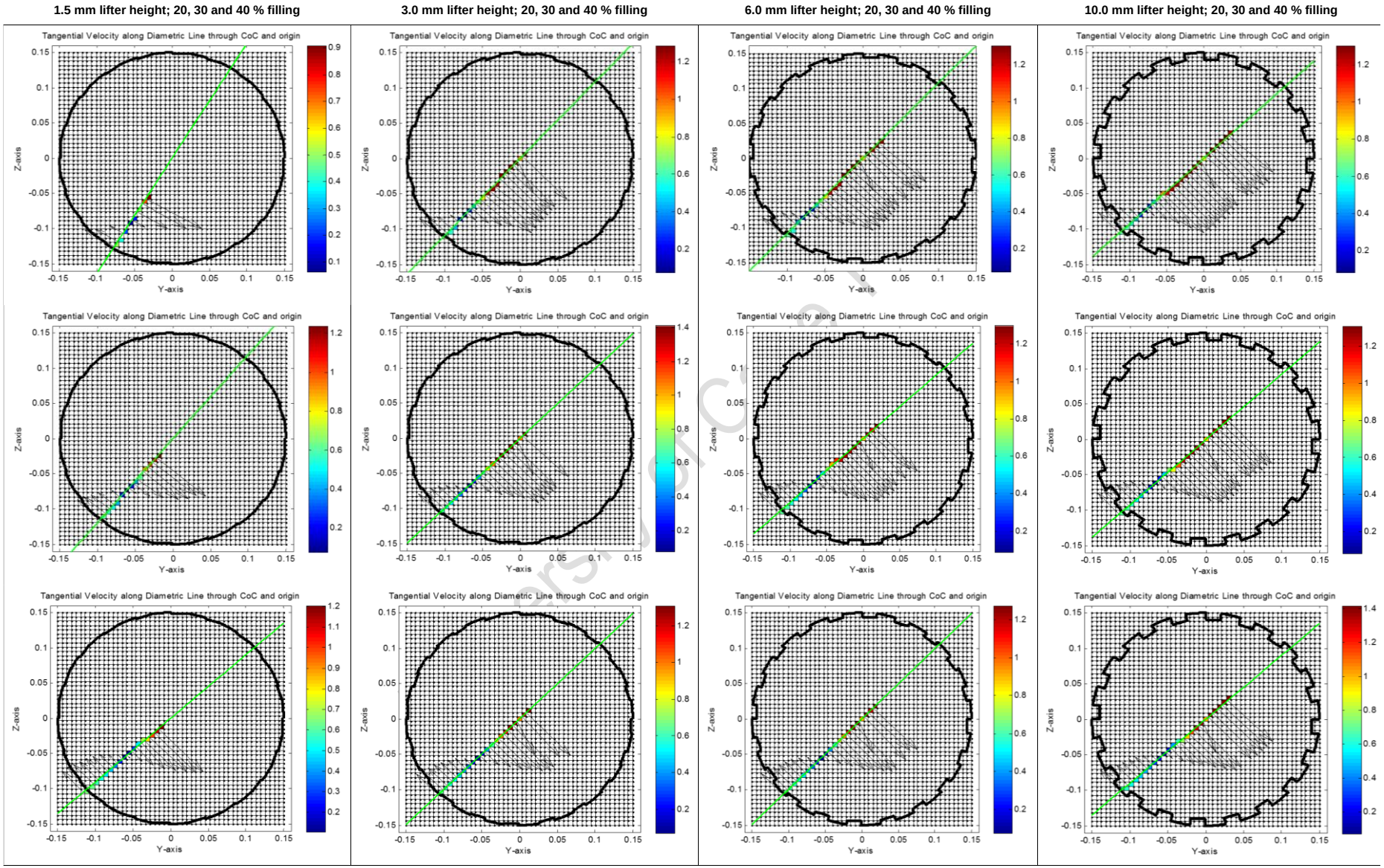

Figure 97: Tangential velocity profile extracted along the diametric line at 55 % critical mill speed for 20, 30 and 40 % mill filling and 1.5, 3.0, 6.0 and 10.0 mm lifter heights.

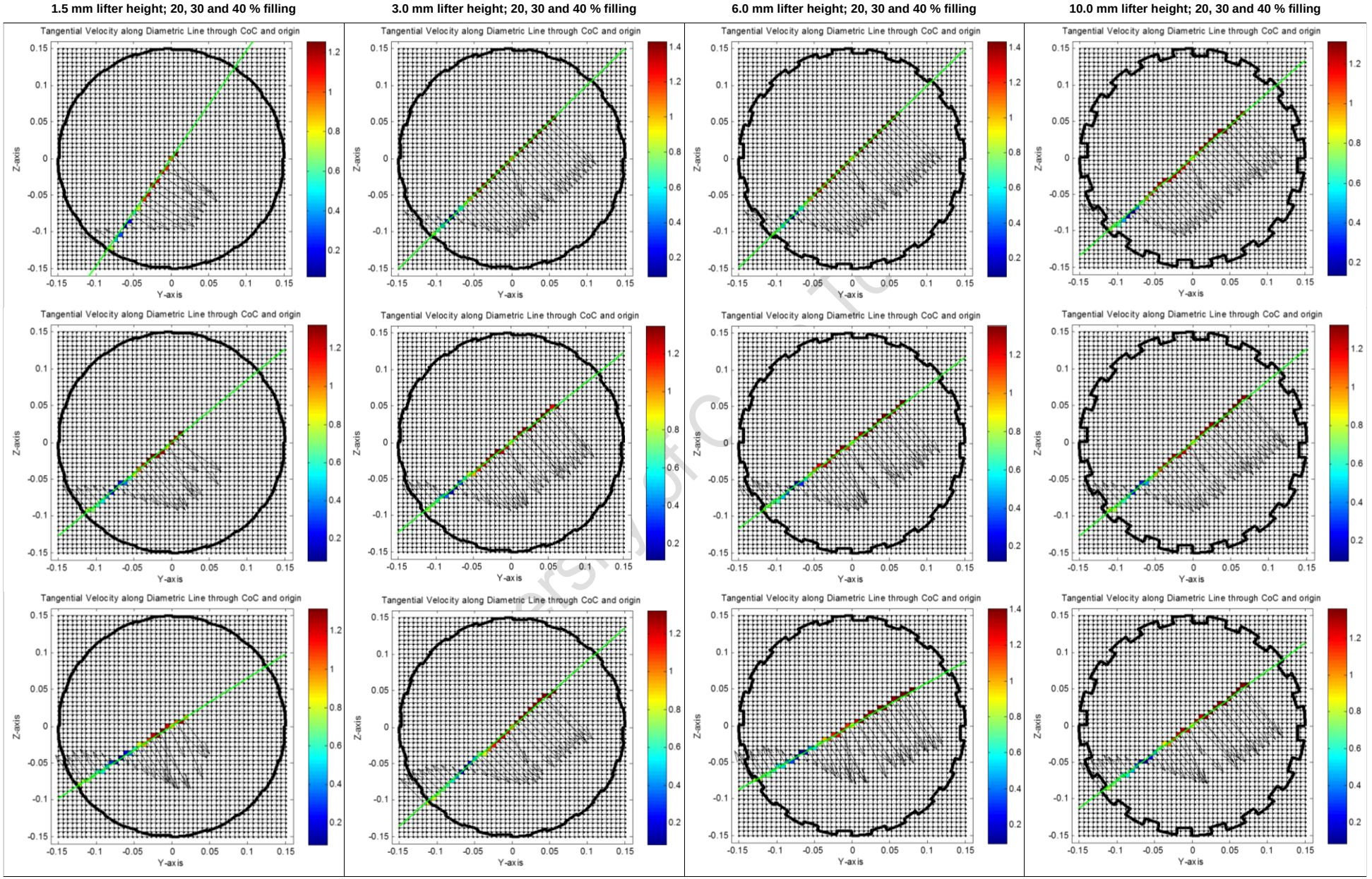

Figure 98: Tangential velocity profile extracted along the diametric line at 70 % critical mill speed for 20, 30 and 40 % mill filling and 1.5, 3.0, 6.0 and 10.0 mm lifter heights.

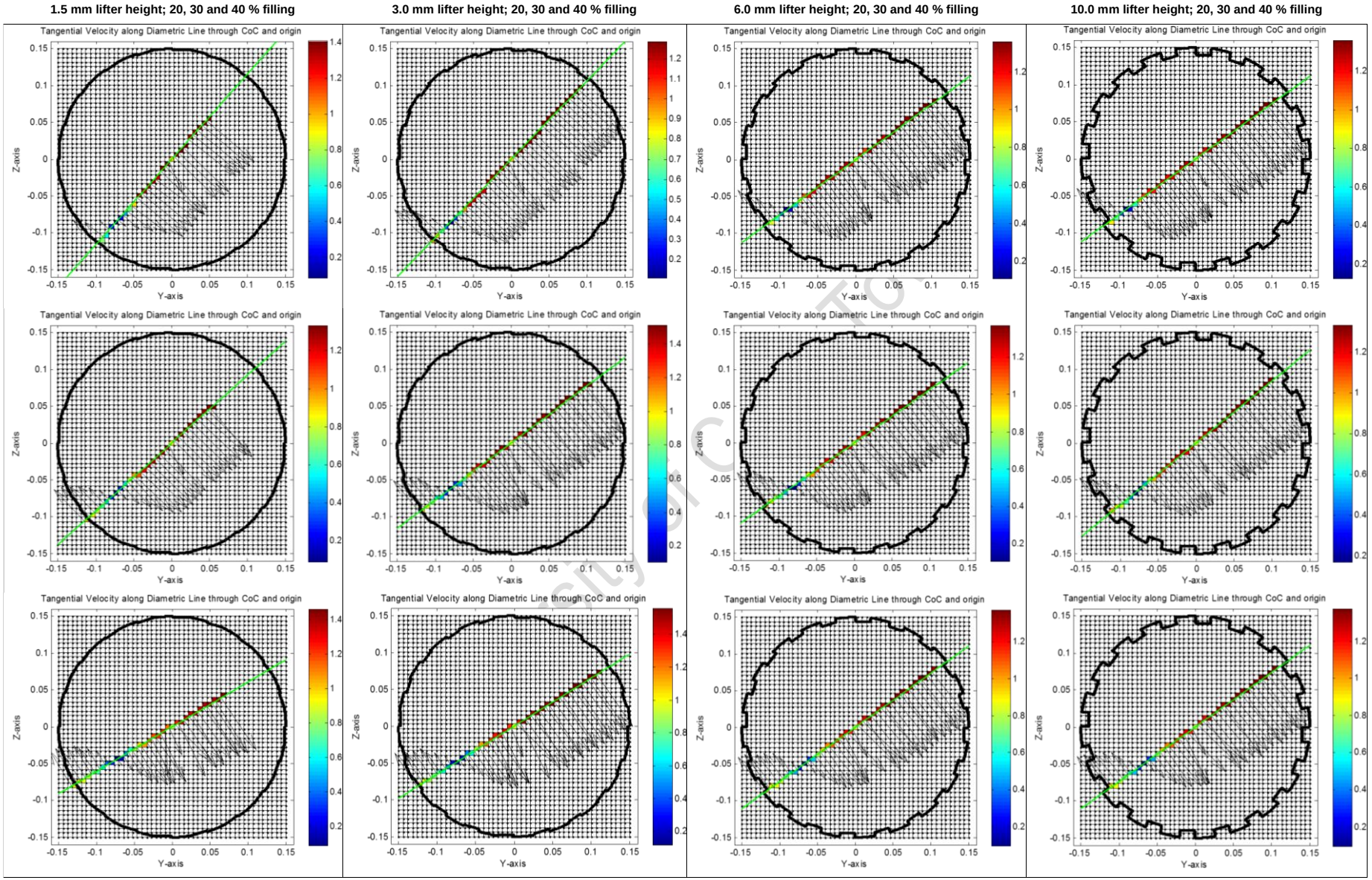

Figure 99: Tangential velocity profile extracted along the diametric line at 85 % critical mill speed for 20, 30 and 40 % mill filling and 1.5, 3.0, 6.0 and 10.0 mm lifter heights.

D.9. Piece-wise Velocity Profile along the Diametric Line

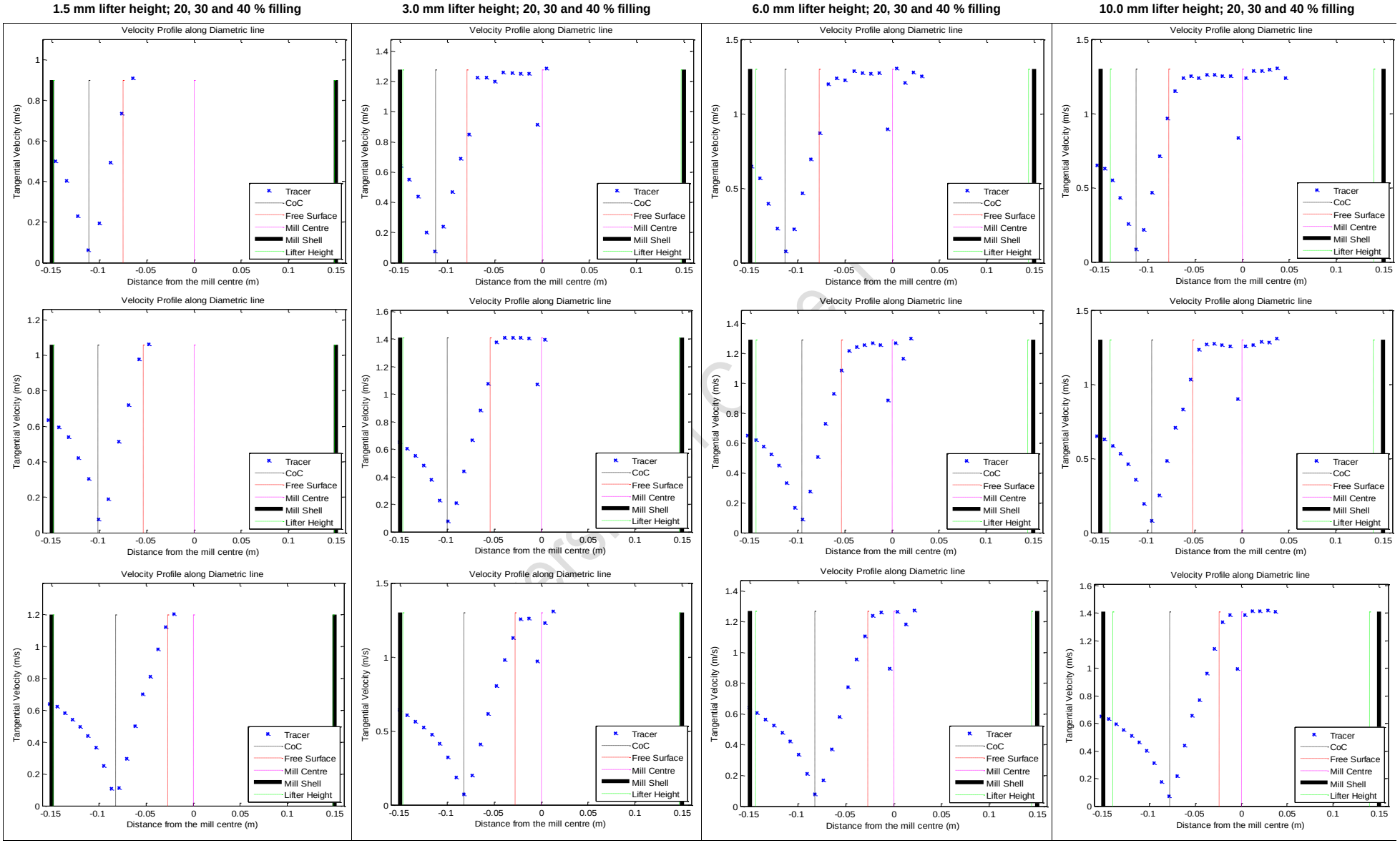

Figure 100: Piece-wise tangential velocity profile along the diametric line at 55 % critical mill speed for 20, 30 and 40 % mill filling and 1.5, 3.0, 6.0 and 10.0 mm lifter heights.

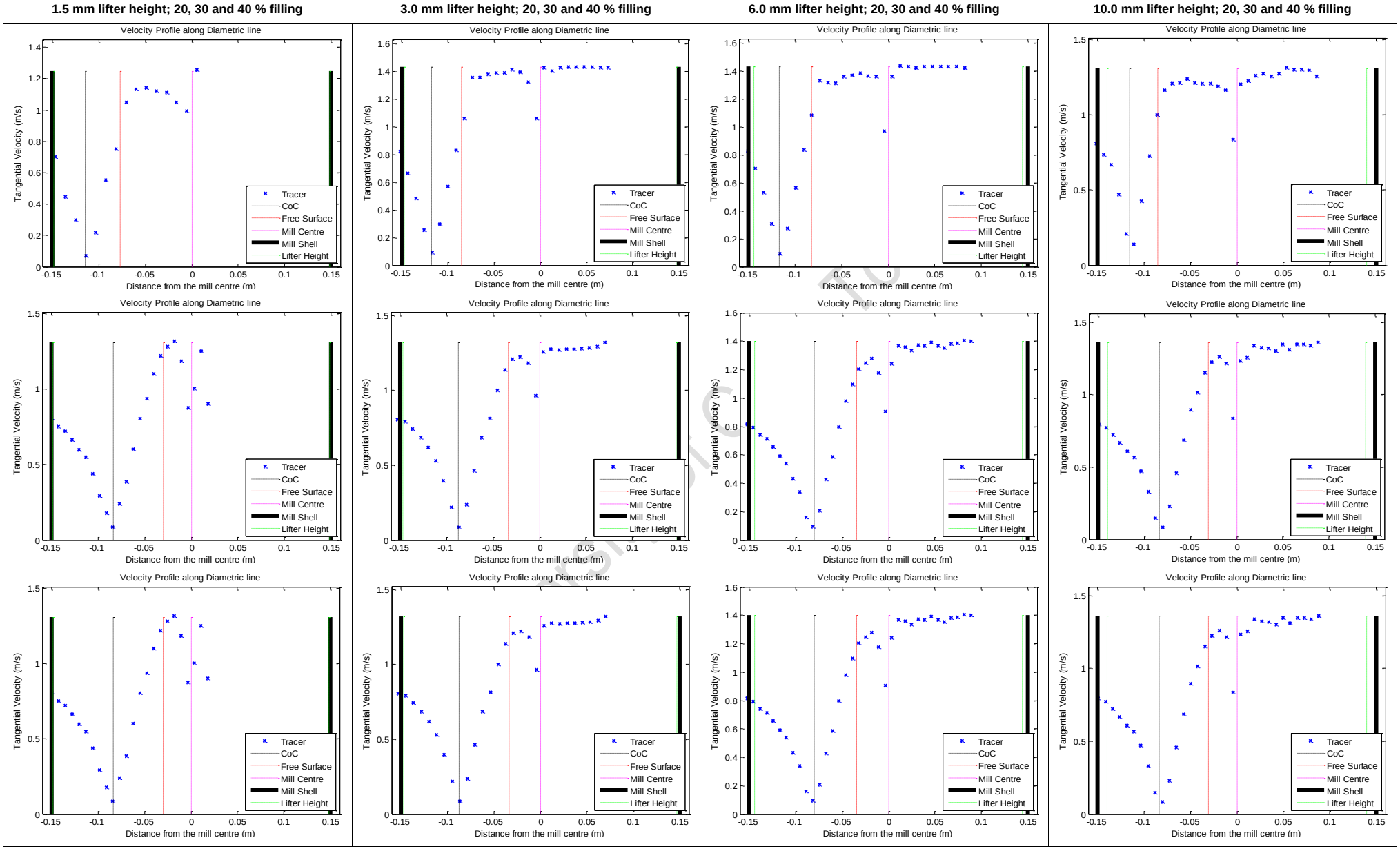

Figure 101: Piece-wise tangential velocity profile along the diametric line at 70 % critical mill speed for 20, 30 and 40 % mill filling and 1.5, 3.0, 6.0 and 10.0 mm lifter heights.

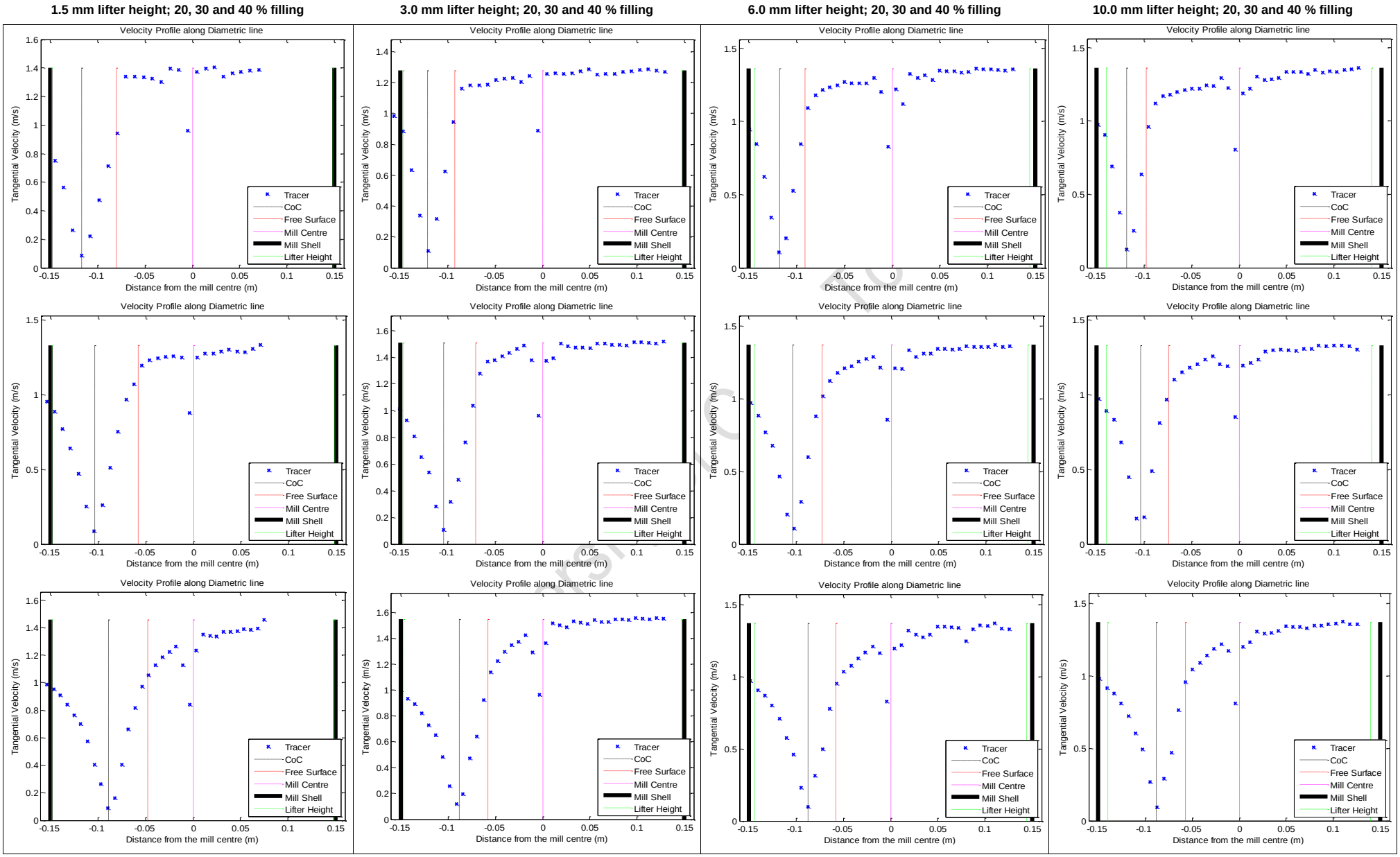

Figure 102: Piece-wise tangential velocity profile along the diametric line at 85 % critical mill speed for 20, 30 and 40 % mill filling and 1.5, 3.0, 6.0 and 10.0 mm lifter heights.

E. Charge Motion

E.1. Centre of Circulation (CoC)

The table below summarises the CoC location coordinates at all operating conditions.

Table 27: Extracted CoC coordinates at all mill filling, critical speed and lifter height settings.

		1.5 mm		3.0 mm		6.0 mm		10.0 mm	
Filling	**Speed**	**y**	**z**	**y**	**z**	**y**	**z**	**y**	**z**
20 %	55 % Crit.	-0.0581	-0.0949	-0.0761	-0.0828	-0.0759	-0.0828	-0.0826	-0.0762
	70 % Crit.	-0.0645	-0.0947	-0.0828	-0.0830	-0.0829	-0.0823	-0.0860	-0.0766
	85 % Crit.	-0.0765	-0.0885	-0.0831	-0.0883	-0.0942	-0.0707	-0.0946	-0.0705
30 %	55 % Crit.	-0.0586	-0.0827	-0.0707	-0.0703	-0.0707	-0.0639	-0.0705	-0.0647
	70 % Crit.	-0.0762	-0.0645	-0.0789	-0.0647	-0.0798	-0.0621	-0.0799	-0.0609
	85 % Crit.	-0.0762	-0.0702	-0.0829	-0.0639	-0.0837	-0.0608	-0.0795	-0.0668
40 %	55 % Crit.	-0.0610	-0.0550	-0.0583	-0.0578	-0.0582	-0.0577	-0.0580	-0.0521
	70 % Crit.	-0.0703	-0.0459	-0.0645	-0.0585	-0.0690	-0.0402	-0.0678	-0.0474
	85 % Crit.	-0.0763	-0.0462	-0.0730	-0.0519	-0.0742	-0.0483	-0.0708	-0.0521

Figure 103 below, illustrates the influence of the lifter height on the height of the CoC above the mill base for changes in the mill filling at 55 %, 70 % and 85 % critical mill speed settings respectively. Figure 104 below illustrates the influence of the lifter height on the CoC inclination angle at all critical speed settings for 20 %, 30 % and 40 % filling respectively.

a)

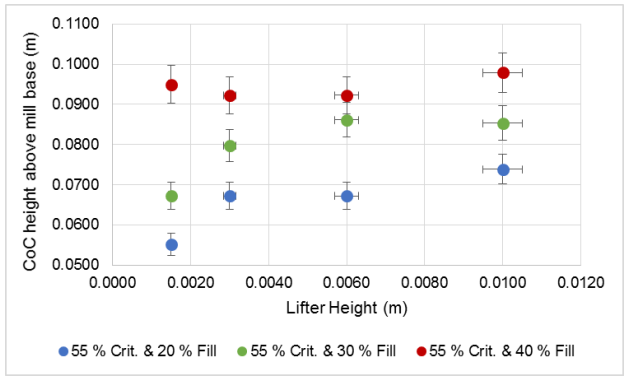

b)

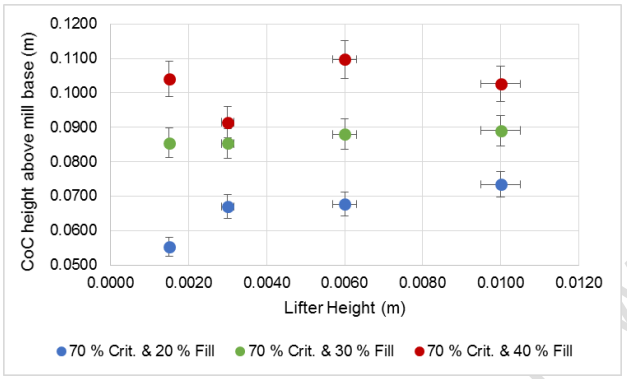

c)

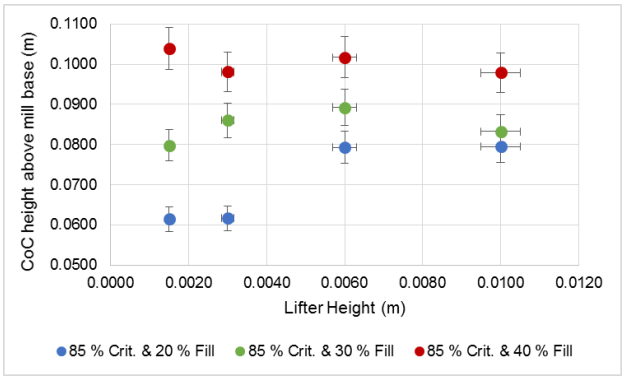

Figure 103: Influence of the lifter height on the CoC height for all mill filling levels at a) 55 %, b) 70 % and c) 85 % critical speed respectively.

a)

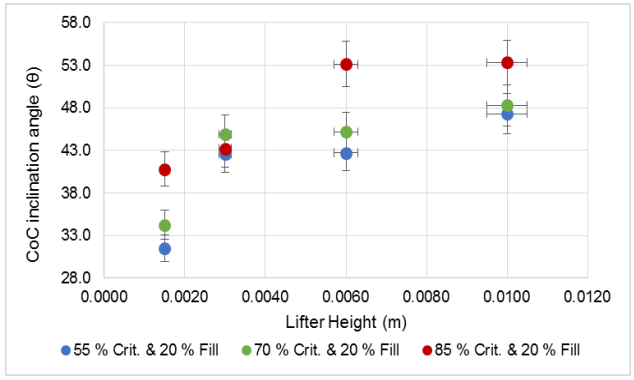

b)

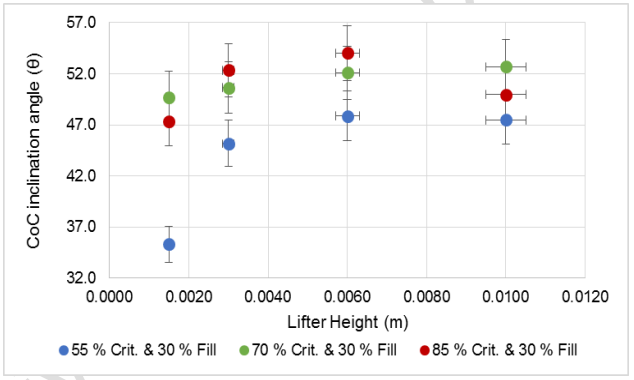

c)

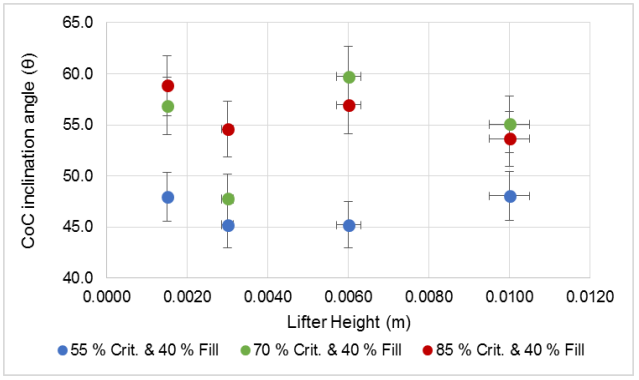

Figure 104: Influence of the lifter height on the CoC inclination angle above the mill base for all critical speed settings at a) 20 %, b) 30 % and c) 40 % filling respectively.

E.2. Shoulder and Toe Locations

The tables below summarise the shoulder and toe location coordinates respectively according to all critical speed, filling and lifter height settings.

Table 28: Shoulder location y-z axis coordinates at all filling, critical speed and lifter height settings.

		1.5 mm		3.0 mm		6.0 mm		10.0 mm	
Filling	**Speed**	**y**	**z**	**y**	**z**	**y**	**z**	**y**	**z**
20 %	55 % Crit.	-0.1446	0.0063	-0.1401	0.0188	-0.1393	0.0193	-0.1401	0.0376
	70 % Crit.	-0.1446	0.0116	-0.1401	0.0376	-0.1401	0.0376	-0.1401	0.0376
	85 % Crit.	-0.1401	0.0376	-0.1339	0.0430	-0.1276	0.0555	-0.1285	0.0430
30 %	55 % Crit.	-0.1330	0.0555	-0.1321	0.0555	-0.1276	0.0555	-0.1222	0.0555
	70 % Crit.	-0.1330	0.0555	-0.1321	0.0564	-0.1222	0.0681	-0.1222	0.0618
	85 % Crit.	-0.1276	0.0681	-0.1285	0.0681	-0.1097	0.0860	-0.1222	0.0797
40 %	55 % Crit.	-0.1213	0.0797	-0.1222	0.0797	-0.1222	0.0797	-0.1213	0.0797
	70 % Crit.	-0.1097	0.0913	-0.1097	0.0860	-0.1097	0.0860	-0.1034	0.0860
	85 % Crit.	-0.1088	0.0976	-0.0963	0.1101	-0.0963	0.1093	-0.0999	0.0913

Table 29: Toe coordinates along y-z axis at all critical speed, mill filling and lifter height settings.

		1.5 mm		3.0 mm		6.0 mm		10.0 mm	
Speed	**Filling**	**y**	**z**	**y**	**z**	**y**	**z**	**y**	**z**
55 % Crit.	20 %	0.0676	-0.1218	0.0613	-0.1218	0.0560	-0.1218	0.0497	-0.1218
	30 %	0.0864	-0.1030	0.0864	-0.1039	0.0801	-0.1039	0.0739	-0.1039
	40 %	0.1043	-0.0851	0.1043	-0.0851	0.0981	-0.0860	0.0981	-0.0851
70 % Crit.	20 %	0.0613	-0.1218	0.0497	-0.1218	0.0466	-0.1187	0.0434	-0.1218
	30 %	0.0864	-0.1039	0.0801	-0.1039	0.0739	-0.1039	0.0739	-0.1093
	40 %	0.1043	-0.0913	0.0981	-0.0976	0.0927	-0.0976	0.0927	-0.0976
85 % Crit.	20 %	0.0613	-0.1209	0.0497	-0.1281	0.0497	-0.1218	0.0372	-0.1281
	30 %	0.0864	-0.1039	0.0739	-0.1155	0.0676	-0.1093	0.0613	-0.1155
	40 %	0.0927	-0.0976	0.0873	-0.1039	0.0864	-0.1030	0.0864	-0.1048

Figures 105, 106 and 107 below illustrate, at each mill filling level for 55 %, 70 % and 85 % critical speed settings, the influence of the lifter height on the movement of the shoulder location. The height of the shoulder above the mill base, distance between the shoulder and the mill centre and inclination angle (°) of the shoulder above the mill centre was assessed. The same is shown for the movement of the toe location in figures 108, 109 and 110 respectively.

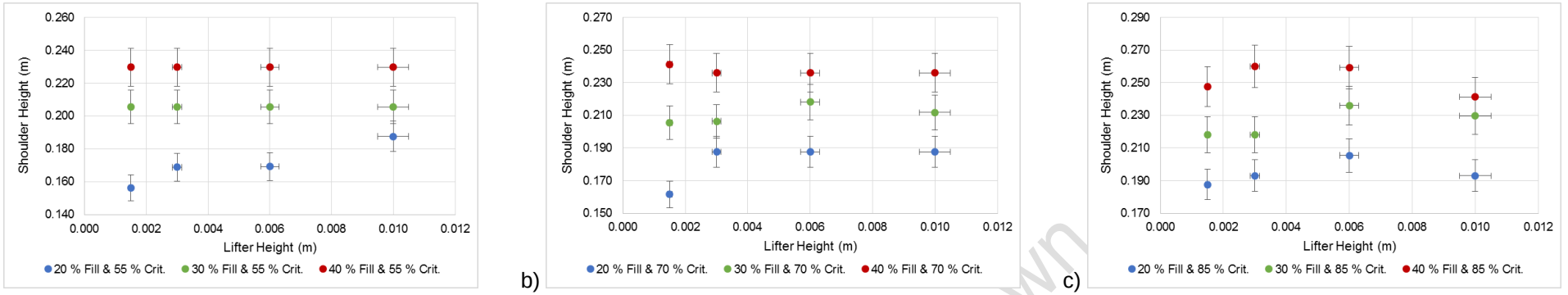

Figure 105: Influence of the lifter height on the shoulder height at all filling levels for a) 55 %, b) 70 % and c) 85 % critical speeds respectively.

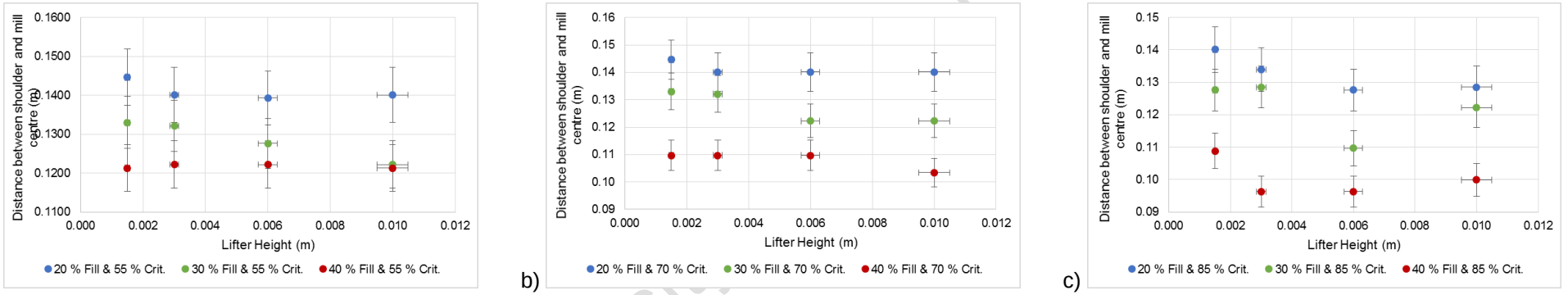

Figure 106: Influence of the lifter height on the distance between the shoulder and mill centre at all filling levels for a) 55 %, b) 70 % and c) 85 % critical speeds respectively.

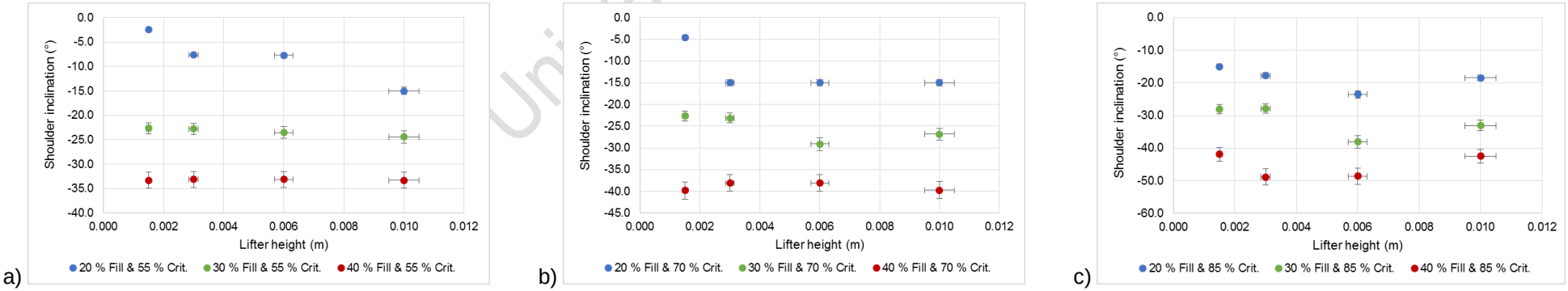

Figure 107: Influence of the lifter height on the shoulder inclination above the mill centre at all filling levels for a) 55 %, b) 70 % and c) 85 % critical speeds respectively.

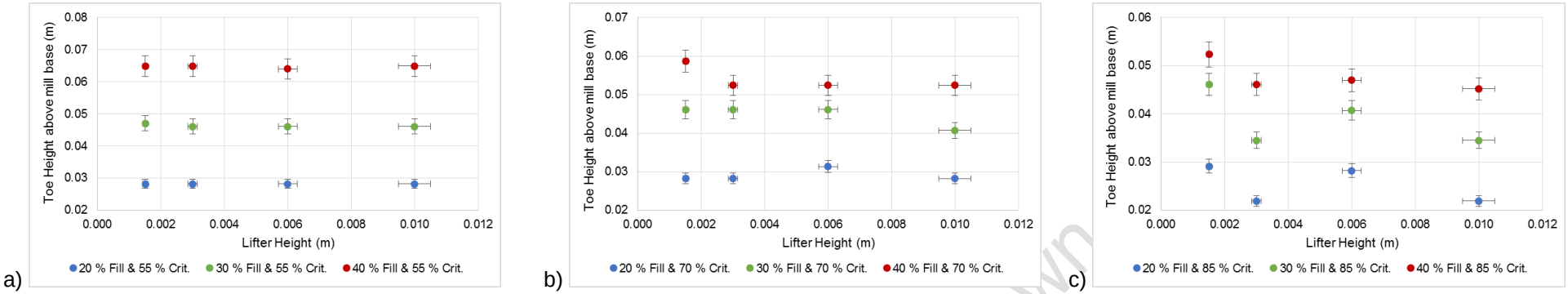

Figure 108: Influence of the lifter height on the height of the toe above the mill base at all filling levels for a) 55 %, b) 70 % and c) 85 % critical speed setting respectively.

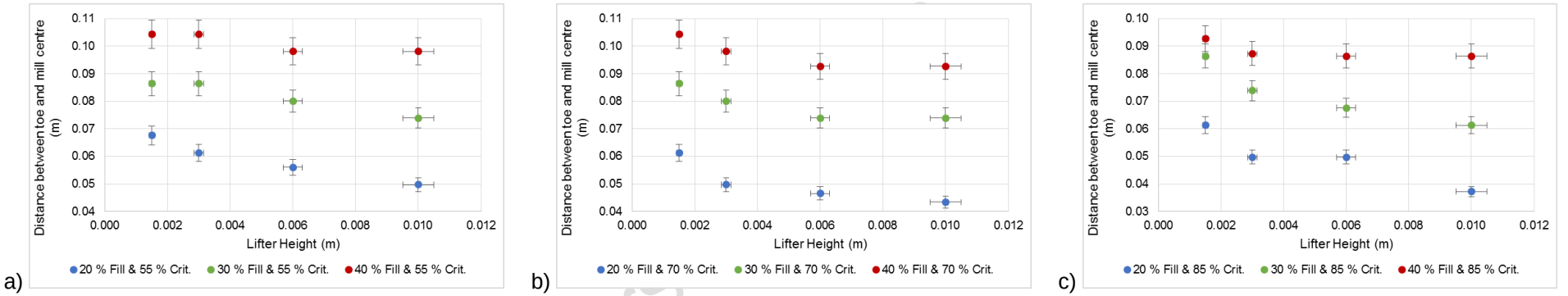

Figure 109: Influence of the lifter height on the distance between the toe and mill centre at all filling levels for a) 55 %, b) 70 % and c) 85 % critical speed setting respectively.

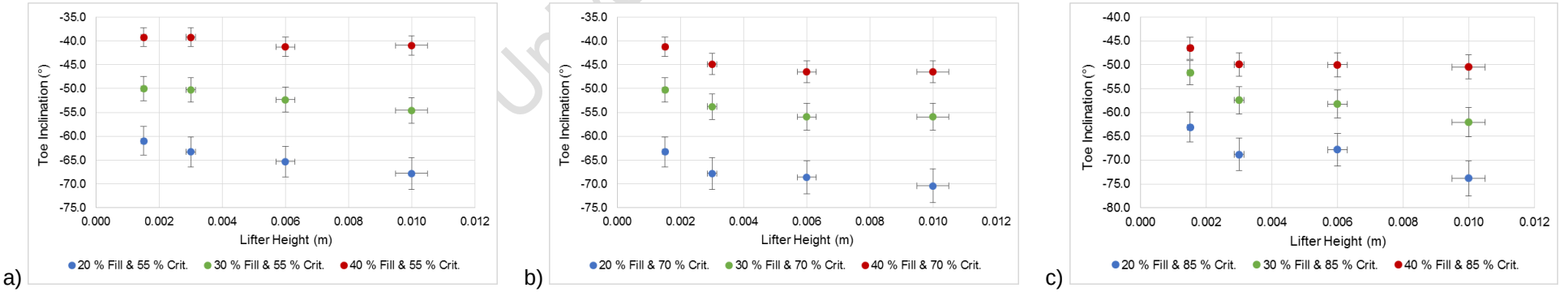

Figure 110: Influence of the lifter height on the toe inclination angle at all filling levels for a) 55 %, b) 70 % and c) 85 % critical speed setting respectively.

F. Maximum power draw analysis

The figure below illustrates the influence of the lifter height on the maximum power draw for all mill filling levels at 55 %, 70 % and 85 % critical speed settings respectively.

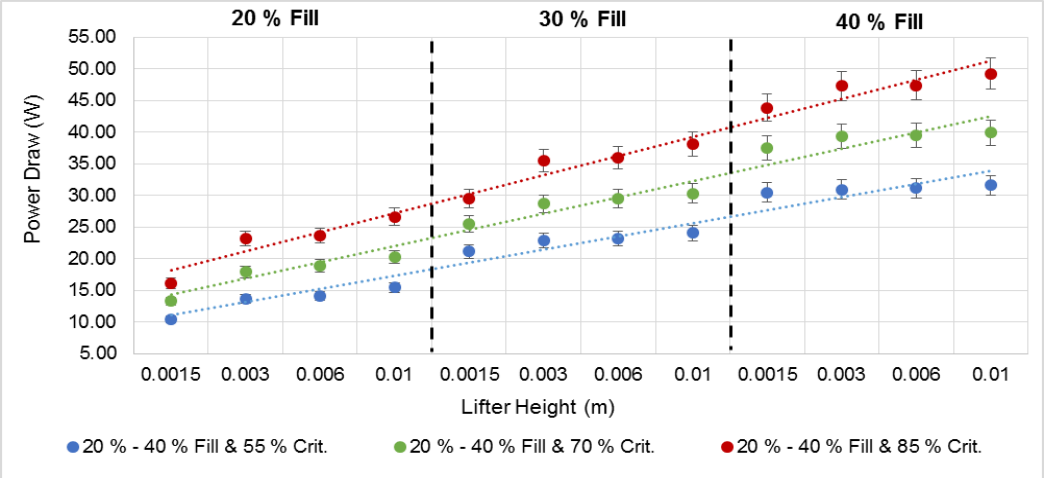

Figure 111: Influence of the lifter height on the highest power draw calculated at all critical speed and filling levels.

The table below summarises the linear trend-line equations and corresponding R^2 values.

Table 30: Linear trend-line equations and corresponding R^2 values for the influence of the lifter height (x) on the highest power draw calculated (y).

55 % Crit.	y = 2.0710 x + 8.9636	R^2 = 0.9567
70 % Crit.	y = 2.5603 x + 11.721	R^2 = 0.9683
85 % Crit.	y = 3.0105 x + 15.125	R^2 = 0.9792

G. Velocity profile along the diametric line

The tables below summarise the velocity profile data at all filling and lifter height levels at 55 %, 70 % and 85 % critical speed settings respectively.

Table 31: Velocity profile data points and corresponding radial distance from the mill centre at 55 % crit. speed and all filling and lifter height settings.

1.5 mm Lifter Heights						3.0 mm Lifter Heights						6.0 mm Lifter Heights						10.0 mm Lifter Heights					
20 % Fill		30 % Fill		40 % Fill		20 % Fill		30 % Fill		40 % Fill		20 % Fill		30 % Fill		40 % Fill		20 % Fill		30 % Fill		40 % Fill	
R (m)	Vx (m/s)	R (m)	Vx (m/s)	R (m)	Vx (m/s)	R (m)	Vx (m/s)	R (m)	Vx (m/s)	R (m)	Vx (m/s)	R (m)	Vx (m/s)	R (m)	Vx (m/s)	R (m)	Vx (m/s)	R (m)	Vx (m/s)	R (m)	Vx (m/s)	R (m)	Vx (m/s)
-0.147	0.500	-0.154	0.634	-0.153	0.642	-0.149	0.6445	-0.151	0.652	-0.151	0.642	-0.150	0.648	-0.153	0.650	-0.151	0.642	-0.154	0.653	-0.154	0.653	-0.152	0.654
-0.135	0.403	-0.143	0.595	-0.144	0.623	-0.140	0.5523	-0.142	0.605	-0.142	0.606	-0.140	0.569	-0.144	0.621	-0.142	0.607	-0.146	0.629	-0.145	0.630	-0.144	0.635
-0.123	0.229	-0.132	0.540	-0.136	0.582	-0.131	0.4406	-0.134	0.551	-0.134	0.565	-0.131	0.466	-0.136	0.578	-0.134	0.566	-0.137	0.550	-0.137	0.584	-0.136	0.596
-0.111	0.064	-0.122	0.423	-0.128	0.541	-0.122	0.1991	-0.125	0.483	-0.125	0.523	-0.122	0.323	-0.128	0.524	-0.125	0.525	-0.129	0.430	-0.129	0.533	-0.128	0.555
-0.100	0.196	-0.111	0.303	-0.120	0.496	-0.113	0.0767	-0.117	0.379	-0.116	0.475	-0.113	0.076	-0.120	0.449	-0.116	0.479	-0.121	0.258	-0.120	0.464	-0.119	0.512
-0.088	0.493	-0.101	0.076	-0.111	0.441	-0.104	0.2392	-0.108	0.226	-0.108	0.412	-0.104	0.225	-0.111	0.334	-0.108	0.422	-0.112	0.085	-0.112	0.356	-0.111	0.464
-0.076	0.734	-0.090	0.189	-0.103	0.364	-0.095	0.4687	-0.099	0.079	-0.099	0.321	-0.095	0.466	-0.103	0.169	-0.099	0.338	-0.104	0.219	-0.104	0.196	-0.103	0.403
-0.064	0.909	-0.079	0.516	-0.095	0.252	-0.086	0.6915	-0.091	0.209	-0.091	0.186	-0.086	0.694	-0.095	0.088	-0.091	0.213	-0.096	0.469	-0.096	0.082	-0.095	0.313
		-0.069	0.720	-0.087	0.107	-0.077	0.8511	-0.082	0.439	-0.082	0.072	-0.077	0.872	-0.087	0.277	-0.082	0.077	-0.087	0.711	-0.087	0.253	-0.086	0.178
		-0.058	0.979	-0.078	0.113	-0.068	1.228	-0.073	0.668	-0.073	0.200	-0.068	1.199	-0.078	0.507	-0.073	0.170	-0.079	0.969	-0.079	0.484	-0.078	0.073
		-0.048	1.062	-0.070	0.296	-0.059	1.2281	-0.065	0.881	-0.065	0.408	-0.059	1.238	-0.070	0.728	-0.065	0.374	-0.071	1.152	-0.071	0.708	-0.070	0.220
		-0.037	1.238	-0.062	0.501	-0.050	1.1996	-0.056	1.075	-0.056	0.616	-0.050	1.226	-0.062	0.931	-0.056	0.584	-0.062	1.237	-0.062	0.829	-0.062	0.439
				-0.054	0.703	-0.041	1.2611	-0.047	1.375	-0.047	0.807	-0.041	1.215	-0.054	1.087	-0.047	0.778	-0.054	1.250	-0.054	1.031	-0.054	0.657
				-0.045	0.812	-0.032	1.2576	-0.039	1.409	-0.039	0.982	-0.032	1.276	-0.045	1.220	-0.039	0.955	-0.046	1.241	-0.046	1.233	-0.045	0.768
				-0.037	0.984	-0.023	1.2542	-0.030	1.410	-0.030	1.130	-0.023	1.270	-0.037	1.242	-0.030	1.107	-0.037	1.263	-0.037	1.268	-0.037	0.961
				-0.029	1.125	-0.014	1.2541	-0.022	1.411	-0.022	1.256	-0.014	1.274	-0.029	1.257	-0.022	1.239	-0.029	1.261	-0.029	1.275	-0.029	1.142
				-0.021	1.204	-0.005	0.9155	-0.013	1.406	-0.013	1.262	-0.005	0.895	-0.021	1.271	-0.013	1.262	-0.021	1.251	-0.021	1.266	-0.021	1.332
						0.005	1.2879	-0.004	1.072	-0.004	0.973	0.005	1.305	-0.012	1.256	-0.004	0.897	-0.012	1.252	-0.012	1.256	-0.012	1.385
								0.004	1.395	0.004	1.232	0.014	1.210	-0.004	0.887	0.004	1.266	-0.004	0.837	-0.004	0.903	-0.004	0.998
										0.013	1.309	0.023	1.280	0.004	1.271	0.013	1.185	0.004	1.238	0.004	1.257	0.004	1.388
												0.032	1.254	0.012	1.166	0.022	1.275	0.012	1.287	0.012	1.266	0.012	1.416
														0.021	1.299			0.021	1.288	0.021	1.287	0.021	1.415
																		0.029	1.297	0.029	1.283	0.029	1.417
																		0.037	1.304	0.037	1.309	0.037	1.409
																		0.046	1.238				

Table 32: Velocity profile data points and corresponding radial distance from the mill centre at 70 % crit. speed and all filling and lifter height settings.

1.5 mm Lifter Heights						3.0 mm Lifter Heights					
20 % Fill		30 % Fill		40 % Fill		20 % Fill		30 % Fill		40 % Fill	
R (m)	Vx (m/s)	R (m)	Vx (m/s)	R (m)	Vx (m/s)	R (m)	Vx (m/s)	R (m)	Vx (m/s)	R (m)	Vx (m/s)
-0.147	0.702	-0.148	0.747	-0.150	0.808	-0.152	0.824	-0.146	0.788	-0.153	0.808
-0.136	0.447	-0.140	0.705	-0.143	0.754	-0.143	0.667	-0.139	0.713	-0.145	0.793
-0.125	0.297	-0.132	0.621	-0.135	0.721	-0.134	0.481	-0.131	0.618	-0.136	0.742
-0.114	0.071	-0.124	0.521	-0.128	0.664	-0.126	0.253	-0.123	0.485	-0.128	0.687
-0.103	0.219	-0.116	0.384	-0.121	0.597	-0.117	0.093	-0.115	0.385	-0.120	0.622
-0.092	0.553	-0.108	0.205	-0.113	0.548	-0.108	0.298	-0.107	0.174	-0.112	0.532
-0.082	0.751	-0.100	0.084	-0.106	0.441	-0.100	0.572	-0.099	0.115	-0.103	0.400
-0.071	1.049	-0.092	0.249	-0.099	0.294	-0.091	0.832	-0.091	0.333	-0.095	0.221
-0.060	1.134	-0.084	0.390	-0.091	0.180	-0.082	1.063	-0.083	0.582	-0.087	0.087
-0.049	1.144	-0.076	0.618	-0.084	0.088	-0.074	1.355	-0.075	0.820	-0.079	0.236
-0.038	1.123	-0.068	0.829	-0.077	0.241	-0.065	1.355	-0.067	0.952	-0.070	0.463
-0.027	1.112	-0.060	1.024	-0.069	0.387	-0.056	1.379	-0.059	1.142	-0.062	0.688
-0.016	1.049	-0.052	1.197	-0.062	0.604	-0.048	1.387	-0.051	1.226	-0.054	0.814
-0.005	0.995	-0.044	1.298	-0.055	0.807	-0.039	1.392	-0.044	1.265	-0.045	1.004
0.005	1.256	-0.036	1.299	-0.048	0.939	-0.030	1.413	-0.036	1.304	-0.037	1.139
		-0.028	1.271	-0.040	1.100	-0.022	1.396	-0.028	1.321	-0.029	1.210
		-0.020	1.266	-0.033	1.219	-0.013	1.320	-0.020	1.255	-0.021	1.226
		-0.012	0.865	-0.026	1.281	-0.004	1.062	-0.012	1.224	-0.012	1.186
		-0.004	1.261	-0.018	1.316	0.004	1.429	-0.004	0.831	-0.004	0.966
		0.004	1.185	-0.011	1.186	0.013	1.403	0.004	1.226	0.004	1.258
		0.012	1.325	-0.004	0.875	0.022	1.428	0.012	1.284	0.012	1.278
				0.004	1.004	0.030	1.430	0.020	1.272	0.021	1.272
				0.011	1.250	0.039	1.431	0.028	1.338	0.029	1.277
				0.018	0.902	0.048	1.431	0.036	1.332	0.037	1.278
						0.056	1.431	0.044	1.328	0.045	1.282
						0.065	1.429	0.051	1.333	0.054	1.288
						0.074	1.428	0.059	1.313	0.062	1.295
								0.067	1.189	0.070	1.324
								0.075	1.349		

6.0 mm Lifter Heights						10.0 mm Lifter Heights					
20 % Fill		30 % Fill		40 % Fill		20 % Fill		30 % Fill		40 % Fill	
R (m)	Vx (m/s)	R (m)	Vx (m/s)	R (m)	Vx (m/s)	R (m)	Vx (m/s)	R (m)	Vx (m/s)	R (m)	Vx (m/s)
-0.151	0.829	-0.151	0.819	-0.152	0.815	-0.152	0.808	-0.150	0.818	-0.153	0.814
-0.142	0.704	-0.143	0.765	-0.145	0.792	-0.144	0.737	-0.142	0.771	-0.146	0.778
-0.134	0.530	-0.136	0.695	-0.138	0.744	-0.135	0.667	-0.135	0.710	-0.138	0.752
-0.125	0.306	-0.128	0.643	-0.131	0.711	-0.127	0.471	-0.127	0.623	-0.131	0.702
-0.116	0.095	-0.120	0.518	-0.124	0.657	-0.119	0.209	-0.119	0.553	-0.123	0.646
-0.108	0.276	-0.112	0.337	-0.117	0.591	-0.111	0.138	-0.112	0.382	-0.116	0.610
-0.099	0.565	-0.105	0.125	-0.110	0.541	-0.103	0.425	-0.104	0.162	-0.108	0.535
-0.091	0.837	-0.097	0.168	-0.103	0.433	-0.094	0.726	-0.096	0.135	-0.101	0.423
-0.082	1.082	-0.089	0.315	-0.096	0.341	-0.086	1.001	-0.089	0.374	-0.093	0.265
-0.073	1.334	-0.081	0.569	-0.089	0.163	-0.078	1.166	-0.081	0.541	-0.086	0.148
-0.065	1.319	-0.074	0.810	-0.082	0.096	-0.070	1.206	-0.073	0.793	-0.078	0.110
-0.056	1.312	-0.066	1.032	-0.074	0.207	-0.062	1.213	-0.065	1.022	-0.071	0.309
-0.047	1.362	-0.058	1.192	-0.067	0.428	-0.053	1.239	-0.058	1.174	-0.063	0.459
-0.039	1.371	-0.050	1.235	-0.060	0.586	-0.045	1.211	-0.050	1.213	-0.056	0.688
-0.030	1.386	-0.043	1.250	-0.053	0.800	-0.037	1.208	-0.042	1.232	-0.049	0.895
-0.022	1.364	-0.035	1.251	-0.046	0.981	-0.029	1.207	-0.035	1.262	-0.041	1.063
-0.013	1.359	-0.027	1.271	-0.039	1.097	-0.021	1.191	-0.027	1.283	-0.034	1.151
-0.004	0.970	-0.019	1.308	-0.032	1.203	-0.012	1.164	-0.019	1.285	-0.026	1.225
0.004	1.361	-0.012	1.139	-0.025	1.249	-0.004	0.837	-0.012	1.206	-0.019	1.263
0.013	1.437	-0.004	0.812	-0.018	1.278	0.004	1.201	-0.004	0.839	-0.011	1.214
0.022	1.430	0.004	1.183	-0.011	1.175	0.012	1.226	0.004	1.219	-0.004	0.836
0.030	1.424	0.012	1.263	-0.004	0.905	0.021	1.259	0.012	1.243	0.004	1.233
0.039	1.432	0.019	1.336	0.004	1.244	0.029	1.274	0.019	1.334	0.011	1.259
0.047	1.431	0.027	1.338	0.011	1.368	0.037	1.258	0.027	1.332	0.019	1.339
0.056	1.431	0.035	1.336	0.018	1.361	0.045	1.272	0.035	1.322	0.026	1.323
0.065	1.431	0.043	1.330	0.025	1.333	0.053	1.314	0.042	1.322	0.034	1.323
0.073	1.430	0.050	1.327	0.032	1.374	0.062	1.299	0.050	1.311	0.041	1.359
0.082	1.424	0.058	1.352	0.039	1.368	0.070	1.301	0.058	1.347	0.049	1.347
		0.066	1.301	0.046	1.391	0.078	1.298	0.065	1.330	0.056	1.313
		0.074	1.270	0.053	1.371	0.086	1.258	0.073	1.307	0.063	1.347
		0.081	1.340	0.060	1.356			0.081	1.281	0.071	1.374
				0.067	1.382			0.089	1.338	0.078	1.363
				0.074	1.389					0.086	1.362
				0.082	1.405					0.093	1.378
				0.089	1.401						

Table 33: Velocity profile data points and corresponding radial distance from the mill centre at 70 % crit. speed and all filling and lifter height settings.

1.5 mm Lifter Heights						3.0 mm Lifter Heights						6.0 mm Lifter Heights						10.0 mm Lifter Heights					
20 % Fill		30 % Fill		40 % Fill		20 % Fill		30 % Fill		40 % Fill		20 % Fill		30 % Fill		40 % Fill		20 % Fill		30 % Fill		40 % Fill	
R (m)	Vx (m/s)	R (m)	Vx (m/s)	R (m)	Vx (m/s)	R (m)	Vx (m/s)	R (m)	Vx (m/s)	R (m)	Vx (m/s)	R (m)	Vx (m/s)	R (m)	Vx (m/s)	R (m)	Vx (m/s)	R (m)	Vx (m/s)	R (m)	Vx (m/s)	R (m)	Vx (m/s)
-0.155	0.885	-0.154	0.957	-0.154	0.989	-0.156	0.984	-0.151	1.011	-0.154	1.013	-0.149	0.946	-0.148	0.969	-0.150	0.983	-0.149	0.976	-0.148	0.971	-0.148	0.979
-0.145	0.697	-0.146	0.886	-0.147	0.952	-0.147	0.885	-0.143	0.926	-0.147	0.991	-0.142	0.847	-0.140	0.884	-0.142	0.917	-0.141	0.907	-0.140	0.891	-0.141	0.915
-0.136	0.563	-0.137	0.773	-0.140	0.912	-0.139	0.636	-0.135	0.810	-0.139	0.924	-0.134	0.624	-0.132	0.771	-0.135	0.880	-0.134	0.693	-0.132	0.835	-0.133	0.879
-0.126	0.266	-0.129	0.643	-0.132	0.843	-0.130	0.339	-0.128	0.654	-0.131	0.853	-0.126	0.343	-0.125	0.677	-0.128	0.813	-0.126	0.376	-0.124	0.683	-0.125	0.810
-0.117	0.087	-0.121	0.473	-0.125	0.764	-0.121	0.110	-0.120	0.538	-0.124	0.770	-0.119	0.110	-0.117	0.468	-0.121	0.730	-0.118	0.126	-0.116	0.452	-0.118	0.725
-0.108	0.223	-0.112	0.254	-0.118	0.703	-0.112	0.317	-0.112	0.285	-0.116	0.708	-0.111	0.203	-0.110	0.206	-0.113	0.663	-0.111	0.254	-0.108	0.171	-0.110	0.602
-0.098	0.476	-0.104	0.089	-0.111	0.576	-0.103	0.626	-0.104	0.105	-0.109	0.561	-0.103	0.529	-0.102	0.107	-0.106	0.509	-0.103	0.638	-0.100	0.181	-0.103	0.494
-0.089	0.715	-0.096	0.261	-0.104	0.403	-0.094	0.948	-0.097	0.317	-0.101	0.353	-0.096	0.847	-0.095	0.291	-0.099	0.299	-0.095	0.962	-0.092	0.489	-0.095	0.267
-0.080	0.944	-0.087	0.512	-0.097	0.264	-0.085	1.161	-0.089	0.483	-0.094	0.206	-0.088	1.091	-0.087	0.599	-0.091	0.151	-0.088	1.122	-0.084	0.812	-0.087	0.096
-0.070	1.338	-0.079	0.754	-0.089	0.092	-0.076	1.183	-0.081	0.762	-0.086	0.115	-0.080	1.180	-0.079	0.879	-0.084	0.151	-0.080	1.169	-0.076	0.969	-0.080	0.293
-0.061	1.340	-0.071	0.967	-0.082	0.161	-0.067	1.183	-0.073	1.037	-0.079	0.358	-0.073	1.216	-0.072	1.015	-0.077	0.415	-0.073	1.181	-0.068	1.104	-0.072	0.471
-0.052	1.336	-0.062	1.070	-0.075	0.406	-0.058	1.186	-0.066	1.275	-0.071	0.640	-0.065	1.232	-0.064	1.124	-0.069	0.603	-0.065	1.198	-0.060	1.152	-0.065	0.763
-0.042	1.326	-0.054	1.197	-0.068	0.661	-0.049	1.218	-0.058	1.367	-0.064	0.794	-0.057	1.248	-0.057	1.177	-0.062	0.840	-0.057	1.209	-0.052	1.183	-0.057	0.958
-0.033	1.301	-0.046	1.231	-0.061	0.820	-0.040	1.227	-0.050	1.376	-0.056	1.062	-0.050	1.270	-0.049	1.209	-0.055	0.963	-0.050	1.221	-0.044	1.206	-0.049	1.046
-0.023	1.398	-0.037	1.247	-0.054	0.972	-0.031	1.232	-0.043	1.407	-0.049	1.224	-0.042	1.260	-0.042	1.225	-0.047	1.033	-0.042	1.220	-0.036	1.235	-0.042	1.092
-0.014	1.385	-0.029	1.257	-0.047	1.058	-0.022	1.205	-0.035	1.433	-0.041	1.295	-0.034	1.263	-0.034	1.254	-0.040	1.090	-0.034	1.242	-0.028	1.260	-0.034	1.142
-0.005	0.961	-0.021	1.260	-0.039	1.127	-0.013	1.243	-0.027	1.461	-0.034	1.322	-0.027	1.261	-0.026	1.274	-0.033	1.135	-0.027	1.240	-0.020	1.206	-0.027	1.185
0.005	1.371	-0.012	1.250	-0.032	1.185	-0.004	0.890	-0.019	1.487	-0.026	1.374	-0.019	1.298	-0.019	1.289	-0.026	1.169	-0.019	1.292	-0.012	1.194	-0.019	1.217
0.014	1.396	-0.004	0.879	-0.025	1.224	0.004	1.259	-0.012	1.376	-0.019	1.423	-0.011	1.200	-0.011	1.216	-0.018	1.209	-0.011	1.225	-0.004	0.852	-0.011	1.171
0.023	1.405	0.004	1.249	-0.018	1.262	0.013	1.260	-0.004	0.963	-0.011	1.333	-0.004	0.829	-0.004	0.855	-0.011	1.064	-0.004	0.804	0.004	1.197	-0.004	0.808
0.033	1.342	0.012	1.276	-0.011	1.128	0.022	1.255	0.004	1.372	-0.004	0.966	0.004	1.221	0.004	1.208	-0.004	0.827	0.004	1.188	0.012	1.217	0.004	1.200
0.042	1.363	0.021	1.279	-0.004	0.841	0.031	1.260	0.012	1.393	0.004	1.363	0.011	1.121	0.011	1.205	0.004	1.195	0.011	1.222	0.020	1.239	0.011	1.234
0.052	1.373	0.029	1.293	0.004	1.233	0.040	1.273	0.019	1.502	0.011	1.389	0.019	1.327	0.019	1.335	0.011	1.310	0.019	1.301	0.028	1.293	0.019	1.307
0.061	1.381	0.037	1.303	0.011	1.352	0.049	1.288	0.027	1.482	0.019	1.500	0.027	1.297	0.026	1.290	0.018	1.320	0.027	1.279	0.036	1.299	0.027	1.293
0.070	1.388	0.046	1.289	0.018	1.344	0.058	1.255	0.035	1.475	0.026	1.488	0.034	1.315	0.034	1.309	0.026	1.290	0.034	1.286	0.044	1.304	0.034	1.298
		0.054	1.287	0.025	1.340	0.067	1.258	0.043	1.474	0.034	1.475	0.042	1.282	0.042	1.309	0.033	1.320	0.042	1.292	0.052	1.300	0.042	1.313
		0.062	1.308	0.032	1.374	0.076	1.256	0.050	1.468	0.041	1.520	0.050	1.349	0.049	1.341	0.040	1.334	0.050	1.333	0.060	1.295	0.049	1.344
		0.071	1.334	0.039	1.372	0.085	1.269	0.058	1.503	0.049	1.511	0.057	1.345	0.057	1.343	0.047	1.347	0.057	1.334	0.068	1.310	0.057	1.339
				0.047	1.376	0.094	1.273	0.066	1.502	0.056	1.503	0.065	1.345	0.064	1.339	0.055	1.370	0.065	1.336	0.076	1.310	0.065	1.337
				0.054	1.390	0.103	1.284	0.073	1.491	0.064	1.503	0.073	1.336	0.072	1.341	0.062	1.269	0.073	1.319	0.084	1.329	0.072	1.331
				0.061	1.387	0.112	1.286	0.081	1.494	0.071	1.526	0.080	1.337	0.079	1.359	0.069	1.369	0.080	1.347	0.092	1.327	0.080	1.348
				0.068	1.398	0.121	1.277	0.089	1.490	0.079	1.524	0.088	1.361	0.087	1.358	0.077	1.372	0.088	1.330	0.100	1.332	0.087	1.347
				0.075	1.460	0.130	1.271	0.097	1.514	0.086	1.519	0.096	1.356	0.095	1.357	0.084	1.378	0.095	1.341	0.108	1.333	0.095	1.357
								0.104	1.512	0.094	1.516	0.103	1.356	0.102	1.357	0.091	1.380	0.103	1.336	0.116	1.326	0.103	1.360
								0.112	1.508	0.101	1.535	0.111	1.354	0.110	1.372	0.099	1.380	0.111	1.347	0.124	1.302	0.110	1.376
								0.120	1.500	0.109	1.530	0.119	1.348	0.117	1.356	0.106	1.387	0.118	1.351			0.118	1.358
								0.128	1.515	0.116	1.524	0.126	1.359	0.125	1.361	0.113	1.367	0.126	1.362			0.125	1.359
										0.124	1.538					0.121	1.365						
																0.128	1.386						

The table below lists the trend-line equations and R^2 correlations for the linear relation between the mill shell and the charge free surface.

Table 34: Linear trend line equations for the velocity profile between the mill shell and charge free surface at all operating conditions.

	20 % Filling					
Lifter Height	**55 % Crit.**		**70 % Crit.**		**85 % Crit.**	
1.5 mm	y = -18.036 x - 2.0407	R^2 = 0.9762	y = -22.569 x - 2.5792	R^2 = 0.9908	y = -25.13 x - 2.9264	R^2 = 0.9945
3.0 mm	y = -22.051 x - 2.5484	R^2 = 0.9899	y = -28.257 x - 3.3566	R^2 = 0.9886	y = -32.18 x - 3.8936	R^2 = 0.9888
6.0 mm	y = -22.581 x - 2.5774	R^2 = 0.9753	y = -29.047 x - 3.4166	R^2 = 0.9859	y = -35.01 x - 4.1314	R^2 = 0.9896
10.0 mm	y = -22.815 x - 2.6539	R^2 = 0.9629	y = -29.310 x - 3.4182	R^2 = 0.9638	y = -38.00 x - 4.4894	R^2 = 0.9769
	30 % Filling					
Lifter Height	**55 % Crit.**		**70 % Crit.**		**85 % Crit.**	
1.5 mm	y = -17.776 x - 1.8659	R^2 = 0.9432	y = -21.145 x - 2.1927	R^2 = 0.9717	y = -23.987 x - 2.5488	R^2 = 0.9827
3.0 mm	y = -19.214 x - 2.0147	R^2 = 0.9506	y = -23.872 x - 2.5221	R^2 = 0.9788	y = -28.101 x - 3.0038	R^2 = 0.9806
6.0 mm	y = -18.890 x - 1.9712	R^2 = 0.9468	y = -23.287 x - 2.4526	R^2 = 0.9672	y = -28.022 x - 2.9715	R^2 = 0.9804
10.0 mm	y = -18.182 x - 1.8859	R^2 = 0.9470	y = -23.403 x - 2.4336	R^2 = 0.9629	y = -28.245 x - 2.994	R^2 = 0.9712
	40 % Filling					
Lifter Height	**55 % Crit.**		**70 % Crit.**		**85 % Crit.**	
1.5 mm	y = -15.367 x - 1.4245	R^2 = 0.9406	y = -18.667 x - 1.7182	R^2 = 0.9550	y = -20.726 x - 1.9185	R^2 = 0.9454
3.0 mm	y = -15.513 x - 1.4277	R^2 = 0.9318	y = -18.482 x - 1.7210	R^2 = 0.9504	y = -22.024 x - 2.0732	R^2 = 0.9378
6.0 mm	y = -15.223 x - 1.3853	R^2 = 0.9285	y = -17.883 x - 1.6176	R^2 = 0.9385	y = -21.160 x - 1.9386	R^2 = 0.9333
10.0 mm	y = -15.148 x - 1.3594	R^2 = 0.9185	y = -17.777 x - 1.6011	R^2 = 0.9390	y = -21.094 x - 1.9071	R^2 = 0.9278

The tables below list the trend-line equations and R^2 correlations for the linear and non-linear relation between the mill shell and CoC location.

Table 35: Linear trend line equations for the velocity profile between the mill shell and CoC location at all operating conditions.

	20 % Filling					
Lifter Height	**55 % Crit.**		**70 % Crit.**		**85 % Crit.**	
1.5 mm	y = - 12.657 x - 1.3329	R^2 = 0.9866	y = - 18.778 x - 2.0723	R^2 = 0.9912	y = - 21.648 x - 2.4401	R^2 = 0.9869
3.0 mm	y = - 16.455 x - 1.7761	R^2 = 0.9722	y = - 21.619 x - 2.4413	R^2 = 0.9962	y = - 25.666 x - 2.9649	R^2 = 0.9786
6.0 mm	y = - 15.333 x - 1.5985	R^2 = 0.9477	y = - 21.610 x - 2.3975	R^2 = 0.9888	y = - 28.425 x - 3.2336	R^2 = 0.9781
10.0 mm	y = - 13.961 x - 1.4266	R^2 = 0.9393	y = - 17.894 x - 1.8429	R^2 = 0.9510	y = - 29.219 x - 3.2889	R^2 = 0.9611
	30 % Filling					
Lifter Height	**55 % Crit.**		**70 % Crit.**		**85 % Crit.**	
1.5 mm	y = - 10.195 x - 0.8671	R^2 = 0.9190	y = - 14.359 x - 1.3193	R^2 = 0.9682	y = - 17.877 x - 1.7246	R^2 = 0.9759
3.0 mm	y = - 10.953 x - 0.9457	R^2 = 0.9471	y = - 15.022 x - 1.3752	R^2 = 0.9823	y = - 19.724 x - 1.8983	R^2 = 0.9758
6.0 mm	y = - 10.10 x - 0.8237	R^2 = 0.9401	y = - 14.338 x - 1.2776	R^2 = 0.9239	y = - 20.034 x - 1.9178	R^2 = 0.9668
10.0 mm	y = - 9.9219 x - 0.7992	R^2 = 0.9317	y = - 13.736 x - 1.1726	R^2 = 0.9487	y = - 19.551 x - 1.8336	R^2 = 0.9224
	40 % Filling					
Lifter Height	**55 % Crit.**		**70 % Crit.**		**85 % Crit.**	
1.5 mm	y = - 7.6527 x - 0.4653	R^2 = 0.9240	y = - 11.067 x - 0.7852	R^2 = 0.9576	y = - 13.805 x - 1.0295	R^2 = 0.9416
3.0 mm	y = - 7.9929 x - 0.5084	R^2 = 0.9384	y = - 10.959 x - 0.7705	R^2 = 0.9281	y = - 14.007 x - 1.0345	R^2 = 0.9509
6.0 mm	y = - 7.7254 x - 0.4698	R^2 = 0.9314	y = - 10.251 x - 0.6642	R^2 = 0.9422	y = - 13.882 x - 1.0130	R^2 = 0.9504
10.0 mm	y = - 7.6159 x - 0.4395	R^2 = 0.9323	y = - 9.9381 x - 0.6249	R^2 = 0.9411	y = - 14.154 x - 1.0267	R^2 = 0.9360

Table 36: Non-linear trend line equations for the velocity profile between the mill shell and CoC location at all operating conditions.

	20 % Filling					
Lifter Height	**55 % Crit.**		**70 % Crit.**		**85 % Crit.**	
1.5 mm	$-122.83x^2 - 44.331x - 3.3537$	$R^2 = 0.9968$	$60.392x^2 - 3.0071x - 1.0517$	$R^2 = 0.9922$	$-118.12x^2 - 53.729x - 4.5977$	$R^2 = 0.9905$
3.0 mm	$-165.96x^2 - 60.0x - 4.6053$	$R^2 = 0.9835$	$-46.949x^2 - 34.236x - 3.2820$	$R^2 = 0.9967$	$-275.62x^2 - 102.03x - 8.2098$	$R^2 = 0.9913$
6.0 mm	$-325.19x^2 - 100.8x - 7.1603$	$R^2 = 0.9967$	$-212.23x^2 - 78.376x - 6.1619$	$R^2 = 0.9987$	$-398.48x^2 - 135.17x - 10.336$	$R^2 = 0.9939$
10.0 mm	$-287.98x^2 - 90.721x - 6.4833$	$R^2 = 0.9984$	$-203.76x^2 - 71.363x - 5.3106$	$R^2 = 0.9687$	$-568.90x^2 - 181.25x - 13.379$	$R^2 = 0.9909$
	30 % Filling					
Lifter Height	**55 % Crit.**		**70 % Crit.**		**85 % Crit.**	
1.5 mm	$-190.94x^2 - 58.725x - 3.8883$	$R^2 = 0.9961$	$-174.07x^2 - 57.660x - 3.9672$	$R^2 = 0.9957$	$-185.65x^2 - 65.79x - 4.7644$	$R^2 = 0.9977$
3.0 mm	$-170.55x^2 - 53.640x - 3.5658$	$R^2 = 0.9984$	$-82.107x^2 - 35.174x - 2.5910$	$R^2 = 0.9878$	$-215.25x^2 - 74.653x - 5.351$	$R^2 = 0.9966$
6.0 mm	$-144.21x^2 - 45.804x - 2.9821$	$R^2 = 0.9923$	$-295.84x^2 - 90.066x - 6.0524$	$R^2 = 0.9949$	$-216.44x^2 - 74.073x - 5.2413$	$R^2 = 0.9862$
10.0 mm	$-157.55x^2 - 49.188x - 3.1887$	$R^2 = 0.9965$	$-272.06x^2 - 82.651x - 5.4753$	$R^2 = 0.9773$	$-476.13x^2 - 141.35x - 9.5345$	$R^2 = 0.9969$
	40 % Filling					
Lifter Height	**55 % Crit.**		**70 % Crit.**		**85 % Crit.**	
1.5 mm	$-112.62x^2 - 34.588x - 2.0248$	$R^2 = 0.9939$	$-118.18x^2 - 38.721x - 2.3509$	$R^2 = 0.9950$	$-186.48x^2 - 59.173x - 3.7101$	$R^2 = 0.9979$
3.0 mm	$-101.14x^2 - 31.546x - 1.8294$	$R^2 = 0.9957$	$-159.98x^2 - 49.322x - 2.9974$	$R^2 = 0.9975$	$-152.13x^2 - 50.584x - 3.1623$	$R^2 = 0.9914$
6.0 mm	$-102.32x^2 - 31.554x - 1.8064$	$R^2 = 0.9938$	$-121.75x^2 - 38.732x - 2.2686$	$R^2 = 0.9943$	$-191.63x^2 - 59.541x - 3.6577$	$R^2 = 0.9772$
10.0 mm	$-94.963x^2 - 29.503x - 1.6475$	$R^2 = 0.9952$	$-133.43x^2 - 41.223x - 2.3908$	$R^2 = 0.9880$	$-208.33x^2 - 63.241x - 3.8378$	$R^2 = 0.9962$

The table below lists the trend-line equations and R^2 correlations for the non-linear relation between the CoC location and charge free surface.

Table 37: Non-linear trend line equations for the velocity profile between the CoC location and the charge free surface at all operating conditions.

	20 % Filling					
Lifter Height	**55 % Crit.**		**70 % Crit.**		**85 % Crit.**	
1.5 mm	$y = -21.197x - 2.317$	$R^2 = 0.9923$	$y = -25.736x - 2.8831$	$R^2 = 0.9905$	$y = -27.266x - 3.1356$	$R^2 = 0.9962$
3.0 mm	$y = -27.100x - 3.019$	$R^2 = 0.9883$	$y = -32.821x - 3.8063$	$R^2 = 0.9890$	$y = -35.488x - 4.2358$	$R^2 = 0.9871$
6.0 mm	$y = -26.095x - 2.9192$	$R^2 = 0.9912$	$y = -33.797x - 3.8866$	$R^2 = 0.9935$	$y = -39.783x - 4.6227$	$R^2 = 0.9976$
10.0 mm	$y = -27.135x - 3.0898$	$R^2 = 0.9895$	$y = -35.255x - 4.0417$	$R^2 = 0.9997$	$y = -47.761x - 5.5371$	$R^2 = 0.9985$
	30 % Filling					
Lifter Height	**55 % Crit.**		**70 % Crit.**		**85 % Crit.**	
1.5 mm	$y = -22.071x - 2.2491$	$R^2 = 0.9850$	$y = -26.735x - 2.6494$	$R^2 = 0.9907$	$y = -27.994x - 2.9097$	$R^2 = 0.9754$
3.0 mm	$y = -26.534x - 2.5933$	$R^2 = 0.9959$	$y = -30.244x - 3.0133$	$R^2 = 0.9583$	$y = -34.511x - 3.5637$	$R^2 = 0.9897$
6.0 mm	$y = -24.843x - 2.4482$	$R^2 = 0.9971$	$y = -28.422x - 2.8806$	$R^2 = 0.9956$	$y = -37.450x - 3.7938$	$R^2 = 0.9727$
10.0 mm	$y = -25.869x - 2.4712$	$R^2 = 0.9784$	$y = -27.421x - 2.7839$	$R^2 = 0.9960$	$y = -36.416x - 3.8037$	$R^2 = 0.9858$
	40 % Filling					
Lifter Height	**55 % Crit.**		**70 % Crit.**		**85 % Crit.**	
1.5 mm	$y = -21.268x - 1.7813$	$R^2 = 0.9930$	$y = -24.913x - 2.1086$	$R^2 = 0.9833$	$y = -27.371x - 2.4299$	$R^2 = 0.9745$
3.0 mm	$y = -23.063x - 1.8745$	$R^2 = 0.9926$	$y = -24.045x - 2.0992$	$R^2 = 0.9788$	$y = -37.137x - 3.1985$	$R^2 = 0.9623$
6.0 mm	$y = -22.888x - 1.8389$	$R^2 = 0.9954$	$y = -27.687x - 2.24$	$R^2 = 0.9861$	$y = -28.062x - 2.5419$	$R^2 = 0.9877$
10.0 mm	$y = -23.678x - 1.8545$	$R^2 = 0.9866$	$y = -24.240x - 2.0257$	$R^2 = 0.9911$	$y = -28.873x - 2.6009$	$R^2 = 0.9936$

The figures below illustrate the difference between the velocity profile and the pressure gradient along the diametric line at all critical speed and filling levels.

55 %, 70 % & 85 % Crit. speed, 30 % filling, 1.5 mm lifter heights

20 %, 30 % & 40 % filling, 55 % Crit. speed, 1.5 mm lifter heights

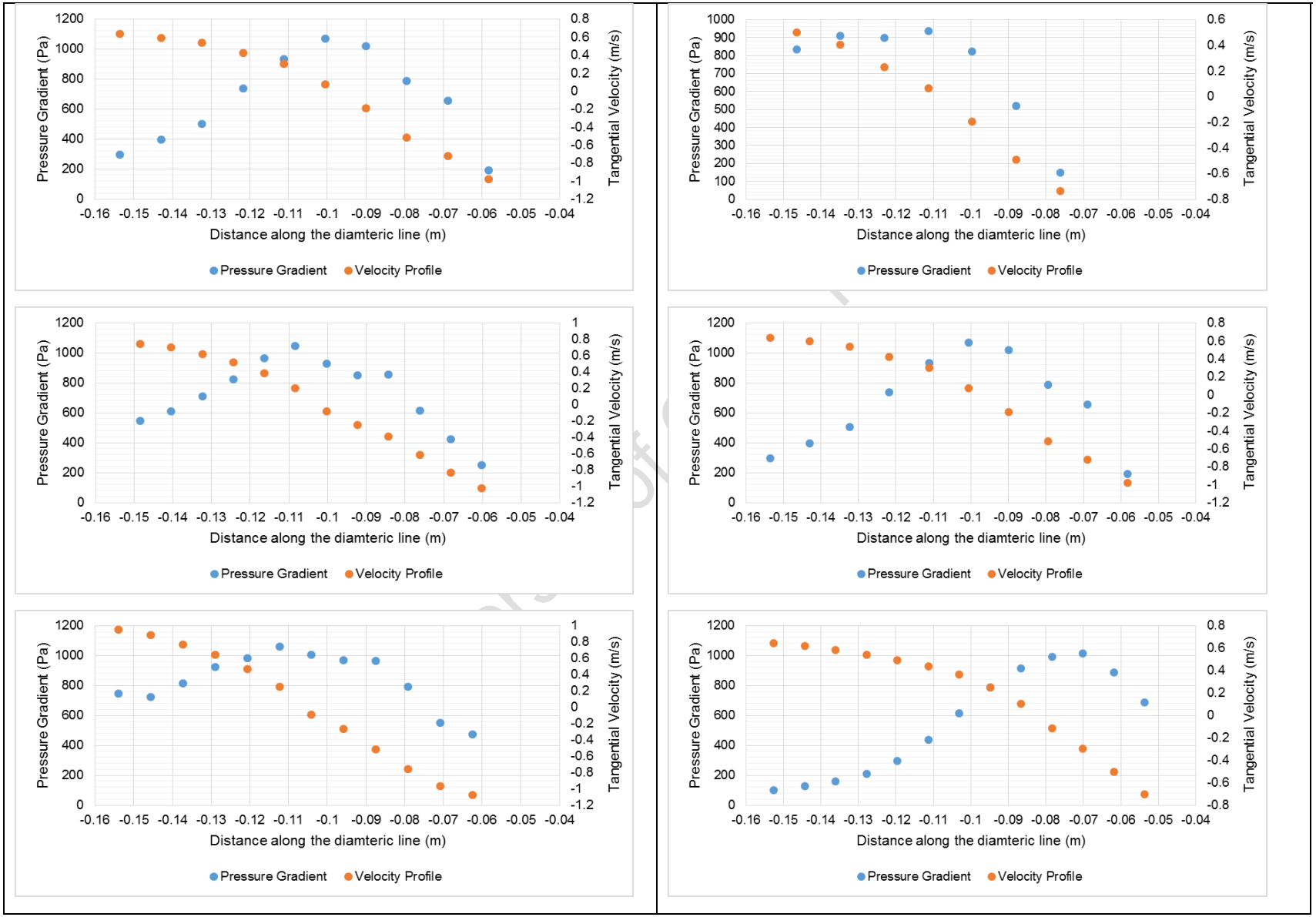

Figure 112: Difference between the velocity profile and pressure gradient along the diametric line at 30 % filling and 55 % crit. speed.